Sensing and Understanding the Resilience of Sandstone

Jessica Maria Irmgard Dassow

BSc and MSc, University of Göttingen

Submitted in fulfilment of the requirements for the degree of

Doctor of Philosophy

School of Geographical and Earth Sciences
College of Science and Engineering
University of Glasgow

October 2018

When stones are incorporated into buildings their mineralogical composition and texture alters to adapt to the new environmental conditions. One of the most common building stones in Scotland is sandstone. Due to its high porosity and mineralogical composition sandstones can be prone to weathering. Scotland's diverse stone built heritage is endangered by frequent changes in environmental conditions such as cyclic wetting and drying and temperature changes caused by insolation. Buildings also face increased pressure through climate change. In Scotland, the decay of sandstone is a serious problem that urgently requires new approaches to preserve built heritage and to reduce maintenance costs. It is therefore important to understand the extent and timescales of weathering processes.

New approaches to assess stone decay are required for deciding on the best conservation strategy for historic buildings. These approaches or tools need to be minimally or non-invasive, portable and provide a consistent method to gain empirical data for evaluation of the progress of weathering. This project aims to develop two new in-situ techniques that can assess the state of decay of building stones beneath their outer surface. The developed techniques use a laser interferometer to measure dilation over time and an ultrasonic drilling tool to estimate the structural properties of the stones. These measurements are joint with micro-climate monitoring of sandstones to enable a combined assessment of stone decay.

The laser interferometer can measure decay induced contraction or expansion of stones on the nanometre scale. Salt crystallisation in porous systems can be examined with very high precision under any temperature and humidity condition that enable salt growth. Characterising dilation events through precise measurement of displacement and its frequency can provide insight on the intensity of decay of the building material. The drying behaviour of different samples (unweathered, weathered and artificially weathered) was monitored to enable the differentiation of rock type and state of decay.

The ultrasonic drilling tool allows identification of changes in the structure of a sample while drilling a hole up to 4 cm depth. By continuously measuring the power required to drill, porosity changes and/or the presence of salt at depth can be mapped. The use of ultrasonic tools enables penetration of the rock with less average force on the stone and a faster progress rate into hard materials without a significant wear effect on the drill bits. Operational settings can be kept constant for different physical properties of the rocks such as compressive strength. Monitoring of the power consumption enables to determine different stone types and the location of salt accumulation/damage in artificially weathered sandstones.

Micro-climate monitoring includes the measurement of temperature and humidity changes at the surface of building stones. The analysis enables an identification of areas that suffer from increased stress caused by frequent and high rates of changes in temperature and humidity. A study at four historic buildings was conducted for nearly two years. The sites

include the University of Glasgow, Dunkeld Cathedral, Jedburgh Abbey and Fort Charlotte (Shetland Islands). Seasonal changes, stone type and north-south elongation were evaluated for determining rocks with increased weathering risks.

The developed techniques provide a more precise identification of stone weathering and allow for better prediction of the decay processes. The techniques allow up-scaling from the lab to the field, and can potentially be used in-situ on historical buildings under site conditions.

Table of contents

List of tables

List of figures

Acknowledgements

First of all I'd like to thank the funders of this project, Historic Environment Scotland (HES) and the University of Glasgow. I am very grateful to have been given the chance to work in one of the most beautiful countries I have ever travelled to. I would also like to acknowledge *Stancliff stones*, *Tradstocks*, Ged Smith from *Forticrete Ltd* and HES for the provision of the sample material from quarries and historic sites. I would also like to thank *Element six* for their help in developing the PCD drill bit and *SAGES* for the financial support.

For their continuous support I'd like to thank my supervisors Martin Lee, Stefan Hild, Patrick Harkness, Larissa Naylor, Maureen Young and my former HES supervisor Alick Leslie. Especially I'd like to thank Martin, who, although very busy, always had an open door and ear for all sorts of problems and usually came up with a solution or, not less valuable, great advise. Many thanks to Stefan for getting me started in Scotland and in the wide field of thinking more like a physicist.

A special thanks goes to the HES staff at the sites that helped in retrieving the samples for monitoring. I'd like to especially thank Laurence Fleck at Fort William for the constant effort in updating the temperature and humidity loggers every few months. Furthermore I like to thank Callum Graham for his advise and expertise on building stones.

At Glasgow University I want to thank Xuan Li for the support with the development of the ultrasonic drilling tool. Special thanks goes to John Gilleece for his continuous help with heavy sandstones and their preparation as well as getting familiar with the Glaswegian dialect. Many thanks to Peter Chung for his excellent expertise in sample preparation at the Imaging Spectroscopy and Analysis Centre, to Kenny for his technical support and driving qualities, and to Gary for his open ear for IT issues.

A special thanks goes to Sapphire for numerous hours spent with me driving to sites, which I only had to repay in cake. Furthermore to Bianca, for the best and necessary breaks we spent together to top up on caffeine or sugar. I also want to thank Margot, Ash and Susan for their company on adventurous weekend trips. To my family for their understanding and to the Archery Club for keeping me busy with other things at the university.
Finally to Annemarie and Sean, my safety buoys. The PhD (and I guess life) would have been very difficult without your constant understanding and support.

Author's declaration

I, Jessica Dassow, declare that this thesis and the work presented in it are my own other than where I acknowledged the work of others. The conducted research has only been submitted to the University of Glasgow and for no other degree or at any other university. Any published or unpublished work by other authors has been given full acknowledgement in the text.

Signed:

_____

Date:

_____

Chapter 1

Introduction

This research focuses on the development of minimally invasive techniques to assess the state of decay of building materials on length scales from nanometres to centimetres. The Chapter gives an overview of the research aims and structure. An introduction to building stone weathering is presented and common in-situ techniques to investigate decay are introduced.

1.1 Research aims and thesis structure

The thesis presents a multidisciplinary approach targeting to improve the assessment of stone decay in-situ. Three minimally invasive approaches are investigated to quantify building stone decay. A laser interferometer, an ultrasonic drilling tool and micro-climate monitoring are developed and/or evaluated during the project.
Comparable empirical data, rather than qualitative observations, are needed to enable an informed assessment of the decay of building materials. Minimally or non-invasive techniques are required to enable a non-destructive assessment of the stone to decide on the best method of preservation. Weathering alters the building material until complete breakdown. Knowing the building stone's new properties, given by the state of decay, informs decisions on replacement of stones and the strategy for their conservation.

The importance of the study lies in the preservation of cultural heritage in Scotland. Scotland's stone built heritage is very varied owing to its great geological diversity. From north to south of Scotland metamorphic, igneous and sedimentary rocks are represented from the Archean with up to 4 billion years old gneiss and other metamorphic rocks (McMillan & Hyslop 2005). This variety can be found in the building stones of entire cities (such as Aberdeen 'the granite city'), villages and historical buildings all over Scotland. The historic buildings include prehistoric structures (such as Skara Brae and Mousa Broch), Roman masonry, churches and castles, palaces and entire street facades, as well as tenement buildings

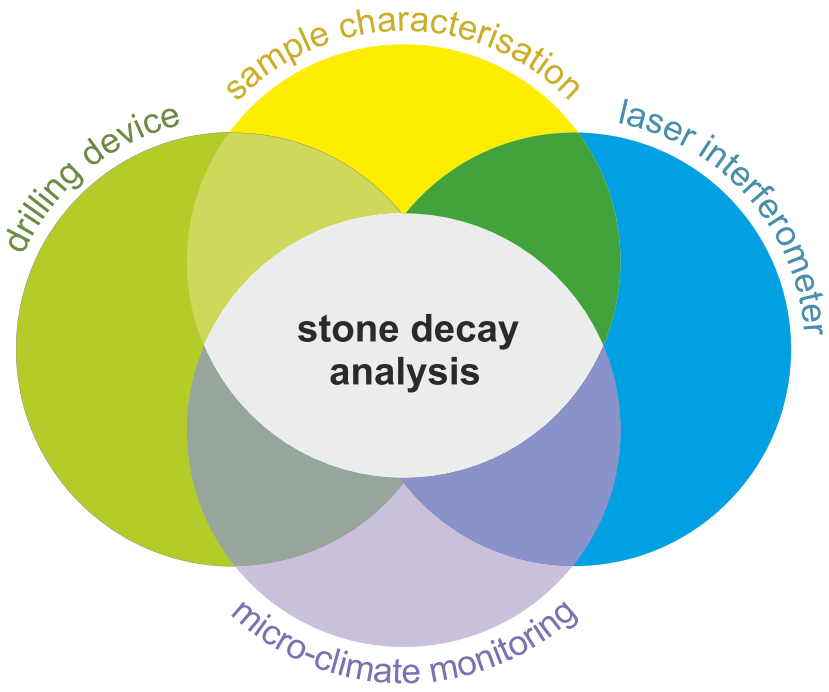

Figure 1.1: Overview of the different sections of the thesis to develop new methods to quantitatively assess building stone decay. In Chapter 2 the sample material is characterised. Chapter 3 includes the work with the laser interferometer and Chapter 4 the drilling tool. Chapter 5 covers micro-climate monitoring of different sites.

and museums. More recent buildings with Scottish building stones include, for example, the Scottish Parliament in Edinburgh. Historic buildings mainly reflect the local geology. Before railway transportation building stones were often quarried within a few kilometres of the construction site.

Scotland has about half a million traditional buildings (before 1919) made of stone, not including bridges and other structures (Gillespie & Tracey 2016). This historic environment is for most overseas visitors what defines Scotland as a nation (Historic Environment Scotland 2017). Over 4.3 million people visited properties of Historic Environment Scotland (HES) in 2016/2017 (Historic Environment Scotland 2017). HES supports 60000 jobs which is around 2.5% of Scotland's total employment (Historic Environment Scotland 2015). In 2015, spending by tourists in Scotland generated around £11 billion of economic activity in the wider Scottish supply chain and contributes around £6 billion of Scottish GDP. This represents about 4.5% of total Scottish GDP (Scottish Government 2017). The number of visits to Scotland in 2016 reached 14.3 million. A preservation of this cultural heritage is therefore of worldwide interest. Recent example of the importance of the restoration of historical buildings in the UK is the £369 million refurbishment of the Buckingham Place that started in 2016 (BBC 2016).

Next to the economic value generated by tourism, the stone industry and conservation has a long tradition in Scotland. More than 3500 quarries have been recorded over the last

centuries all over Scotland (Gillespie & Tracey 2016). Sedimentary rocks are the largest group of quarried stones in the UK with the highest number of active quarries producing the greatest volume of building stones (BGS 2007). In Scotland, over 40000 tonnes of building stones are produced annually, around 80% of which compromise sand- and siltstones. Over the last decade the country exported 60000 - 200000 tonnes of building stones with an average value of roughly £550 per tonne (Gillespie & Tracey 2016); however, Scotland still imports more building stone than it exports. Compared to cement and brick, only half the amount of CO_2 arise from the production of building stones such as granite and sandstone (Gillespie & Tracey 2016). Another environmental benefit is the reduction in length of transport routes when using local stones.

In Scotland, the decay of sandstone is a serious problem that urgently requires new approaches to preserve built heritage and to reduce maintenance costs (Scottish Government 2014, Hyslop et al. 2006, Hyslop & Albornoz-Parra 2008). It is therefore important to understand the extent and exact timescale of weathering processes. In the past decades buildings have faced increased pressure through climate change. More and better non-destructive, in-situ, quantitative techniques to analyse decay precisely are needed. The level or state of decay is often evaluated visually and subjectively. Better tools that unify and classify the damage investigations are still required.
A detailed characterisation of the damage enables the decision for the best conservation strategy. The laser interferometer allows precise measurements of expansion and contraction of stones. The observation of frequencies of those processes should help identifying underlying weathering processes. The ultrasonic drilling device enables a constant and easy penetration of building stone. During drilling, a feedback signal allows deduction the physical properties of the rock while drilling a small hole of 3 mm diameter. Environmental monitoring, with temperature and humidity recordings, is needed to asses the behaviour of the building stones during a year. It helps to make predictions about future trends and allows identification of areas of sever decay or that are likely to develop future failures.

Structure of the thesis

The next section of the Introduction gives an overview of sandstone weathering, causes and influences and how building stone decay can be investigated with non-destructive or minimally destructive techniques. Chapter 2 covers the sample material with a detailed petrological description and the artificial weathering of some samples. Chapter 3 includes the function and application of the laser interferometer. The following Chapter describes the development of the ultrasonic drilling tool for in-situ rock characterisation. Chapter 5 covers the use of environmental or micro-climate monitoring to evaluate the localisation of decay. The last Chapter combines the results and conclusions to assess the performance of

the techniques under the aspect of minimally invasive sandstone resilience investigation.

1.2 Sandstone weathering

1.2.1 Sandstones

Sedimentary rocks cover 75% of the Earth's surface (Press et al. 2008). They can be grouped into clastic, biogenic, chemical and other sedimentary rocks (such as pyroclastic sedimentary rocks). Sandstones belong to the clastic sedimentary rocks along with conglomerates, breccias and mudstones. The formation of this group is characterised through their composition of cemented mineral grains and rock fragments. After the transport and deposition of the mineral grains and rock fragments, the rocks are lithified through diagenesis. Diagenesis includes the compaction and cementation of the rock. Especially clastic sediments allow the deduction of the source region of the rock fragments but also the conditions of transport and diagenesis. The sediments are used to reconstruct the paleoclimatology as well as the paleogeography.

Sandstones mainly contain quartz, feldspar and other lithic fragments (such as micas or oxides). One of the most common classifications for sandstones was introduced by *Dott* combining the mineralogy and matrix of the rock (Pettijohn 1975). Figure 1.2 gives an overview of the nomenclature for sandstones.
The constituent grains of sandstones are mostly sand sized (0.063 - 2 mm). Sandstones are described through their mineral composition, matrix content and textural properties such as grain size, grain sorting, grain angularity, grain contacts, and fabric properties such as orientation and bedding. These properties are sometimes summarised with the term *maturity*. *Compositional maturity* describes the amount of quartz compared to the unstable minerals (clay minerals, feldspar) from mature to immature (only small amounts of quartz). *Textural maturity* summarises the content of matrix, and the sorting and roundness of the grains. Immature sandstones are characterised in this case by high content of clay sized particles and poorly rounded and sorted grains (Boggs-Junior 2014).

Because of the diversity in their mineral composition, as well as texture and formation conditions, the physical properties of sandstones can vary significantly. Physical proprieties include for example density, porosity, permeability but also uniaxial compressive strength (UCS). UCS of sandstones can be very low or go up to above 100 MPa. The porosity can vary from 0.5 to 35% with average porosities of 15 - 20% (Pettijohn 1975).
Structural properties of sandstones are often characterised by their strength (stress and strain properties). It describes the load that a material can withstand before failure or plas-

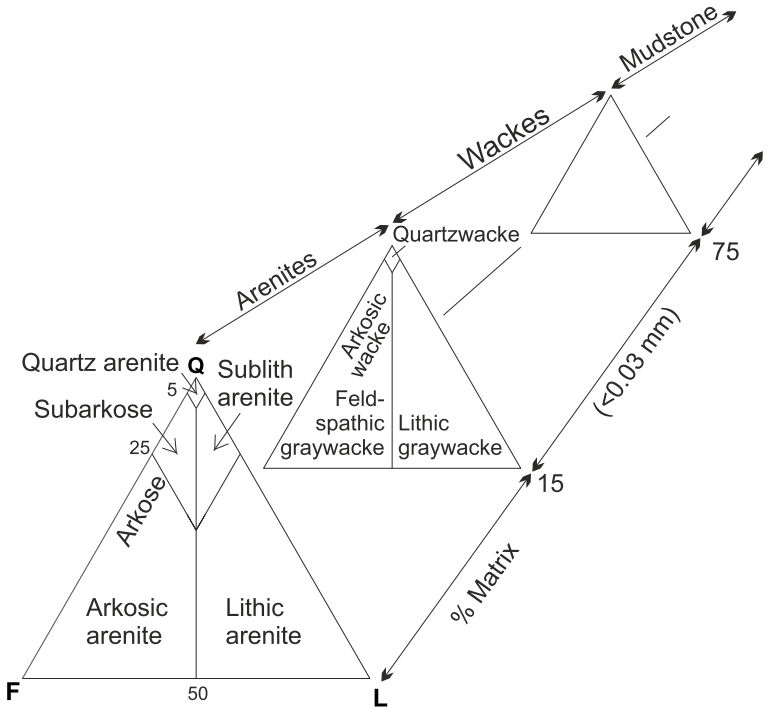

Figure 1.2: Classification of terrigenous sandstones from Pettijohn (1975). The first QFL-diagram (quartz, lithic fragments and feldspar) shows the nomenclature for arenites with matrix contents smaller than 15%.

tic deformation. Uniaxial compressive strength of a material is the maximum compressive load/stress the sample withstands until failure. Furthermore tensile and shear strength are commonly used for evaluating material strengths (Figure 1.3). Uniaxial stress describes the directed force per area.

The strain of the material describes the deformation per unit length. In terms of stress-strain the elasticity describes the reversible behaviour of a material after an applied stress. The ratio of stress and strain is given by the Young's modulus and the Poisson's ratio (the ratio of the transverse and axial strain).

In this context, the hardness of rocks does not refer to the *Mohs scale of mineral hardness*, scratch hardness or other measures of hardness. Usually and in this work the term refers to the strength of the material, in detail the uniaxial compressive strength.

In comparison to other building stones, sandstone can be shaped and quarried easily. This fact, as well as its local accessibility, contributed to the use of sandstones as an attractive and frequent building material in the last centuries until the present day globally. Scotland has at the moment 17 open sandstone quarries that are used for building stone extraction (Cameron et al. 2014). Seven of those quarries are constantly active. Most sandstones in Scotland are Carboniferous in age followed by the Devonian and Permian sandstones both most frequently occurring in the Midland Valley.

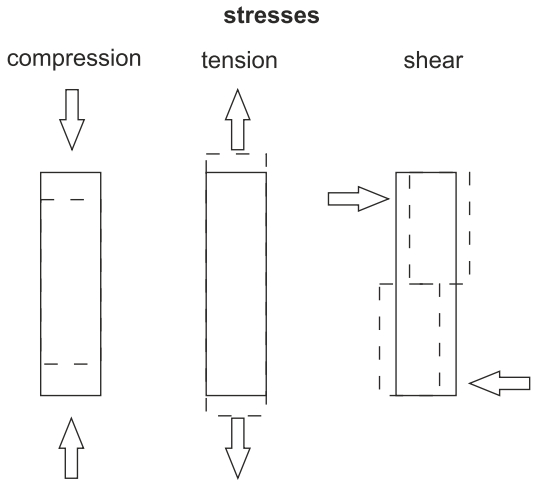

Figure 1.3: Compressive, tensile and shear stress on a rectangle sample.

1.2.2 Weathering of building stones

When building stones are exposed at the Earth's surface their mineralogical composition and texture alters to adapt for the new environmental conditions. This change in the physical and chemical properties of the stone is called weathering.
Accompanied by this change is usually the loss of material described by certain forms of weathering such as sanding, lamination or complete detachment of the building stone. A detailed catalogue of forms of weathering caused by different processes is presented in the *Illustrated glossary on stone deterioration patterns* (ICOMOS 2008). The terms introduced in the glossary are commonly used to describe weathering visually.

Weathering processes can be divided into biological, physical and chemical. These processes can act simultaneously or combine without clear boundaries.
Biological weathering describes decay caused by living organisms. It can be further divided into physical (-biological) processes, such as pressure of growing roots, and chemical-organic weathering, that includes for examples acids from bacteria that enhance dissolution of minerals.
Physical weathering is described as processes that cause fragmentation/breakdown of the rock without significant alteration of the mineralogical composition. A few common processes that cause physical weathering are listed below. Stress on the rock can be generated from volume changes of mineral phases in contact with the rock. Freeze and thaw are commonly used examples of physical weathering (Rüdrich et al. 2005, Rossi-Manaresi & Tucci 1991, Rüdrich & Siegesmund 2007). The increase in volume of ice trapped in pores can disintegrate all types of minerals. A similar process is caused by salt. The salts can expand during crystallisation or during hydration and exert enough pressure to overcome the rocks internal strength.

Water is an important factor contributing to physical weathering, not only because of its active role in damaging through heavy rainfall or abrasion of water/ice, but also through its contribution in hygric (in relation to the relative humidity) and hydric dilation, freeze and thaw cycles and salt crystallisation (Warke & Smith 1998, Rüdrich & Siegesmund 2007, Rodriguez-Navarro et al. 2000, Scherer 1999).
Heat or temperature changes also induce physical weathering. Insolation can cause internal stress in rocks when surfaces heat up more quickly than the rest of the rock. The opposite effect, quick cooling, can cause crack and disintegration of grains. Other forms of internal stress are caused by cyclic wetting and drying that leads to severe damage of the rock (Scherer 2004, Coussy 2006). Stress-release or increase from weight on the rock can add compressional or tensile stresses and increase weathering rates. An example of a small, micrometer scale crack can be seen in Figure 1.4.

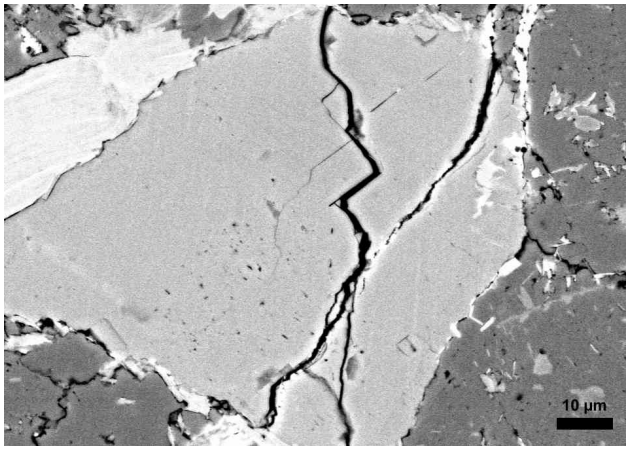

Figure 1.4: Electron back scatter image of a crack developing in a feldspar grain.

Chemical weathering describes processes that alter the mineralogical and chemical composition of the rock. Phase changes, formation of new minerals and the dissolution of minerals are common processes involving reactants from the rock, atmosphere and pore space (McGreevy et al. 2000, Arnold & Zehnder 1989). Chemical weathering is usually a slower process compared to biological and physical weathering as reactions happen under comparably low temperature condition, i.e. <30° C (Boggs-Junior 2014). Water is one of the main drivers of this type of decay as it supplies reactants. Other important factors for this type of weathering include the rock composition itself, gases, acids and salts that interact with the building stone.
Salt weathering is one of the most damaging forms of building stone decay. Special attention in this thesis is paid to the factors that enhance and cause this type of weathering, which will be further described in the next sections. When water dissociates, it forms H^+ and OH^-, which can act as a weak acid on silicate minerals (hydrolysis). Together with dissolved CO_2 the solution enables exchange reactions and therefore the formation of new

mineral phases. Gases that interact with the minerals can be O_2 and CO_2 causing dissolution of some minerals (Papida et al. 2000, Ruiz-Agudo et al. 2007, Grossi & Murray 1999). Next to hydrolysis other forms of chemical weathering include oxidation and reduction, ion exchange and hydration (see Section 1.2.3). Oxygen dissolved in water can cause for example iron to change its charge (Fe^{2+} to Fe^{3+}, oxidation). Other cations might be lost from the crystal lattice of the mineral to maintain electrical neutrality. Another common type of chemical weathering is the solution of minerals. When CO_2 dissolves in water carbonic acid is formed (Equation 1.1). Carbonic acid can ionise in water and leave hydrogen ions that increases its acidity (Equation 1.2). Carbonate minerals (such as calcite and siderite) are specially prone to increased levels of acidity. Calcite for example dissolves (Equation 1.3).

$$H_2O + CO_2 \longrightarrow H_2CO_3 \tag{1.1}$$

$$H_2CO_3 \longrightarrow H^+ + HCO_3^- \tag{1.2}$$

$$CaCO_3 + CO_2 + H_2O \longrightarrow Ca^{2+} + 2\,HCO_3^- \tag{1.3}$$

Weathering of building stones is determined by the rock properties (pore network and mineral composition) and the given environmental conditions (the whole system that rock is exposed to). Mineral composition, pore network properties and environmental conditions influence each other. Figure 1.5 gives an overview of the most important factors in weathering. The next section covers how the mineral composition and the pore network in combination with the environmental conditions determine weathering processes.

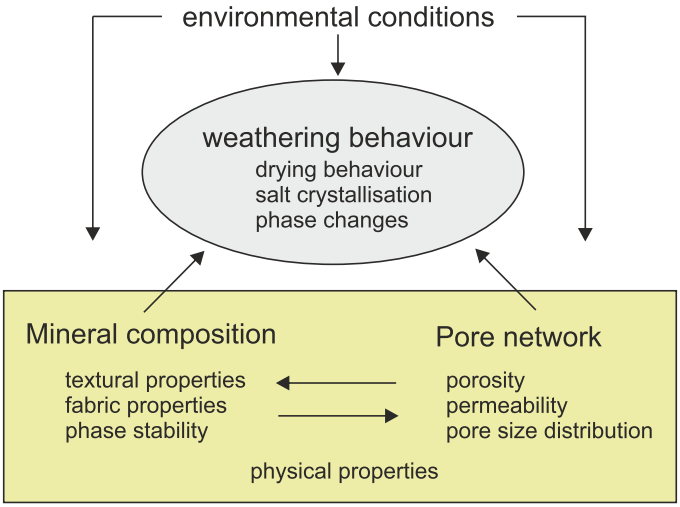

Figure 1.5: Overview of factors that determine the weathering behaviour of a building stone.

1.2.3 Mineral composition

The mineralogy of the rock directly influences its weathering behaviour including rate of weathering. Composition can dictate the grain size distribution and grain shapes, which again influences the pore size distribution. The composition including the cement of the sandstone also influences structural properties such as the strength of a material. Small changes in the composition can lead to significant differences in the weathering rate (McKinley et al. 2003). The change in composition can alter for example the permeability or strength of the rock resulting in a vulnerability to salt weathering. Decreased strength leads to increased weathering.

Weathering rates vary for different types of minerals. The stability of common sand-sized minerals is summarised in Figure 1.6. These rates can vary under certain environmental conditions, for example different pH. The most stable phases are quartz, K-feldspar and certain types of clay minerals which are therefore common in building stones after long exposure to the earth's surface. The decaying minerals can provide reactants to form new, more stable phases. In this context two groups of minerals that enhance weathering are described: clay minerals and common building salts. Furthermore in the next section a particular focus is on the link of mineral composition and pore properties to dilation processes in the stone that enhance weathering.

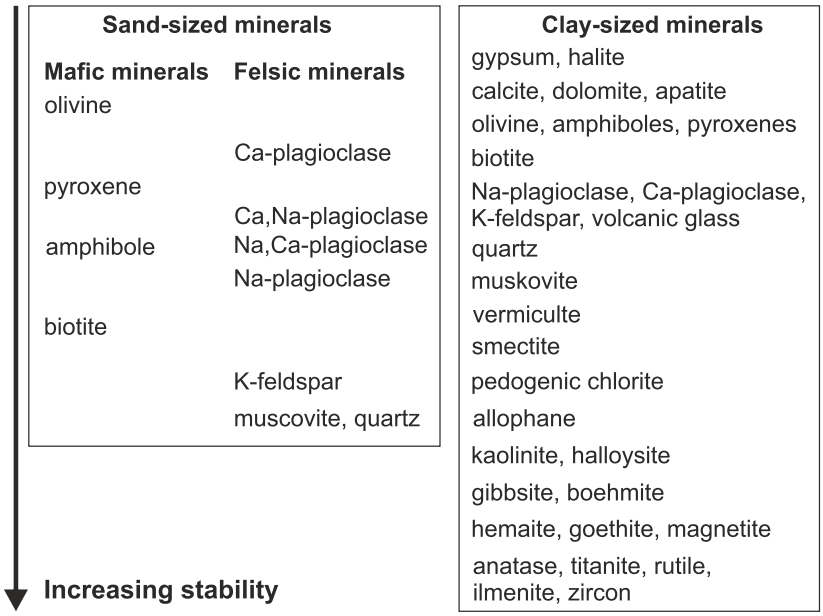

Figure 1.6: Stability of sand and clay sized minerals under weathering from Boggs-Junior (2014).

Thermal dilation of minerals

When minerals are heated an expansion can usually be observed (Equation 1.4), that is linear, if the temperatures and temperature differences are not too high. The length (l) of the sample expands with increasing temperature (T) and the linear expansion coefficient (α).

$$\frac{\Delta l}{l_0} = \alpha \times \Delta T \tag{1.4}$$

Table 1.1 gives an overview of different building stones and minerals that show an anisotropic expansion depending on the crystal orientation.

Table 1.1: Linear expansion of some building stones and minerals at 0 - 60° C or *0 - 30° C from Kocher (2005). For the minerals the expansion along the axes of the crystal lattice a and c are given.

stone/ mineral	α $[10^{-6}/K]$	
quarzite	11.0 – 12.5	
sandstone	10.0 – 12.5	
slate	9.5 – 11	
granite	6.5 – 8	
marble*	4.0 – 7	
dolomite	7.0 – 10	
	a	**c**
quartz	13.24	6.99
calcite	−5.7	25.57
halite	38.59	–

Changes in temperature caused by daily cycles of sun insolation can cause an expansion of the material which can be irreversible. Thermal stresses lead to crack formation and disintegration of grains in marble (Rüderich 2003). Furthermore water saturation can increase the difference of thermal expansion and contraction (Siegesmund & Dürrast 2011). Kocher (2005) suggests, the thermal stresses are similar to the hygric stresses for several building sandstones and should be given a higher priority when evaluation weathering behaviour.

The temperature of the rock depends on its absorption, reflectance (in particular albedo, the diffuse (scattered) reflection of solar radiation) and its emissivity (the ability to emit thermal radiation in comparison to an ideal thermal radiator, a black body). Lighter coloured rocks have a higher albedo and should therefore show slower surface temperature changes. When measuring absolute temperature of those rocks during insolation, the lighter coloured rock might therefore have a lower temperature. When rock temperature is lower than the ambient temperature, the darker rock will heat up quicker. When the rock temperature exceeds the ambient temperature and insolation stops, the hotter rock could give away the thermal

energy quicker as the thermal gradient between the colder and hotter system is higher. This situation can therefore mean that the lighter rock has higher surface temperatures during a measurement in the cooling phase (Hall et al. 1997).
The thermal stresses on the rock are also influenced by thermal conductivity of the stone. The thermal conductivity of a sandstone strongly depends on its composition, porosity, moisture content as well as pressure and can be anisotrop depending for example on the bedding (Eppelbaum 2014). An increased conductivity characterises sandstones with lower porosities, lower temperatures and higher pressures.

Clay minerals

Most clay materials originate from weathering processes through the dissolution of other minerals, especially silicates (Velde 1992). An example is the formation of kaolinite through the dissolution of feldspar (orthoclase) after hydrolysis (Equation 1.5).

$$2\,KAlSi_3O_8 + 2\,H^+ + 9\,H_2O \longrightarrow Al_2Si_2O_5(OH)_4 + 2\,K^+ + 4\,H_4SiO_4 \tag{1.5}$$

Clay minerals in sandstones can be found as sand-sized or smaller components, part of the cement and/or filling secondary pore space.
Next to the pH, the clay minerals that are stable are mainly dictated by water-rock interaction, which initiates weathering. This interaction is influenced for example by rock type, climate, temperature, humidity and pressure. Changing conditions will result in a change in the clay mineral composition (Velde 1992, Houseknecht & Pittmann 1992).

Clay minerals are mainly hydrous aluminosilicates (Okrusch & Matthes 2005). They can contain traces of Mg, Fe and/or other cations mainly from alkali and alkaline earths. Clay can refer to the term *clay minerals* as well as the grain size. After Wentworth (1922) clay consists of particles with grain sizes smaller than 3.9 µm. For clarity when considering *clay minerals* the term *clay* should not be used.
Clay minerals belong to the phyllosilicates, which have a layered sheet-like structure (Pettijohn et al. 1987). The basic unit of this structure is formed by Si^{4+} or Al^{3+} ions closely surrounded by oxygen ions (or OH^- for Al^{3+}). Together they typically form tetrahedral anions of SiO_4^{4-} and octahedral anions of $Al(OH)_6^{3-}$ (Figure 1.7). Covalent bonding through the sharing of oxygen ions links the tetra- and octahedra along their *a* and *b* crystallographic directions (Figure 1.7). Along the *c* direction those stacked layers of tetrahedra and octahedra build up to several micrometres (Velde 1992). In the interlayer of some clay minerals (smectite) the negatively charged layers are held together by interlayer cations through van der Waals attraction (Madsen & Müller-Vonmoos 1989).

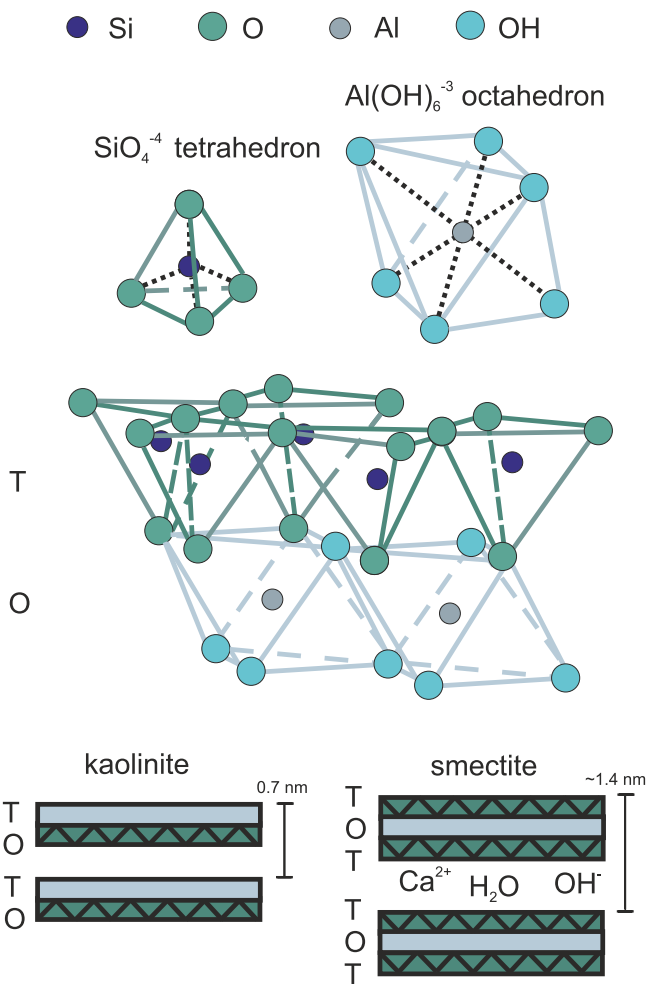

Figure 1.7: Schematic diagram of the structure of clay minerals after Pettijohn et al. (1987), Worden & Morad (2003). SiO_4 tetrahedra (T) and $Al(OH)_6$ octahedra (O) are linked by sharing O^- and form layers of several micrometre, that build up clay minerals such as kaolinite or smectite. In the interlayer of smectite exchangeable cations can be hydrated or water can be bound by weak van der Waal's forces (Worden & Morad 2003).

Depending on the structure, composition and/or properties different groups of clay minerals are distinguished. These groups include for example swelling or non-swelling clay minerals or di- or trioctahedral clay minerals given by the charge of the ion at the octahedron end (Okrusch & Matthes 2005, Worden & Morad 2003). When identifying the clay mineral content of sandstones usually five groups of phyllosilicates are considered, distinguished by their structural properties (Worden & Morad 2003, Pettijohn 1975): kaolin, illite, chlorite, smectite and mixed layers group.

The kaolinite interlayer is connected by O-H-O bonds, van der Waal's force or hydrogen bonds (Velde 1992, Worden & Morad 2003). Similar to smectite (Figure 1.7), illite has a TOT structure, also called 2:1 structure. Mainly K^+ cations are present in the interlayer to balance the charge. Illite does not show swelling behaviour because of its strong O-K-O bonding (Worden & Morad 2003). Chlorite has a TOT-O or 2:1:1 structure and shows no

clay swelling. Smectite shows less K^+ binding and a large amount of exchangeable cations that can be hydrated. Additionally water is bound in the interlayer through weak van der Waal's forces (Worden & Morad 2003).

The type, amount, distribution and morphology of clay minerals can significantly influence the properties of sandstones such as the permeability and porosity (Worden & Morad 2003, Aksu et al. 2014). Different clay minerals occupy different spaces in the pore network. For example, thick coating of grains with illite or chlorite can reduce the permeability but leaves the porosity relatively uninfluenced (Worden & Morad 2003). A reduction in permeability can be caused by fibrous pore-bridging clay minerals like illite in comparison to a 'clean' sandstone with the same pore geometry (Worthington 2003). Chlorite was found to maintain porosity through inhibiting quartz overgrowth (Anjos et al. 2003, Worden & Morad 2003, Wilson 1994). When coating detrial (abraded or not local) grains chlorite can as well be a pore filling clay. Authigenic (locally formed) clay minerals reduce permeability of sandstones (Howard 1992, McKinley et al. 2003). Diagenitic growth of illite at the expense of kaolinite and feldspar can cause reduction in permeability (Bjorlykke & Aagaard 1992). For swelling clay minerals, permeability depends on the matrix grain size. A reduction in porosity might not lead to a reduction in permeability (Aksu et al. 2014).

Hygric and hydric dilation of clay minerals

Length changes of minerals caused by humidity changes (hygric) and water immersion (hydric) can apply high stress on building stones during drying and wetting. Benavente et al. (2008) showed the highest correlation of decay (measured as weight loss) and hygric dilation, compared to other properties of building stones. If the rock is confined by an external load and can not expand/shrink, the stresses that build up can easily exceed the tensile strength of rocks. The expansion causes compressive stresses (but also shear forces opening cracks parallel to the surface) on the rock and shrinkage causes tensile stresses (Jimenez-Gonzalez et al. 2007). High strain rates of more than 5 mm/m have been measured for several clay bearing sandstones (Kocher 2005, Rüdrich, Bartelsen, Dohrmann & Siegesmund 2011). Most sandstones have lower rates.

The type of clay mineral, its distribution and of course the structural properties of the rock along with its composition, textural properties and anisotropies, determine how severely a rock will be damaged by swelling and shrinking. Also the amount of water saturation and sorptivity play an important role. Rapid changes in the water saturation can therefore lead to increased damage. Another important factor is the rate at which the stresses are experienced. Sandstone can show a viscoelastic behaviour (Jimenez-Gonzalez et al. 2007). Jimenez-Gonzalez et al. (2007) find that drying after complete saturation exerts a higher (tensile) stress on the rock than any wetting processes. The maximum stress exerted on an

outer layer of a rock that is either completely dry or wet, compared to the stone are estimated with Equation 1.6. The calculation includes the viscoelastic modulus E of the dry (d) or wet (w) stone, the free swelling strain (ϵ_s) and the Poisson's ratio (υ_d).

$$\sigma_d = \frac{E_d \epsilon_s}{1 - \upsilon_d} \tag{1.6}$$

Two main mechanism are distinguished for the swelling of clay minerals: intra-crystalline or inter-crystalline (osmotic) swelling (Figure 1.8). Intra-crystalline swelling describes a hydration (addition of water to ion/crystal structure) of the interlayer cations. The polarised water molecules, which are distributed around the cations, can built up several layers of water and exert pressures of up to 400 MPa, for example for montmorillonite (Madsen & Müller-Vonmoos 1989). This inner-crystalline swelling can also double the volume of montmorillonite.

Osmotic swelling describes this repulsion of forming double layers. The adsorption of water by Na-montmorillonite can lead to complete disintegration of the clay layers. The sodium cations move to the surfaces as more water arranges in the interlayer (Madsen & Müller-Vonmoos 1989). The pressure induced by osmotic swelling is with around 2 MPa significantly lower than the intra-crystalline swelling (Madsen & Müller-Vonmoos 1989). Unlike intra-crystalline swelling, osmotic swelling can act on all clay minerals, as the source of the repulsion is the concentration difference of the ions held to the surface and the ions in the pore water.

When water saturated, the mechanical strength of rock decreases, which is mainly attributed to the swelling of clay minerals but also caused by poro-mechanical properties (Cherblanc et al. 2016, Rüdrich, Bartelsen, Dohrmann & Siegesmund 2011, Zhao et al. 2017). Laboratory scale samples show a reversible effect of the dilation after a few cycles of wetting and drying (Colas et al. 2011). Whereas long term exposure of high humidities (97%) or water saturation combined with frequent drying can lead to the deterioration of the building stone i.a. through the reduction in tensile/flexural strength (Cherblanc et al. 2016, Kocher 2005, Sorace 1996).

Salt minerals

Salt in building stones can originate from atmospheric pollution (especially sulfates), rising ground water, deicing salts, aeolin input, sea water, metabolic activity from microbes, and from the mortars and building materials itself (Desarnaud et al. 2015, Scherer 2004, Arnold & Zehnder 1989). Common salts found in building stone include gypsum ($CaSO_4 \cdot 2\,H_2O$), halite (NaCl), sylvite (KCL), thenardite (Na_2SO_4), Epsom salt ($MgSO_4$), and several different phases of these salts (Steiger et al. 2008, Serafeimidis & Anagnostou 2014).

Structural damage due to cycles of expansion and contraction of the sandstone can be

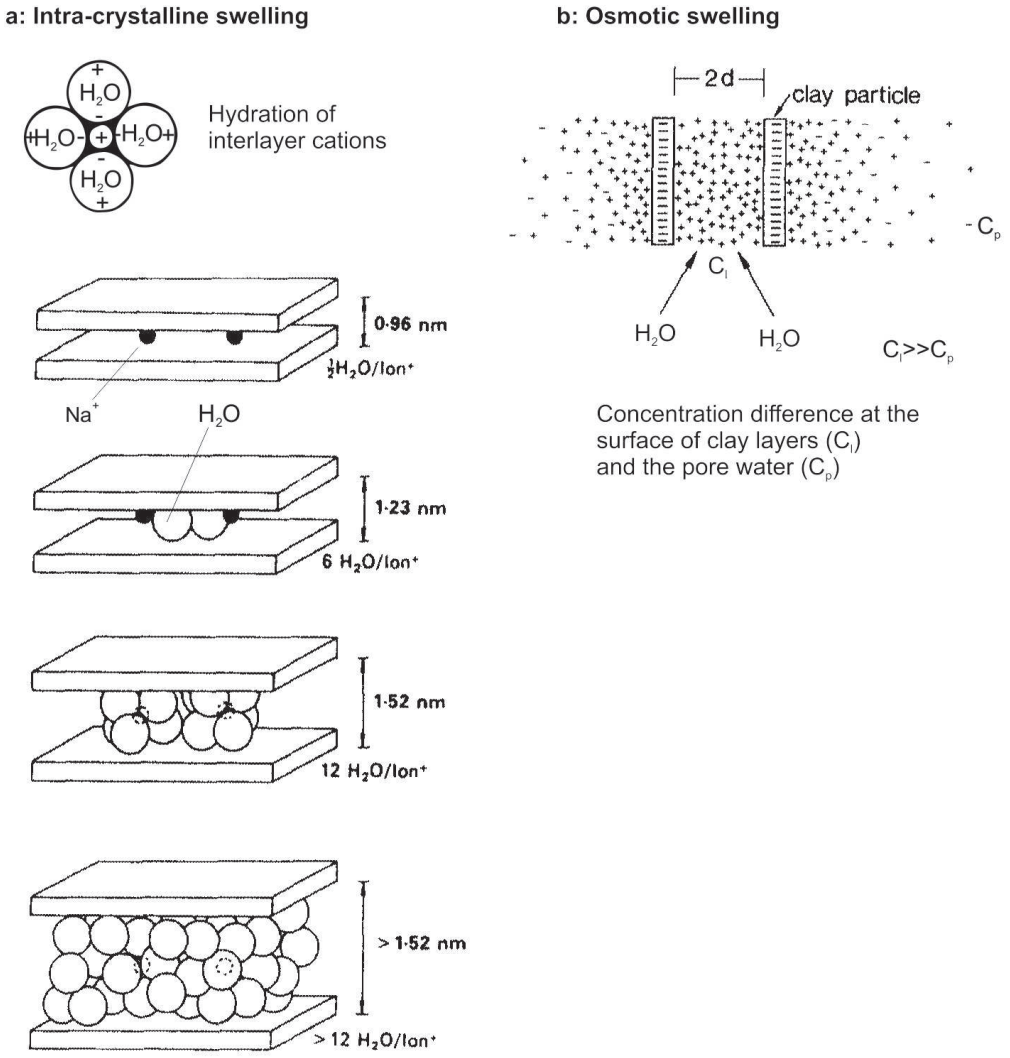

Figure 1.8: Two mechanisms of clay swelling after Madsen & Müller-Vonmoos (1989). a: intra-(inner)crystalline swelling caused by the hydration of the exchangeable interlayer cations. b: osmotic swelling caused by the concentration difference of the ions near the clay layer surfaces and the ions in the pore water surrounding the clay layers. The distance (d) depends on the valence and radius of the ions in the doublelayer and the ions concentration in the pore water.

caused by salt crystallisation in the pores of the rock. When salt grows in the pore network it can accumulate high pressure against the pore walls and crack the surrounding minerals (Scherer 1999, 2004). The processes of salt crystallisation are described in the following section with respect to the pore network properties.

When salt crystals in the building material are dissolved again, for example through water migrating through the rock, the salt ions can be partially washed out and leave a weaker sandstone because of its increased porosity (Graham 2016). Drying of the rock will initiate salt crystal growth again (or dehydration) and the overall damage will increase for each wetting and drying cycle the sandstone experiences.

The hydration of salts such as magnesium sulfate and sodium sulfate can cause severe damage on account of high hydration pressures (Steiger et al. 2008, Balboni et al. 2011, Scherer 2004). For example the (structural) phase transition during hydration of the salt Na_2SO_4 (thenardite) to $Na_2SO_4 \cdot 10\,H_2O$ (mirabilite) can cause a volume expansion up to three times of its previous volume (Laue 2002).

1.2.4 Pore network properties

Compared to other building stones, the pore properties of sandstones make them highly prone to decay processes involving water and salt. These properties include high porosities as well as high permeability and sorptivity. In the following section the influence of pore network on weathering is described in regard to temperature and humidity/moisture changes.

Porosity and pore size distribution are two of the most influential structural properties for predicting the durability of a building material (Ordonez et al. 1997). Depending on the connection of the pores, several types of porosity are distinguished. Open porosity or effective porosity describes the pores that can be accessed by fluids or gases. Absolute porosity includes the open porosity as well as the closed porosity. The latter describes isolated or disconnected pores (Siegesmund & Dürrast 2011, McKinley & Warke 2007). Furthermore the porosity is characterised by its formation. Primary and secondary porosities are distinguished depending on the petrogenesis. Secondary porosity is formed during diagenesis or post-sedimentary. A change of porosity during weathering is therefore a special case of secondary porosity (Siegesmund & Dürrast 2011). The porosity usually correlates with strength of the material and high porosities with vulnerability to salt crystallisation (Rüdrich, Bartelsen, Dohrmann & Siegesmund 2011, Bourges 2006).

Pore sizes are classed into micro-, meso- and macropores. The limits of the classification vary from authors and in literature often no reference is given when discussing pore types. For example the maximum size of micropores is set to be smaller than 500 nm or smaller than 2 nm, whereas commonly it is assumed to be smaller than 100 nm (Siegesmund & Dürrast 2011). Capillary pores are usually defined for 1 µm - 1 mm (Figure 1.9) and are the main drivers of water absorption of porous materials. Moisture adsorption however describes the interaction of the atmospheric moisture with the surfaces of the stone by hydrogen bonds and van der Waals forces (Siegesmund & Dürrast 2011).

Benavente (2011) describes pore size distribution as one of the most important pore structure parameter when evaluating stone decay. The presence of large amounts of smaller capillary pores and micro-pores (a bimodal pore size distribution) is related to severe salt decay (Rüdrich et al. 2007, Rossi-Manaresi & Tucci 1991, Graham 2016). An unimodal dis-

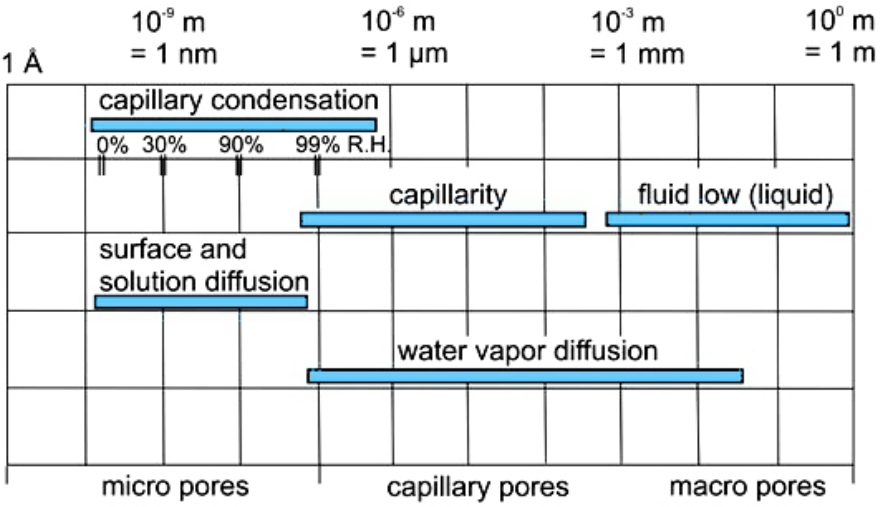

Figure 1.9: Pore size classification from Siegesmund & Dürrast (2011) with major transport mechanisms.

tribution of pore radii and a small volume of micropores is related to a better resistance against salt weathering (Rüdrich et al. 2005). Flatt (2002) finds the most damage for mesopores, that can evolve after crystallisation damage in sandstones (Adamovic et al. 2011). A correlation of hygric swelling and reduction in UCS under water saturation for eight types of sandstones was found by Demarco et al. (2007). They also correlate large amounts of micropores with a strong reduction of UCS when water saturated. Moisture expansion can be present without clay minerals. The amount of micropores plays an important role in the moisture expansion in tuff where clay minerals are absent (Wedekind et al. 2012).
Rad et al. (2015) show increased efflorescence with fewer fine pores at the surface, whereas Espinosa-Marzal & Scherer (2013) finds increased pore clogging with greater volumes of smaller pores, although depending on salt type this behavior can change. The properties of the salt/solution and the pore network are therefore both important for predicting trends for salt precipitation. For NaCl Eloukabi et al. (2013) found increased crusty efflorescence (crust sealing drying surfaces) for finer porous medium and a patchy efflorescence (maintained evaporation rates) for coarser porous media.

Permeability describes the ability of a fluid with a given viscosity to migrate through a porous system under certain temperature and pressure conditions. Permeability is mainly influenced by capillary forces which are again influenced by the pore space distribution or grain size distribution. Well sorted grains in a sandstone usually have higher permeability than unsorted grains (Heubeck 2007). As discussed above, clay mineral content plays an important role.
Permeable sandstones allow the migration of solutions into the interior of the stone. Especially the near surface permeability controls the water intake of the stone. It can be sig-

nificantly altered by salt crystallisation, especially efflorescence (McKinley & Warke 2007, McCabe et al. 2011). Pores at the surface can be blocked and moisture and salt can accumulate behind the surface resulting in a decrease in permeability. Several cycles of salt crystallisation and solution can also increase the permeability developing a *secondary permeability* (McCabe et al. 2011). Permeability can therefore be indicative of deterioration or vulnerability to weathering (McKinley & Warke 2007).

Water adsorption of the stone reflects the pore network properties and can be indicative of changes in the pore network and therefore decay. It can be also used to estimate its weathering resistance (Vandevoorde et al. 2013). Salt crystallisation can significantly increase the sorptivity.

Drying and evaporation in porous materials

In addition to hygric and hydric dilation another important process that enhances weathering is drying of the building stone.
The pressure gradient in the porous system during drying can cause shrinkage of the sample and its pores. This pressure is a combination of for example capillary pressure, osmotic pressure and disjoining pressure (Scherer 1990).
Capillary pressure (p_c) is defined by the Young-Laplace Equation 1.7,

$$p_c = \frac{2\gamma\, cos\theta}{r_{sl}} \tag{1.7}$$

with γ the interfacial tension (γ), the contact angle of the liquid and the surface (θ), and the radius of the interface (r_{sl}). Instead of the radius Scherer (1990) uses the surface to volume ratio for the pore space.

Osmotic pressure can occur from a concentration difference when the evaporating liquid contains ions that accumulate near the drying front and if too small pores prevent a balance through back flow. The disjoining pressure can cause hygric/hydric dilation without any clay-minerals in the rock especially under the presence of micro-pores with sizes of 0.1 µm (Rüdrich, Bartelsen, Dohrmann & Siegesmund 2011). The pressure i.e. describes the pressure difference in a small wet film (thin film) that surrounds surfaces of pores compared to the pressure in the surrounding bulk material (Butt et al. 2003, Derjaguin & Churaev 1974). The disjoining pressure (Π_D) is defined in Equation 1.8 as the change of Gibbs free energy (G) with distance, x (normal to the interacting surfaces) over the area A of the surfaces (for constant temperature, volume and surface area (T, V, A).

$$\Pi_D = -\frac{1}{A}\left(\frac{\partial G}{\partial x}\right)_{T,V,A} \tag{1.8}$$

The disjoining pressure evolves from a combination of several other processes that cause the repulsion of the two interfaces. Source of the pressure can be electrostatic interactions for example dispersion forces, hydration forces and the overlap of electrical double layers (Butt et al. 2003, Jamtveit & Hammer 2012). Fluids confined between mineral interfaces (such as the thin films) play an important role in pressure solution of minerals, especially for grain contacts such as quartz and mica (Anzalone et al. 2006). The disjoining pressure can be as high as 100 MPa for wet films of only a few nanometres in contact with mica (Jamtveit & Hammer 2012). Any chemical treatment or even weathering can alter this pressure or the wet film.
Webb et al. (2011) found no repulsing forces for a quartz-halite system. The oppositely charged surfaces in contrary attract each other. The repulsive forces and the pore size distribution could be the reason why some salt contaminated sandstones contract during weathering as seen in Rüdrich & Siegesmund (2007).

During drying the migration of the fluid can be described with two main transport processes: Darcy's law and diffusion. Darcy's law describes the flux of the fluid ($\boldsymbol{J}$) that is proportional to the gradient in pressure of the liquid ($\nabla \boldsymbol{P}_L$) and the permeability (k) divided by the viscosity of the liquid (η_L) as well as the density of the liquid (δ_L) and the gravitational acceleration (Equation 1.9) . The diffusion ($\boldsymbol{J}_D$) is described by Fick's law (Equation 1.10) with the concentration gradient ($\boldsymbol{C}$) and the chemical diffusion coefficient ($\boldsymbol{D}_c$).

$$\boldsymbol{J} = -k\frac{\delta_L}{\eta_L} g \times \nabla \boldsymbol{P}_L \tag{1.9}$$

$$\boldsymbol{J}_D = -\boldsymbol{D}_c \times \nabla \boldsymbol{C} \tag{1.10}$$

Three different stages of drying can be distinguished, that are influenced by the migration of the fluid through the porous system (Figure 1.10). During those stages different variables become more important: mainly the pore size, which influences the capillary effect, therefore also the pore size distribution, permeability and properties of the drying solution as well as environmental conditions.
The first drying phase is defined by a constant capillary transport of solution to the surface. This process results in a wet film on the surface that enables a constant drying or evaporation rate (Rad 2014). Large pores near the surface dry before small pores that are still filled with solution. The fluid is transported to the small pores at the surface by capillary driven flow (Rad et al. 2015).
In the constant rate period the largest shrinkage can be measured as well as the highest drying stresses (Scherer 1990). The largest compressive stresses occur near the drying surface due to the tension in the liquid being the largest in that area (as the pressure gradient is the

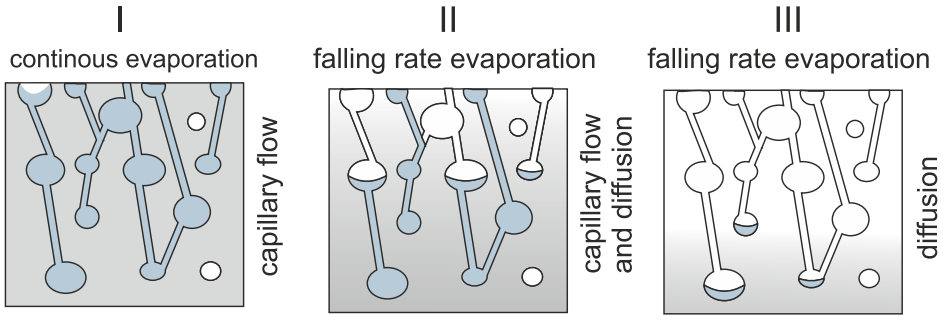

Figure 1.10: Stages of drying with continuous evaporation (I), and falling rate evaporation (II and III). In the first stage a constant supply of liquid is given through capillary transport of liquid to the surface. In the second and third phase the drying regime moves below the surface with an increased transport by diffusion. Initially the evaporation is still mainly at the surface and some capillary flow is present.

highest at the surface). The difference in stresses caused by shrinkage can cause cracking. The damage is depended on the sample size, evaporation rate and strength of the sample (Scherer 1990).

Small pores at the surface continuously evaporate more fluid as long as the capillary pressure gradient towards the surface is higher than the ambient vapour pressure (Scherer 1990, Rad et al. 2015). The evaporation rate is therefore mainly controlled by the fluid properties, pore network properties and the environmental conditions (Matiasovsky & Mihalka 2014). The second drying phase starts when the evaporation rate is greater than that of capillary flow from the pores. The drying regime moves below the surface which results in a lower drying rate because the distance of the drying front to the exterior increases and therefore the capillary gradient. Some diffusion occurs in this state (Scherer 1990) but mainly continuous flow to the new drying front occurs. Evaporation takes place mainly at the stone's outer surface, which causes a cooling of the surface compared to the ambient temperature. The evaporation rate is here sensitive to temperature and vapor pressure (Scherer 1990).
In the third stage of drying the flow of liquid to the surfaces comes to a halt because liquid near the surface will get isolated. Diffusion appears and evaporation is moved inside the sample (Scherer 1990). The highest stress are now in the still saturated areas, whereas the dried areas can expand due to stress relief.

In the transition between stages I and II the continuous liquid paths gradually disconnect until a new drying front forms below the surface (Rad 2014). The transition of those stages is highly influenced by pore sizes. Large pores can transport more solution per time, whereas small pores have a slower transport but they keep the transport steady for a longer period. This means that sandstones with large pores will quickly go to the second drying stage, which will have the drying place in the inside of the rock (Asmussen 2007).

Capillary condensation causes an accumulation of solution in the small channels or pores, that can close the channels for diffusion. Small pores only dry for relative low humidities whereas in bigger pores water only condenses at 100%RH (Asmussen 2007).
The position of the drying front is especially important if the solution contains salt ions. The first drying stage will lead to a transport of the ions through the pores to the surface, which will cause a surface crystallisation of the salts called efflorescence (Figure 1.11). This efflorescence can block the pores but can also develop its own pore network (Gupta et al. 2014). Efflorescence can be of several centimetres without causing significant damage to the rock. The highest amount of salt precipitation occurs at the end of the first drying stage (Rad 2014). Increased heating rates can enhance evaporation and the onset of subflorescence (Gomez-Heras & Fort 2007).

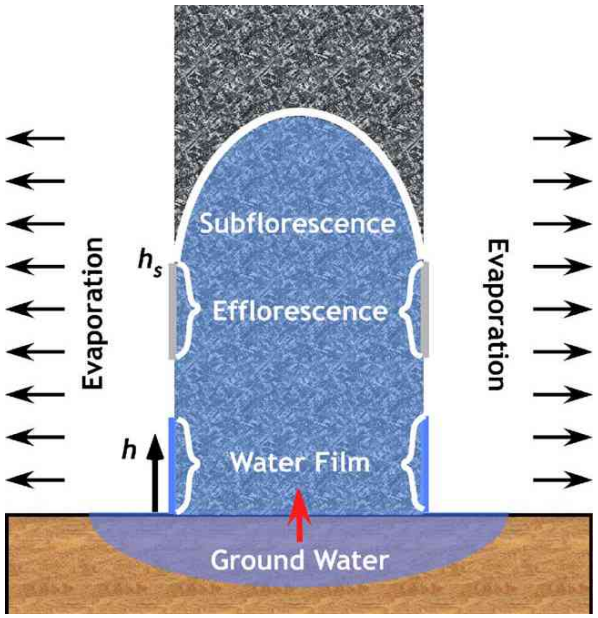

Figure 1.11: Rise of water in a building stone wall of porous materials: Ground water rises in a porous material and mobilises salt ions in a wall (from Scherer (2004)). A water film develops at the outside of the material when the evaporation rate is lower than water supply by constant capillary flow. Salt does not crystallise due to diffusion of the salt ions in all directions. Efflorescence can appear when salt ions accumulate around the surface until supersaturated, as the capillary flow decreases. At height h_s (steady state) capillary rise supplies as much water as evaporates. After that point the evaporation moves to the inside of the porous material where salt accumulates below the surface and causes crystallisation below the surface (subflorescence).

The second stage of drying of a salt solution will cause the crystallisation to occur in the inside of the rock (crypto- or subflorescence). If the solution transport is blocked, the crystal size is limited in a pore. A continuous transport with new salt solution enables a bigger crystal. Even when the solution supply is blocked, the salt can get hydrated through the contact of water vapour and therefore still increase its volume.
The evaporation rate from salt solutions is lower than with pure water because the salt

solution reduces the vapour pressure (Rad 2014, Desarnaud et al. 2015, Espinosa-Marzal & Scherer 2013). Different salts and their concentration change the properties of the solution and therefore the drying rates. A $MgSO_4$-solution in comparison to Na_2SO_4-solution has a greater density and higher viscosity, which means that salt is more likely to crystalise further from the surface (Ruiz-Agudo et al. 2007). Colas et al. (2011) analysed the dilation behaviour of clay-rich sandstones contaminated with NaCl and Na_2SO_4. They found a significant change in the dilation for the NaCl contaminated samples under cyclic wetting and drying. Next to the expansion due to salt crystallisation, hydration processes can also alter the drying behaviour of salt contaminated samples (Juling et al. 2004).
In addition to the salt type and concentration, cycles of wetting and drying under certain environmental conditions alter the distribution of the salt and the place of nucleation of salt crystals which then change the drying behaviour of the rock (Desarnaud et al. 2015). The drying behaviour is also strongly influenced by evaporation rate at the beginning of the drying from a salt solution. High humidities, that normally decrease evaporation, can prevent in this case the formation of a blocking efflorescence by rapid evaporation and therefore maintain the evaporation of the rock (Gupta et al. 2014). Temperature and humidity influence this process significantly (Warke & Smith 1998).
During drying salt ions accumulate to high concentrations and salt crystallises. Any crystallisation processes begin from a supersaturated solution. This supersaturation can be influenced or achieved through the right temperature and humidity conditions. In the section below salt crystallisation is discussed with respect to the pore properties.

Crystal growth in porous systems

Two conditions of nucleation are distinguished during crystallisation from meta-stable supersaturated solutions. A spontaneous nucleation is unlikely to occur because an energy barrier (due to the crystal-liquid interfacial energy) must be overcome so that random clusters can form a stable nucleus (homogenous nucleation). Homogenous nucleation only occurs for example for very pure water at -38° C (Scherer 1999). In porous materials water can freeze at -7 to -15° C by heterogeneous nucleation. Therefore a nucleation agent provides surfaces with low interfacial energy (crystal solid interfacial energy). Cracks can act as nucleation sites as they increase the contact between substrate and crystal. The crystal growth stops when the equilibrium between the saturated solution and the crystal is reached.
Furthermore primary nucleation describes rapid crystallisation because of many impurities as well as high supersaturation. Secondary nucleation happens when salt crystals partially dissolve or are exposed to high humidities. The salt solution can move through pores again and recrystallise from the 'old' crystal nuclei.
The main factors influencing salt growth are: concentration, supersaturation or activity of

the salt, the pore network (including pore sizes and shapes) and interfacial energies such as the repulsive force between salt and the confining pore surface (Scherer 2004). High supersaturation is for example caused by drying of solutions especially salt mixtures, changes in pressure and/or temperature or the dissolution of thenardite (Lindström et al. 2014, Flatt 2002, Rodriguez-Navarro et al. 2000). The latter is therefore attributed to the severe damage that the (re-)crystallisation of the salt causes.
The difference of the chemical potential ($\Delta\mu$) of a liquid and the crystal is given by Equation 1.11 as the driver of the crystal growth (Scherer 1999). It can be calculated with the activity of the solution (a) and the activity of a solution in equilibrium with a large crystal (a_0) as well as the gas constant (R) and temperature (T).

$$\Delta\mu = R_g T ln(\frac{a}{a_0}) \tag{1.11}$$

After Everett (1961) crystals in large pores will grow first, because crystals in smaller pores reach constrains quickly and are therefore less favourable to grow. The chemical potential in a big pore is smaller than the chemical potential in small pores. In addition to chemical potential, the degree of supersaturation is essential for the crystal growth. A crystal in a small pore would need a higher supersaturation to grow compared to the bigger pore. Therefore the crystal in the big pore can increase as long as the supersaturation is given. When the crystal reaches the walls of a large pore and still has a supply to supersaturated solution, its chemical potential is still lower than the one in the surrounding smaller channel/pore, so it will increase its size even against the pore walls. In other words, once the constrains given by the pore walls are reached in the larger pores, crystals can grow further against the constrains as the supersaturation in the small pore needs to be higher and the solubility in the big pore can be still smaller due to capillary pressure (Putnis & Mauthe 2001, Lecampion 2010). This behaviour explains why the crystal in the larger pores (<100 nm) will increase growing against the pore walls before crystals in surrounding smaller pores will grow (Steiger 2005*a*, Scherer 1999). Growth will stop when the crystal is in equilibrium with the solution or the supply of solution is interrupted.

When crystal growth is limited by the size of a pore, a pressure against the limiting material can be developed. The driving forces of this pressure are mainly supersaturation (from solution) and undercooling (from melt/for ice) (Scherer 1999). An essential requirement for continuing crystal growth against the pore walls and developing a pressure, is that the constrained crystal face remains in contact with a supersaturated solution. The film that forms can occur between grains/pore walls because of the disjoining pressure. The thin film acts as a transport medium which accelerates or enables diffusion and chemical reactions. Repulsive interaction caused by the differences in interfacial energies between a crystal and

particles/pore walls have to be present to maintain this film (Scherer 1999). A chemical potential arises that will prevent contact of the crystal and particle so that the crystal pushes any particle away while growing and maintaining a thin film in between the two.
Several different approaches to calculate the pressure of crystals growing against the pore wall are used in the literature (Steiger 2005*b*). Steiger (2005*a*) combines the approaches from Correns & Steinborn (1939) including the supersaturation of the solution with the approach from Everett including the interfacial energies. The combined equation is limited for crystallisation under non hydrostatic stresses and crystal sizes under 100 nm as well as an anisotropic stress so that the faces of the crystal are loaded differently. The pressure of a crystal (Δp) with the loaded faces (i) can be determined using Equation 1.12. In this Equation the pressure is calculated with IAP, the ionic product (including water activities and activities coefficient) and K the equilibrium constant equilibrium (Ping & Beaudoin (1992), Benavente et al. (2014)), the molar volume (v_n) and the gas constant (R) and temperature (T) as well as the crystal-liquid interfacial energy (γ_{cl}), the change in area (A) and volume (V).

$$\Delta p_i = \frac{RT}{v_n} ln \frac{IAP}{K} - \gamma_{cl,i} \frac{dA_i}{dV} \tag{1.12}$$

The calculation of crystallisation pressure from Equation 1.12 by Steiger (2005*a*) was improved by Espinosa-Marzal & Scherer (2008) adding the capillary pressure and the change of the molar volume by the developing crystal to the equation. Equation 1.12 can be simplified for the equilibrium crystallisation of crystal in a specific pore structure (Figure 1.12 a+b). The pressure of a crystal that grows in a cylindrical pore (p_x) can be calculated with Equation 1.13 (Derluyn 2006). A large crystal that grows in a spherical pore connected to cylindrical pore channels with radius p_C, experiences a crystallisation pressure that can be calculated with Equation 1.14 after Everett (1961) focussing on the curved interfaces instead of the supersaturation.

$$p_x = 2\gamma_{cl} \frac{1}{r_P} - \gamma_{cl} \frac{1}{r_P} = \gamma_{cl} \frac{1}{r_P} \tag{1.13}$$

$$p_x = 2\gamma_{cl} (\frac{1}{r_C} - \frac{1}{r_P}) \tag{1.14}$$

Both calculations indicate lower pressure for larger pores. Large pores can exceed high pressures in a non-equilibrium situation when for example during drying a supersaturated solution is confined between the crystal and pore wall but still able to evaporate (Figure 1.12 c). Ions cannot be transported to the unconfined faces of the crystal, so with ongoing evaporation the stress eventually exceeds the strength of the pore wall or it exceeds the disjoining pressure. The disjoining pressure kept the pore wall and crystal at distance but if overcome will result in the crystal growth in contact to the pore wall (Scherer 2004). In Figure 1.12 d the large pores (3 and 4) might get isolated from the solution, which would

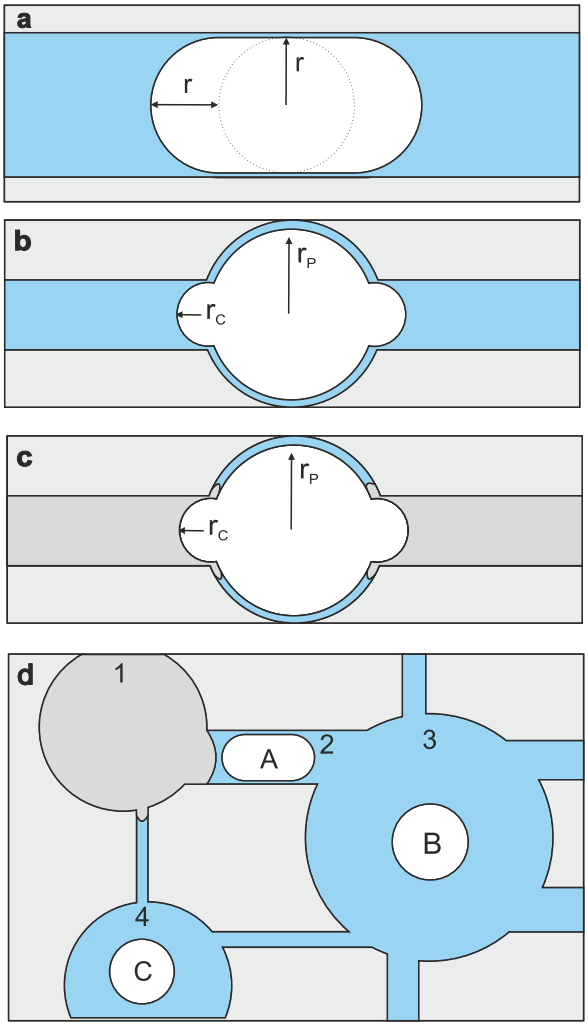

Figure 1.12: Crystal growth with radius *r* in a cylindrical pore (a) and a spherical pore (b) from a supersaturated solution, in blue (Steiger 2005*a*). Nonequilibrium situation (c) when an increased evaporation lead to an isolation of the thin film in between the pore wall and the crystal face (Scherer 2004). Pore network (d) with a dried pore 1 and nucleation in pore 2, 3 and 4. Crystal A is confined by the pore walls, whereas crystal B and C will grow in the expense of crystal A (Flatt 2002).

allow the crystal in the smaller pore (2) to reach equilibrium (Flatt 2002). If the connection of the pores persists, the smaller crystal in the pore (2) will disappear in the expense of the crystals in the larger pores (B and C).

Because high supersaturation can be maintained during crystal growth, the pressure is expected to be larger than the pressure calculated with the equilibrium state of the crystal (Derluyn 2006). Pressures up to 100 MPa can accumulate against the pore walls that exceed the strength of most building stones (Steiger 2005*b*). There is a maximum pressure for crystallising sulfates given by their hygrpscopic properties. Hydrates will form under high pressure (Linnow & Steiger 2005). Increasing temperatures can enhance the pressure applied by salt crystallisation after complete water saturation followed by drying (Stahlbuhk et al. 2014). A single pore is unlikely to cause failure of a body (Scherer 1999). Individual

small cracks also will not trigger fracture (Royne & Jamtveit 2015) but the spatial accumulation of salt crystals causes failure of larger bodies.

1.3 Investigating building stone decay

This section covers in-situ tools to investigate decay with respect to characterising physical properties of building stones. In the Chapters 3, 4 and 5 the individual techniques and their background are described in detail. The techniques presented in this section use similar approaches to the investigated methods in this project. The focus is set on Structural Health Monitoring as there are several links to the laser interferometer investigation and conventional drilling techniques in cultural heritage for the relation to ultrasonic drilling.

Over the last century, several devices and methods have been developed to assess the properties and decay of building stone. Gaining empirical and reproducible data to compare the state of decay is an active area of research and standard methods and tools have to be defined. The following sections give a short overview of commonly used devices to analyse the mechanical/structural properties, mineralogical or on site environmental properties of samples with minimally invasive (such as drilling techniques) and non-invasive methods. *Non-destructive Testing* (NDT) or *Non-destructive Tools* include for example acoustic emission, ultrasonic testing, optical metrology and other methods. Techniques that are similar or follow similar principles to the laser interferometer and the ultrasonic drilling device are introduced.

The analysing technique depends on the aim of the study, the material and/or budget. The combination of several NDT techniques is common to assess the state of decay of a building. Summaries of case studies and further reading of individual techniques can be found in Siegesmund & Snethlage (2011), Menendez (2016), Bourges (2006), Svahn (2006). A single technique that allows complete assessment of physical and mineralogical properties does not exist yet but the continuous advance in non-destructive testing leads to an increased reduction of tests needed to evaluate the state of decay.
Common techniques that characterise the building stone properties are summarised in Table 1.2 and briefly introduced in the following paragraph. From the change in properties of the stone, the state of decay can be assessed. The first step in evaluation the state of decay is visual examination of the building. The *ICOMOS* provides a detailed catalogue with images of types of weathering and their nomenclature including erosion, forms of detachment or forming crusts.
The properties of the stones on site are commonly investigated with multiple tools. In-situ chemical composition can be measured by X-ray fluorescence, laser florescence and break-

Table 1.2: Common, minimally or non-destructive techniques for in-situ investigations of building stones characteristics from Török (2010).

Physical properties	**Measuring techniques**
Colour	Colour chart, Colorimeter
Reflectance	Reflectometer
Temperature	Thermometers
Water content	moisture Conductometer, thermographic imagery
Water absorption	Karsten pipe, Contact sponge method
Surface roughness	Micro-photogrametry
Surface morphology	Digital imaging, LiDAR
Strength	Micro-drilling resistance, Schmidt hammer, Duroscope
Apparent density	US pulse velocity measuring devices, US edge probe
Chemical/ mineralogical properties	
Mineralogy	Portable XRD
Major elements	Portable XRF, UV-visual spectroscopy, Raman, Fluorescence
Trace elements	UV-visual spectroscopy, Raman spectroscopy
Organic compounds	FTIR-spectroscopy (Fourier Transformed Infrared Reflectance)

down spectroscopy (Benedetti et al. 2006, Vivi, Bernikola, Hatzigiannakis, Melessanaki & Pouli 2013). The moisture content of rocks is usually examined through electrical resistance or conductivity changes with small electrodes embedded into the building stones (Basheer et al. 2008). The test is minimally invasive as the probes need to be placed in the stone. Other non-invasive techniques to investigate moisture can be found in Orr et al. (2016). Injecting an electrical current into the material to monitor its resistivity can also be used for the identification of minerals and porosity (Menendez 2016).

Evanescent-Field Dielectrometry enables the mapping of moisture and salts in building materials (Riminesi & Olmi 2017). It uses the dielectric contrast of dry and wet materials as well as the ionic conductivity of salt solutions and relates them to the shift in resonance frequency of the material when wet and dry. Further calibration and knowledge of the material is needed. Depending on the sensor size an spherical volume with a radius of 2 cm is analysed. The sensor has been used on paintings in-situ and shows promising results for

lab based stone tests (Riminesi & Olmi 2017).
Ultrasonic velocity measurements have been applied since the 1970s and correlation of propagation speed and physical properties (strength, density, porosity) has been confirmed for several building stones, especially for carbonates (Török 2010, Bourges 2006). The transmitter (pulse emission source) and a receiver are commonly placed between the investigated material with a known distance to analyse the wave propagation speed. Transmitter and receiver can also be placed on the same surface (Menendez 2016).

Optical metrology describes techniques that utilise the wave nature of light to investigate objects. In cultural heritage non-destructive optical techniques to evaluate dimensional changes of objects are frequently used (Kottke 2009, Gomez-Heras et al. 2008). Profilometry describes techniques to capture the profile of objects to asses surface roughness or material loss and salt decay. Commonly 3D laser profilometers are used (Kottke 2009). Photogrammetry describes the process of evaluation object by photographic images (2D or 3D). 3D Laser scanning includes close range or long range application such as LiDAR (*light and radar*) to monitor changes in shape or size of objects (Kottke 2009). Lorenzoni et al. (2016) used an optical monitoring system to monitor the crack opening at a fresco surface. Speckle Pattern Interferomerty has been used for a few applications in cultural heritage and is described further in the Chapter 3 (Jarad et al. 2005, Juling et al. 2004). The technique has been used to monitor surface displacement and damage of art work such as paintings and wood (Vivi, Bernikola, Leissner, Bertolini & Camuffo 2013, Vivi et al. 2012, Krzemien & Lukomski 2014). Inaudi et al. (1994) and Inaudi (2004) use an all-fiber Michelson interferometer to investigate deformations of bridges or tunnels (Inaudi 2004). *Interferometric Real Aperture Radar* is also used to monitor structure vibration for Structural Health Monitoring. Operating in the microwave region this method has the advantage over other proximal/remote sensing techniques that it is not influenced by local environmental conditions such as insolation (Luzi et al. 2014).
Infrared thermography shows promise to monitor heat released during crystallisation to determine salt decay and salt type in building stones (Vazquez et al. 2015). It is commonly used to map moisture and other moisture induced weathering processes including detachment, cracks and biological weathering. Changes in conductivity or trapped air help to identify alterations in the investigated material.

1.3.1 Structural Health Monitoring

Structural Health Monitoring is a common technique in civil engineering for damage identification and monitoring of large buildings and constructions especially for bridges, but also wind turbines and spires of churches (Peeters et al. 2001, Dong & Song 2010, Cunha

et al. 2013, Ubertini et al. 2016). Within Structural Health Monitoring several techniques are applied from NDT to destructive/invasive techniques.

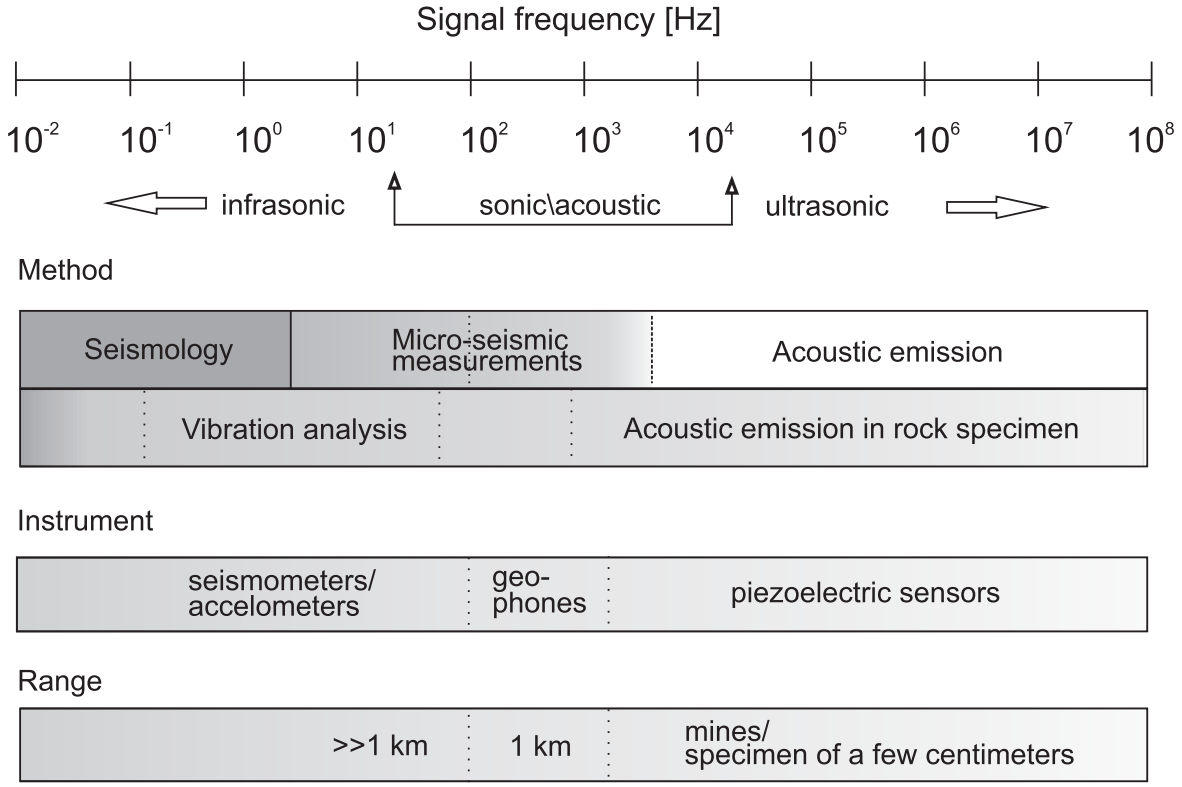

Figure 1.13: Overview of the frequency and method used to analyse different areas/ranges and events, modified from Manthei & Eisenblätter (2008).

A common minimally to non-invasive technique is *Vibration Analysis*. It identifies changes in the eigenfrequencies (see Chapter 4) of the measured structures to the simulated eigenfrequencies of the 'healthy' structure. The techniques has only been sporadically used for historic buildings including measurements at churches and amphitheaters (Ubertini et al. 2016, Lorenzoni et al. 2016). Lorenzoni (2013), Stefano & Ceravolo (2007) used accelometers and displacement analysis for the vibrational analysis of historical buildings.

Another common technique, *Acoustic emission*, is described in the following section. Acoustic emission (AE) is a non-destructive test method used in Structural Health Monitoring for buildings, mines or laboratory sized test specimen ranging from metals to rocks. The application is similar to approaches in seismology or high and low frequency micro-seismic measurements of mines (Figure 1.13). In cultural heritage AE has only been used for a few investigations (Strojecki et al. 2011, Carpinteri & Lacidogna 2006, Suarez del Rio et al. 2010), but has great potential. In-situ tests, where the changing temperature and humidity is used as an applied stress influence, were performed on wood to investigate the state of an 18th century wardrobe (Strojecki et al. 2014).

The formation of cracks or deformation of a material rapidly releases elastic energy. These transient pulses of elastic wave energy (Figure 1.14) are described as acoustic emission events (Lockner 1993). Since the 1930s this technique has been used to investigate the stability of rocks and has been widely used in geotechnical engineering and of course earthquake monitoring (Potvin & Hudyma 2001). Acoustic sensors attached to the solid material of investigation detect the sound pressure level at a threshold of usually 30 dB to 60 dB depending on the material and environment to achieve a high signal to noise ratio (Li et al. 2010).

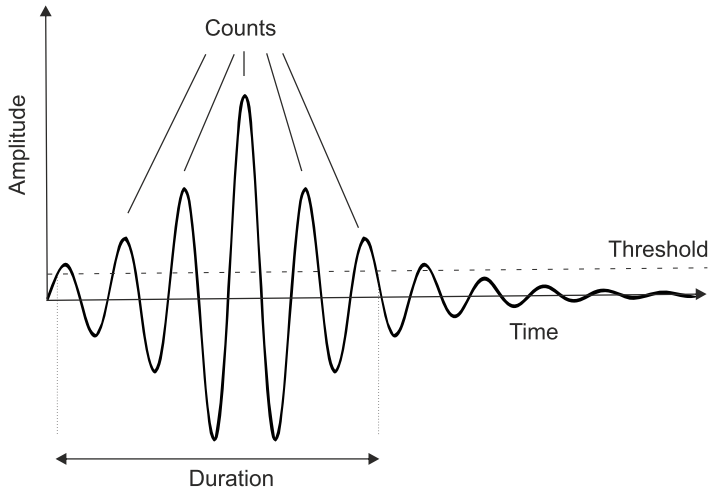

Figure 1.14: Acoustic emission event are mainly described by their frequency given by the measured counts of the duration of the signal limited by the set threshold.

Similar to the underground investigation in seismology, elastic waves are used in AE to monitor the propagation and location of deformation, crack formation and high stresses. Information about the size, deformation mechanism and the investigated medium itself can be obtained.

The number of acoustic events increases with deformation, such as inelastic strain, and can be used to estimate the damage of the investigated rock (Kim et al. 2016, Meng et al. 2018, Fortin et al. 2009). The techniques vary in the scale where they are applied and therefore in the recorded frequency windows (Table1.3). Earthquakes, large and long lasting events, are recorded at frequencies up to several Hertz by sensors that can be kilometres away. Events measured for large distance or areas of a few hundred m^2 occur with frequency ranges below 3 kHz (Figure 1.13).

AE events such as dislocations in the microscopic scale can generate high frequencies several times above the acoustic range (Manthei & Eisenblätter 2008). The recording of those high frequency events has to be at short distance as the elastic waves attenuates more quickly with the sound propagating. Small distances below 20 m or rock specimen with sub-grain sized source events are usually in the range from 1 kHz to 2 MHz. The piezo-

Table 1.3: Seismic signal parameters for small and large events from Manthei & Eisenblätter 2008.

Parameter	**Large event**	**Small event**
Pulse duration	long	short
Frequency range	low	high
Seismic energy	high	low
Frequency of occurrence	rare events	frequent events
Covered area	large	small

electric sensor for AE detection is attached to the sample's surface and commonly includes a damping element to avoid reflections of the signal and damp signals around the resonance frequency. The sensors measure frequencies of the event from 1 - 100 kHz.
The arrival time of the different wave components (P- and S-waves) and their propagation speed are used to determine the location of the AE. The frequency of certain amplitudes has been studied further beginning with the Richter magnitude scale down to magnitude analysis of rock specimen in the lab (Scholz 1968, Lockner 1993). The frequency of occurrence of the events itself is not well studied (this is not to be confused with the frequency range of the recorded signal; see Table 1.3).
As an example, large scale investigations (up to 100 kilometers) record around 10000 events over a month. The count strongly depends on the investigated structure as well as the measured frequency of the events (10 - 1000 Hz) and the magnitude. Foreshock and aftershock events of a large magnitude event have been investigated at lab scale and intensively studied to make predictions of rock failure (Lockner 1993). Aftershock events N are found to decrease over time (t) with the relation described in Omori's law (Equation 1.15). Next to the constants k and c, the decaying rate p has been added later to the empirical law.

$$N(t) = \frac{k}{(t+c)^p} \tag{1.15}$$

Mogi (1969) analysed the time interval between AE events and found that the frequency n of the time interval τ follows an exponential decay of the time interval and a constant β. With increasing stress levels the constant β decreases (Equation 1.16). He also concluded that the events occur with a Poisson distribution, meaning at random and independently (Manthei 2018).

$$n(\tau) = e^{-\beta \cdot \tau} \tag{1.16}$$

Events are often found to appear in clusters (temporal and spatial related events.) Studies on different materials showed both independent and clustering of interdependent AE events (Nishizawa & Nomo 1990, Lockner 1993). The dependence seems to be related to the

stress applied and the set time frame and magnitude investigated.
Manthei (2018) showed for rock salt specimen under a load of up to 75 MPa a Poisson distribution for the recorded AE events. For two investigated event clusters with several hundreds of events, the number of AE events in a 15 s time window most likely appeared in groups of 4 or 10 events. This would correspond to a frequency of occurrence of 0.27 and 0.67 Hz.
It is unclear if the event rates occur with any dependency of the type of source or just randomly; also, what is counted as an event depends on the set threshold, and large cracks that occur slowly might not be included in the high frequency measurement.

A new approach matched AE investigation for samples under load with moisture contents (Tao & Zheng 2018). Sun et al. (2016) and Zhang et al. (2014) used the dominant frequency (of 100 kHz) of the signal to determine a link between moisture content and AE signals of a sandstone sample. Grapsas & Shokri (2014) used AE to evaluate evaporation from porous media. A correlation of the AE events and evaporation water loss, as well as particle size and shape of the porous media and area invaded by air, was observed.
Investigating fire damaged sandstones was the aim of some studies to link AE and temperature induced structural changes under load (Kong et al. 2016, Sirdesai et al. 2018). Sandstone with increasing NaCl-concentration showed an increased strength and fewer AE events under load (Huang et al. 2018).

1.3.2 Drilling tools

Drilling techniques are used in cultural heritage as a minimally invasive method to investigate the subsurface decay of building materials. It has been shown that they can characterise structural properties of the rocks and detect salt layers beneath the surface of a rock (Modestou et al. 2011, Siegesmund & Snethlage 2011, Fratini et al. 2006). This section gives an overview of the drilling technique, an example of a commercially available tool and the difficulties that can be encountered.
Drilling compromises the breakage of rock and removal of its ground material. When the stone's tensile shear or compressive strength is overcome, the stone breaks. Intergranular bonds can be broken by shear or tensile force (for example shear cutting force leads to fracturing). Breakage or grain crushing is caused mainly by compression force on the sample or impact forces by axial thrust from the weight on bit; therefore, UCS is usually used as a figure of merit in the discussion of rock hardness.

The usage of drilling tools in heritage building materials started in the early 20th century with a manually operated drilling resistance machine from Julius Hirschwald (Pamplona

et al. 2007). Hirschwald used a variable load on top of the device and rotatable sample holder to measure the number and duration of rotations applied to a wheel. This wheel needs to be turned to rotate the sample such that the cutting edge with the certain load loosens more and more grains, therefore drilling into the rock. Following this approach, drilling tools have been developed to analyse the difference in time needed to drill a hole with certain depths with constant rotation speed and pressure.

An example of a recent development is the DRMS (Drilling Resistance Measurement System) from *SINT*, available since 2001. The drilling tool, measuring the applied force to drill a hole, is proposed as a standard method to investigate rock hardness (Tiano et al. 2000). A micro-drilling tool to investigate the hardness of rocks and potentially the weathering is described in Stavropoulou (2006). The tool has a similar performance and set-up as the DRMS. Early developed tools include *DURABO* and *TERSIS* (Siegesmund & Snethlage 2011). The main advantages of the DRMS include its portability (weighing only 5.5 kg) and ability to be used both vertically and horizontally, thus stones do not need to be removed and data are obtained immediately. Changes of rock hardness and structural properties can be measured and located in relation to the depth of the hole drilled. This is especially advantageous compared to other methods investigating the rock hardness that provide information from an undefined region near the surface of the rock (such as the *Equotip*). The tool also does not place special requirements upon the surface or dimensions of the samples.
The DRMS has two motors to ensure a constant rotation speed from 20 - 1000 rpm (rotation per minute) and penetration rate from 1 - 80 mm/min. Depending on the properties of the rock, these parameters need to be adjusted to enable penetration. Keeping these parameters constant during drilling, the device measures the applied force through a load cell and the drilling position with respect to the surface of the sample is calculated from the constant progress rate. The drilling reaches up to 50 mm depth.
The limit of the applied force, for a provided 5 mm drill bit (*Diaber* from *SINT*), can reach 100 N. This corresponds to apatite, having a Mohs hardness of 5 (Pamplona et al. 2007). The usage of a smaller drill bit (3 mm) decreases the surface contact area and could allow drilling through harder materials; though the use of larger diameter drill bits can lead to a more sensitive measurement (Pamplona et al. 2007). When using different drill bit diameters the exerted force should be given in N/mm (the applied force divided by the diameter of the drill bit) instead of MPa (Pamplona et al. 2007). Pamplona et al. (2007) also suggest a link to other methods for investigating the mechanical properties of rocks, such as scratch hardness or uniaxial compressive strength, to reduce the number of tests to characterise sample properties.
An exponential correlation between drilling resistance (measured via the DRMS) and the

Mohs hardness of minerals is indicated (Pamplona et al. 2007). Further investigations suggest a linear correlation between drilling resistance and UCS (Theodoridou et al. 2012). Thomson et al. (2013) links UCS with the energy needed for grinding a rock. Al-Naddaf et al. (2013) showed a negative linear correlation between drilling resistance and porosity. When comparing the measured porosities, from for example hydrostatic weight, it is important to distinguish between the total porosity and the effective porosity (excluding isolated pore spaces, which cannot be reached by fluids or gases). It is also possible to predict the porosity for lithologies with similar mineral aggregation (Al-Naddaf et al. 2013). Several analyses with the DRMS show the possible identification of different sedimentary layers, different grain sizes and resistance, and micro- and macrocracks (Valentini et al. 2008). Modestou et al. (2011) describes a successful location of salt crystallisation within limestone samples using the DRMS. The salt front in porous materials can be mapped using the increased force of resistance of salt accumulation and/or of pore clogging in the samples. Holes with a depth of 10 mm were drilled into the samples which had been treated with different salt solutions. The salt crystallised in different areas (under the same drying conditions) caused by different densities, saturations and viscosity; in other words with varying movement through the sample (Modestou et al. 2011).

The difficulty of comparing data from drilling tools is caused by the deviation of drill bits, cutting tool wear, dust transport problems, and the lack of comparison between drilling resistance, strength, and hardness (Pamplona et al. 2007). Different types of drill bits vary in hardness and shape of the bit. An ideal bit would cause no scattering. If the wear of the tip increases quickly, it is important to have a comparison sample which enables this effect to be corrected at the analysis stage. Commonly a very homogenous material such as an artificial reference stone (porcelain) or *Maco* (by *Corning*, fluorophlogopite mica and borosilicate glass) is used for this purpose (Al-Naddaf et al. 2013, Valentini et al. 2008, Pamplona et al. 2007). Investigations using halite as a calibration material for drilling were made by Pamplona et al. (2010).
These 'calibration' materials are used at the beginning and at regular intervals during the tool's working life. Based on the drilled length and resistance of the first hole, the measured drilling forces are corrected (Rodrigues & Costa 2004). Moreover, each drill bit should be used under defined conditions, i.e. only for one type of stone and for a specific purpose during the entire lifetime of the drill bit. The authors also suggest that instead of using a "universal" calibration material, a similar stone to that under study should be kept as reference, since the measured wear effect can be very different for materials with different composition and abrasiveness, even if the initial drilling resistance value is similar. The regular use of a similar reference as the investigated abrasive rock will decrease the lifetime of the drill bit further.

Another method to overcome the wear effect of the tips is the pilot hole method. It is used in mechanical engineering to reduce the chisel edge contribution on the thrust force (forward force produced by the engine). The chisel edge describes the connection of the cutting edges at the tip of a drill bit. For example, Won & Dharan (2002) pre-drilled composite laminates with a pilot hole so that the bounded layers would not separate due to the thrust force and the drilling process would occur without delamination. Mimoso & Costa (2006) measured for marble and a soft limestone a force reduction of 55% and 72%, respectively, by using a 5 mm drill bit over a 3 mm pilot hole. However, such reduction of the drilling resistance narrows the measured values to a range where differences between stone types and grain cohesion (before and after consolidation treatment) are closer to the resolution limit of 1 N. In drilling resistance measurements, indentation corresponds to the initial part of the drilling process in which the force grows rapidly and where drilling is mainly characterised by hammering. Mimoso & Costa (2006) used the pilot hole technique to reduce this effect. The technique also allows the use of less expensive drill bits without diamond tips and reduces packing of the removed material. The technique provides a good application for a small numbers of holes but gets increasingly time consuming for in-situ applications.

1.4 Conclusion for the research

Sandstones are one of the most important building stones in Scotland. Their mineralogical composition as well as the pore network make them susceptible to a wide range of weathering processes. When evaluating the influence of the mineral composition and the environmental conditions on weathering, especially water and temperature are the driver for the change in composition. Water mobilises and transports salts and other reactants through the porous system. Cyclic changes in water and heat are the most important weathering factors (Benavente et al. 2008, Weiss et al. 2004, Arnold & Zehnder 1989) and considering them is mandatory when monitoring damage (Sohn 2007). Environmental monitoring of buildings is important for predicting the material behaviour, decay mechanisms and for modeling the long term behavior and properties of historical buildings (Benavente et al. 2014, Warke & Smith 1998). Micro-climate monitoring focuses on small area environmental conditions that can exceed the macro environment (Warke et al. 1996).
Predicting stone decay is difficult under changing environmental conditions especially with the uncertainty of climate change and the heterogeneity of building materials (Benavente et al. 2008). Under a changing climate increased amount and duration of wetting are predicted to lead a change in weathering to more chemical based weathering as for example moisture can propagate deeper in the rock and changes in moisture gradients increase (McCabe et al. 2013). The difficulty of diagnosing problems are enhanced by the constant change of the building material itself through weathering and the presence of salts.

Drying of porous systems triggers weathering processes. The evaporation rate of salt saturated solutions influences where crystallisation takes place. Changes in temperature, pressure or humidity can strongly influence evaporation. It is therefore important to know the time window in which those changes happen when evaluating the influence on the evaporation rate.

Understanding the magnitude and exact timescale of the complex interaction of the mineralogical, poro-mechanical and environmental conditions will help in identifying the most suitable conservation strategy. Non-destructive or minimally invasive tools are needed to assess the state of decay. Several approaches exist that in combination allow us to gain a better understanding of the weathering on site. Tools that reduce the amount of tests and an improvement of the quality of the measurement as well as a better reliability are still needed to make an informed decision (Vandevoorde et al. 2013).
In summary the most damaging weathering processes cause dilational changes caused by wetting and drying, salt crystallisation or hydration of minerals. These factors are strongly influenced by environmental conditions, mineral composition and pore network properties and also cause an alteration of those. NDT tools that address dilational changes and structural changes can therefore track some of the most damaging causes of weathering. The influence of the operator on the NDT tools should be as small as possible. An easy handling of the tool with a long life time and low costs should be considered when developing tools for cultural heritage.

For the investigation of new NDT tools, this project will include a detailed characterisation of the sample properties (Chapter 2). The mineralogy with the common components and especially identification of large clay contents are essential. The textural and compositional properties of the samples are needed to evaluate the performance of the developed techniques for decay investigation.
The laser interferometer will a add non-destructive tool to the test series that will focus on weathering processes that cause dilation to identify the state of decay. Changes in the volume of stones are linked to high stresses on the sample. A constant monitoring of these before they are even visible with the eye can identify building materials that are prone to severe decay. The building material can be characterised without any sampling. Similar to acoustic emission but at different frequency ranges and by the analysis of length changes, the properties of the stone and therefore also weathering processes can be tracked with a nanometre precision. The tool and its application are described in Chapter 3.
Chapter 4 includes the development of a minimally invasive drilling tool. The ultrasonic drilling tool addresses the problems of conventional drill tools to overcome limits in the penetration of hard materials as well as the adjustment of settings for different rock types.

A tool that enables a penetration of varying rock types with constant settings would allow for better comparison of the different samples. The handling of the tool should allow for a constant holding of the tool that is not influence by the tool operator. Abrasive stones reduce tool life and the need of expensive maintenance or drill bits. A reduced tool wear would enable a longer life of the drill bit and therefore increase repeatibility of tests. Furthermore, the tool needs to be able to track structural changes in the rock caused by weathering processes.
Environmental monitoring of historic sites allows to track one of the main drivers of decay, humidity/moisture and temperature changes. The local micro-climate can vary which leads to different weathering rates on one building. The monitoring of temperature and humidity will help to identify areas of increased risk of decay through the analysis of the amount and frequency of changes in the micro-climate. Chapter 5 includes the micro-climate monitoring at four sites all over Scotland.

Chapter 2

Samples and Methods

This chapter gives an overview of the provenance, quarries, use and petrography of the samples analysed in this study (Figure 2.1). The thesis focusses on sandstones from Scotland and England which are and were used as building materials. During this project these stones were used in experiments that utilised a drilling device, an interferometer and iButtons. In Scotland sandstone is the prevalent building stone. In the UK sedimentary rocks (including sandstone and limestone) are the most common building stones (BGS 2007).
Four popular replacement stones and weathered building material from four sites in Scotland (provided by *Historic Environment Scotland*) were analysed. The four replacement stones, provided by *Tradstocks* and *Standcliff Stones*, include blonde and red sandstones with varying physical properties. The diverse physical and mineralogical composition of the stones allows the evaluation of performance for the different types of developed tools. Identifying changes in physical properties like porosity can indicate different stages of decay. The investigation of the unweathered or 'fresh' quarry sample in comparison to the same weathered sample shows how the tools can monitor proceeding building stone decay and how data in the field can be used. The study sites were chosen to cover the diverse climate to which building stones are exposed to in Scotland. The HES sites include Fort Charlotte at Lerwick on the Shetland Islands, Dunkeld Cathedral in central Scotland, and Jedburgh Abbey in the borders. Additional samples include sandstone from the spire of the University of Glasgow (collected during restoration work), and a carbonate-rock from Anston in England. This sample was used to test the performance of the drilling tool for the second biggest group of building stones in the UK (BGS 2007).

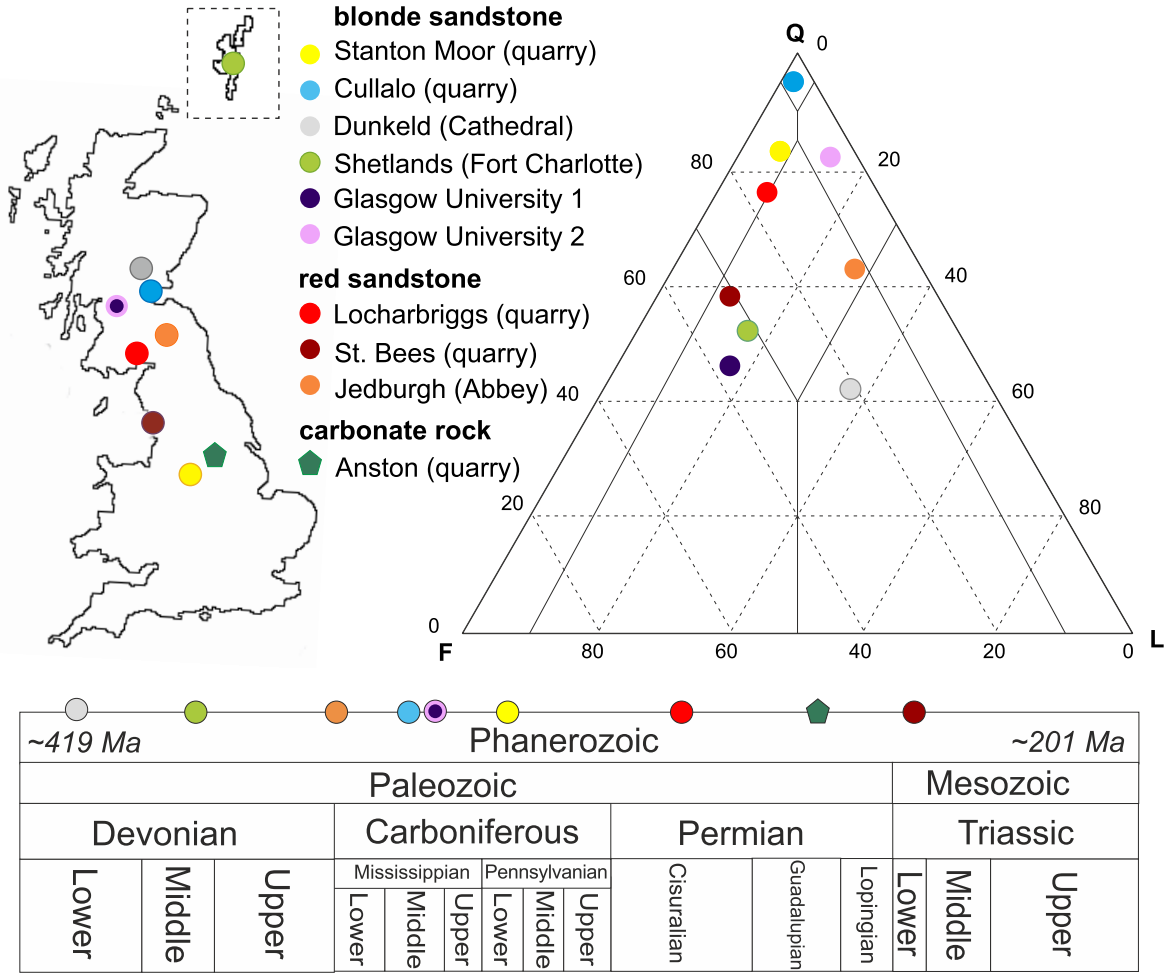

Figure 2.1: Overview of the samples: Site location, sandstone composition with contents of quartz (Q), feldspar (F) and lithic fragments (L), and chronostratigraphical classification. The ternary diagram of sandstone composition was drawn after Pettijohn et al. 1987 and a 300 point count method was used (see Section 2.1).

2.1 Methods

2.1.1 Microscopy

Thin sections

Thin sections of rocks have a thickness of < 30 µm and were studied by optical microscopy and scanning electron microscopy. The bulk sample of the rock is cut with a diamond saw and impregnated with epoxy resin (*Buehler epo-heat*). A blue dye powder is added to the epoxy mix to improve the contrast of the pore space and the grains. After the sample is placed under vacuum for 10 minutes, it cures for approximately 2 hours. Grinding steps with 30 µm, 20 µm and < 12 µm aluminium oxide powder on a glass plate reduce the sample thickness to < 30 µm. After the grinding steps, a pre-polish with < 5 µm silicon carbide minimises scratches and evens hard mineral boundaries. Next the sample surfaces

are polished with aluminium oxide powder (< 1 and 0.3 µm) and colloidal silica (0.04 and 0.06 µm). This creates a smoother surface in order to decrease electron scattering. Ultrasonic baths should clean any used polishing and grinding material. A carbon coating of 20 nm for non-conductive samples is applied with *Q150T ES* carbon coater improving the secondary imaging signal and reducing artifacts through charging and beam damage by heating.

Polarised light microscopy

A petrographic microscope is a type of light microscope that is used to identify the mineral composition in thin sections. This microscope has two polarisers and a rotatable sample holder. Polarisers are oriented perpendicular to each other, acting as cross-polarisers. The light after the first polariser with only one direction of oscillation can not pass the second polariser. Depending on the crystal lattice of some (optical anisotrop) minerals, the light is redirected and can pass the second polariser. Different levels of extinction can be observed as well as characteristic colours caused by interference. Two petrographic microscopes were used: *Zeiss Axioplan* and *Olympus BX41*. Images were taken with a *Nikon DS-Fi1* camera and the *NIS-Elements F3.0 software* on the Zeiss microscope. The Olympus microscope used the *Olympus DP25 camera* and the *cellˆB software (v2.8)*.

Scanning Electron Microscopy

A scanning electron microscope (SEM) was used for imaging (secondary and back scatter electron images) and chemical analysis (energy-dispersive X-ray spectroscopy). When a focussed electron beam reaches and scans the surface of a sample (in a raster pattern), several interactions with the sample atoms can occur. Depending on the approach, those interactions are recorded by different detectors. The measurement is usually done under a vacuum of $< 10^{-5}$ mbar to avoid damage of the electron source or scattering of the electrons.
The electron beam can interact with the sample surface via excitation of secondary electrons (SE). This effect occurs near the surface of the sample and is usually detected by a scintillator. The light signal of the detector is converted into an electrical signal, where each scanned point has a certain intensity creating a grey scale image of the surface.
Back scatter electrons (BSE) emerge from deeper areas of the sample than SE. The intensity of this signal is strongly depend on the atomic number of the scanned material. Heavy elements show stronger scattering than lighter elements. BSE are therefore used to distinguish light and heavy (brighter) elements in the image.
Energy-dispersive X-ray spectroscopy (EDX) uses the characteristic X-rays emitted by the sample. The electron bean can excite individual electrons out of atoms. The resulting electron energy gap is filled with an electron of a higher energy level. The released energy that is emitted in form of radiation is characteristic for the element and the energy level of the electron. The characteristic X-ray radiation can be used for a quantitative chemical

analysis.
Two SEM were used in this study (*Quanta 200F FEI* and *Zeiss Sigma VP*) at the Imaging Spectroscopy and Analysis Centre, University of Glasgow. For the image analysis accelerating voltage of 10 - 20 kV with a varying working distance between 5 - 10 mm were used. The operational setting for EDX are 20 kV and a working distance of 8.5 mm. EDX uses the Oxford Instrument INCA software. The probe current is constant at 1 nA.

Point count for QFL

For the classification of sandstones, the mineral composition given by the amount of quartz, feldspar and lithic fragments is needed. After Dickinson (1970) at least 300 points in a thin section should be identified to classify the sandstone. The point count was done with optical and electron microscopy.

Image analyses: Porosity

Binary images of the thin sections enable an estimation of the porosity of the sample.
The amount of black pixels (pore space) in relation to the total number of pixels in binary images is counted. When converting a grey scale image (from SEM and optical microscopy) into a binary image, the used threshold can introduce a variation of sometimes up to $\pm 5\%$ porosity. The porosities described in this Chapter are calculated in MATLAB.

2.1.2 X-ray diffraction

X-ray diffraction (XRD) enables qualitative analysis of the clay fraction ($< 2\,\mu m$) of the samples. X-ray diffraction uses X-ray radiation and its scattering/reflection at the atoms of the sample to identify characteristic interplanar distances in the crystal lattice of minerals (Equation 2.1). Maximum interference of the used radiation with wavelength λ (see Chapter 3) occurs when a multiple (n) of this wavelength equal the scattering angle (θ) and the distance d in the crystal lattice.

$$n\lambda = 2d\,sin\theta \tag{2.1}$$

The preparation of bulk material samples includes breaking the sample with a hammer and grinding with mortar and pestle. The sample powder is then mixed with acetone and placed on a glass slide.
In order to analyse sandstones that have a clay content smaller than 5% of the total volume, the clay needs to be extracted (Tucker 1988). The samples are carefully pushed into smaller pieces with the mortar and pestle to avoid alteration of the clays by too much force/grinding. About 5 g of sample are added to 35 ml of deionised water and placed into an ultrasonic bath for 10 min for further disaggregation of the clays. The clay fraction is separated from the bulk material with a centrifuge, where the different settling velocities

of particles are used to extract the intended particle sizes.

$$v = \frac{2}{9}\frac{(\rho_p - \rho_f)}{\mu} g r^2 \tag{2.2}$$

In Stoke's law (Equation 2.2) the velocity (v) of the sinking particles is dependent on the radius of the particle (r) the acceleration g (gravity for settlement in a tube), density of the particles and settling fluid ($\rho_{p/f}$), and the viscosity of the settling fluid (μ).
Stoke's Law accounts for spherical particles, non-turbulent medium with low particle interactions, and constant temperatures. The solution, with the fine particles still in suspension, can then be extracted with a pipette. The remaining, deionised water is then evaporated at 50° C in an oven. To account for orientation during settling or differential settling due to different sizes the dried material is mixed again and diluted with acetone. The suspension is placed on a glass slide.
An *ARL X'TRA* Powder Diffractometer from *Thermo Fisher Scientific* at the Engine Shed (HES, Stirling) is used for the analysis. A 2θ-scan is run from 5 - 50° with cobalt K_α-radiation. The measurement time is 60 s for every 1°. Current is set to 44 mA and voltage to 44 kV. A 0.05 mm divergence slit, 0.07 mm anti-scatter slit, and a 0.12 mm acceptance slit are used. The gained 2θ-scans are analysed with *X'Pert High Score Plus* using the *International Centre for Diffraction database* (ICDD).

2.1.3 Micro-computed tomography

Micro-computed tomography or X-ray micro tomography (XCT or μCT) is an imaging technique that uses several X-ray images of cross sections of an object for constructing a 3D model of the object. The technique enables quantification of porosity and an assessment of damage to rocks through changes in the pore network (see Chapter 4).
A *XTH320 Nikon XT H 225 LC* X-ray computed tomography system was used for the scans of Cullalo, Locharbriggs and Stanton Moor at the *Advanced Materials Research Laboratory*, Strathclyde University. The settings vary depending on the sample and range from 140 - 170 kV and 40 - 55 µA with a 0.25 mm Cu-filter. 3141 images were taken during the sample rotation of 360°. The detected intensity, depending on the absorbed or scattered X-rays, is converted into a greyscale image. The voxel size depends on the sample size. For smaller samples (1 cm x 1 cm x 2.5 cm) the voxel size is $\sim$ 8 µm and up to $\sim$ 50 µm for the biggest sample (6 cm x 8 cm x 10 cm).
The images were analysed in *Avizo 9*. Image analysis can introduce errors through the manual setting of the pore range. These errors are propagated when the connectivity of pores is analysed. Furthermore, the resolution of a few microns (excluding pores below this limit) adds another error when the pore size distribution or connectivity is examined.
For the analysis of damage in the samples the length of the pores was used to determine

the occurrence of cracks. For the pore size distribution the pore channels were separated and the equivalent spherical diameter of the irregular shaped pores was calculated. This diameter describes the diameter of a spherical pore with the same volume.

2.1.4 Artificial weathering

Some of the samples were artificially weathered to enable controlled damage of the stones. They were then analysed with the ultrasonic drilling tool and the laser interferometer. Several Cullalo, Locharbriggs, Stanton Moor and Anston samples were exposed to cyclic wetting and drying with NaCl- and Na_2SO_4-solution based on the treatment by Modestou et al. (2011). The sample sizes included large samples for the drill tests (8 cm x 5 cm x 8 cm) and smaller samples for the laser interferometer (1 cm x 1 cm x 2.5 cm).
To induce subflorescence, four sides of the samples were coated with epoxy. The top and the bottom of the samples were uncoated to enable interaction with the environment. One of the uncoated sides was treated with a water repellent (5% sodium methylsiliconate solution). This solution was applied onto the surface with a brush.
The water repellent was left to dry for 24 hours followed by another 24 hours in an oven at 70° C. The untreated sides of one sample batch were placed into a 14% Na_2SO_4-solution. Another batch was placed into 14% NaCl-solution. The unsealed face was exposed to the solution for 3 hours. This was followed by a drying phase of 24 hours in the oven at 45° C. The cycle of wetting and drying was repeated four times. After each cycle a test specimen was cut into sections to monitor the progression of subsurface damage.

2.2 Sample description

The following sections include a detailed description of the geological background and petrographical properties of the sample material. Table 2.1 summarises the petrophysical and poromechanical properties of Cullalo, Stanton Moor and Locharbriggs, the three used most sandstones in this project. The information in the table and pore network properties are derived from Graham (2016), a previous work on the samples. Figure 2.2 displays the pore size distribution of these three stones. The porosities in the description of all stones are derived from the image analysis as described in Section 2.1.1.

Table 2.1: Summarised petrophysical and poromechanical properties of the three used most sandstones Cullalo, Locharbiggs and Stanton Moor from Graham (2016).

Sandstone type	**Cullalo**	**Locharbriggs**	**Stanton Moor**
Porosity [%]	18	23	13
Open porosity [%]	14	17	12
Pore size distribution	unimodal	unimodal	bimodal
Permeability [mD]	579	211	7
Water absorption [%]	5.4-6.2	9.4-10.5	4.3-4.9
Saturation	0.64-0.76	0.73-0.83	0.8-0.99
Uniaxial compressive strength [MPa]	49	28	51

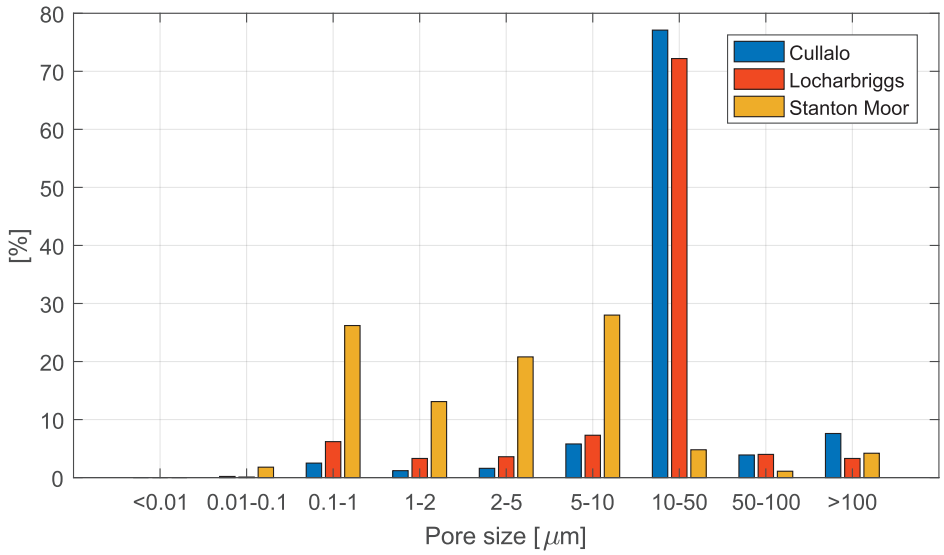

Figure 2.2: Pore size distribution for the sandstone samples Cullalo (blue), Locharbriggs (red) and Stanton Moor from *Mercury Intrusion Porosimetry* by Graham (2016).

2.2.1 Cullalo

Geological background

Cullalo, or Cullaloe, is a grey, Carboniferous sandstone from Fife. Geikie (1900) describes the stone as part of the Burdiehouse Limestone and Oil shale Group in the Calciferous Sandstone Series which is now the Strathclyde Group. In Hyslop et al. (2009) Cullalo lies within the Sandy Craig Formation of the Strathclyde Group. Sediments of the Strathclyde Group in east Fife are deposits of upward coarsening, deltaic cycles and units of upward-fining fluvial deposits (MacGregor 1968, Waters et al. 2011). Igneous intrusions are frequent through the group. The Sandy Craig formation contains alternating layers of mudstones, siltstones and sandstones with limestones and dolostones (Hyslop et al. 2009).

Cullalo is quarried near Aberdour (Fife). Its quarry was reopened in 2004. The stone was

used in Edinburgh in the 19th century, for example for the High Kirk of St Giles, which was given a new facade with Cullalo in 1829. Parts of the western colonnade of the royal Scottish academy also include Cullalo sandstone (Bunyan et al. 1987). For many decades the stone has been used in the Forth Estuary area. Cullalo is now used as a replacement stone for the petrographically similar Craigleith sandstone in Edinburgh, for example replacing buildings on the Royal Mile (Bunyan et al. 1987, Hyslop et al. 2009).

Petrographic description

Detrital mineralogy: Cullalo is a mature quartz arenite containing less than 10% lithic fragments and nearly no feldspar. Grains are moderately to well sorted, including mainly grains around 150 to 250 µm in size. *Texture*: Bedding can sometimes be seen in hand samples. The grains are subangular to subrounded. The grain contacts are primarily long contacts or point contacts (Figure 2.3). Polycrystalline quartz is frequent. *Cements:* Quartz overgrowth is common.

Trace minerals: Muscovite occurs sporadically. The main lithic fragments are kaolinite and titanium oxide and to a smaller amount iron oxide. Zircon appears as a trace mineral with grain sizes of 20 µm. K-feldspars occur very rarely (<1%) as fragments. *Porosity:* The porosity calculated from image analysis of a thin section is around 18%.

2.2.2 Locharbriggs

Geological background

Locharbriggs is a red Permian sandstone quarried at Locharbriggs near Dumfries from one of the oldest and largest quarries in Scotland (Stancliffstones 2012). The stone belongs to the Locharbriggs Formation of the Dumfries basin. This basin contains extensive accumulation of flash-flood Doweel Breccia and the interbedded, older Locharbriggs sandstone, that crops out in the north western part of the basin (McMillan 2002, Stone et al. 1996). Near the surface these formations are alternating with the younger Palaezoic rocks (McMillan 2002). The grain shapes indicate an aeolian origin from a dry climate (desert) with the occasional interbedded fluvial breccia (Bunyan et al. 1987, McMillan 2002).

Locharbriggs is a popular building stone in Glasgow and has been used for decades for example at the Kelvingrove Art Gallery, the steps and floor of BBC head quarters in Glasgow, and for several buildings in Edinburgh like the Caledonian Hotel (Bunyan et al. 1987, McCallien 1938).

Petrographic description

Detrital mineralogy: Locharbriggs is a submature subarkose sandstone. 5% of the quartz grains are polycrystalline. *Texture:* The sorting is good to moderate with layers of grain sizes varying around 150 µm and 300 µm. The grains are (sub)rounded and show mainly

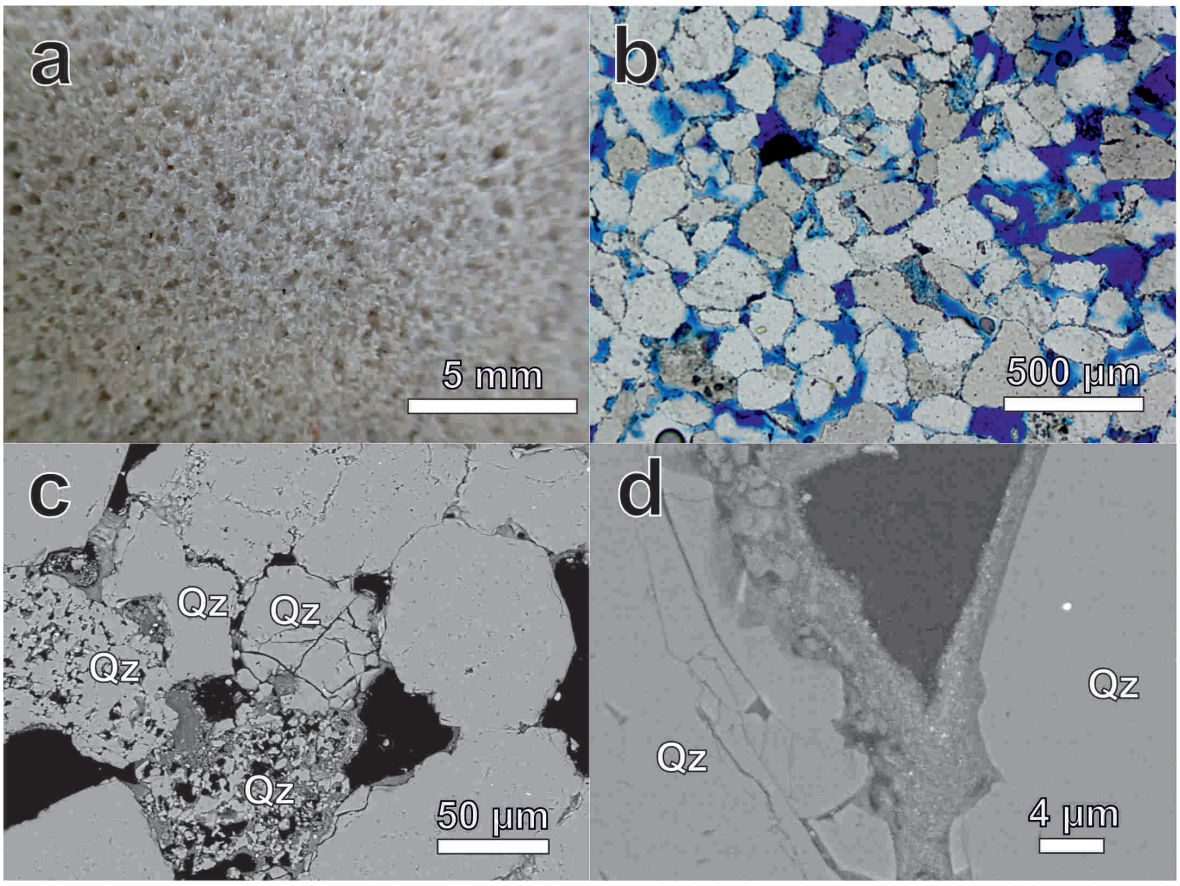

Figure 2.3: Cullalo sandstone. a: hand specimen. b: thin section under plane polarised transmitted light (pores dyed blue). c: BSE image of two disintegrated quartz (Qz) grains adjacent to less weathered quartz grains. Both grains are replaced primarily by kaolinite. Pore space is black. d: SE image of the clay coating between two quartz grains: kaolinite with very fine Fe-oxide particles. Pore space is black.

long and concave-convex grain contacts. Bedding can be seen in hand samples as well as in the thin section through sorting of grain sizes and layers with more abundant clay minerals. Cross-lamination can be seen in hand samples. *Cements:* Quartz overgrowths occur rarely. Feldspar (mainly K-feldspar but also with various amounts of sodium up to albite) and quartz grains show very common clay rims (Figure 2.4 c). Some quartz grains, and most feldspar grains have been replaced by kaolinite or show other forms of diagenetic alteration. Other clays are needle-shaped Mg-silicates, most likely illite. Illite and smectite are listed next to kaolinite in Baraka-Lokmane et al. (2007) as common clays in Locharbriggs. Iron oxides (mainly hematite) are frequent with crystal sizes of several micrometres up to 150 µm. Very few traces of iron can be found in the clay rims around the grains . In Penn et al. (2001) a study of reddish clay rims in sediments from Virginia identified nanocrystalline goethite. These rims only contain low levels of Fe next to the main components Al and Si, similar to the findings of Locharbriggs' clay rims (Chapter A Figure A.1). *Trace minerals:* Titanium oxide sporadically occurs with crystal sizes of 10 µm. Trace minerals are muscovite and less frequent zircon with sizes up to 50 µm. *Porosity:* The porosity calculated from image

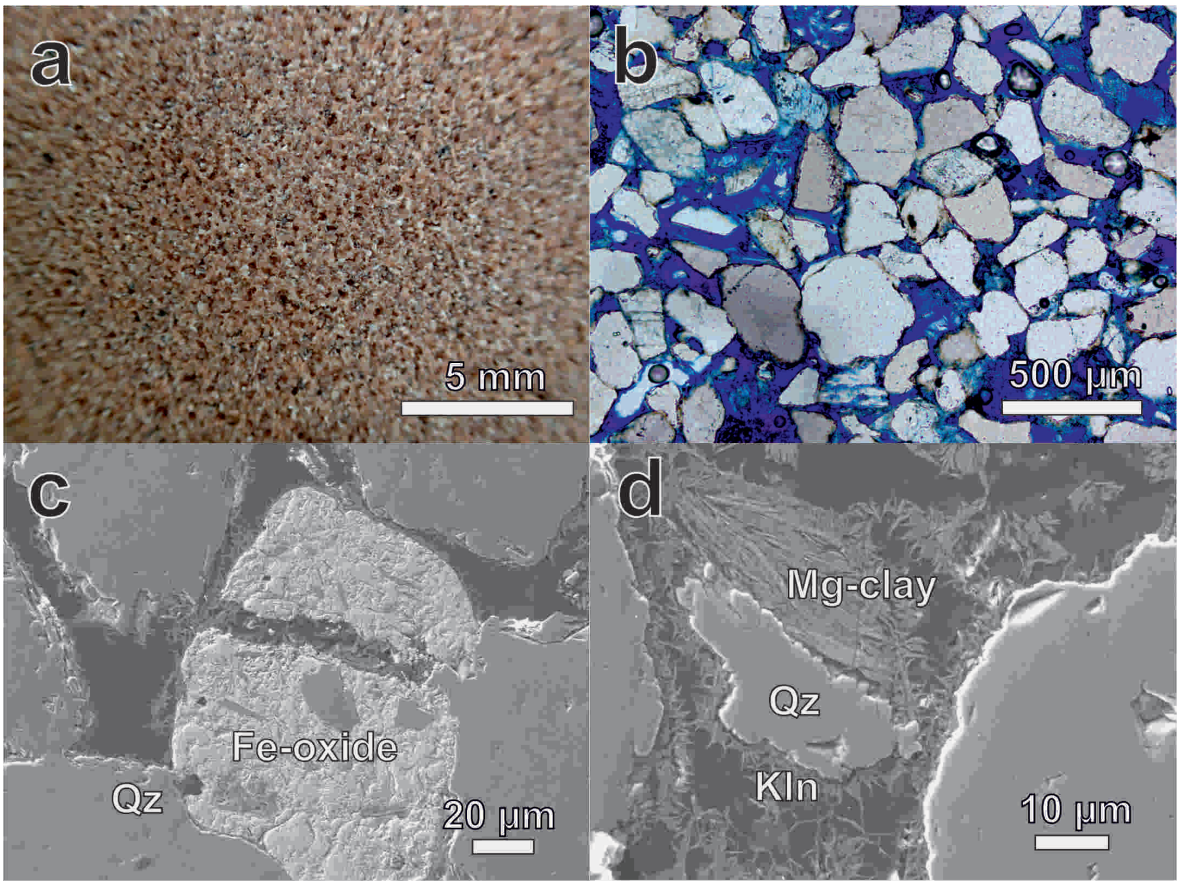

Figure 2.4: Locharbriggs sandstone. a: hand specimen. b: thin section under plane polarized transmitted light (pores dyed blue). c: SE image of Fe-oxide grain of more than 100 µm with adjacent quartz (Qz) grains that have a fine kaolinite coating. d: SE image of quartz surrounded by kaolinite (Kln) and a Mg-rich clay.

analysis of a thin section is around 19%.

2.2.3 Stanton Moor

Geological background

Stanton Moor is quarried in Dale View Quarry Derbyshire, and belongs to the Carboniferous sandstones of Ashover Grit in the Millstone Grit Group (Ainsworth & Pearson 2002). The Ashover Grit sandstones are mainly fluviatile deposits linked to a turbiditic delta system (Waters 2009). The stone is used for building in Scotland and for replacement of typically blonde sandstone. Examples include Our Dynamic Earth (Edinburgh), residences in Glasgow, Edinburgh, and London (Stancliffstones 2012), and replacement works at Lerwick Townhall (Shetland Islands) as well as at the University of Glasgow. The sandstone is prone to subflorescence (salt crystallisation beneath the surface), but has a good durability (Graham 2016, BRE 1997 and 2000).

Petrographic description

Detrital mineralogy: Stanton Moor is a blonde subarkose mainly containing quartz, K-feldspar (largely microcline), and Na-feldspar (largely plagioclase, Figure 2.5 a). Muscovite grains, several hundred micrometres in size, are abundant. *Texture:* Stanton Moor has a poor sorting with grain sizes from 10 to 500 µm (Figure 2.5 b). Most grains are > 200 µm. The grains show concave and convex as well as long contacts.
Cements: Quartz cement including euhedral quartz is common (secondary pyramidal growth on the original quartz grains) and smaller amounts of clay cement also occur (Figure 2.5 c). In addition to kaolinite, other aluminosilicates occur between detrital grains. Chains of needle-shaped crystals as well as layered clay minerals with intermittent iron or titanium oxides occur in clusters of maximum of 10 µm (Figure 2.5 d). Combining EDX, SEM, and XRD these clays are possibly mixed forms of phlogopite and clinochlore. The chain-like clay is likely chlorite. *Trace minerals:* Rutile was identified using Raman spectroscopy. Rarely, iron oxides and strongly etched feldspar can be found. Titanium and iron oxide typically occur as < 2 µm grains in the clay/pores, but sporadically as grains from $10 - 100$ µm. *Porosity:* The porosity of the sample is around 14% with pore sizes ranging from < 10 µm up to 500 µm.

2.2.4 St. Bees

Geological background

St. Bees is a dark red sandstone quarried on the West coast of Cumbria. The new red sandstone of early Triassic age belongs to the Chester formation in the Sherwood Sandstone Group (Ambrose et al. 2014, Barnes et al. 1994). The deposits are mainly from a braided fluvial system (Holliday et al. 2005). St. Bees is used as a building stones throughout the UK, and as a replacement stone, for example at Liverpool Cathedral (Stancliffstones 2012).

Petrographic description

Detrital mineralogy: St. Bees is a submature lithic arkose (Figure 2.1). *Texture:* The grains are moderate to well sorted and mainly (sub)angular with sizes around 150 µm. The grain contacts are mainly long to concave-convex (Figure 2.6 d). Bedding can sometimes be observed in hand samples as well as in the thin section through oriented grains, especially micas. Some grains show diagenetic alteration or complete replacement.
Cements: The cement of the sample is composed of clays with iron oxides but also calcite is abundant and replaces grains. Quartz overgrowths are rare. *Trace minerals:* Apatite, titanium, and iron oxide occurs sporadically with grain sizes between 50 to 100 µm. Clays are primarily illite, which is often needle shaped and occurs together with micas and hematite (Figure 2.6 c and d). *Porosity:* The porosity is around 20%.

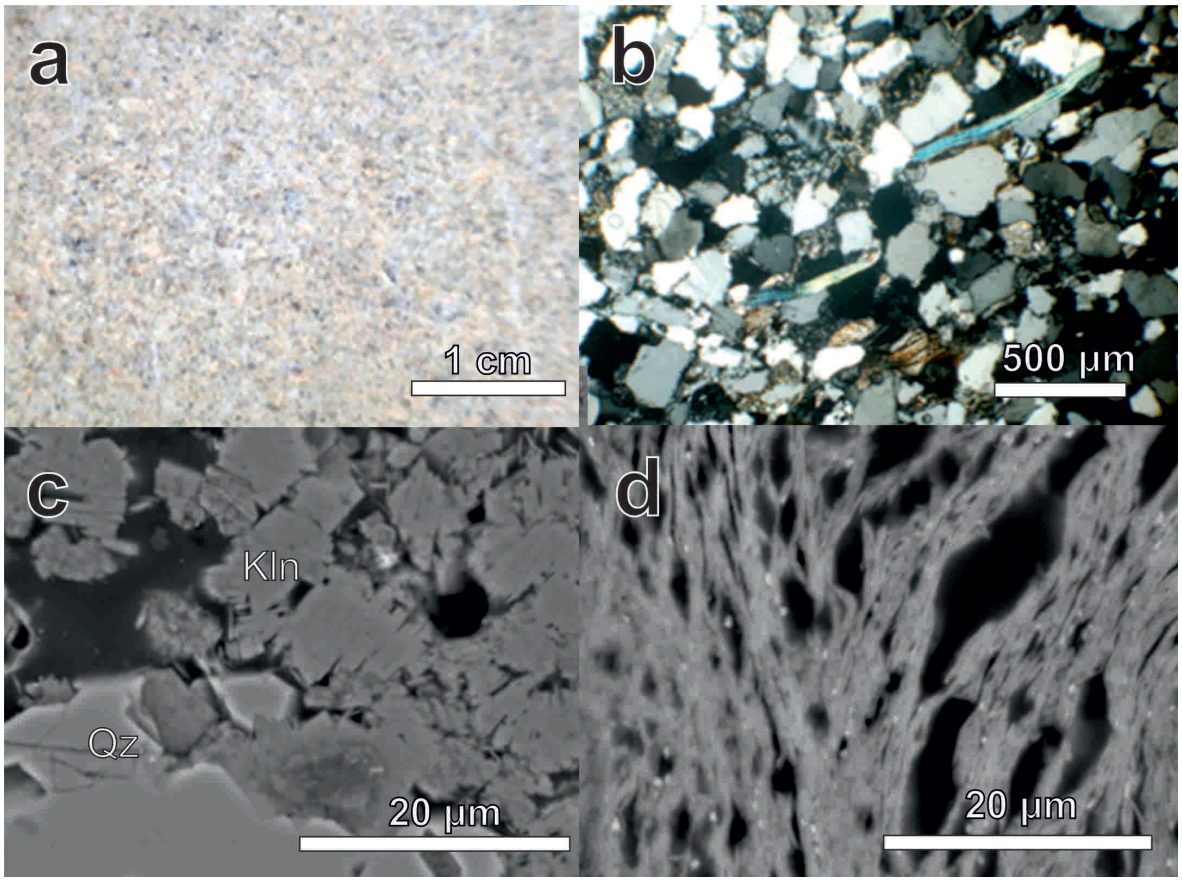

Figure 2.5: Stanton Moor sandstone. a: hand specimen; b: thin section between crossed polarisers. c: BSE image of the pore space (black) filled with kaolinite (Kln) next to a quartz grain (Qz). d: BSE image of layered clay with grains of iron and titanium oxide (white grains). The pore space is black.

2.2.5 Dunkeld

Geological background

Dunkeld cathedral is built from a pale grey stone that strongly weathers. The oldest part of the building is the choir, built in 1318 (Rotherford 1903). Stones from the former church were used to build part of the gable. The building was completed with the tower in 1501 (Rotherford 1903). For over 700 years the stone has been exposed to the climate and, during the reformation, even fires. Due to its strong decay, the stone is now replaced by Forest of Dean sandstone.

The building stones for Dunkeld Cathedral were most likely quarried at Gelly Burn, 8 km south east of Dunkeld (Armstrong et al. 1985). The sandstone belongs to the lower Devonian Teith formation (Armstrong et al. 1985). The Teith Sandstone Formation is part of the Strathmore group, the youngest group of lower Devonian rocks of a major basin in the Midland Valley of Scotland. The Teith Formation begins with mudstones of the Cromlix Formation and is overlain by grey sandstones with upwards fining beds from fluvial cycles (Armstrong et al. 1985). The deposits are most likely have a recycled orogenic provenance

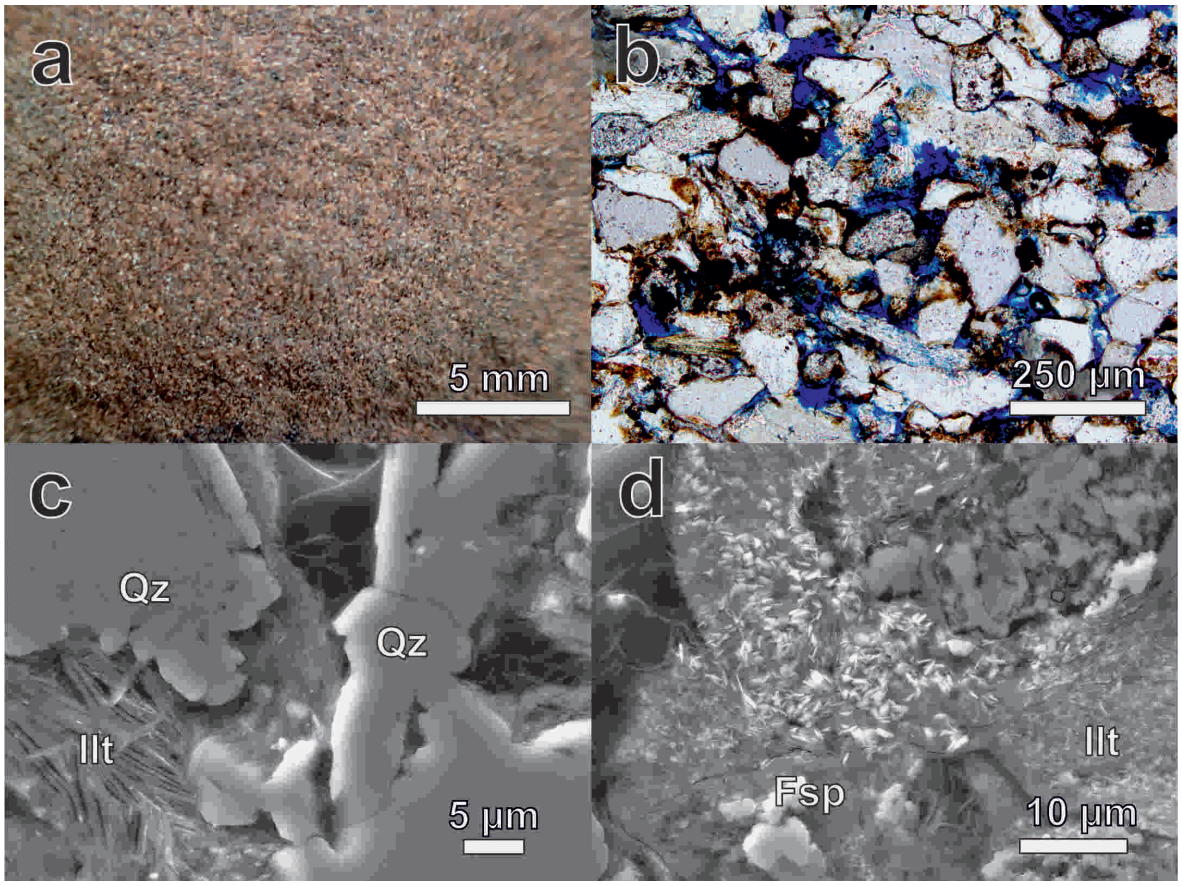

Figure 2.6: St. Bees sandstone. a: hand specimen. b: thin section under plane polarised transmitted light (pores dyed blue). c: SE image of needle shaped illite (Ilt) in between altered quartz (Qz) grains. d: SE image of large accumulations of illite replacing weathered feldspar (Fsp) grains.

(Phillips 2007) with intermittent deposition from local alluvial fans.

Petrographic description

Detrital mineralogy: The weathered sandstone of Dunkeld cathedral is a feldspathic litharenite with strongly decaying grains and high amounts of clays and micas (Figure 2.7 b). Quartz comprises about 40% of the sandstone and the grains show dissolution on their corners (Figure 2.7 c), as well as cracks and/or nearly complete replacement by clay minerals. Feldspar (with 60% plagioclase and 40% K-feldspar) shows very similar, strongly decaying grains until complete replacement by clay minerals.

Texture: The texture of the stone is defined by mainly fine to medium-grain sizes around 150 µm, with well to moderately sorted grains. Due to weathering the shape of the grains is strongly disorted. The contacts are floating to tangential, with rarely occurring long contacts. Cross-bedding can be seen in the hand sample as well as under the microscope.

Cements: Clay minerals are frequent replacing grains or occur sporadically in pores. Mainly kaolinite is replacing quartz. The more common clay is a Mg-Fe clay. The layers of this clay contain iron oxide particles, smaller than 1 µm. XRD analysis suggests an iron rich

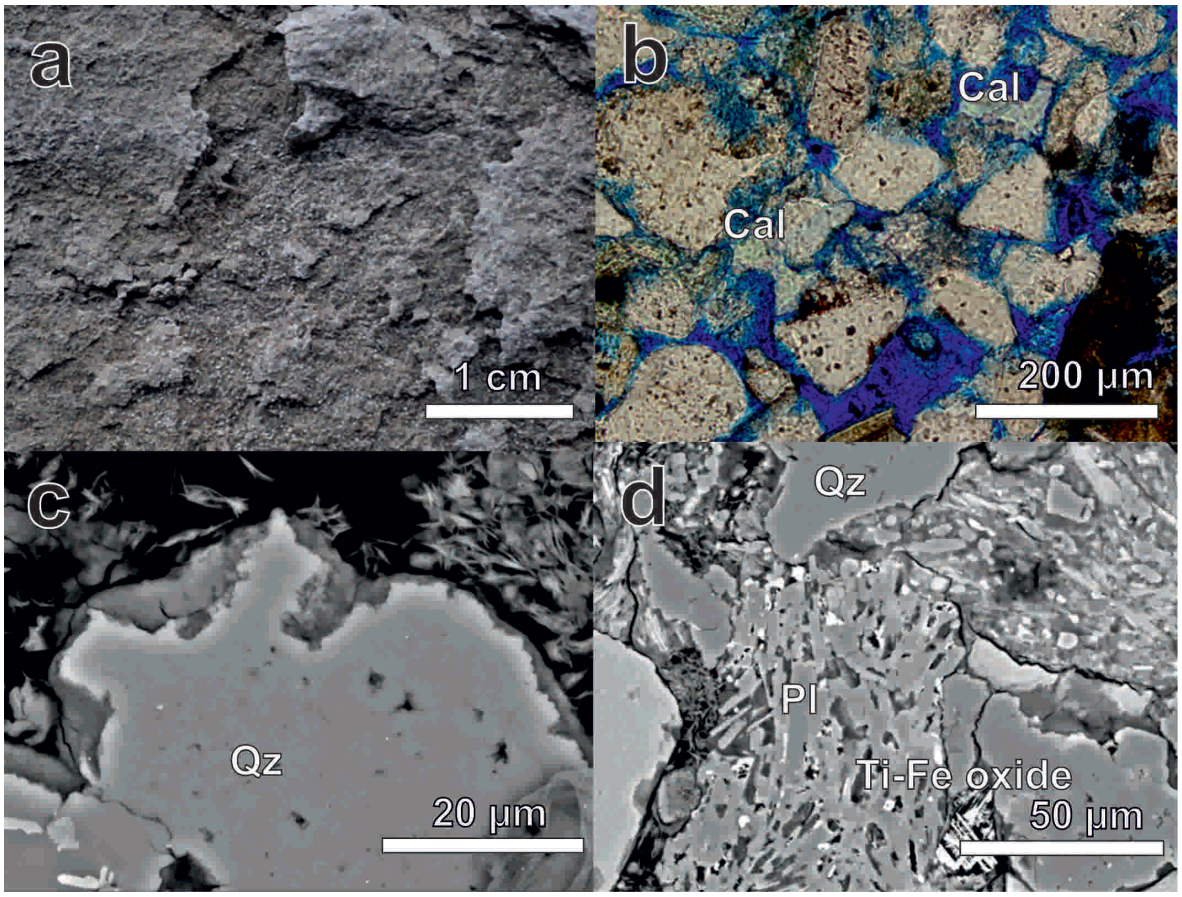

Figure 2.7: Dunkeld sandstone. a: hand sample. b: dyed thin section under plane polarised transmitted light with high lithic content with calcite (Cal), micas and clays (light to dark brown). c: BSE image of a decaying quartz (Qz) grain. Grain borders have started to dissolve. In the porespace scattered Mg-Fe clay can be found. d: BSE image of a disintegrated plagioclase (Pl) in contact with quartz (Qz), Mg-Fe clay and Ti-Fe oxides.

clinochlore. In addition to clays, micas are common. Calcite makes up 5% of the total grains. Calcite grains of 50 to 100 µm are common and rarely calcite is replacing other grains. Iron and/or titanium-oxide crystals can be seen sporadically (Figure 2.7 d). *Porosity:* The porosity is around 8%.

2.2.6 Shetland Islands

Geological background

Fort Charlotte, located in Lerwick, Shetland, was built in 1665, and reconstructed in 1781 (Carlisle 1813). Many buildings in Lerwick have been built with Lerwick sandstone. The quarry is assumed to be south Stony Hill, just above Clickimin Loch (Mykura 1976). Other known quarries, mainly for freestone, include Knab near Lerwick, and at the Ord on Bressay (Heddle & Mainland 1920).

Most sedimentary rocks on the Shetlands are in the Old Red Formation. Usually three groups of geographically distinct basins containing Old Red sandstone are distinguished

(Mykura 1976). The Old Red sandstone of the south-east mainland include the Devonian rocks of the Lerwick sandstone, and the sandstones of the islands Bressay, Noss, and Mousa, all with small lateral extent. The origin of the deposits is assumed to be alluvial to lacustrine. Surrounding breccias indicate that Lerwick lay in a valley crossed by torrential rivers in the Devonian (Mykura 1976).

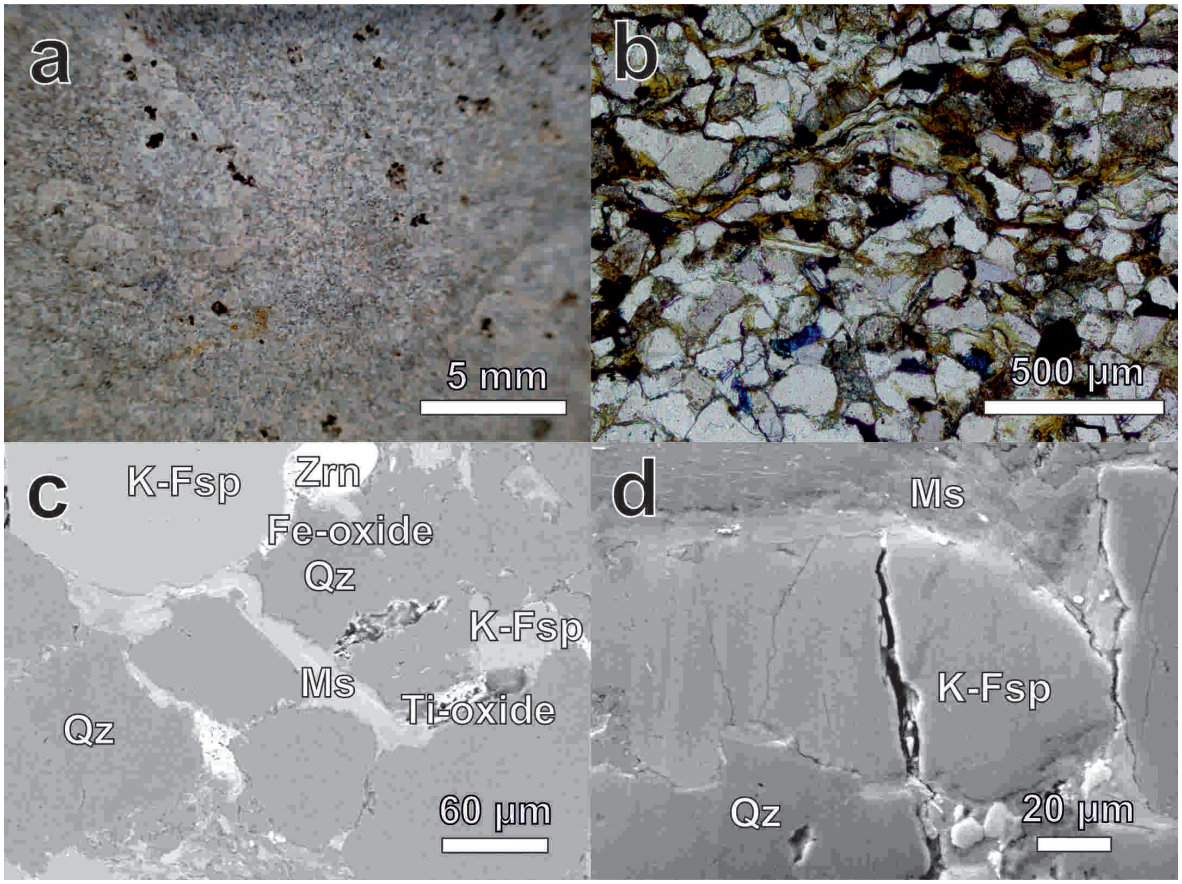

Figure 2.8: Shetlands sandstone. a: hand specimen. b: thin section under plane polarised transmitted light (pores dyed blue). c: BSE image of quartz (Qz), K-feldspar (K-Fsp), Ti- and Fe-oxides, zircon (Zrn), and mica (Ms). d, SE image of a large crack in a grain of K-feldspar below muscovite. Small grains of Ti- and Fe-oxide as well as zircon are embedded in clays that fill the secondary pore space.

Petrographic description

Detrital mineralogy: The composition of the sample is a lithic arkose. The feldspars are 50% K-feldspar and 50% of Na-feldspar, both of which are heavily decayed. About 20% of the quartz grains are polycrystalline. Quartz and K-feldspar show different stages of weathering. *Texture:* It is poorly sorted, typically with grain sizes from $< 50\,\mu m$ up to $500\,\mu m$ (average of $200\,\mu m$). Grains are subangular to subhedral. Grain contacts are mainly long and sutured. Bedding can be identified in hand sample as well as in the thin section through oriented micas and clay minerals. *Cements:* The cement in this densely packed sample is clay with detrital micas (Figure 2.8 c).

Trace minerals: Usually traces of Fe- and Ti-oxides can be found as well as calcite. Zircon

appears sporadically. Traces of halite could be identified with XRD. The XRD analysis also suggests an illite or illite mix as the dominant clay. *Porosity:* The porosity is very low (4%), with occasional big pores of up to 300 µm.

2.2.7 Jedburgh

Geological background

Jedburgh Abbey, first mentioned as an Augustinian priory (Cruden 1960, Royal Commision 1956), was founded in 1138. The abbey was built over nearly 100 years (Hourihane 2012). The west front of the cloistral building is from the late 12th century. The Abbey itself, as well as parts of the south range, include at least two sandstone types from fine to medium-grained: a blonde variety and red variety. All stones show moderate to severe weathering like sanding, flaking and/or alveolar decay. Previous studies on these upper Old Red Sandstones of the Church identified several different salts in the building including Na_2SO_4, NaCl, KCl, $CaCl_2$, and $CaSO_4$ (Kamh 2004). The lime mortar used during construction is thought to contribute to the high carbonate contents of the building stone.

The south front of the Jedburgh Abbey with kitchens, refractory, and abbot's lodging is partly built with strongly decaying, dark red sandstone. It is characterised by a strong delamination and differs from the other varieties. Samples are taken from this 'flaggy' red sandstone. The stone is found in parts of the wall or at the cellarage, is likely to have originated from outcrops very close to the abbey (MacGregor & Eckford 1952). The same stone has also been used to remodel the refectory and infirmary (Lewis & Ewart 1995). Most of the colourful building stones of the Abbey itself were provided from more than one local quarry, less than two kilometres from Jedburgh: Ulston Moor providing yellow to sometimes reddish stone, as well as Tudhope quarry, Ferniehirst and Hundalee quarry (Royal Commision 1956, MacGregor & Eckford 1952).

Around Jedburgh a famous unconformity can be seen: steeply folded rocks of the Silurian are overlain by nearly horizontal sandstones and marls of the upper Old Red (MacGregor & Eckford 1952, Pringle 1948). In that area the boundary of deposits of the upper Old Red to Carboniferous is sometimes missing, no fossils or volcanic activity mark the border (Pringle 1948).

The deposits of the upper Old Red around Jedburgh show two main groups: conglomerates and interbedded sandstones with marls (Greig 1971). The conglomerates are mainly made of greywacke and igneous rock fragments from small intrusions in the lower Palaeozoic. The main part of the deposits at Jedburgh is a soft and crumbly dark red and brown arenite (Greig 1971). A semi-arid continental climate is indicated by wind rounded grains of the sandstones as well as sun cracked surfaces. These can also be linked to periodic desiccation (Greig 1971).

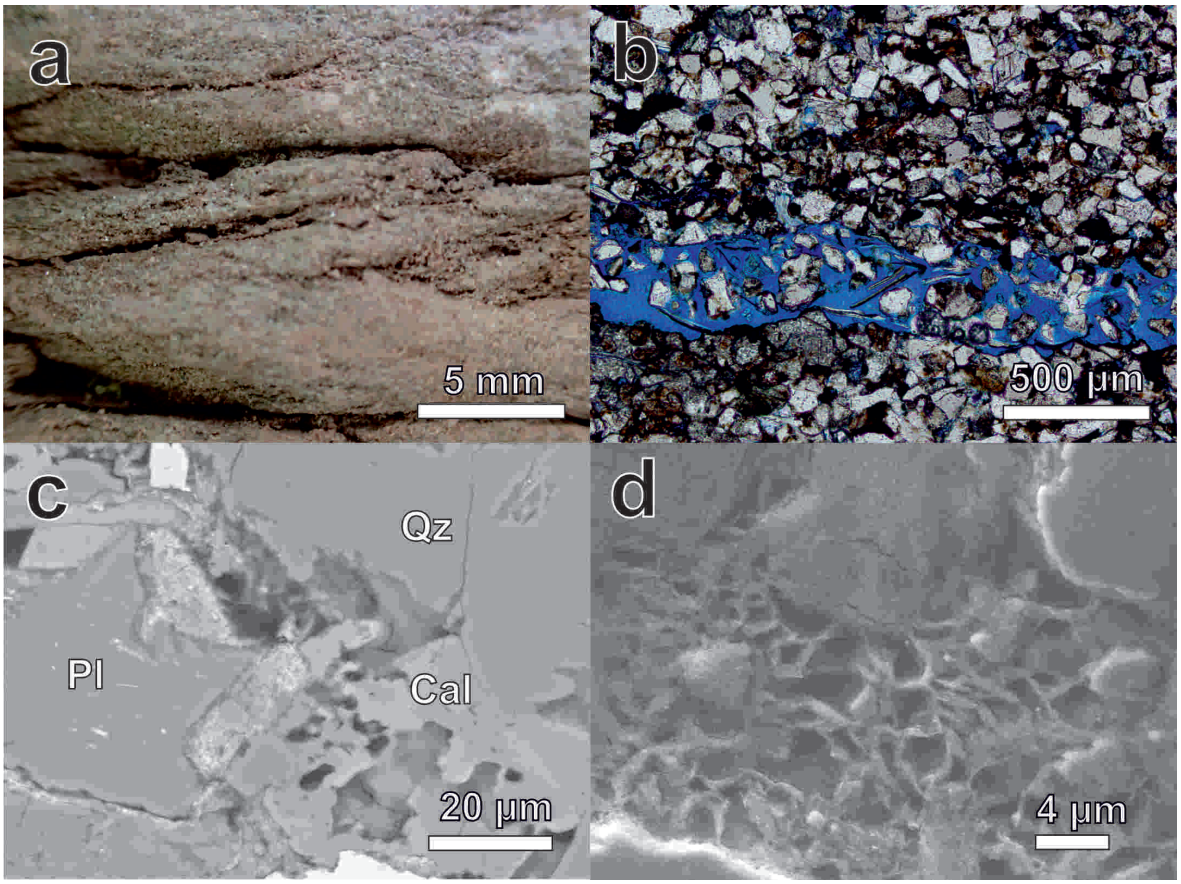

Figure 2.9: Jedburgh sandstone. a: hand specimen. b: thin section under plane polarised transmitted light (pores dyed blue) with densely packed grains except for frequent fractures/gaps. c: SE image of plagioclase (Pl) partly replaced by clay with adjacent calcite grains (Cal) and quartz (Qz). Pore space is dark. d: SE image of clays taking over pore space (probably illite).

Petrographic description

Detrital mineralogy: The dark red sandstone of the south front is a litharenite. Most feldspar is K-feldspar with a small amount of plagioclase. Muscovite is common throughout the sample and in a range of grain sizes. *Texture:* This strongly weathering, fine grained stone has moderately sorted grains usually from 50 to 250 µm. Grain contacts are mainly long. The grains show partly euhedral growth with a few angular grains but due to the strong weathering many grains have altered shapes. Microcline in particular is highly decayed. Bedding can be seen in the hand sample as well as in the thin section due to grain orientation and veins. *Cements:* Calcite, dolomite and clays make up the cement.
Calcite and dolomite replace grains with crystal sizes up to 150 µm (Figure 2.9 c). Iron and titanium oxide are frequent. Clay is seen as an overgrowth but also in veins and completely replacing grains. XRD analysis identified kaolinite and at least two more clays are dominant in the sample: most likely an illite mix form, clinochlore and/or chlorite. Previous studies of HES found smectite (Young 2011). *Porosity:* The porosity is around 7%, but occasionally shows gaps of several hundred microns parallel to the bedding.

2.2.8 Glasgow University

Geological background

The building of Glasgow University used a wide variety of sandstones, but also includes other rock types such as granite, marble and limestone (as well as concrete and brick). The university was moved from High Street to Gilmorehill in 1870 and new buildings have been added since (Kerr 1928). The main building (Gilbert Scott building) is characterised by blonde, local sandstone of various quarries mainly of Carboniferous age. The Lion and Unicorn Staircase is the oldest part of the University (1670) which was moved in 1872. The blonde sandstone of this part was presumably quarried in the city centre (Burton 2013). One of the local quarries for the main building was at Gilmorehill (now Western Infirmary). This stone was used for the bulk of the walls (Lawson 1981). It can be easily distinguished of the other blonde sandstones by its dark lamination and severe decay. The dressing of the outer walls is Kenmure sandstone from Bishopbriggs. In the quadrangles the dressing is made of sandstone quarried in Giffnock (Lawson 1981). Both of these blonde sandstones are characterised or combined in Hyslop & Albornoz-Parra (2008) as type B2 (blonde building stones of Glasgow) as their appearance and composition are similar. Some windows are decorated with pillars of red sandstone from Bonhill (Dunbartonshire). The dressing at Bute Hall is Old Red sandstone from Chapelhall quarry near Airdrie. The flagstones of the floor are made of Old Red sandstone from Carmyllie quarry near Arbroath. External steps and landings are made of Craigleith sandstone from Edinburgh (Lawson 1981).

Two of the main local building stones were sampled to be analysed in detail: the Gilmorehill sandstone and the Bishopbriggs sandstone. Both were collected from the spire of the main building during replacement works on the tower in 2016 and both are from the Clackmannan Group in the Carboniferous (Hall et al. 1997). The Gilmorehill sandstone belongs to the Limestone Coal Formation, comprised of cycles of coal, mud, siltstone, sandstone, and limestone deposits (Bluck 1973). The sandstones are of deltaic origin (Hall et al. 1997). Fossilised trees were discovered at Gilmorehill in 1868 during the quarrying of the stone (McCallien 1938).

The Bishopbriggs sandstone (as well as Giffnock and Huntershill quarry sandstone) belongs to the Upper Limestone Formation (also part of the Clackmannan Group), that overlies the Limestone Coal Formation. Deposits of shallow sea and shorter lasting deltaic conditions form at least four cycles of limestone, mudstone and sandstone (McCallien 1938, Hall et al. 1997).

Petrographic description

Detrital mineralogy: Gilmorehill sandstone is a lithic arkose (Figure 2.1 University sample 1). Occasionally polycrystalline quartz grains occur in the sample. Muscovite occurs frequently and grains are usually oriented parallel to the bedding. *Texture:* The grains

are well sorted, typically > 150 µm, and angular, but show altered grain boundaries (Figure 2.11 c). The grain contacts are primarily long contacts. Bedding can be identified micros- and macroscopically as parallel dark layers of clays. A ripple lamination occurs in hand sample. These characteristic dark layers of kaolinite include smaller grains (several microns) of iron, titanium and magnesium oxides. The oxides also appear as grains with sizes of > 10 µm. *Cements:* Kaolinite also replaces grains of quartz and K-feldspar. Quartz grains occasionally show quartz overgrowth but most grains, including feldspar, show altered grain borders and cracks until complete replacement (Figure 2.11 d). *Trace minerals:* Apatite can be found sporadically. Zircon grains appear as a trace mineral of a few micrometer. Dolomite is uncommon making up less than 1% of the rock. XRD analysis showed traces of halite. *Porosity:* The porosity is around 18%.

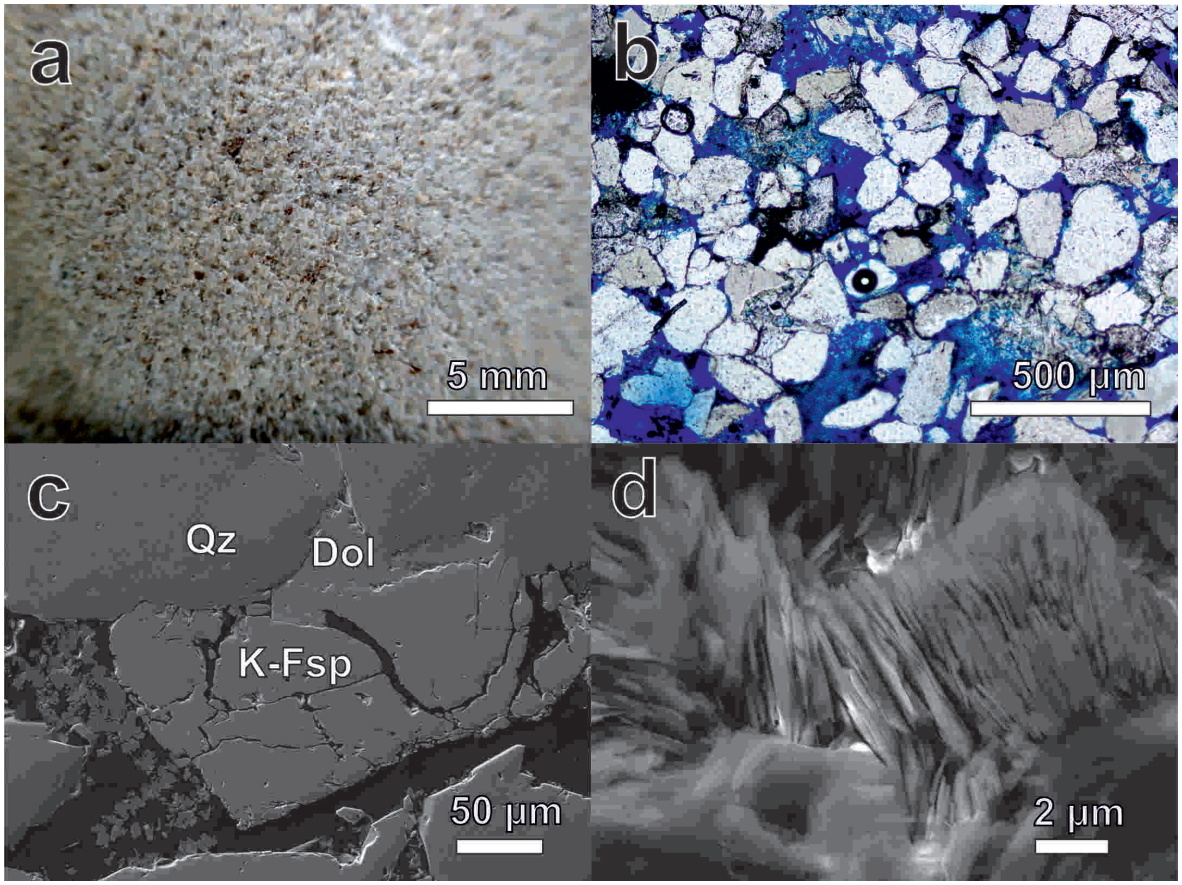

Figure 2.10: Bishopbriggs sandstone. a: hand specimen. b: thin section under plane polarised transmitted light (pores dyed blue) mainly long and point to point contacts of the grains. c: SE image of a strongly decaying K-feldspar grain (K-Fsp) with adjacent dolomite (Dol) filling the space between the K-feldspar and further quartz (Qz) grains. d: SE image of kaolinite sheets in a 'book', abundant in the sample.

Detrital mineralogy: Bishopbriggs sandstone is a sublitharenite (Figure 2.1 University sample 2). Rarely polycrystalline quartz occurs. *Texture:* Grains are > 200 µm in size and are well to moderately sorted. Most grains are angular to subangular. The grain contacts

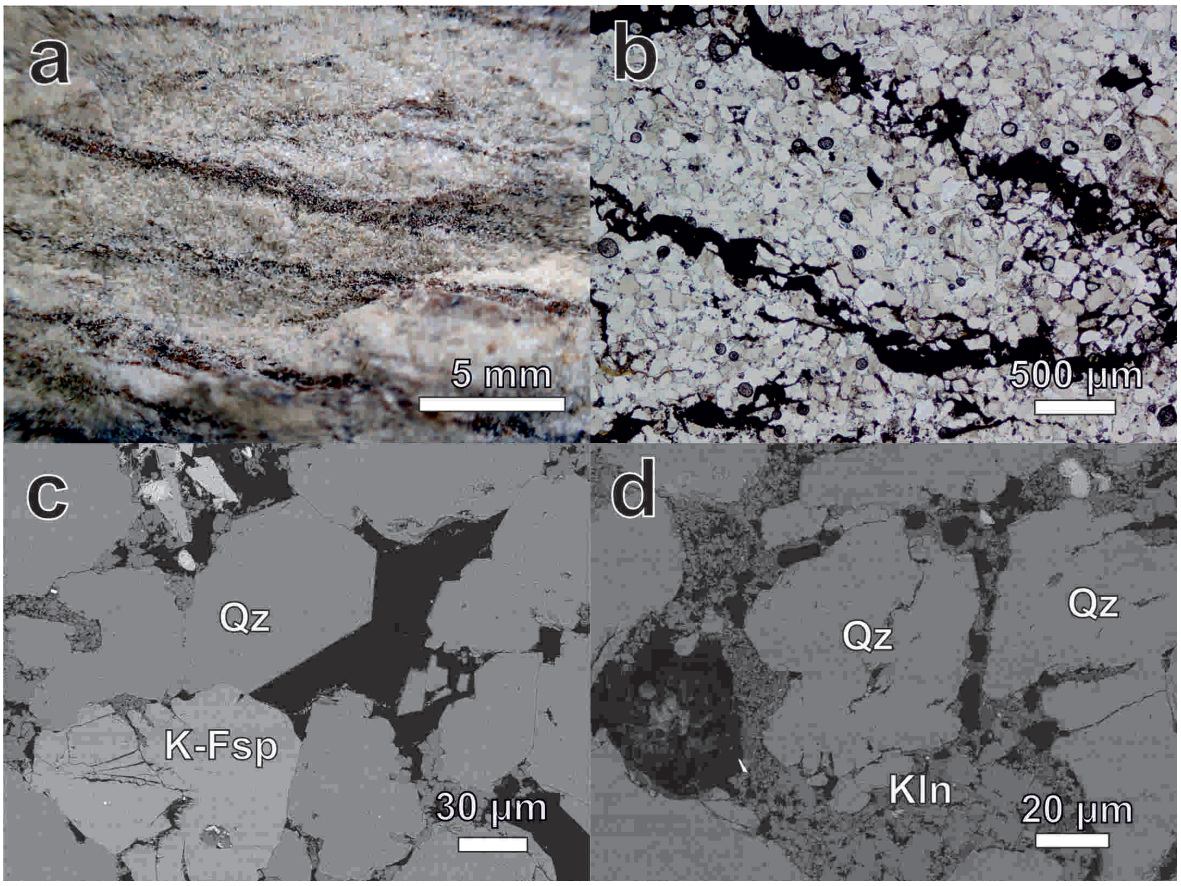

Figure 2.11: Gilmorehill sandstone. a: hand specimen. b: thin section under plane polarised transmitted light: dark layers of clays and lithic fragments with increased pore space, next to quartz dominated grains with very low porosity. c: BSE image of quartz grains with altered grain borders in tight contact to neighbouring grains. The centre shows euhedral quartz (Qz) overgrowth. K-feldspar (K-Fsp) grains usually show stronger weathering, increased cracking and disintegration. The grains are surrounded by kaolinite. d: quartz grains starting to dissolve with kaolinite (Kln) replacing them.

are mainly long with concave-convex contacts. The grain boundaries are usually altered. K-Feldspar is rare and shows the beginnings of replacement by clay. *Cements:* Quartz overgrowths can be found but mainly dolomite acts as a cement.
The dominant clay is kaolinite (Figure 2.10 d). About 11% of the grains are dolomite, filing pore space or as grains of up to $> 300\,\mu m$. *Trace minerals:* Apatite can be found sporadically, as well as zircon and iron sulphide. *Porosity:* The porosity is around 16%.

2.2.9 Anston

Geological background

Anston limestone from the Cadeby Formation, until 194 known as the (lower) Magnesian Limestone (Lott & Cooper 2005), is part of the Zechstein Group (Lott & Richardson 1997). This basin margin of marine limestones shows variation in colour, fabric and lithology that

reflect local changes in depositional facies and complex diagenesis (Harwood 1986, Kaldi 1986, Lott & Cooper 2005). The environment varied from sabkha to lagoon to open marine shelf (Kaldi 1986). The mineral composition of the formation is characterised by a mean dolomite content of 46% (Lott & Cooper 2005). Mainly through dolomitisation some of the primary fabric is lost (making it difficult to place them into sedimentary facies) (Harwood & Smith 1986, Kaldi 1986, Lott & Cooper 2005).
Anston was used in buildings including the houses of parliament in London. The construction began 1839. Most of the limestone was used for the upper fabric (Lott & Richardson 1997). Anston quarry is assumed to be Norfall quarry (North Anston) and Stone Ends quarry in Anston (Radley 1965). The samples are derived from an outcrop at Kiveton Park near south Anston. The outcrop is close to one of the original quarries (near quarry street in Anston). Building stones from the Cadeby Formation are still quarried from north Nottinghamshire to Catterick (Lott & Cooper 2005).

Petrographic description
Anston is a carbonate rock mainly consisting of dolomite. In smaller amounts calcite can be found. Traces of Na, Si, Al, and P can be identified. No grains or texture can be observed in the sample (Figure 2.12 a-d). The bulk of the sample is micritic (less than <10% are grains). After Folk/Dunham's classification and after Dunham/Wright the sample can be described as a crystalline carbonate, meaning no texture is recognisable (Pettijohn 1975, Flügel 2004), or as a dolostone, after its mineral composition. Crystal sizes can be detected at low magnification and are around 100 µm .

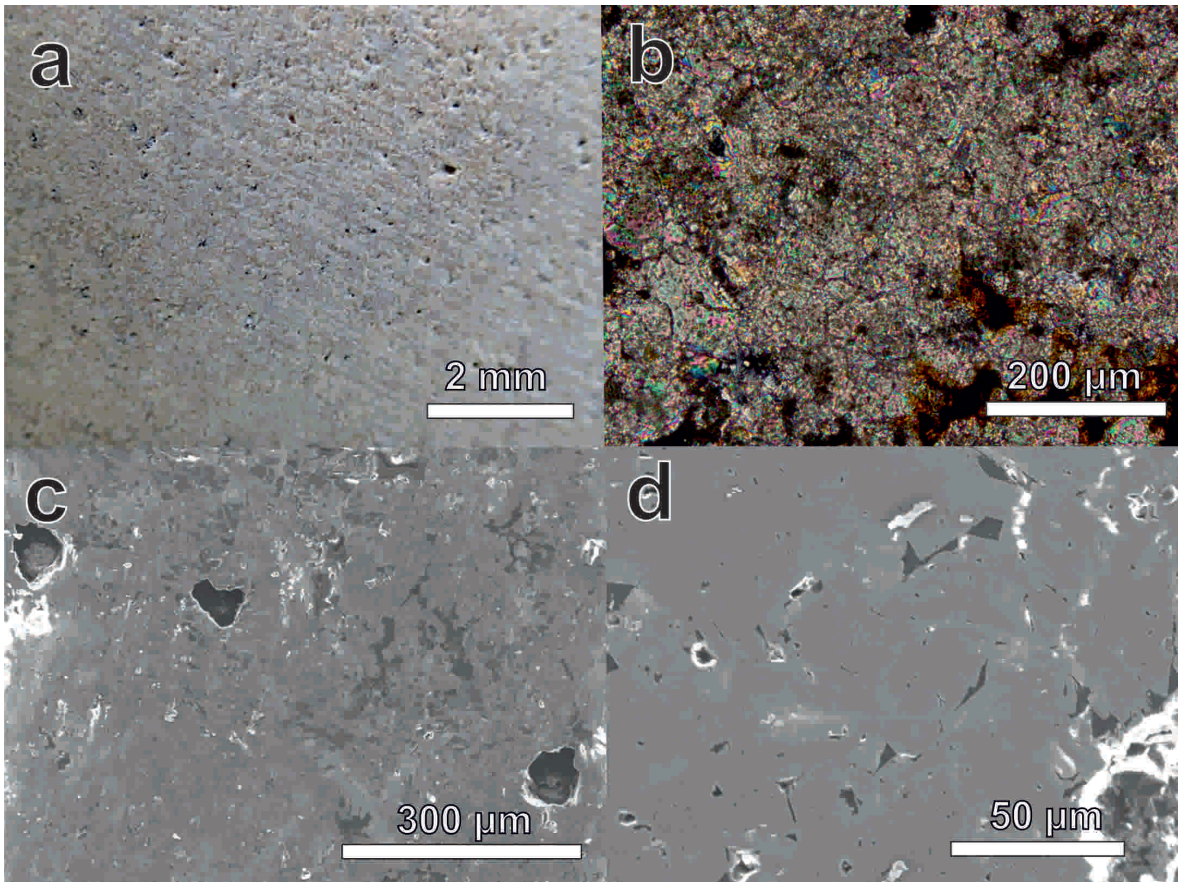

Figure 2.12: Anston carbonate rock. a: hand sample. b: thin section under crossed polarisers shows a nearly uniform calcite/dolomite. c: SE image of the sample (mainly dolomite) with pore space. d: BSE image of a close-up of the dolomitic limestone: grain /crystal sizes or other components can hardly be distinguished.

2.3 Summary

The sandstone samples from Scotland and England show a diverse composition with varying physical properties. Kaolinite is the most common clay mineral of the quarry samples as well as the weathered samples from the sites. Identifying the clay content is difficult as the quantities of the clay fraction are very small. The weathered samples from the sites show, due to the weathering of quartz and feldspar, higher contents of lithic fragments.
The weathered samples are all characterised by low strength as they can be disintegrated easily by hand or low force. The disintegration or detachment usually occurs along the bedding. The stone colour of the samples (red or blonde sandstones) varies and can not be linked to physical properties or the classification of the sandstone.
The porosities of the samples vary from 4% (weathered samples from Lerwick) to 19% (unweathered Locharbriggs samples). The weathered samples show unexpected low porosities. One reason is the very dense bulk material whereas large gaps or fractures appear only along the bedding in those samples. In the bulk material the decreased porosity is caused

by clays and other cementing minerals filling secondary pore space. The image analysis of those densely packed sections show therefore low values of porosity. Other techniques to investigate porosity should be applied to confirm the results.
The porosities of Cullalo and Stanton Moor measured by Graham (2016) match the porosities determined by the image analysis in this study. Only Locharbriggs shows a 4% lower porosity than the measurements by Graham (2016) (Table 2.1). This can be due to the heterogeneity of Locharbriggs samples. Nevertheless, the mineralogy and textural properties of Cullalo, Locharbriggs and Stanton Moor match the results from Graham (2016) of stones from the same quarries. The author's pore network characterisation is therefore used for further references during the performance tests of the tools for these samples (Chapter 3+4).

Chapter 3

Laser interferometer

This chapter describes the use of a laser interferometer to investigate sandstone decay by analysing precise changes in stone dimension. The method offers a totally new approach in cultural heritage to estimate decay processes. In this project, length changes caused by various weathering processes such as swelling of clay minerals or salt crystallisation were analysed at a scale from sub-nanometres to several tens of micrometres. The chapter starts with an overview of the topic and the research aim. The methodology covers the operation of a laser interferometer (EUCLID) and verification of the EUCLID with a vibrometer and a piezoelectric crystal. A focus is improving the measurement through determining noise and temperature effects. The chapter closes with deformation measurements of different building stones when saturated with water and damaged through sodium sulfate. The measurements are divided in the time and frequency domain.

3.1 Introduction

The aim of the project is to use a laser interferometer for non-destructive testing (NDT) of building material.
In cultural heritage, non-destructive techniques are needed to give a precise analysis of the building material (see Chapter 1). The aim of the project is to investigate the possibilities of a portable, high precision NDT device to characterise effects of building stone decay in-situ. The performance of a compact size laser interferometer (EUCLID) was assessed for its use to characterise weathering induced length changes in the submicrometre scale.
The laser interferometer is used to gain information in two different ways:

1. Time domain measurements: expansion and contraction of sandstones are used to deduce their physical and mineralogical properties. The displacement of the sample over time also enables investigations of the state of decay.

2. Frequency domain measurements: inference of how often displacements of a certain

magnitude appear in a certain unit of time (frequency). Assuming the displacement is caused by several repeated events, it might be possible to identify a characteristic frequency range. This would then act as a 'fingerprint' to identify the cause of movement. The measured frequency spectrum therefore allow us to 'listen' to the underlying decay processes.

Measuring length changes

Changes in length smaller than several millimeters are commonly measured with dilatometers or strain gauges. Strain gauges use the change of electrical resistance of a metal film as it is deformed. The accuracy of such devices depends on the measured length and is usually around 1% but can reach up to 0.001%. Dilatometers, mainly linear variable differential transformers (LVDT), use a constant contact pressure of the measured object that when in motion induces a change in current in the coils. Lab based tools can measure a resolution of up to 10 nm. The method uses a direct contact to the measured sample (usually a quartz rod) to gain an absolute position signal, that needs to be converted into a unit of length. An example of a lab based device is the *Linseis* Laser Dilatometer of the Pico-series that can measure with a resolution of up to 0.3 nm (Ge et al. 2016, Linseis 2018). The system includes a Michelson interferometer, a tube where the sample is placed vertically and a furnace is used to heat up the sample with a gas/vacuum control.
Length changes of decaying building materials have been mostly measured with LVDT in the lab (Derluyn et al. 2008, Lubelli et al. 2006, Rüdrich, Bartelsen, Dohrmann & Siegesmund 2011, Juling et al. 2004, Kocher 2005). The LVDT is connected to a climate chamber to simulate different environmental conditions to induce length changes. The focus is set on characterising the hygric and hydric dilation and the expansion that salts cause in porous building materials (see Chapter 1). The resolution of the measured displacement is usually 10 - 100 nm with an accuracy of 300 - 500 nm (Colas et al. 2011, Linnow & Steiger 2005, Rüdrich, Bartelsen, Dohrmann & Siegesmund 2011). The investigated length changes vary with stone type, bedding direction and weathering process, and are commonly between $0.1 - 1$ mm/m. For sample sizes of a length of 2 cm, the displacement will be several micrometers.
An in-situ technique to track displacements includes the use of LVDT or expandable rulers that are used to track cracks on walls when attached before and after a crack (Lorenzoni 2013). Strain gauges were used by Asmussen (2007) and Suarez del Rio et al. (2010) to characterise the expansion of salt crystallisation in sandstones or track expansion.

Interferometry in cultural heritage

Interferometry for length investigations of any materials has been used since the late 19 th century going back to Michelson and fringe counting (Badami & de Groot 2013). Laser interferometers can be used for accurate measurements of displacement at small scales ($<$ 1 mm

and down to $10^{-18}\,\mathrm{m}/\sqrt{\mathrm{Hz}}$) and at large scales of up to kilometres for space based applications. Interferometers are used for investigations of surfaces, motion, precise alignment, thermal expansion of minerals and porous materials (Masuda et al. 2000, Kirk & Williamson 2012), and for the detection of gravitational waves with a resolution of up to $10^{-18}\,\mathrm{m}/\sqrt{\mathrm{Hz}}$ for up to 1000 Hz (Abbott et al. 2016).
Laser interferometers usually do not measure absolute distance, but a very precise measurement of changes in displacement in the order of the used wavelength or below. The recorded signal has a direct relation to the unit length and the measurements can be done without any physical contact between sensor and sample.
The careful setup, calibration (see Sections 3.4) and filtering of the desired signal has the potential to be of benefit in the investigation of weathering processes (Gülker et al. 2007, Vivi et al. 2012). Gülker et al. (2007) used microscopic speckle pattern interferometry to detect submicrometer surface changes on porous materials induced by salt crystallisation. The technique analyses the speckled light that is reflected from rough surfaces. Instead of a displacement measured at one point, the changes of a surface are investigated. For more information on the processing of speckle pattern see Gülker et al. (2007), Kreitlow et al. (1994). Juling et al. (2004) recorded the dilation of $MgSO_4$ loaded, fritted glass samples with electronic speckle pattern interferometry (EPSI). Drying behaviour and phase changes due to hydration of the porous material were observed. A similar experiment was undertaken by Jarad et al. (2005). Using EPSI is similar to the use of lasers for surface investigations such as LiDAR. Subsurface processes in building materials can leave traces on the surfaces and can be therefore detected with the technique (Vivi et al. 2012, Vivi, Bernikola, Leissner, Bertolini & Camuffo 2013). Inaudi et al. (1994) and Inaudi (2004) used an all-fiber Michelson interferometer to gain displacement measurements of high resolution of up to 0.01 micrometer at 1 Hz and higher. The tool has been used over the last decade to investigate deformations of bridges or tunnels and show great potential for the use of historical buildings (Inaudi 2004).

Similar to the measurement of acoustic emission (see Chapter 1), a fingerprint of weathering events could be identified from the occurrence of repeated displacement changes. For acoustic emission (AE) events, such as small cracks in the investigated materials, the time statistic or time windows of the events are not well researched (Manthei & Eisenblätter 2008). Randomly occurring events are suggested, but also events following an exponential decay law after a main event with large amplitude (see Chapter 1). Temporal or spatial clustering of events has been found for rock specimen of several centimetres under load for intervals of several seconds to 10 min. In relation to AE investigations, the laser interferometer enables the detection of nanometre displacements over days and does not require an event that emits elastic waves. Continuous processes could be monitored. Investigations on the frequency of displacements could be therefore used to deduce the type and strength of weathering processes.

3.2 Methodology

A laser interferometer was used to measure the movement of a mirror that is attached to a sandstone. The displacement (expansion or shrinkage) of a sandstone sample can vary for example during drying and wetting due to the presence of salts and clay minerals. The magnitude of the displacement allows deduction of the sample's physical and mineralogical properties, as well as its state of decay. The stone's properties, such as clay content and porosity, need to be considered when investigating rates of movement for decay analysis.

3.2.1 Principle of an interferometer

In interferometers, an incident light beam is split to travel different paths and recombined. The light beams are reflected at mirrors (one attached to the investigated object). The way the reflected light beams interfere (interference pattern), due to the wave nature of light, can tell us which path length the beams traveled and therefore the displacement of the investigated object.
The light source in an interferometer is usually a laser. The beam source has to be coherent to get a useful measurement, which means the light beams ideally have a constant phase difference/well-defined phase at a given position, the same frequency, and the same orientation (polarisation). The coherence length needs to be larger than the path length difference of the two paths. When correlated waves meet, they can combine (interfere) constructively or destructively depending on their relative phase. The resulting wave amplitude can have a larger amplitude (constructive) or a smaller amplitude (destructive interference). Totally constructive and totally destructive interference are the limit cases and are shown in Figure 3.1.

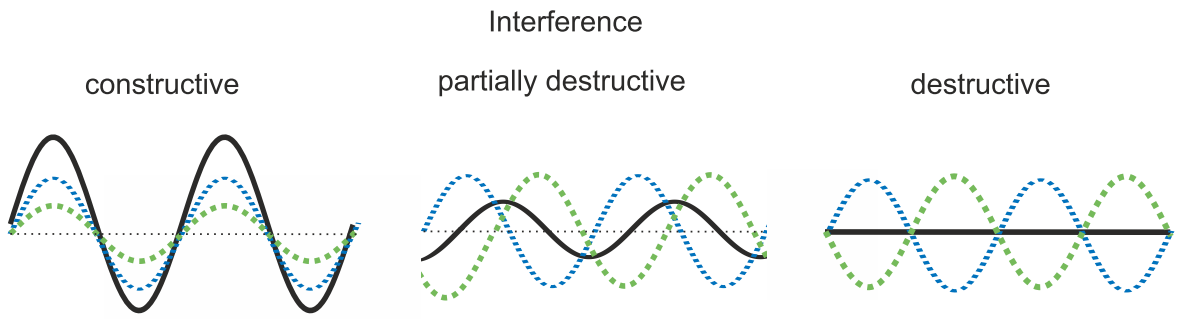

Figure 3.1: Interference of two waves (blue and green) combined into a resulting wave (black). Constructive interference occurs when the two overlapping waves combine in phase. The resulting wave has a larger amplitude. Destructive interference occurs when the phase difference is 180°. An example of partially destructive interference is shown in the centre with the phase difference close to 180°.

Laser light can be described as a sine wave (equation 3.1) with amplitude A, angular frequency ω (with $\omega = 2\pi f$), and phase ϕ. The phase of the wave can be described with equation 3.2. The phase is determined by the path length l that the light beam travels and the wavelength λ.

$$y(t) = Asin(2\omega t + \phi) \tag{3.1}$$

$$\phi = \frac{2\pi}{\lambda} l \tag{3.2}$$

A common type of laser interferometer is a Michelson interferometer. Here one optical device, the beam splitter, splits the beam and later recombines the light beams. Figure 3.2 shows a simple light path in a Michelson interferometer. The laser beam is divided and a reference beam travels a known path (path 1) back to the beam splitter.

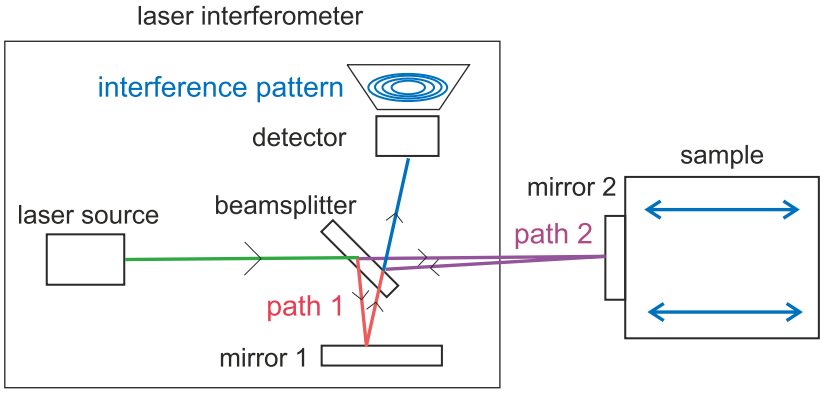

Figure 3.2: Sketch of simple beam path in a Michelson interferometer. For better comprehension colours and angles are added to the path of the beam. The beam is split at the beam splitter and the first beam is reflected at a mirror (mirror 1). The second beam is reflected at a different mirror (mirror 2) attached to the investigated object. Both beams are then recombined at the beam splitter and the resulting interference pattern is detected.

The second or 'test' beam is reflected at a mirror attached to the object under test. When this beam reaches the beam splitter again, it has travelled a different path length and gained a phase difference with respect to the reference beam. The overlapping light beams, with a phase difference, form an interference pattern displaying bright and dark fringes (maxima or minima due to the constructive/destructive interference). From a bright fringe (maximum intensity of the constructive interference) to the next bright fringe, the change in path length must be λ. This means the mirror has moved by $\frac{\lambda}{2}$ as the beam travels the same way back. The changing pattern is therefore dictated by the displacement.
The detection (usually with a photodiode) of the intensity of the fringes only allows determination of the displacement of the mirror, but not the direction of the movement. For example after a maximum or minimum it is unclear which direction the displacement takes. A second signal from the same source is therefore added, that has a phase difference with

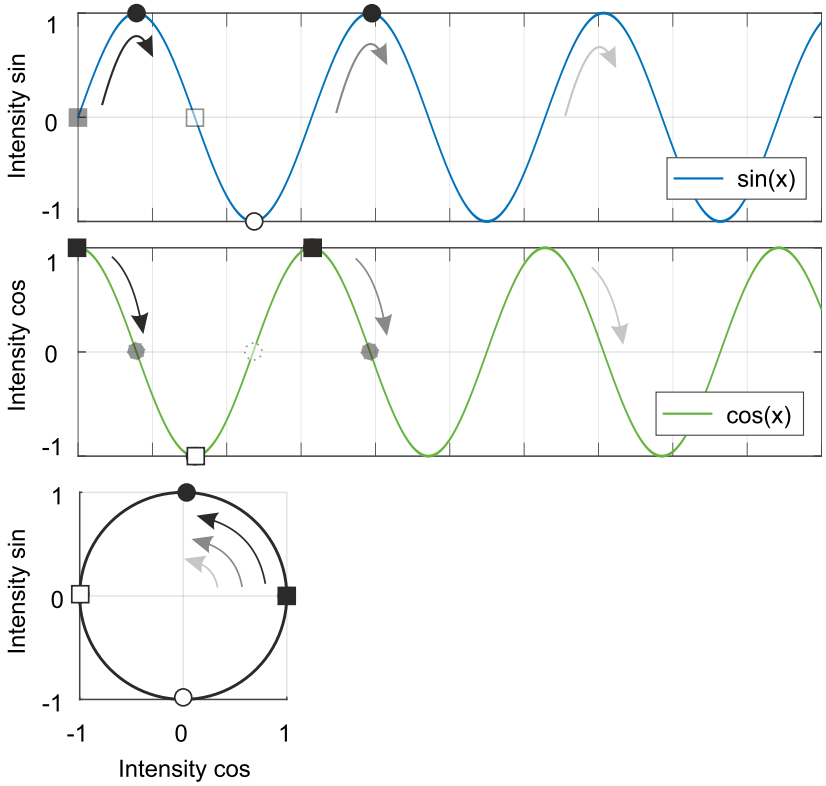

Figure 3.3: Formation of a circular Lissajous figure. When plotting the intensity of a sine wave (blue) and a cosine wave (green), the resulting figure will always be a circle. The dot and square help to follow the path of the intensity over time.

respect to the first signal. This signal is never at the same maximum/ minimum amplitude at the same point in time as the first signal.

Homodyne interferometers usually use *quadrature* detection, which means that, after the interference of the beams, the signal is split into two signals, where a fixed phase difference (90°) is imposed on one of the beams. The other beam with no offset travels to the first detector. In the end two different interference patterns are detected by two photodiodes to determine both the amount and direction of the motion of the tested object.

The intensities of the two signals (the recombined beam and shifted beam) can be monitored (Figure 3.3). For a phase shift of 90° the resulting figure will ideally form a circle. These figures, called Lissajous figures, are created by the combination of two sinusoidal oscillations, out of phase by 90°, such as the two signals from the interferometer. (Lissajous figures can be observed for instance at a sand pendulum where a moving pendulum points on a freely hanging, moving plate, filled with sand.)

When the first signal is for example a sine wave and the second wave is a cosine their maxima will be offset by 90° (Figure 3.3). When combining the intensities of the waves with this 90° offset, a circle is formed. In contrast, with different frequencies and phase offsets between the two waves, the Lissajous figure can show very different curve shapes. The shape can therefore be used to identify the differences (frequency and phase difference)

of the two waves to improve the alignment of the mirror.

3.2.2 EUCLID

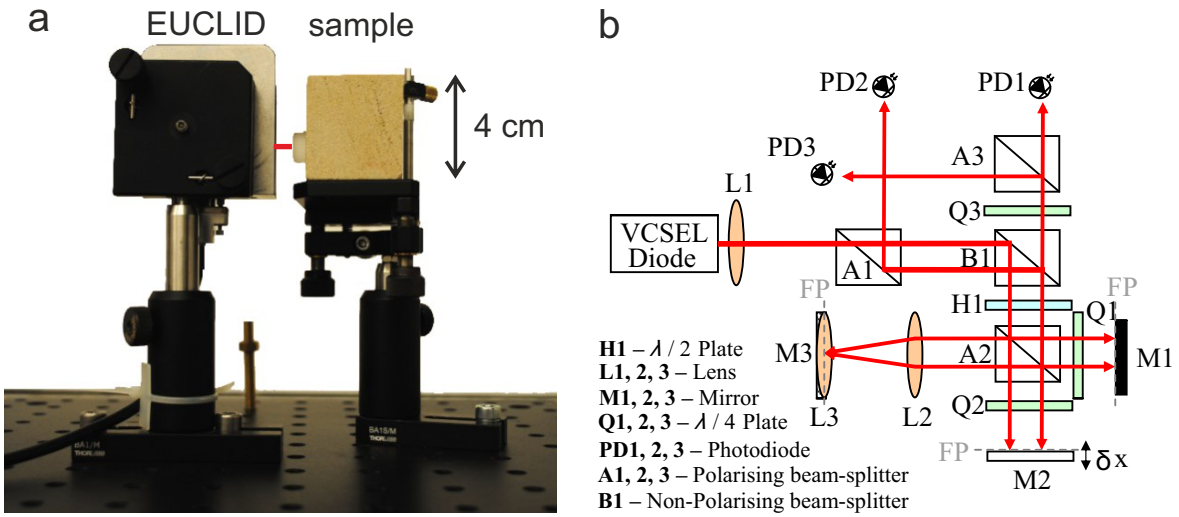

Figure 3.4: Easy to Use Compact Laser Interferometric Device (EUCLID). a: Set-up of the EUCLID attached to an optical breadboard. The initial setup as seen here includes two posts that hold the EUCLID and the sandstone sample. In red is the path of the beam towards the object under test. b: beam path with key components from Aston (2011).

The laser interferometer, used in this project, is a homodyne, polarisation based Easy to Use Compact Laser Interferometric Device (EUCLID) from Alta Innovations Ltd, developed at the University of Birmingham. Displacement measurements with a sensitivity of up to $50\,x\,10^{-12}\sqrt{\text{Hz}}$ at 1 Hz should be possible (Aston 2011).

The EUCLID (Figure 3.4) has an integrated laser source of wavelength ~667 nm. The working distance is 7 mm (shown in red in Figure 3.4). The mirror (*Thorlabs BB05-E02*) has a diameter of 12.7 mm and is attached to the sample with super glue. The sample with the mirror needs to be aligned to gain a good contrast between constructive and destructive interference. An oscilloscope was used to display the Lissajous figure to improve alignment of the two beams.

As the EUCLID is a so-called 'double pass interferometer' (Figure 3.4), a full rotation around the full Lissajous circle (λ) means the mirror has moved by $\frac{\lambda}{4}$ ($\sim$ 167 nm).

A third signal from another detector is used to remove any offset between the two other signals (Bradshaw 2015). For the derivation and more information on the development of the EUCLID see Aston (2011) and Bradshaw (2015).

An example of the output of the first and second detector is displayed in Figure 3.5. When the mirror on the sample is in motion, meaning the path length of one of the beams is changing, the cursor position on the Lissajous figure (still a circle) will change. The phase

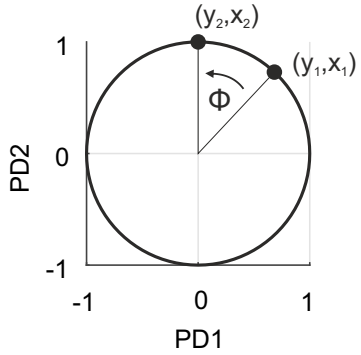

Figure 3.5: Lissajous figure with two signals starting at position (x_1, y_1) and after a full circle at position (x_2, y_2) because the path length of one of the signals has changed.

difference ϕ (Equation 3.3) of these two positions can be used to calculate the displacement of the mirrors. In equation 3.4 the displacement D is calculated from equation 3.2.

$$\phi = arctan\frac{y_2}{x_2} - arctan\frac{y_1}{x_1} \tag{3.3}$$

$$\Delta D = \frac{\phi}{2\pi}\frac{\lambda}{4} \tag{3.4}$$

Data acquisition

The provided LabVIEW application allows easy operation of the tool. Data acquisition rates of 400 Hz or high resolution measurements of 20000 Hz can be recorded. Sample rates can be set to 250 kHz or 1 MHz. The EUCLID can be calibrated further to improve the shape of the Lissajous figure through changing the gain and offset of the three detectors (Aston et al. 2013).

The measurements were taken in a laboratory with no windows. Temperature and humidity measurements were collected every 120 s with a thermochron and a hygrochron (see Chapter 5). When the sandstone sample was big enough, sensors were placed on top of the sample or close to the sample on the optical breadboard. Displacement and the nearby environment was continuously recorded for data sets of up to five days.

3.2.3 Data treatment

All data were analysed with MATLAB and ligoDV. The collected temperature and humidity data were smoothed using a moving average of 35 for around 2000 data points (Figure 3.6). The displacement was downsampled to 120 s. The data points were resampled using linear interpolation. For the combination of the measured temperature and displacement data (see Section 3.4.2) two approaches were used. The first one is a χ^2 test where the calculated data was fitted to the measured data. The next approach is the basic fitting function provided in MATLAB that likely uses a similar approach. The measurements of the sandstone samples

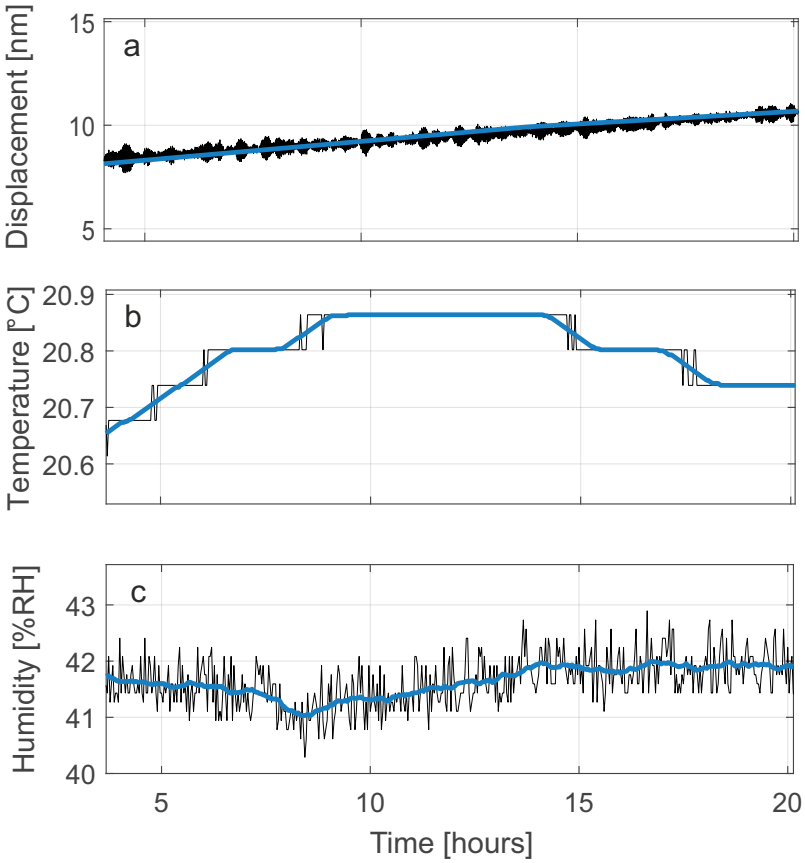

Figure 3.6: Applied correction of the collected data. a: linear interpolation to downsampled the displacement to 120 s measurements. b and c: moving average of 35 for 2000 data points on the temperature and humidity.

were then corrected by the determined temperature influence.

For the frequency domain analysis the uncorrected displacement data was used. The discrete Fourier transform (DFT) was calculated. The DFT is used to analyse the amplitude and periodicity (frequency) of the sinusoidal components that form the overall displacement time series. The fast Fourier transform (FFT) is an algorithm to estimate the DFT.
The resulting spectrum shows the frequencies (Figure 3.7) and amplitude spectral density for specified measurement intervals. If the displacement signal for a given interval is cut not at the exact end of a period, the spectrum will show additional frequencies to describe this half cut signal (spectral leakage). Because any real time window is finite, leakage always occurs (Inman 2009). To mitigate this effect the signal can be multiplied with a so-called 'window function' to force the signal outside the window/the interested frequency range to 0. For the displacement data in this chapter a Hanning window is used.
The gained spectrum does not directly show how often a certain frequency appears or develops over time. Instead the line height is an average of the spectral content at that frequency during the measurement period of one single FFT. Depending on the measured

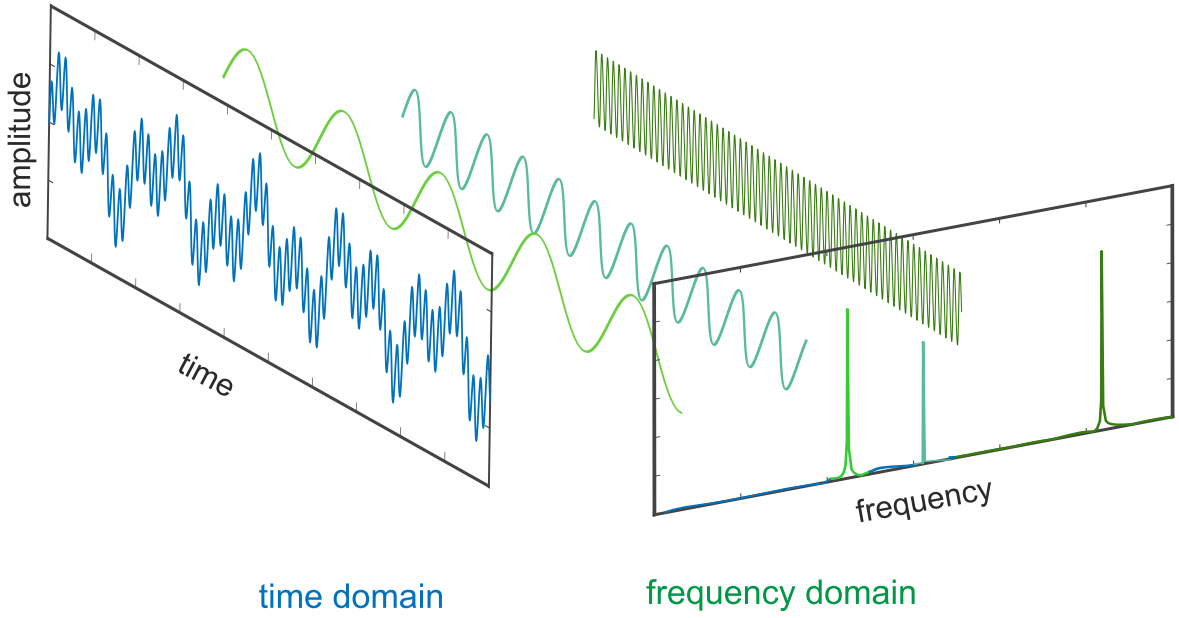

Figure 3.7: Time domain plot showing a wave signal (blue) over time combined of three waves with different frequencies (green). On the right the spectrum is shown with the peaks of the three different frequencies.

time interval some information is lost if a certain signal with a very high amplitude only lasts for a short time during the measurement. Another frequency might appear constant during the measurement but has only a small magnitude.
In a spectrogram this information is displayed to show the variation of the frequencies over time. The displacement/magnitude in a spectrogram is colour coded using a heat map (see section 3.5.2) with time and frequency on the x and y axis, respectively.
The spectrogram combines the spectral resolution but also the time dependence of spectral features. For illustration this can be simplified to a song or melody. When comparing a spectrogram to music, the spectrogram would be similar to the note sheet. It tells us when which note is played (frequency over time) and how loud the note was played (power density, 'heat' at certain frequency). Whereas the spectrum would show us which notes are used in the song and the displacement plot would tell us when the song is played loudly.
The data rate of the EUCLID (< 20000 Hz) enables to play the recorded displacement and the associated frequencies as sound. We could therefore 'listen' to any characteristic decay events that happen during the human audio range of around 20 - 20000 Hz.

3.3 Displacement verification of the EUCLID

A piezoelectric crystal (*Thorlabs PK2JA2P2*) with an attached mirror was used to verify the calibration of the EUCLID. The piezoelectric crystal provides a reproducible movement at

a chosen frequency and amplitude or sets of frequencies and amplitudes. The expected amplitude can than be compared to the amplitude/displacement measured by the EUCLID. The inverse piezoelectric effect is explained in Chapter 4.

A sinusoidal voltage is applied on the crystal and converted into a periodical displacement where the amplitude and frequency of the movement can be controlled.
A commercial vibrometer (*Polytec OFV-5000*) was used for a second measurement of the displacement of the piezoelectric crystal. It usually compares the frequencies of a reference beam to a beam that is sent to a moving object. A known frequency shift is added to the second beam (heterodyne detection) and this beam is then sent to be reflected at the surface of the object. When the object is in motion the frequency will change depending on the object's position (Doppler shift). This shift in frequency or in other words the velocity of the object $\hat{v}$ is recorded as a voltage signal with a given conversion factor of 1 mm/s/V. The resulting displacement at its maximum $\hat{x}$ at frequency f is given by equation 3.5. This is derived from equation 3.1 when its derivative is at maximum for $x(t) = 0$.

$$\hat{x} = \frac{\hat{v}}{2\pi f} \tag{3.5}$$

For the vibrometer the oscillation of the piezoelectric crystal was set to an amplitude of 10 V and a frequency of 1 kHz (and for a second measurement to 100 Hz). For the EUCLID the oscillation of the piezoelectric crystal was set at a frequency of 1, 5 and 10 Hz, also with an amplitude of 10 V. *Thorlabs* states an expected performance of the piezoelectric crystal: at 25° C and without any load, the displacement should be 1 µm at 10 V.
The different frequencies for the two devices are chosen to make the visual reading as accurate as possible. A frequency of 100 Hz or 1 kHz on the EUCLID is more difficult to separate from other occurring frequencies, so that a slower movement of the piezoelectric crystal is preferred. The high frequency on the vibrometer is used to reduce the error while reading the voltage from an oscilloscope.
Table 3.1 compares the collected displacement data of the piezoelectric crystal measured by the vibrometer and the EUCLID laser interferometer. The vibrometer detects a voltage of 2.2 V for 1 Hz and 304 mV for 100 Hz. This corresponds to a displacement of 0.4 µm on average for the peak amplitude (Equation 3.5). An example of the EUCLID measurement for 10 Hz is displayed in Figure 3.8. Five peak to peak displacements are measured and show an average peak amplitude of 0.38 µm.
The measured displacements with both tools show a good correlation (0.42 and 0.4 µm) and indicate a trustworthy measurement with the EUCLID for an applied voltage of 10 V on the piezoelectric crystal. Considering the resulting velocities and displacements were read visually, the total error will be around 0.04 µm, about 10%, acceptable for showing conformity of the tools. The difference of the quoted *Thorlabs* displacement could be caused

Table 3.1: Piezoelectric crystal displacement for 10 V given by *Thorlabs* and measured with a vibrometer and EUCLID.

	Thorlabs	vibrometer		EUCLID		
frequency [Hz]	-	100	1000	1	5	10
amplitude [µm]	1	0.48	0.35	0.41	0.4	0.38

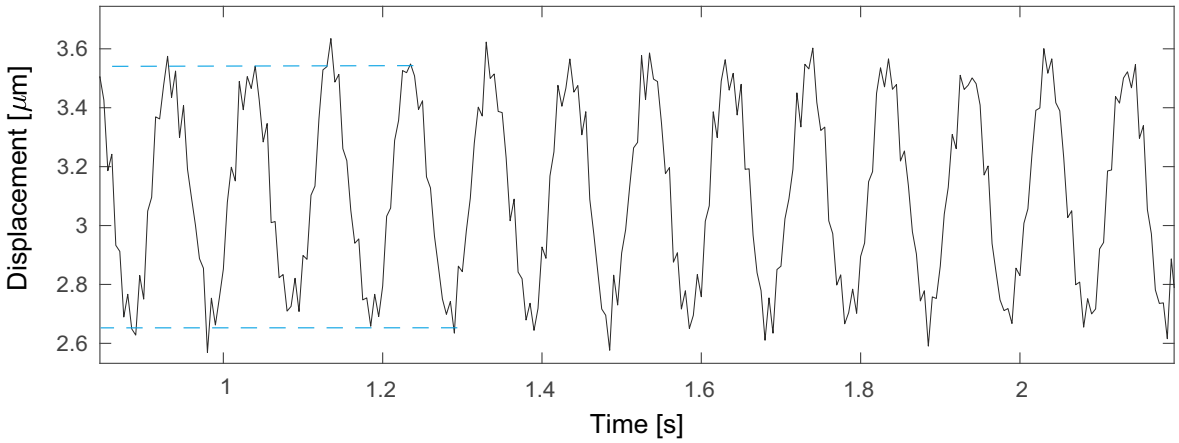

Figure 3.8: Time-series of the piezoelectric crystal oscillation at 10 Hz (10 V) measured with the EUCLID. The dashed lines show the peak to peak displacement.

by the weight of the mirror and/or a temperature difference during the two measurements.

Probability of displacement changes

During a quiet and undisturbed measurement, the EUCLID should not detect significant rises in the displacement (no obvious external influences that cause dilation of the sample). Two measurements of the displacement of a Stanton Moor sample overnight were undertaken to see how frequent rises appear both for a reference measurement and a wet sample that dries over night. The slopes of the displacement were calculated with an overlapping sliding window of 60 s.

The first graph shows the probability of rises over 60 s windows during 20 hours. Figure 3.9 shows a normal distribution for the slopes of the reference measurement. The wet sample shows an increase in slopes above 0.1 µm/min. Similar results were seen for the other reference of Locharbriggs and Cullalo (Figure 3.10). For the wet and salt treated measurements, the frequency of the slopes varies for all samples. Depending on the rock type and drying process, the distribution and position of the slopes (m) vary (Figure 3.10). A common trend can not be identified except for the normal distribution of the reference measurements.

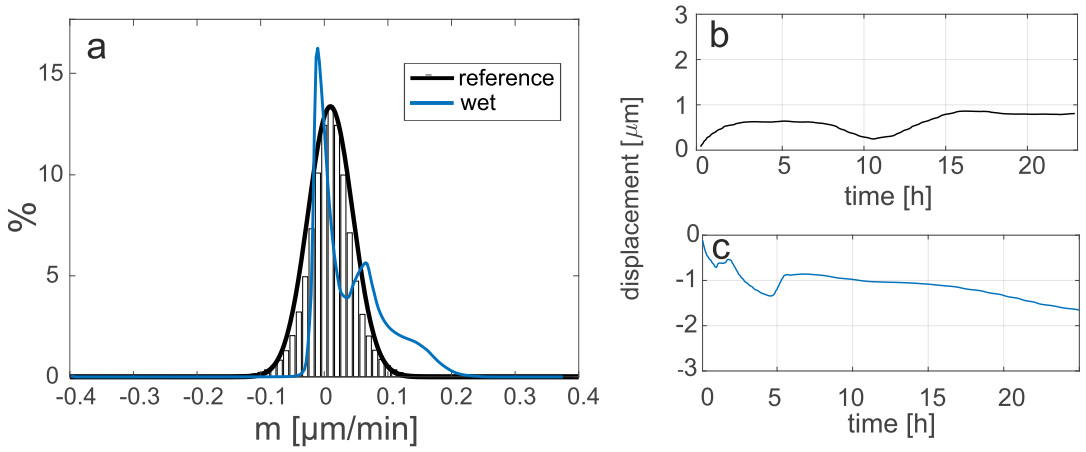

Figure 3.9: Probability of changes in displacement. a: the change in displacement (m) in µm over 60 s was calculated for a measurement over 20 hours. The frequency of certain displacements changes (in %) is shown in black for a reference measurement of a Stanton Moor sample. Most changes in displacement are withing 0.1 µm/min. The histogram are displayed from -0.4-0.4 µm/min. In blue are the changes in displacement during 60 s for a wet Stanton Moor sample that dries over 20 hours. The bins are displayed as a line plot for better comparison. b: displacement over time for the reference Stanton Moor sample. c: displacement over time for the wet Stanton Moor sample.

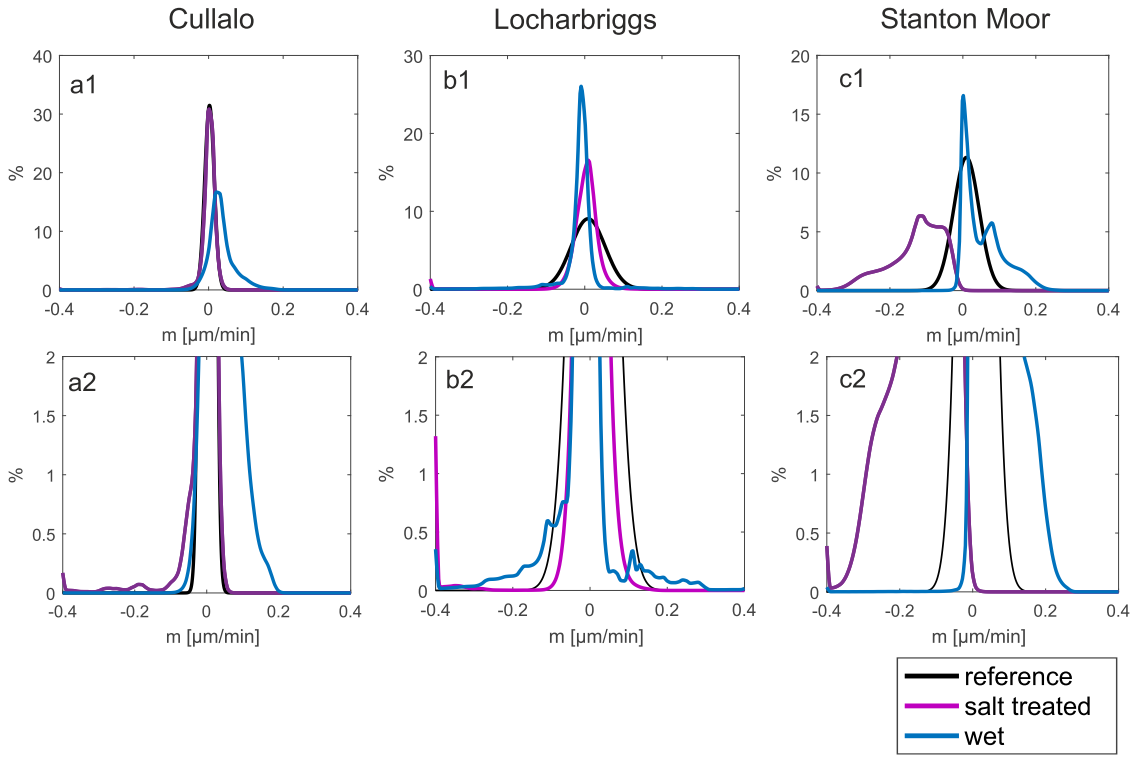

Figure 3.10: The change in displacement (m) over 60 s was calculated for measurements over 16 hours with a Cullalo (a), Locharbriggs (b) and Stanton Moor (c) sample. The frequency of certain displacements changes (in %) is shown in black for a reference measurement, in pink for a salt weathered and wet sample and in blue for a wet sample. The second row shows a zoom of the measurements for up to 2%.

3.4 Improvement of the assembly

The setup of the EUCLID and sample assembly strongly influences the quality of the measurement. The spectra of different setups were analysed to reduce background noise and improve the resolution of the measurements. Time resolved measurements were used to identify the effect of temperature changes on the whole assembly.

3.4.1 Noise reduction through setup variation

The spectra from measurements over 60 s and data rates of 20 kHz were compared. The variable setup includes the use of different tables, where the optical breadboard with the assembly was placed, posts to hold the EUCLID and sample, and rubber feet under the breadboard. The components were varied as following:

1. The EUCLID and sample both mounted to posts that were screwed to the optical breadboard (as seen in Figure 3.11) versus the EUCLID and sample directly attached to the optical breadboard. The breadboard is sitting on four rubber feet.

2. A pressed wood table desk versus a granite table with a 200 kg granite plate standing on motion damping feet, both setups without posts but with rubber feet.

3. The optical breadboard sitting directly on the granite table without rubber feet versus the optical breadboard sitting on four rubber feet.

Mounting the EUCLID and the sample directly to the plate instead of using posts leads to an improved sensitivity by a factor of more than 100 (Figure 3.12 a). Peaks are damped but stay at the same position (such as 20 Hz). Comparing the amplitudes at 40 Hz, the new setup decreases the amplitude from 4×10^{-4} to $9 \times 10^{-7}\,\mu m/\sqrt{Hz}$, which is in this case a reduction by a factor of more than 400. Sub-nanometer motion can be observed with this setup.
Comparing the granite table and the pressed wood desk, between 10 Hz and up to 10 kHz the residual (background) motion is reduced (Figure 3.12 b). The peaks stay roughly at the same frequency. Some peaks are damped (such as 110 Hz), some are not influenced by the type of table (such as 20 Hz). At 40 Hz, for example, the maximum amplitude for the granite table is $5 \times 10^{-7}\,\mu m/\sqrt{Hz}$ and for the desk $3 \times 10^{-6}\,\mu m/\sqrt{Hz}$. The change of tables reduces the amplitude by a factor of 6 at 40 Hz.
Without rubber feet underneath the breadboard the sensitivity of the measurement can be improved (Figure 3.12 c). The residual motion is reduced for the whole spectrum. Looking again at 40 Hz, the amplitude decreases by a factor of 3 (at 40 Hz for $7 \times 10^{-7}\,\mu m/\sqrt{Hz}$ and $2 \times 10^{-6}\,\mu m/\sqrt{Hz}$). For frequencies above 100 Hz, adding feet to the setup helps to dampen some residual motion in the measurement. The black graph shows no significant

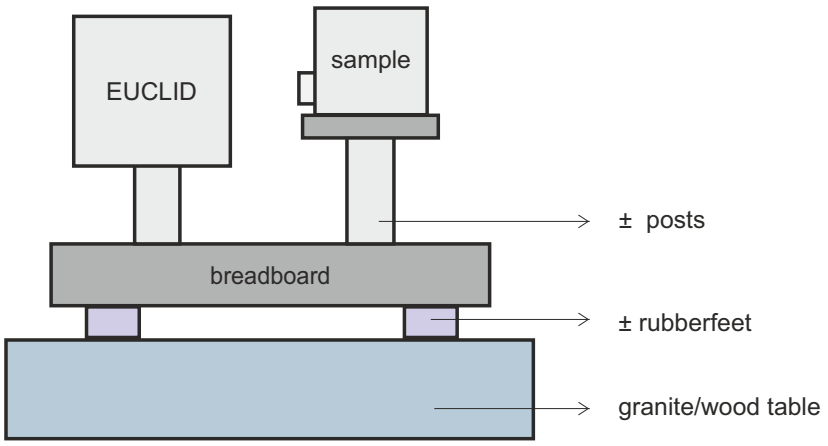

Figure 3.11: Assembly setup: the interferometer and the sample (4 cm during the tests) were placed on posts attached to the optical breadboard. The board is placed upon four rubber feet, which are sitting on a table. When no posts were used, the interferometer was attached directly to the board with screws and a small plate holding it in place. Next to the use of posts, the type of table and the use of rubber feet were varied for the measurements.

peaks after 100 Hz. A setup that is as sensitive as possible should have no rubber feet. However, if looking for an unknown change in the spectrum for frequencies above 100 Hz, rubber feet appear to be beneficial.
The highest amplitudes occur at frequencies below 5 Hz. This motion is reduced when the setup is undisturbed for several hours. Most likely temperature differences between the different components causes this effect.

3.4.2 Temperature influence on the setup

When measuring the displacement (x) every influence (such as humidity changes or noise) on the displacement needs to be specified to distinguish those from the actual intended displacement changes. 'Blank' measurements were undertaken to investigate whether it is possible to compensate for environmental/noise driven displacement effects. One of the biggest influences on the displacement measurement at room conditions is the temperature change. The change in length (ΔL) (or displacement D) varies with the change in temperature (ΔT), where l_0 is the length of the component and α is thermal coefficient (Equation 3.6 from Equation 1.4).

$$\Delta L = \alpha \cdot l_0 \cdot \Delta T \tag{3.6}$$

During a blank measurement the thermal influence on every component of the setup (Figure 3.13) should be constant and is combined as the thermal coefficient α_{all} of all parts of the setup. A constant (k) is set to cover the thermal coefficient and the length of the components (L_{all}) in Equation 3.7.

$$k = \alpha_{all} \cdot L_{all} \tag{3.7}$$

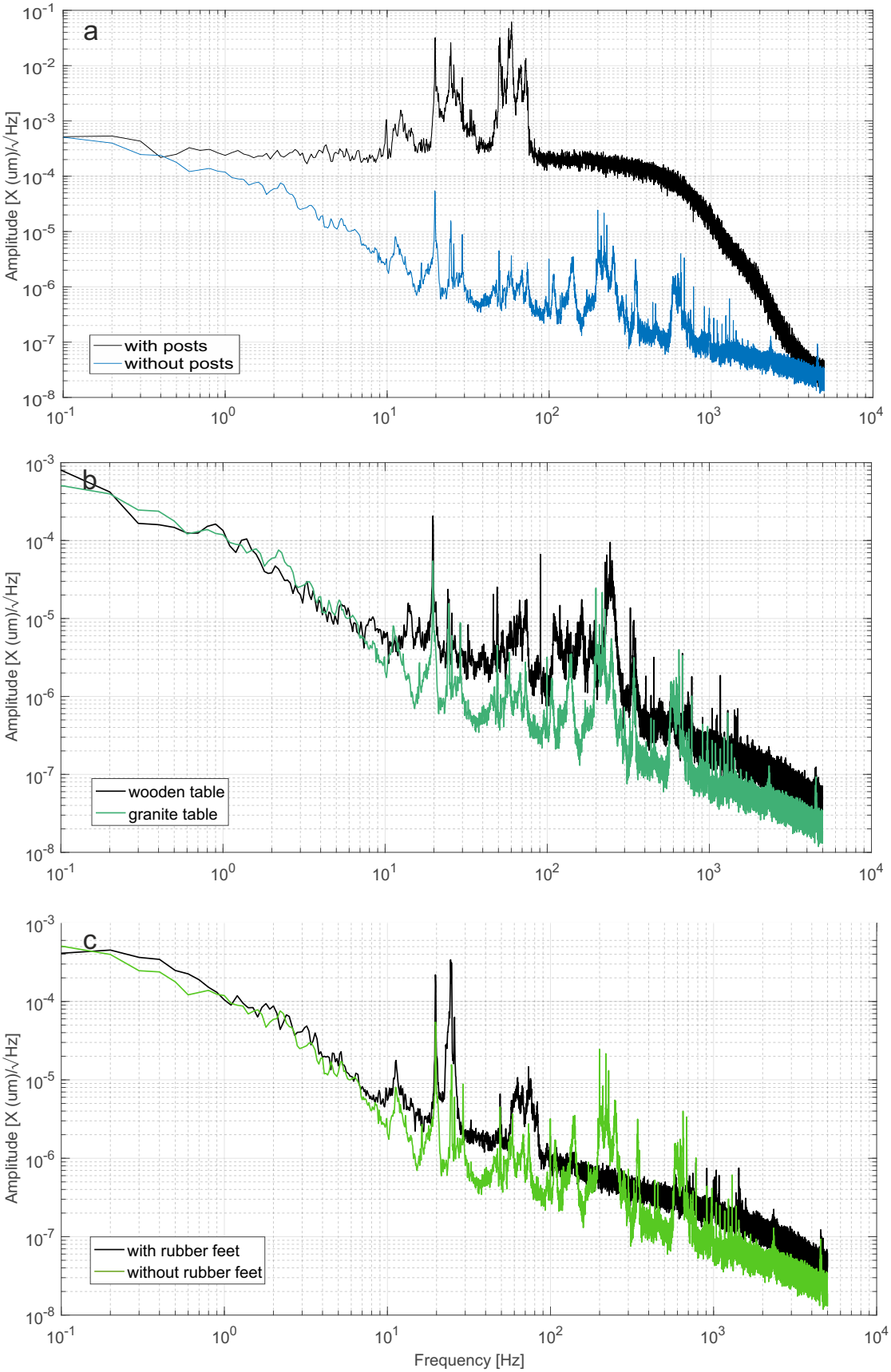

Figure 3.12: Spectra comparison with data rate of 20 kHz over 60 s for different setups. a: shows the displacement spectrum of the sample with (blue) and without (black) posts. b: shows the displacement spectrum of the sample on a granite table (blue) and a pressed wood desk (black). c: shows the displacement spectrum without rubber feet (green) and with rubber feet (black).

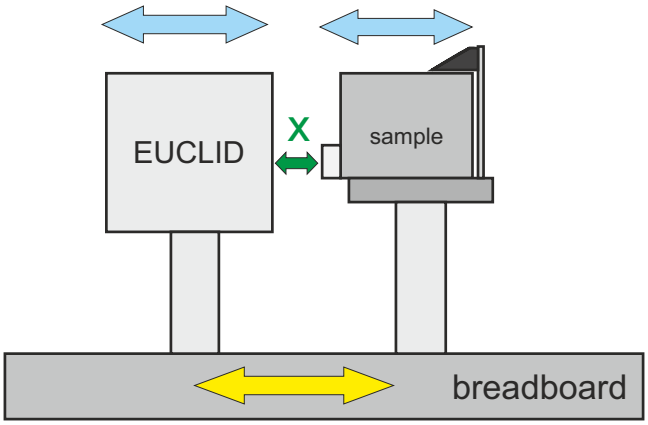

Figure 3.13: Set-up of the EUCLID on posts. When temperature increases, the components expand which leads to a changing displacement (x) as a sum of the movement of the different parts. The blue arrows demonstrate an expansion that leads to a decreasing x when the temperature rises, whereas the yellow arrows show an expansion that will cause the displacement to increase for rising temperatures.

In theory a changing temperature causes the same change in displacement over time. This influence can then be subtracted from any measurement to gain a displacement without the thermal influences.
When monitoring the temperature changes over time ($T(t)$), k can be approximated for a calculated displacement (D_{calc}) with an offset (c) in Equation 3.8. A good fit for k will be gained when the actual displacement D measured by the EUCLID is the same as the calculated displacement, D_{calc} (Equation 3.9). A χ^2-test was used to approximate k. A quadratic dependence was also checked and excluded.

$$D_{calc} = k \cdot T(t) + c \tag{3.8}$$

$$D_{calc} - D = 0 \tag{3.9}$$

An aluminium cube (4 cm) was used as a sample to determine the temperature influence on the experimental setup. The expansion and contraction of the metal cube should not be influenced by changes in humidity in comparison to a sandstone sample. The main influence is expected to be the aluminium breadboard, the aluminium cube and the interferometer itself. The expansion coefficient for aluminium is $\sim 21\,\mu m/m\,K$. If ~ 8 cm of aluminium are involved in the expansion and contraction, a displacement of up to $1.68\,\mu m/K$ is expected. Small temperature and humidity sensors, Thermochrons and Hygrochrons (see Chapter 5), were used to approximate the temperature and the humidity close to the sample. The experimental setup and the influence of temperature are described in the following. The four main setups include measurements with posts, without posts (including new calibration of the EUCLID for 120 hours measurement and 40 hours measurements), an insulated box and

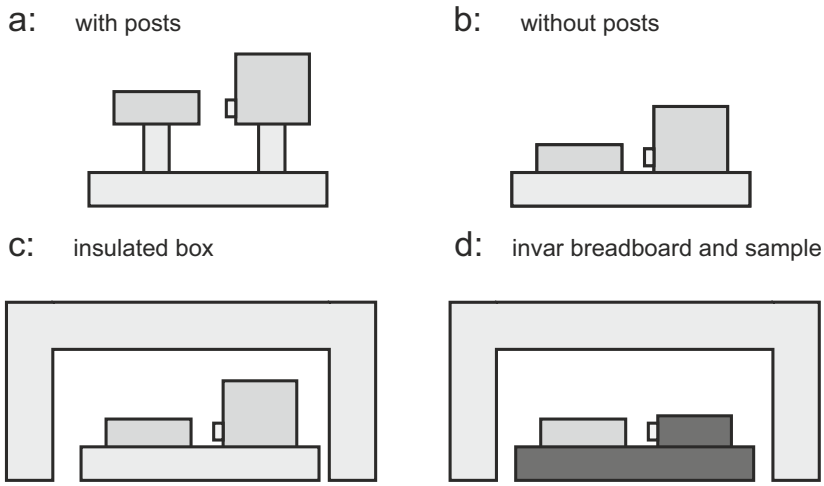

Figure 3.14: Various setups. a: The EUCLID and sample sitting on posts. b: The same setup without posts. c: An insulated box covering the sample and EUCLID. d: The aluminium breadboard and sample replaced by Invar.

the use of an Invar optical breadboard (Figure 3.14).

Several measurements were undertaken with the setup in Figure 3.13. An example measurement over 100 hours shows that a linear fit is not possible (Figure 3.15). A constant linear slope k is expected, when plotting temperature against displacement from equation 3.8. Basic linear fitting in MATLAB shows two main slopes for $0.8\times$ and $2.5\times$ temperature with different offsets c. A good fit can therefore be gained for small parts of the measurement ($\sim$ 16 hours) but not for k and c for the whole measurement.
The setup must therefore include components that do not react in a linear manner as expected. Different thermal capacities and/or a hysteresis effect could be the source of this change. To reduce the number of components that could influence the whole measurement, the use of posts with screws and clamps was avoided. As described earlier this also increased the sensitivity of the measurements.

The test with a metal cube and the setup without posts was repeated (setup b). The cube and the EUCLID are fixed with plates and screws to the breadboard. In Figure 3.16 b the displacement and temperature show a nearly linear relation. When approximating k over a continuous measurement of 50 hours (Figure 3.16 a), there is a good fit to the measured displacement.

The measurement was repeated with the cube in a slightly different position and newly calibrated EUCLID to see if the value of k is repeatable. For the next measurements the value of k changed and was up to 10 times larger. The changed setup did not solve the nonlinear behaviour of the assembly.
Without moving of any of the components but a new calibration of the EUCLID, the measurement of the metal cube was repeated to see if k has a constant value. For a second

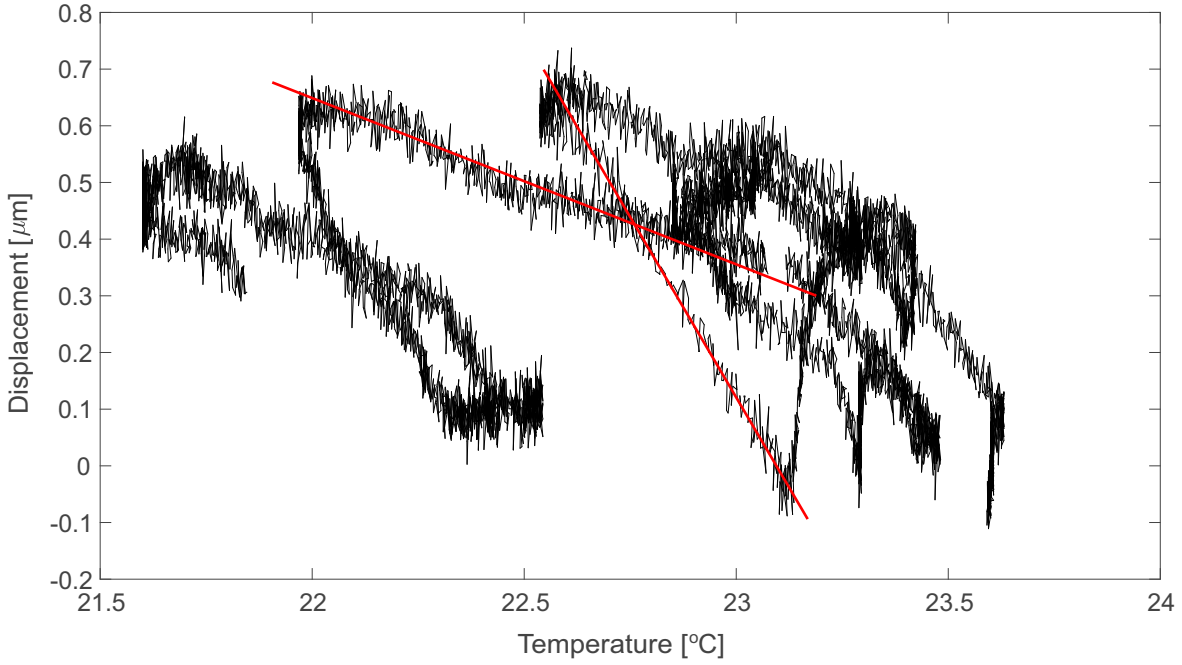

Figure 3.15: Displacement measurement of a metal cube over 100 hour with posts (setup a). The temperature is plotted against displacement. The measurement can be characterised by two different slopes (red). The instability of this setup is below a micron over several days of measurements.

investigation the cube was not moved nor calibrated. Both set of experiments show changing values for k.

Constant measurements of up to seven days also showed a changing value for k. The displacement of the metal cube in the following example is displayed for up to five days with an unchanged setup (Figure 3.17).

Temperature in the room varies around $2^{\circ}\,C$ and shows a similar shape to displacement (Figure 3.17). The humidity drops for the first 40 hours and mainly rises for the last hours of the measurement. A good fit of the calculated displacement to the measured displacement could not be obtained when approximating k for the whole length of the measurement. For the first 60 hours the calculated displacement matches the measured displacement well for a k value of 46. The same value results in a poor fit for the last hours of the measurement (Figure 3.18).

When determining k for a smaller time range (85 to 100 hours) of the above example, a good fit can also only be gained for one half of the graph (Figure 3.19). For the first 10 hours of the smaller data set the temperature drops (Figure 3.17 hours: 85 to 95); the displacement also decreases, leading to a resulting value of k around 102 (Figure 3.19 a). After this temperature drop of $\sim$ 0.04 K/hour, the temperature rises with $\sim$ 0.1 K/hour. During this temperature rise the calculated k is 57 (Figure 3.19 b). A good fit of this data set cannot be obtained with just the changing temperature included in the fit.

The point at which k changes can be identified in Figure 3.19 a after 10 hours of the small

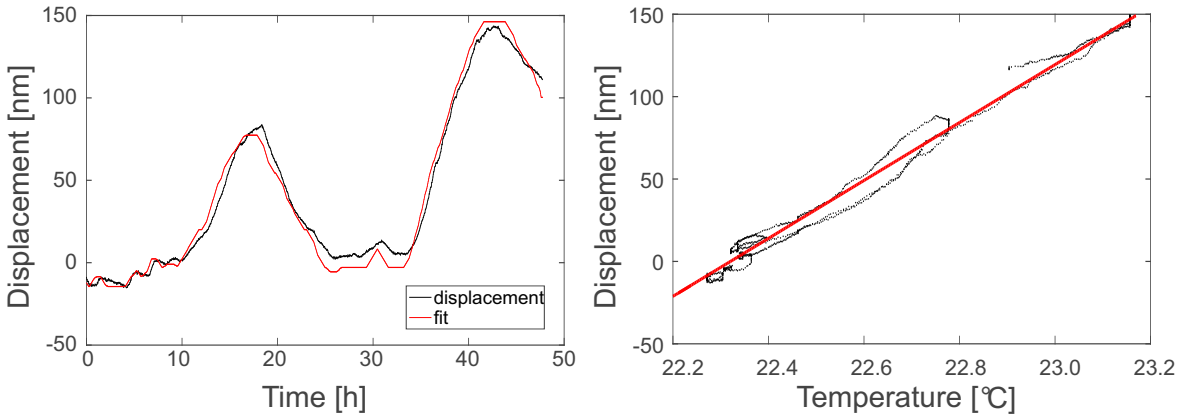

Figure 3.16: Measurement of a metal cube over 50 hours without posts (setup b). a: Displacement change over 50 hours. In black is the measured displacement and in red the calculated displacement (fit) including the measured temperature data. b: Displacement change over 50 hours versus temperature.The red line shows a linear fit with the slope k. Both fits use k=171).

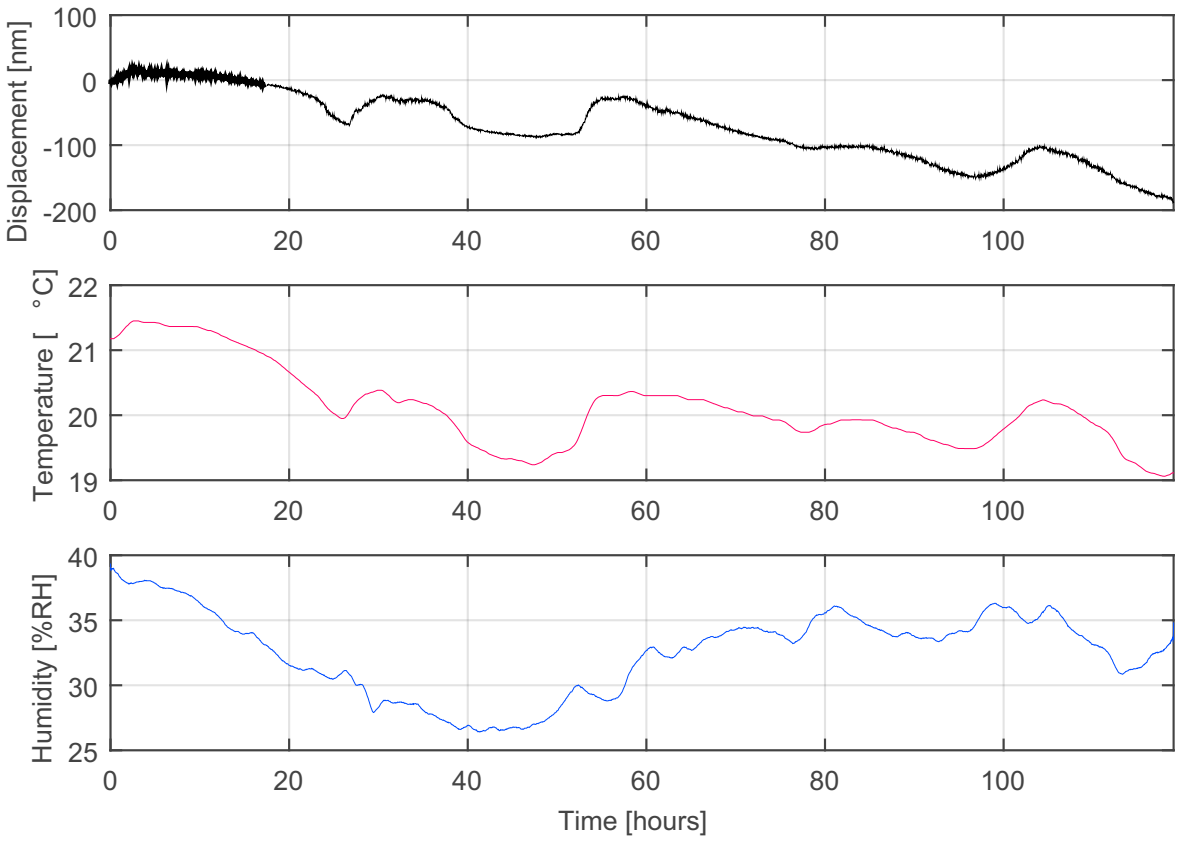

Figure 3.17: Displacement, temperature and humidity are measured over 120 hours without posts (setup b). The displacement (black) varies over 200 nm with a changing temperature (red) of 2° C and a humidity (blue) change of 15%RH.

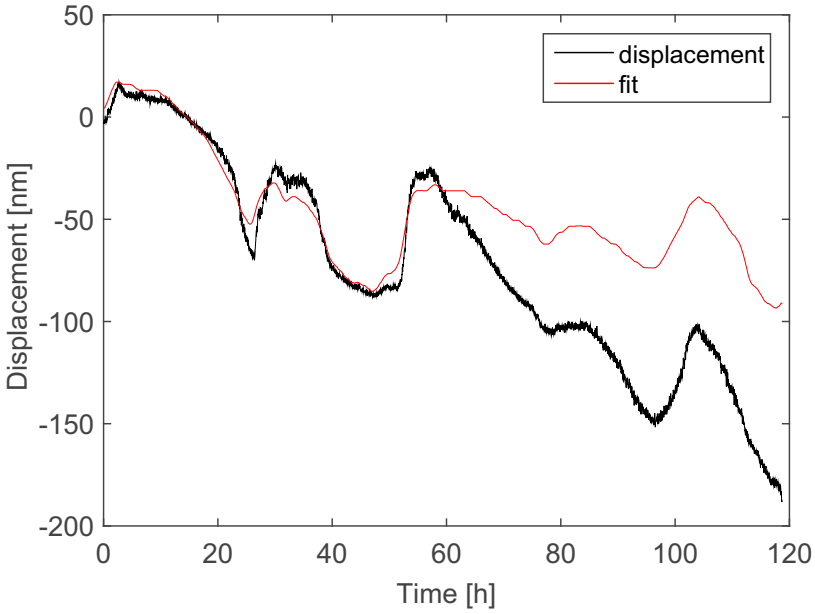

Figure 3.18: Temperature fit of the first 60 hours of a 120 hours displacement measurement (setup b). Fitting gives k = 46 for t=0<60 h with an offset of -1175.

data set. At this point the temperature changes from falling to rising, but also the rate of the temperature change per hour is different. The change in displacement for both falling and rising temperature is 50 nm. This result again shows the sensitivity of the setup to temperature changes and could be again caused by hysteresis and different thermal capacities but at a smaller scale (several 10s of nanometres) than the previous setup with the poles.

The next example shows that even during a temperature drop over 35 hours, k is not constant (Figure 3.20). k changes from 99 to 50 after the first 16 hours (Figure 3.21). A good fit with the measured temperature cannot be obtained with this variation in k. No temperature rise causes the changing k value (Figure 3.20). The temperature changes in the first 13 hours with $\sim$ 0.1 K/hour and in the last hours with 0.05 K/hour. Compared to the previous measurement where a quicker change in temperature (0.1 K/hour) goes with a smaller value for k of 55, here it is the quicker change of temperature that goes with a bigger value of k of 100. For the first 13 hours in this example the displacement changes by 200 nm and for the last hours it only changes by 100 nm. The rate of temperature change has no constant influence on determining k.

An insulation box was used to cover the complete setup (Figure 3.14 d) to reduce the temperature and humidity variation. The box has a 15 cm thick roofing insulation covered with aluminium foil and was placed over the interferometer and cube on the granite table. A measurement of 50 hours shows the temperature decreasing only by 0.5° C and a humidity change of 2%RH for the course of the whole measurement (Figure 3.22). The maximum change in displacement is smaller than 4 nm during the 50 hours.

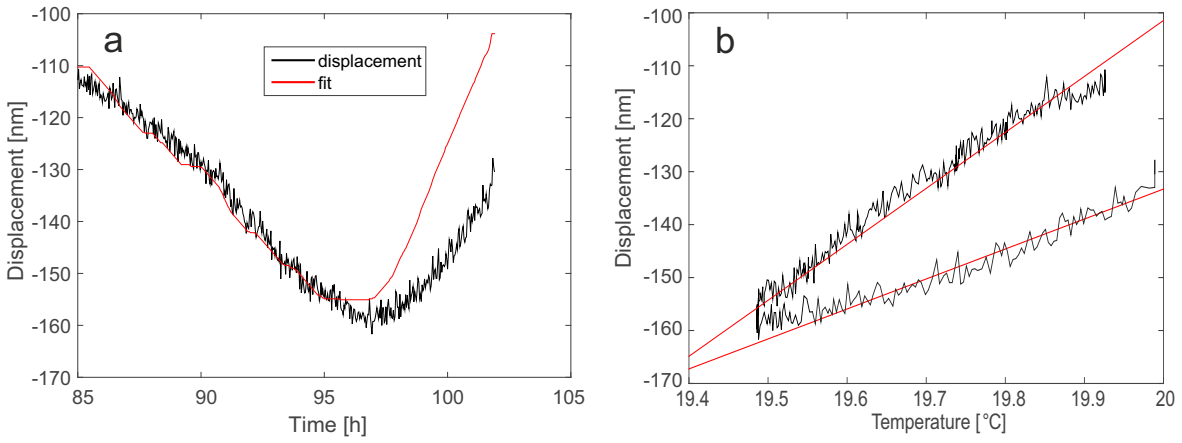

Figure 3.19: Displacement measurement for 120 hours (setup b). a: Temperature fit for the hours 85 to 100. When determining k for the first 10 hours the fit does not match the last hours. b: Temperature plotted against displacement of the hours 85 to 100. The data can be separated into two ranges: for the first 10 hours the slope is around 100 and for the last hours the slope is 50. The linear regression in red.

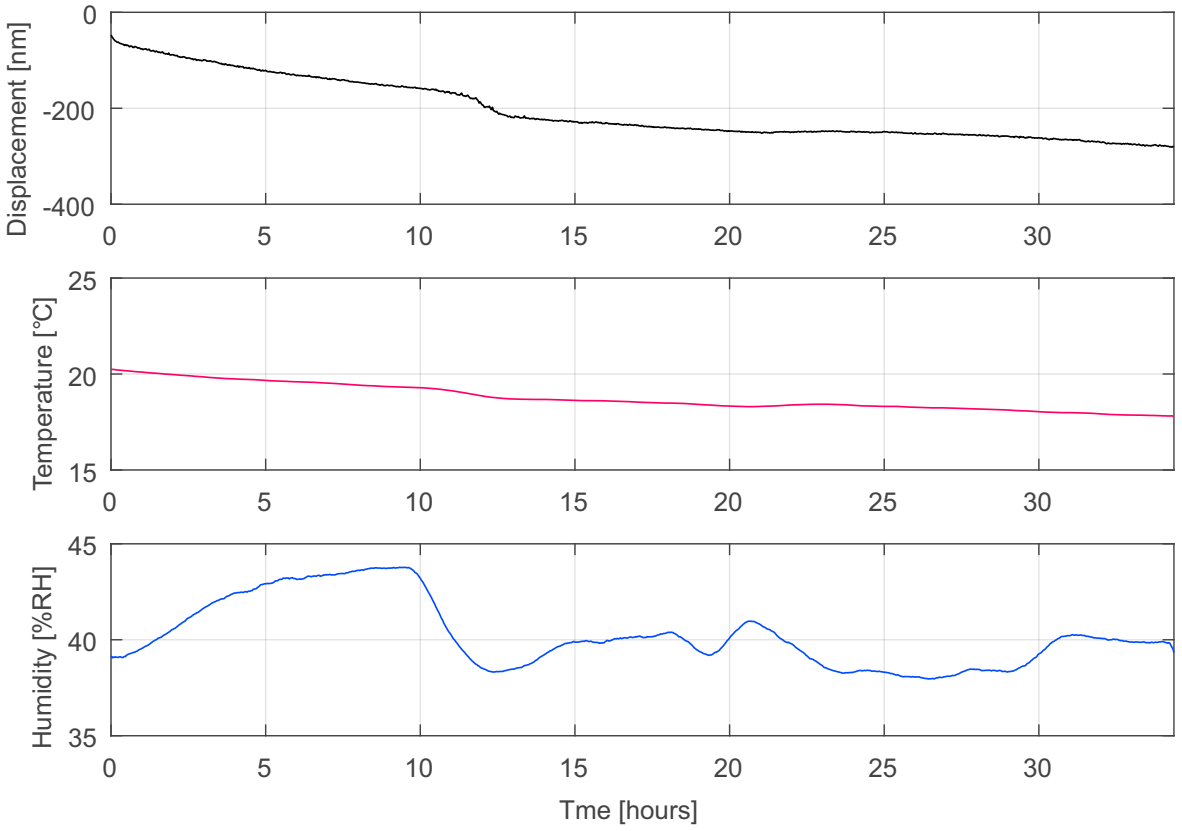

Figure 3.20: Displacement measurement over 40 hours (setup b) with temperature and humidity recording. The displacement varies over 250 nm with a changing temperature of 3° C and a humidity variation of 6 %RH.

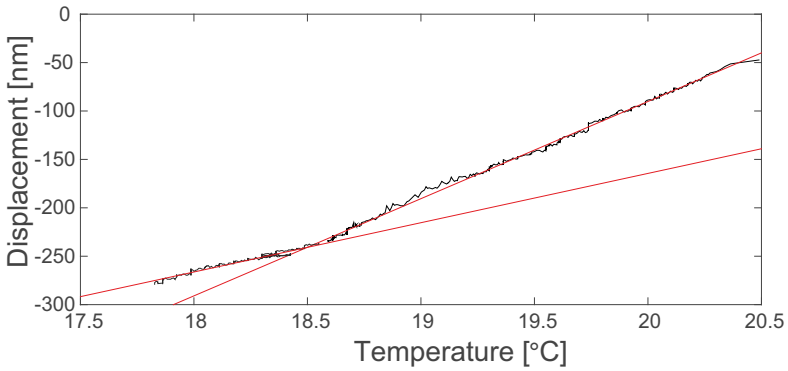

Figure 3.21: 40 hours measurement (setup b). Temperature is plotted against displacement. A change in the slope appears after the first 16 hours with linear regression in red.

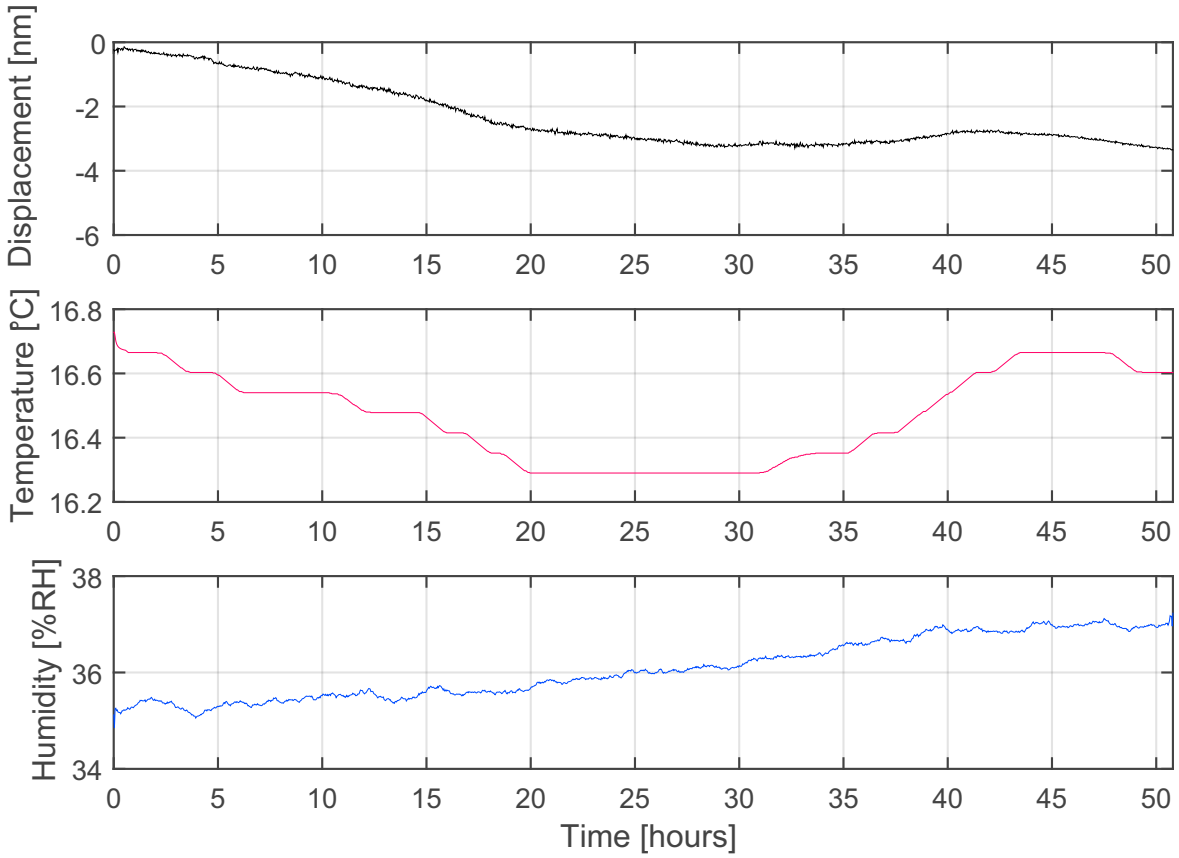

Figure 3.22: Displacement, temperature and humidity change over 50 hours under an insulated box (setup c). The temperature and humidity variation is reduced and the change in displacement decreases to 4 nm during the measurement.

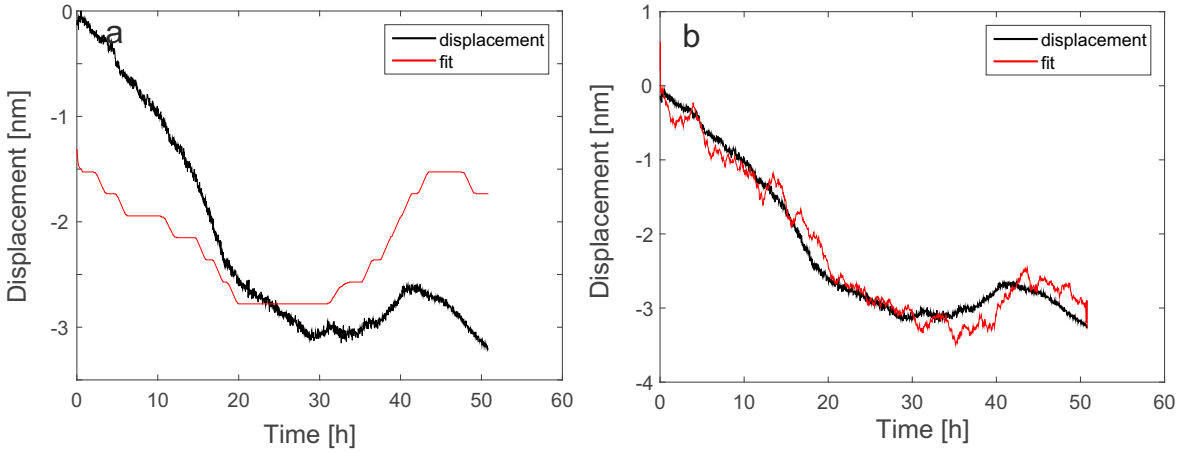

Figure 3.23: Insulated box measurement (setup c). a: Temperature fit over 50 hours with k ranging around 3 with an offset of −242. b: Temperature and humidity fit of 50 hours under an insulated box. When determining k_1 it ranges around 4 and k_2 around −1 with an offset of −207.

Temperature shows a similar trend as the displacement (Figure 3.22). At 0 and 45 hours the temperature reaches the same values, here 16.7° C: however when comparing the displacement at 0 and 45 hours, it does not go back to the same values, it decreases. The humidity rises constantly in this measurement. When approximating k a good fit cannot be gained with the temperature data (Figure 3.23 a).

Adding the humidity into the model of the calculated displacement, the humidity could provide the missing linear decrease of the displacement seen in Figure 3.22. Including the humidity changes (Equation 3.10) to the model allows a fit with a constant value for k_1, the temperature influence, and k_2, the humidity influence. Both can be calculated to gain a good fit for the measured displacement (Figure 3.23 b).

$$D_{calc} = k_1 \cdot T + k_2 \cdot H + C \tag{3.10}$$

Figure 3.23 shows a comparison where an improved fit can be obtained. The temperature influence in this measurement would be approximately 4 times larger than the humidity influence.

In the described example humidity can be used to gain a better fit. Checking the previous examples with the same approach to include the humidity, the fit of the previous examples does not improve. The test with the insulated box worked well for very little changes in temperature and humidity that were achieved through a day without heating in the laboratory and the added insulated box.

To further improve the setup and to try to minimise its hysteresis, an Invar breadboard was designed. Invar has a low thermal coefficient of 1.5 µm/m K (Quantum Alloys Ltd 2005). Instead of the aluminium cube and aluminium plate (21 µm/m K), that fixed the sample and

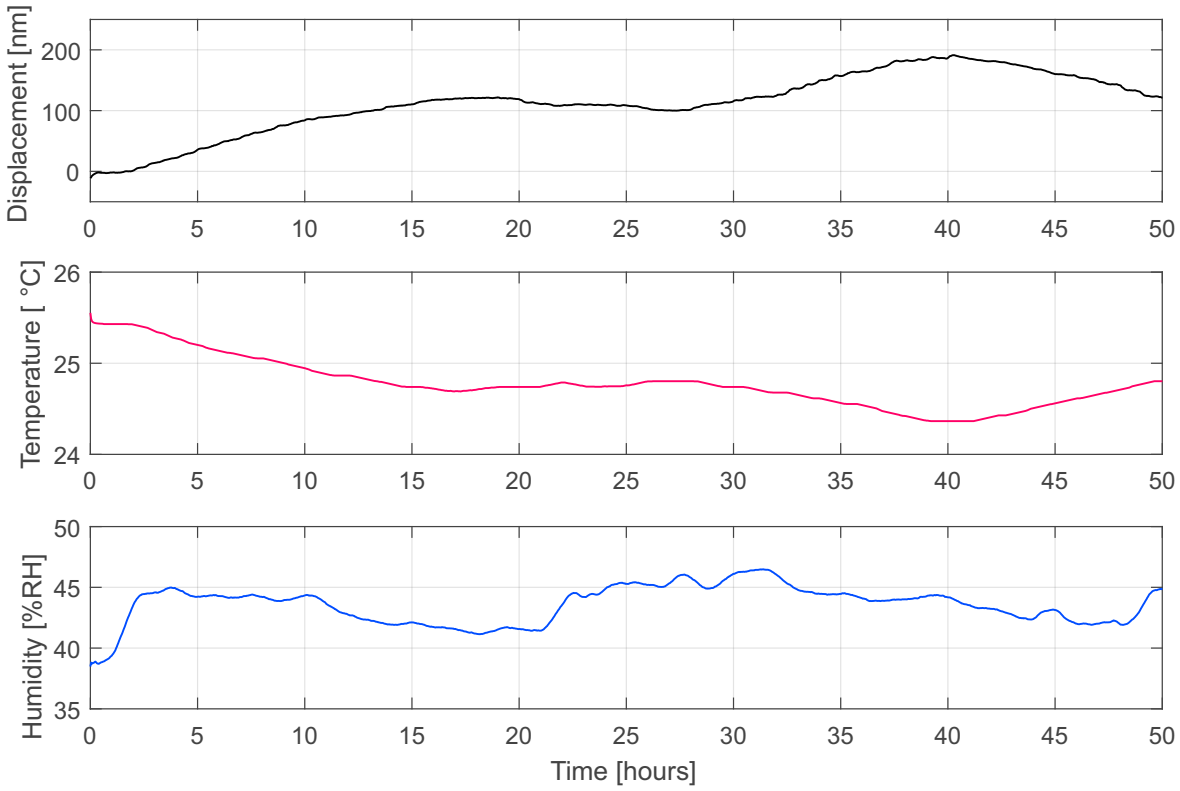

Figure 3.24: Invar sample and breadboard measurement (setup d). Displacement, temperature and humidity change over 50 hours under an insulated box. The temperature varies about 1° C and the displacement increases to 200 nm during the measurement.

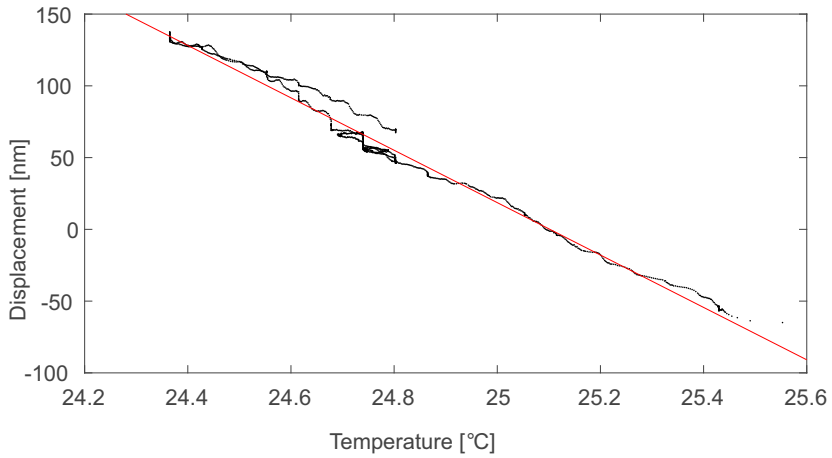

Figure 3.25: Invar sample and breadboard measurement: temperature is plotted against displacement and a linear fit (in red) is possible.

EUCLID to the breadboard, an Invar sample (20 x 12.7 x 12.7 mm) and Invar plates were used. During a 50 hour measurement the temperature changed by about $1^{\circ}C$ and the maximum displacement was about 200 nm (Figure 3.24). The expected change for the Invar components should be around 80 nm.

When analysing the temperature influence with the Invar components the fitting was improved through the nearly linear behaviour during the 50 hours (Figure 3.25). With increased changes in temperature there is still a hysteresis effect that can not be excluded. Also the fact that the temperature sensor only approximates the temperature of the components needs to be considered as well as the different thermal capacities of the parts. Another effect caused by the temperature is an optics thermal drift. Depending on the configuration this drift can be as high as 300 nm/K or as low as 20 nm/K (Badami & de Groot 2013).
When measuring displacement with the EUCLID, the resolution while be in the picometer range. An exact assignment of the causes of displacement is, at this scale, not possible. Aston (2011) states a wavelength temperature tuning coefficient for the EUCLID of 0.04 nm/K. Furthermore Aston (2011) also notes a drift of $\sim$ 30 nm of unknown source for a measurement of 500 s. A list of uncertainties that influence displacement laser interferometers is given by Badami & de Groot (2013). When measuring weathering induced length changes in the micrometer scale, an error of overall several nanometres can be assumed.

3.4.3 Final setup

The best set-up for the most linear behaviour during temperature changes includes the use of the Invar breadboard under an insulated box. For the investigations with sandstone this setup was used to determine the temperature influence on every sample. A reference/'blank' measurement was undertaken for each sample (Figure 3.26) and k was determined with a linear fitting. This approach provided the value for k that is used to 'correct' the measurements to be as uncoupled as possible from temperature drifts (Table 3.2). Five different sandstone types were investigated: Cullalo, Locharbriggs and Stanton Moor (including a Na_2SO_4 treated version), and the weathered building stones from Jedburgh and Dunkeld (see Chapter 2). The displacement was normalised to mm/m depending on the sample length. The sample size was kept small ($10 \times 10 \times 25$ mm) for two main reasons: the first was to use only little original building material from the historic sites as possible. The other reason was the idea that a smaller sample sizes will reduce the number and therefore frequency range of possible weathering related expansion/contraction events. The measurement duration ranged from 30 to 120 hours.

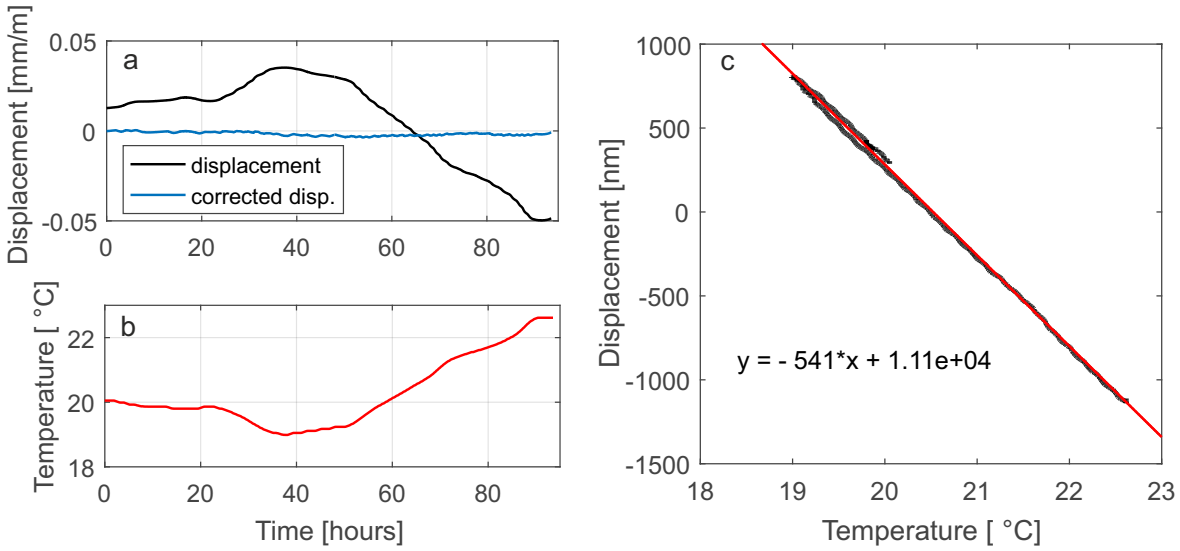

Figure 3.26: Locharbriggs measurement over 90 hours to determine the temperature influence k. a: displacement of the reference/'blank' measurement in black and the temperature corrected displacement in blue. b: temperature variation over 90 hours and c: the temperature plotted against the displacement with a linear fit.

Table 3.2: Temperature influence k during a 'blank' measurement of different sandstone samples.

stone type	Cullalo	Locharbriggs	Stanton Moor	Dunkeld	Jedburgh
k [nm/° C]	-530	-540	-790	-640	-820

3.5 Sandstone measurements

3.5.1 Time domain measurements

The tests included eight sandstone samples (see Chapter 2) and their drying behaviour after water saturation. The samples include Cullalo, Locharbriggs and Stanton Moor. Weathered samples from Dunkeld and Jedburgh were also investigated. Artificially weathered samples (see Chapter 2) include Cullalo, Locharbriggs and Stanton Moor. The tests were performed on Na_2SO_4 contaminated samples (14% solution), as NaCl contaminated samples did not show any signs of decay after three cycles of wetting and drying. All test samples were measured perpendicular to the bedding.

Unweathered samples

The three unweathered samples were saturated in water for 24 hours. The small sample size ($1 \times 1 \times 2.5$ cm) and the high ratio of surface to volume (~ 5) allows a quick saturation of the rock. The displacement, temperature and humidity was measured for 50 hours of drying. The measurement was repeated three times for each sample under room conditions. After the samples were taken out of the water bath with gloves, they were immediately placed

in front of the interferometer. A thermochron was placed on top of the sample and the hygrochron was placed in close distance to the sample.
Figure 3.27 shows the change of displacement (corrected by the temperature influence) and the change in the close range humidity of the Cullalo, Locharbriggs and Stanton Moor sample. The displacement of the three repeated measurements for each individual sample show similar gradients although the humidity of the room during the measurements can vary with up to 10 %RH and the room temperature with up to 2 °C.
The drying process starts with a phase of nearly no displacement, the same for all samples. This phase is the longest for Locharbriggs (5 hours) and the shortest for Stanton Moor (3 hours). The close-by humidity increases first (which is due to the sensor itself) and stays at a nearly constant level. This initial constant phase is followed by a rapid shrinkage of the samples and a rapid decrease in the close-by humidity. The Locharbriggs sample shows the steepest drying curve ($0.05\frac{\mathrm{mm/m}}{\mathrm{h}}$) and reaches a stable size after around 10 hours. The Stanton Moor sample and the Cullalo sample show a slower contraction ($0.01\frac{\mathrm{mm/m}}{\mathrm{h}}$) that is followed by a third phase of drying with even slower contraction. The Cullalo sample reaches the third drying phase after around 10 hours whereas the Stanton Moor sample needs around 20 hours. A constant size is reached after 35 hours for the Stanton Moor sample. A similar gradient can be followed for the humidity measurements although in the last phase of drying the humidity seems to reach a constant value sooner. Although the change in size of the Cullalo is very small after 40 hours, the Cullalo sample has not fully reached a constant size.

In Chapter 1 three drying stages were described depending on the evaporation rate given by the water content of the rock which equals the loss in weight during drying. A constant rate evaporation (I), and a falling rate evaporation (II and III). These drying stages can be adapted for the shrinking of the sample. Franzen & Mirwald (2004) gives the deviation of the weight loss per time to assess the drying rate of the sample. He divides the first drying stage (I) further into two sub stages: I a describes a strong decrease in the drying rate and I b describes nearly no change in the drying rate (or sometimes a small increase of the drying rate).
A steady stage evaporation that leads to a constant close range humidity and nearly no change in displacement describes the first phase of drying in the test which can be correlated to the drying stage I a with a very low but steady drying rate. Although Franzen & Mirwald (2004) measures a loss in weight for this constant drying rate, the displacement of the sample nearly does not change at all. The next phase of drying in the tests is characterised by an increased linear dilation with therefore a constant slope for the change in dilation. The evaporation rate is still constant and this phase can be described as drying stage I b. After stage I the change in dilation with time decreases which describes the onset

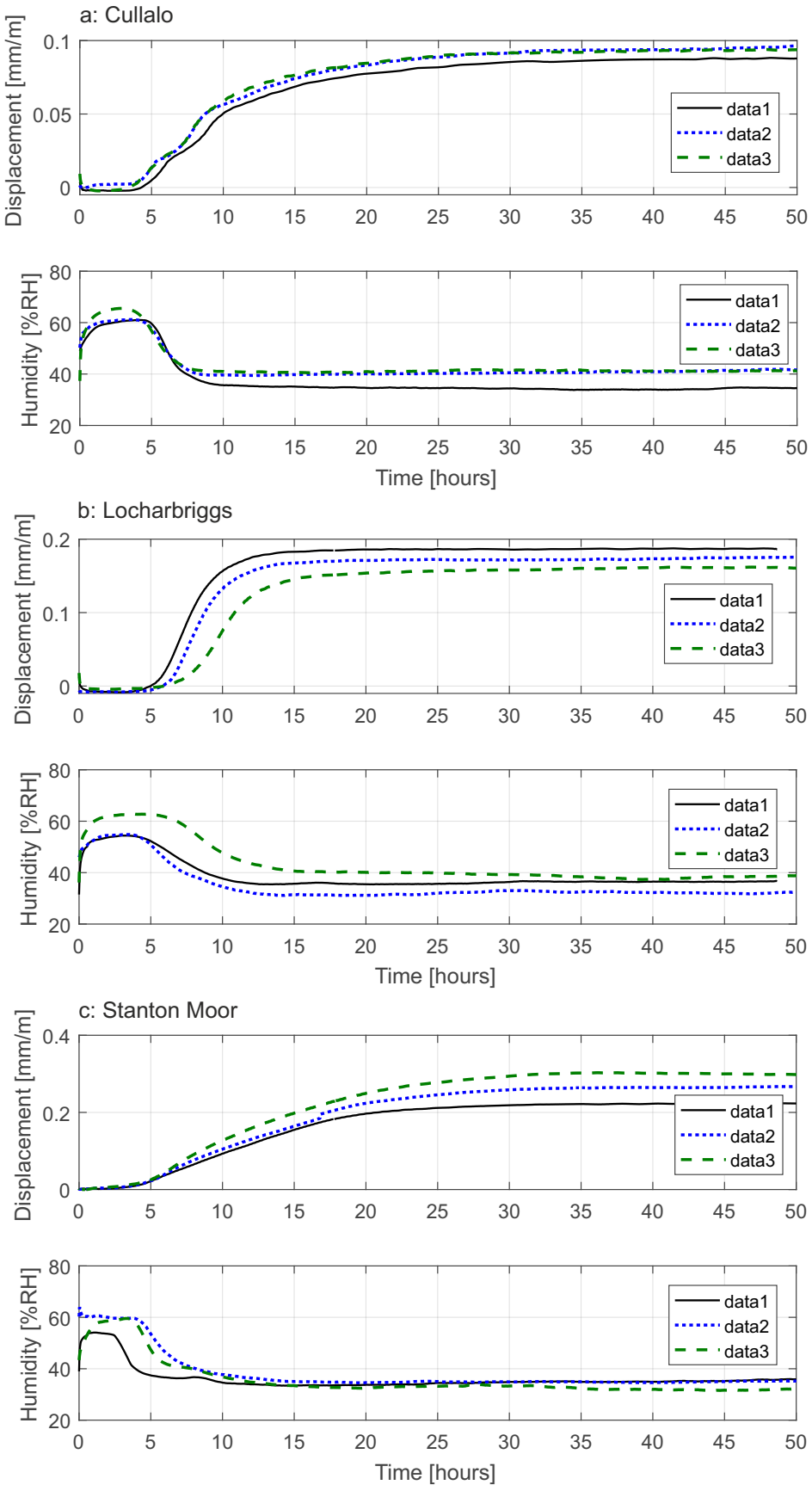

Figure 3.27: Displacement of drying sandstone and nearby humidity measured for 50 hours after a 24 hour water bath. An increase in x, the displacement, indicates a contraction of the sample. a: Three measurements of a Cullalo sample, b: Locharbriggs sample and c: Stanton Moor sample.

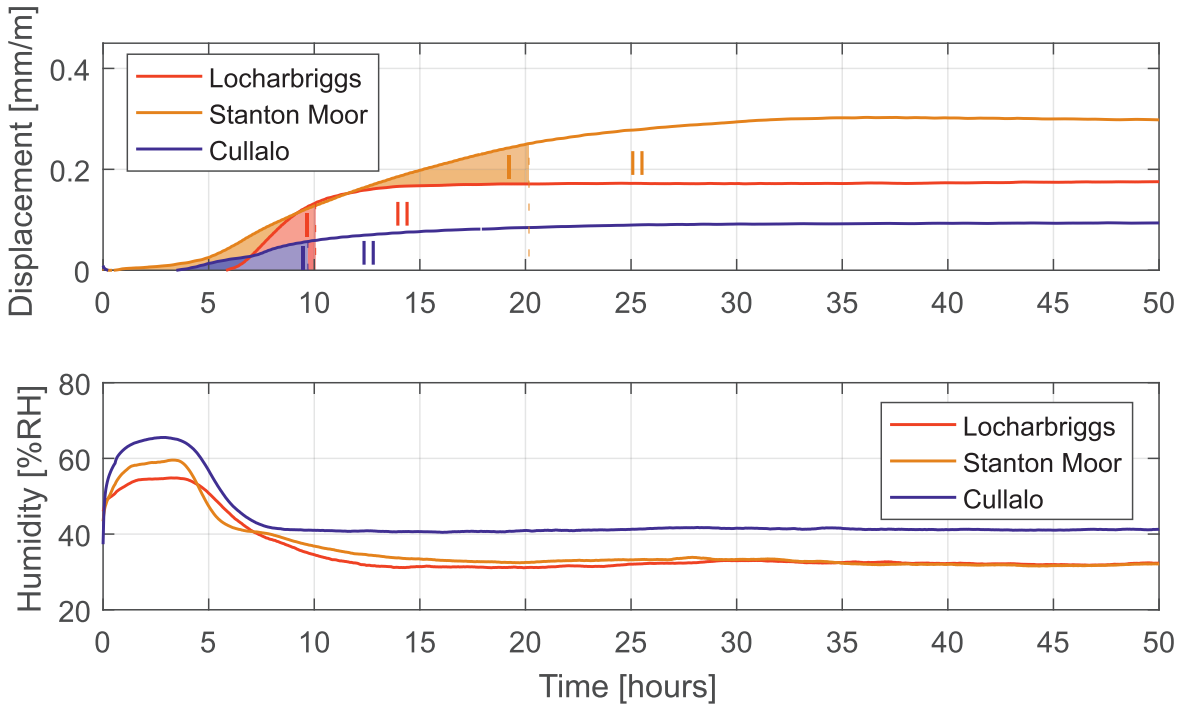

Figure 3.28: Displacement of drying sandstones and nearby humidity measured for 50 hours after a 24 hour water bath. Different drying behaviour for the three investigated samples Cullalo (blue), Locharbriggs (red) and Stanton Moor (yellow). Phase I of the contraction/drying is characterised by larger slopes. The end of phase I is approximated by the intersection point of the tangens of the curve's inflexion points with the tangens of the increasing constant displacement after > 15 hours.

of drying stage II. The evaporation rate is decreasing with time. The third stage of an even slower evaporation state. The onset of stage III can not be clearly identified for the samples. Figure 3.28 displays the drying stages.

Comparing the three sandstones, drying stage I b is very short for the Cullalo and Locharbriggs samples and extended for Stanton Moor. A discontinuity in stage I b can be observed in all Cullalo measurements (Figure 3.27 a). The drying curves, or shrinkage curves, correlate well with the measured pore network properties in Graham (2016). Stanton Moor is characterised by a large amount of small pores (see Chapter 2). Small pores keep the evaporation constant for a longer time but the transport of fluid is slower. The low permeability of Stanton Moor slows down the fluid transport further.

The different drying behaviour of Cullalo could be caused by a long period of slow evaporation by diffusion. The pore size distribution of Cullalo and Locharbriggs are similar but the permeability of Cullalo is smaller. The latter is even smaller for Stanton Moor, but could in this context explain the different behavior of Locharbriggs and Cullalo. Still the pore size distribution seems to be an important influence in the drying rate. The change in the dilation rate observed for Cullalo in stage I b needs to be confirmed for other sample sizes. Although present in all three measurements, tests from Graham (2016) do not mention any variation in the drying process.

The maximum displacement during drying of the three samples is given for Stanton Moor with 0.3 mm/m (Figure 3.28). This is followed by Locharbriggs with 0.18 mm/m and Cullalo with less than 0.1 mm/m. Cullalo does not show any traces of clay minerals, which explains the low hygric dilation (assuming a reversible drying process). Traces of non-swelling clay minerals where found in both Locharbriggs and Stanton Moor. In respect to the composition and the water absorption as well as the capillary absorption of Stanton Moor and Locharbriggs (see Chapter 2) a larger hygric expansion was expected for the Locharbriggs sample. The difference of the two samples might therefore be caused by osmotic swelling of some of their trace minerals.
Despite the different room conditions for the samples during the measurement, the shape of the drying curve is characteristic for the individual samples and can be used to distinguish the sandstone types with the different pore network properties.

Weathered samples
The next samples that were investigated are from Dunkeld Cathedral and Jedburgh Abbey. The weathered samples were measured perpendicular to the bedding after a 24 h water bath. The measurements were repeated three times.
The shrinkage of the samples starts immediately compared to the three unweathered samples (Figure 3.29). The Jedburgh sample shows a nearly constant change of displacement for 6 hours. In the third measurement there is plateau that indicates a small expansion (Figure 3.29 a).
The other two measurements show the same trend but not as clearly. After the more or less constant change of dilation of stage I b, the drying rate slows down quickly in stage II after 6.5 hours. The three measurements of the Jedburgh sample show a greater variation than the previous unweathered samples. For the Dunkeld sample a similar drying behaviour can be observed. In stage I b a step with a small expansion of the sample just before 7.5 hours can be seen (Figure 3.29 b). After 5 hours the sample shrinks quickly until 9 hours. Stage II of the drying phase with a slow evaporation/drying rate follows. The overall displacement is greater than 1 mm/m for Jedburgh and up to 0.9 mm/m for Dunkeld (Figure 3.30). This rate is ten times larger than for the previously measured unweathered Cullalo sample. The expansion in the drying stage I b could indicate a possible phase change that results in a pressure build up. Although petrographic analysis did not show any sulfates and the dehydration usually goes along with a decrease in volume. An initial crystallisation and the dissolution could be the source as some salts have several metastable phases. Another source could be the compressional stress of shrinkage, that on the other hand leads to an expansion perpendicular to the bedding. This idea could be checked for measuring the samples parallel to their bedding. As a similar expansion can be observed for the unweathered Cullalo, the effect might be due to pore network properties, such as a anisotropic relief from

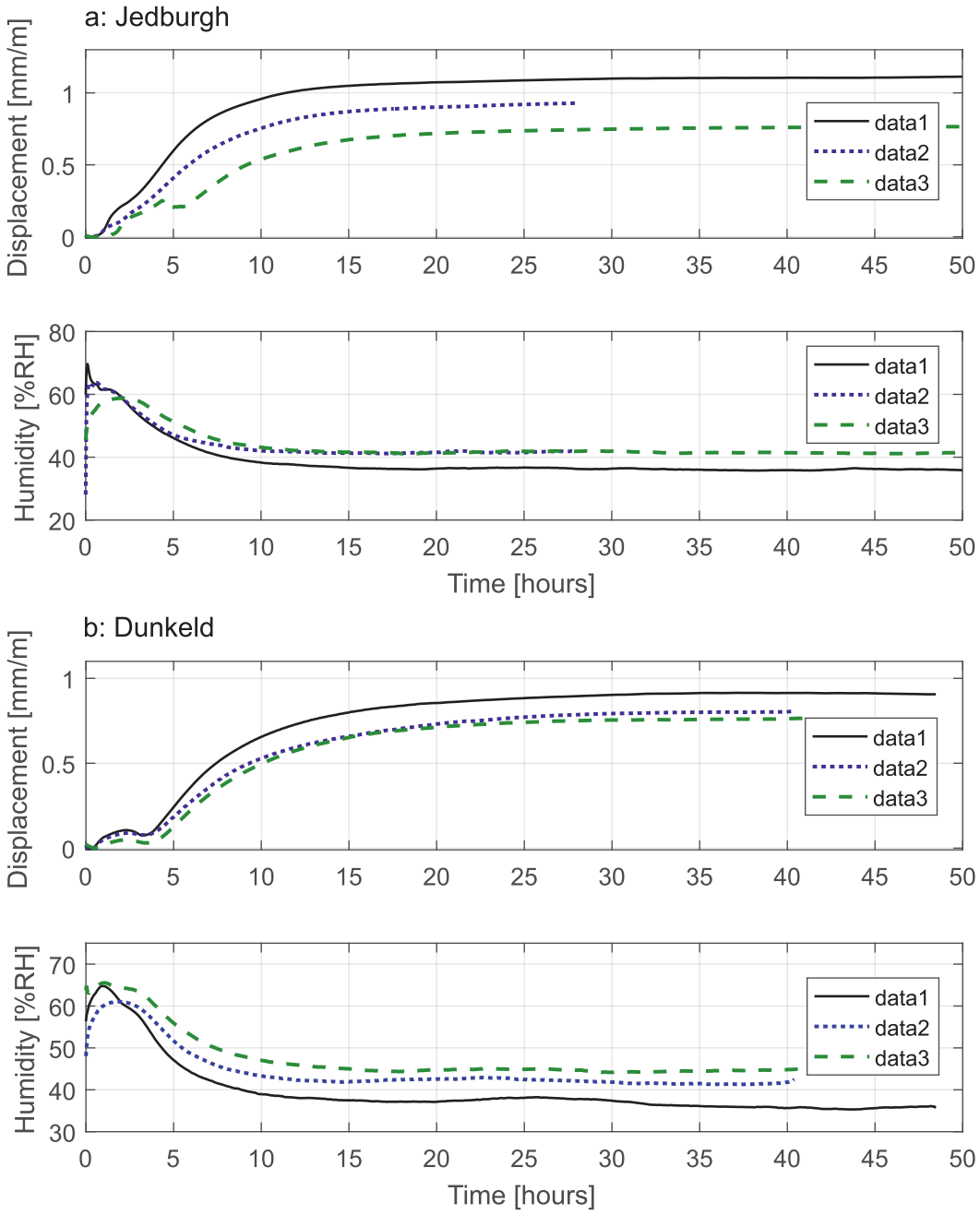

Figure 3.29: Displacement of drying sandstone and nearby humidity measured for up to 50 hours after a 24 hour water bath. a: Three measurements of a weathered Jedburgh sample and b: Dunkeld sample. An increase in x, the displacement, indicates a contraction of the sample.

capillary stresses.

Artificially weathered samples

The last measurements includes the artificially weathered samples of Cullalo, Locharbriggs and Stanton Moor (see Chapter 2). The samples were treated with a 14% Na_2SO_4-solution for several drying and wetting cycles. The dry sample was then placed into a water bath for 0.5 hours and the drying process was monitored for 90 hours.

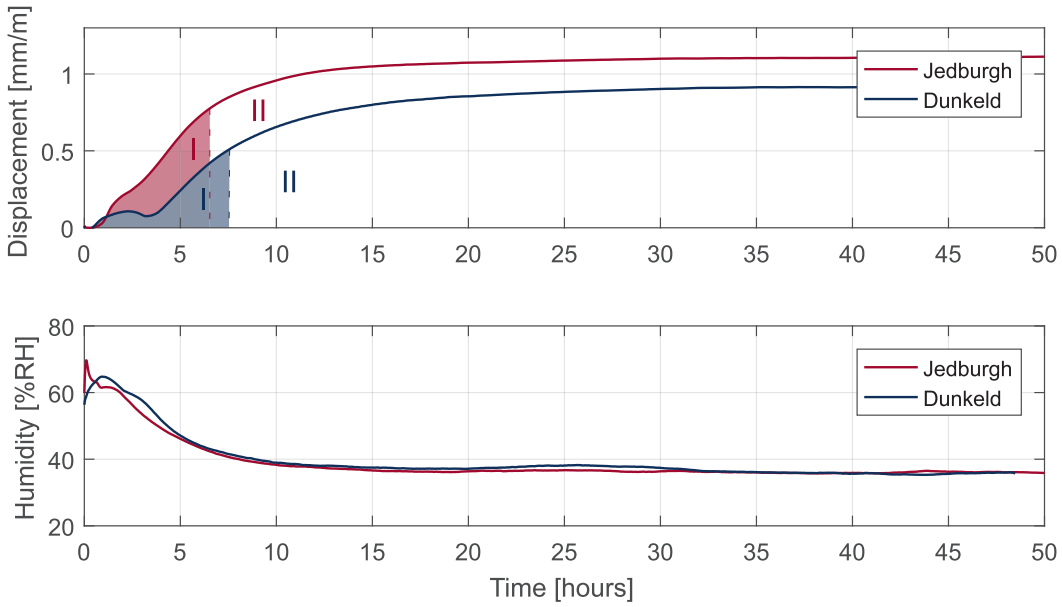

Figure 3.30: Displacement of drying sandstone from Jedburgh (pink) and Dunkeld (purple) and nearby humidity measured for up to 50 hours after a 24 hour water bath. Again an increase in x, the displacement, indicates a contraction of the sample.

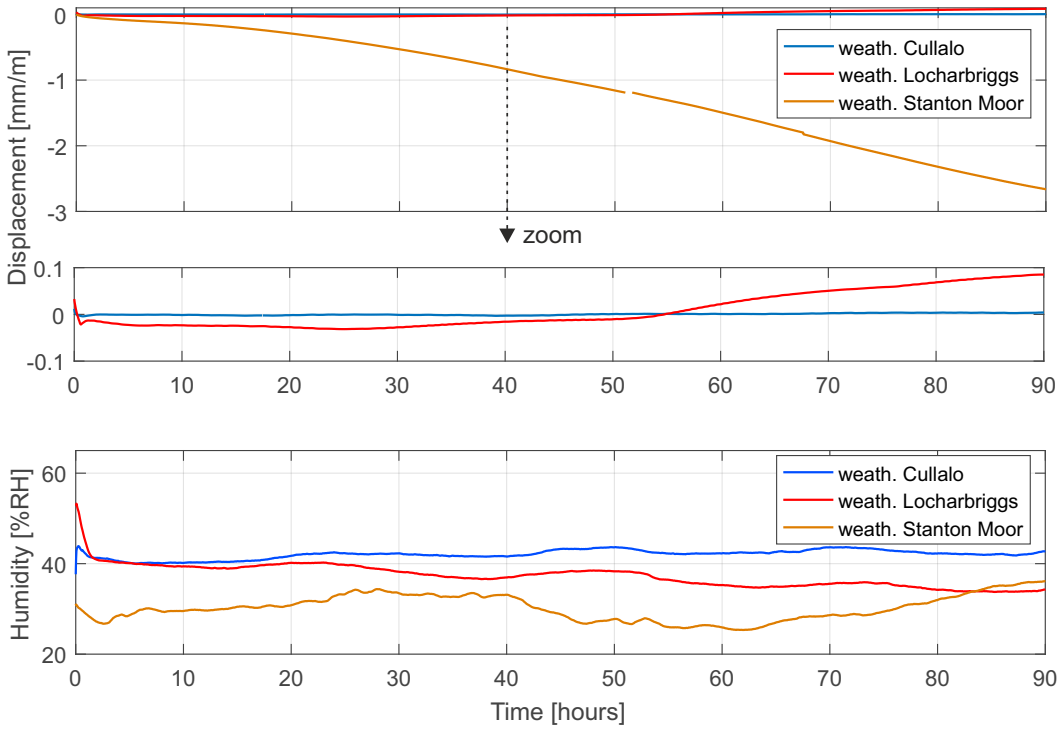

Figure 3.31: Displacement of drying sandstone and nearby humidity measured for 90 hours after a 0.5 hour water bath. Different drying behaviour for the three samples Cullalo, Locharbriggs and Stanton Moor, all treated with several wetting and drying cycles of Na_2SO_4. The Stanton Moor (yellow) shows the largest expansion. A zoom of the displacement -0.1 - 0.1 mm/m is displayed to follow the movement of the Cullalo (blue) and Locharbriggs (red).

The Cullalo and Locharbriggs sample show nearly no change in displacement after the short water immersion (Figure 3.31). Locharbriggs shows a small expansion and then a contraction after 55 hours of nearly 0.1 mm/m. This could be due to the hydration of the sodium sulfate with the subsequent dehydration of the salt. The same process occurs in the Cullalo sample, but does not result in a significant change in the sample size. A contribution to this difference in volume change of the sandstone types can be that the compressive strength of Cullalo is nearly double the amount than Locharbriggs.
The Stanton Moor sample visually showed the strongest decay. It also showed the largest displacement (Figure 3.31). After the short water bath it does not shrink but expands to up to 3 mm/m in 90 hours. This is assumed to be mainly caused by hydration, the high volume expansion of thenardite to mirabilite. Hydration should be followed by dehydration and salt crystallisation. Both processes can not be distinguished during the continuous expansion of the sample. Stanton Moor is very prone to subflorescence mainly due to its bi-modal pore size distribution (Graham 2016). The tests confirm this result and underline how quickly the damage can happen and how clearly this behaviour can be distinguish from other sandstone types.
Drying of salt contaminated porous materials is next to the shrinkage of the sample strongly influenced by salt crystallisation (usually expansion) and/or hydration and dehydration processes. The crystallisation or hydration of salts makes it hard to predict the behaviour of the drying sandstones as pores can be blocked and the evaporation can be influenced (see Chapter 1).
Again all three samples show a different drying behaviour and can be distinguished. The behaviour also changed compared to the unweathered samples (although this time the water immersion was just half an hour). Colas et al. (2011) showed the change of dilation in salt-contaminated sandstones can be used to highlight behaviour changes under cyclic changing relative humidity. This is especially prolonged for NaCl. In the presented test the Na_2SO_4 contaminated Stanton Moor sample showed quick and severe damage compared to NaCl, why the Na_2SO_4 contaminated samples were chosen.

The tests showed promising preliminary results for a new way of estimating stone decay/properties.

- In summary when comparing for example an unweathered (Stanton Moor), weathered (Dunkeld), and artificially weathered (Stanton Moor) sample, different drying behaviour can be observed (Figure 3.32) and used to characterise the samples.
- The tests with the different sandstone types allowed to distinguish them due to their different drying behaviour. A characteristic drying behaviour for each stone type was observed with the greatest contraction given for Stanton Moor and lowest observed for Cullalo.

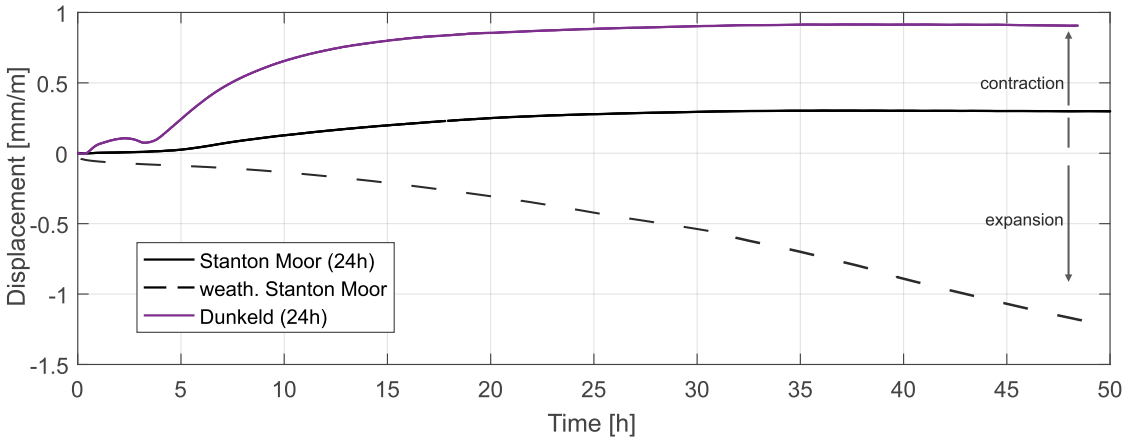

Figure 3.32: Displacement of drying Stanton Moor sandstones (black) and Dunkeld sandstone (purple) measured for 50 hours. The Stanton Moor sample (unweathered) and Dunkeld sample (weathered) were soaked for 24 hours in a water bath and show different drying behaviour. Another artificially weathered Stanton Moor sample (dashed line), treated with several wetting and drying cycles of Na_2SO_4 was immersed in a water bath for 30 min and shows very different drying behaviour than the unweathered or weathered samples.

- Different stages of weathering can be identified from the drying behaviour after water saturation of 24 hours or 0.5 hours. For example Stanton Moor shows the greatest expansion when contaminated with Na_2SO_4. For exact identification of the stage of weathering, the drying conditions (such as temperature and initial water saturation) need to be known, as well as information of the stone type.

3.5.2 Frequency domain measurements

The frequency domain measurements analyse the occurrence of displacement events of the sandstone samples. An artificially weathered sample was monitored with a high resolution sampling rate of 20 kHz. The Stanton Moor sample (20 x 10 x10 mm) was treated with 14% Na_2SO_4-solution in four repeated cycles of wetting and drying (see Chapter 2). After the treatment the sample, which is prone to subflorescence, several fine cracks on the surface appeared.

The sample was immersed in a water bath for 2 minutes and placed in front of the interferometer. Measurements were taken for 5 minutes at the start of the drying process, after half an hour and five more times with the last one 28 hours later due to the large data size of the high resolution measurements. During the 28 hours visible cracks appeared mainly perpendicular to the surface (Figure 3.33).

Figure 3.34 shows the measured displacement of the sample during the first 5 minutes of the drying process and after 30 min as well as the corresponding spectrograms. Noticeably brighter bands of increased displacement appear over the whole displayed frequency range.

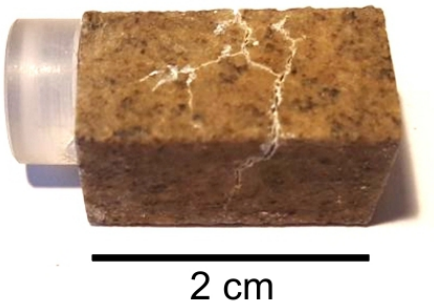

Figure 3.33: Stanton Moor sample with attached mirror shows cracks after cyclic treatment with 14% Na_2SO_4-solution. The sample was saturated in water for 2 minutes and then left to dry for more than 24 hours.

For the first measurement they appear every 11 s and every 25 s. For the second measurement the bands appear less frequent, every 25 s and 60 s. Looking at the displacement of the measurements, at the same time a reoccurring change in slope can be seen (see arrows Figure 3.34). The expansion of the sample is 0.4 µm/min in the first five minutes and slows down to 0.16 µm/min after half an hour. These bands or jumps in the displacement can be identified as artifacts. When considering previously measured spectra of the displacement as well as the spectrum from this measurement, the largest peak is located at 25 Hz with an amplitude of $10^{-3}\mu m/\sqrt{Hz}$. For a displacement of this size that appears 25 times a second, we can expect a displacement of 2.5 nm/s. The largest displacement would therefore only give an overall displacement of 130 nm/min.

The provided description of the EUCLID (Aston et al. 2013) states that a movement of 4 cm/min should not be exceeded. It can be seen that at lower speed the EUCLID produces artifacts. Therefore we need to look at the data in between those bright bands for the following analysis.

Figure 3.35 shows the spectra of a 15 s measurement from an untreated Stanton Moor reference sample, the Stanton Moor sample (dry) that was treated with 14% Na_2SO_4-solution and the same sample that is still wet after 30 minutes of drying. The comparison of the three spectra shows very small differences. Interestingly the spectrum of the measurement that has the largest movement shows has the highest sensitivity. The highest sensitivity was expected for the 'calm' reference measurement. The first 5 minutes of the wet sample look similar to the references.

In the range of 1 - 10 kHz with an upper sensitivity limit of around 10^{-6} µm no change in the reference sample or salt weathered sample could be identified.

From acoustic emission tests (see Chapter 1) we expect the signal of a microscopic crack to be at higher frequencies than the investigated range of up to 10 kHz. Cracks from me-

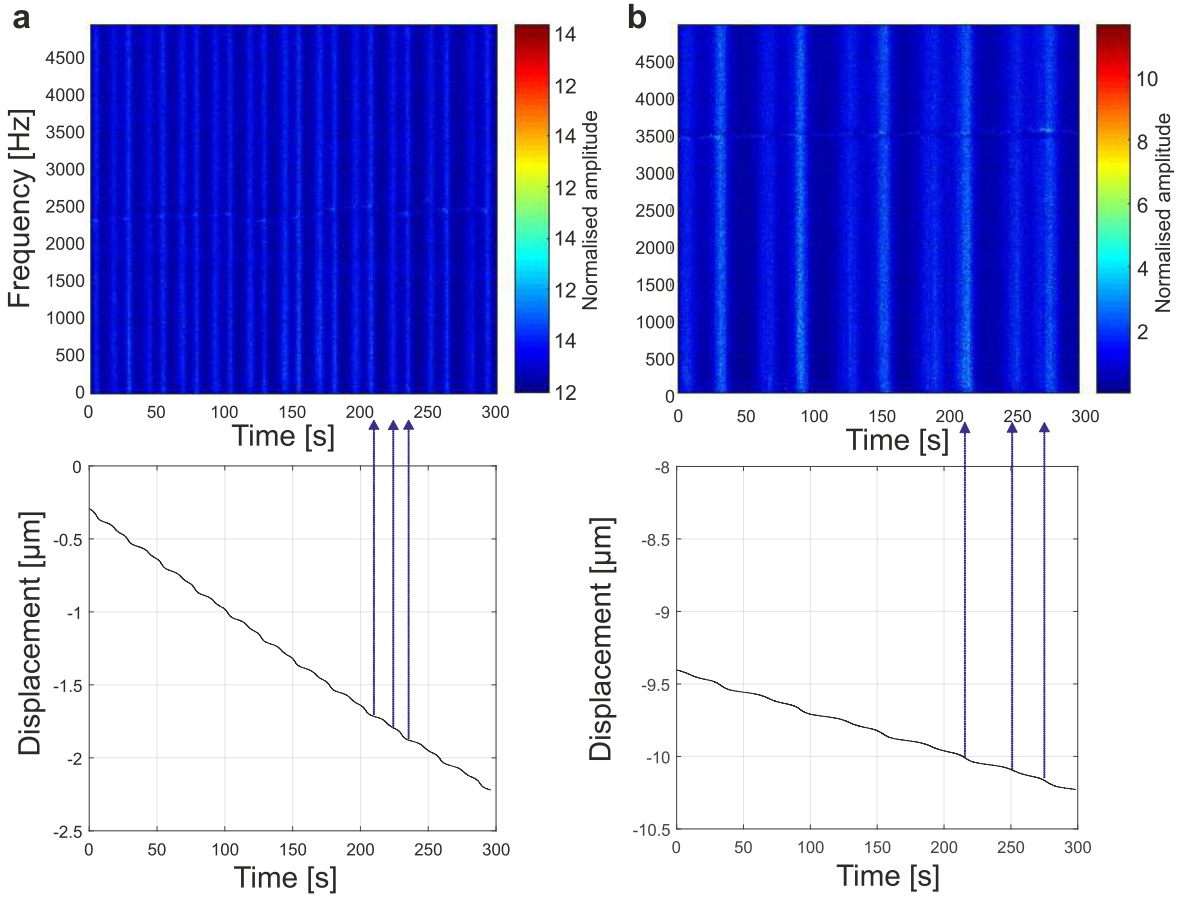

Figure 3.34: Normalised spectrograms of a Stanton Moor sample after 2 minutes of water saturation previously treated with 14% Na_2SO_4 solution. a: The first 5 minutes of the measurement are displayed in a spectrogram and below the corresponding displacement change over time. b: Half an hour after the water saturation of the same experiment a second measurement was undertaken for 5 minutes. The spectrograms show bands of increased displacement that match the change of slope in the displacement (see blue arrows).

chanical loads of several MPa have been recorded around 100 kHz. We therefore do not expect the same signal to be detected by the EUCLID. Although the frequency of the event occurrence might be in a range to be detected by the EUCLID. A clustering of events (group of events happen at spatial and temporal constrains) could also show a certain frequency range that could be identified with the EUCLID. For these analysis it would be important to investigate different ranges of displacement amplitude. A range of magnitudes might appear with a characteristic frequency pattern. If the amplitude is set to high, it could again fall outside the detection range of the EUCLID if those events would not appear frequent enough and vice versa. The same is true for the set limits of clusters. If they are set too frequent the range might be too high for the long term investigation of the EUCLID.

The described approach assumes that the wetting/drying and salt crystallisation events show a Poisson distribution. The next three examples describe changes in the events frequency found for rocks under load. Lockner (1993) for example described the fault propa-

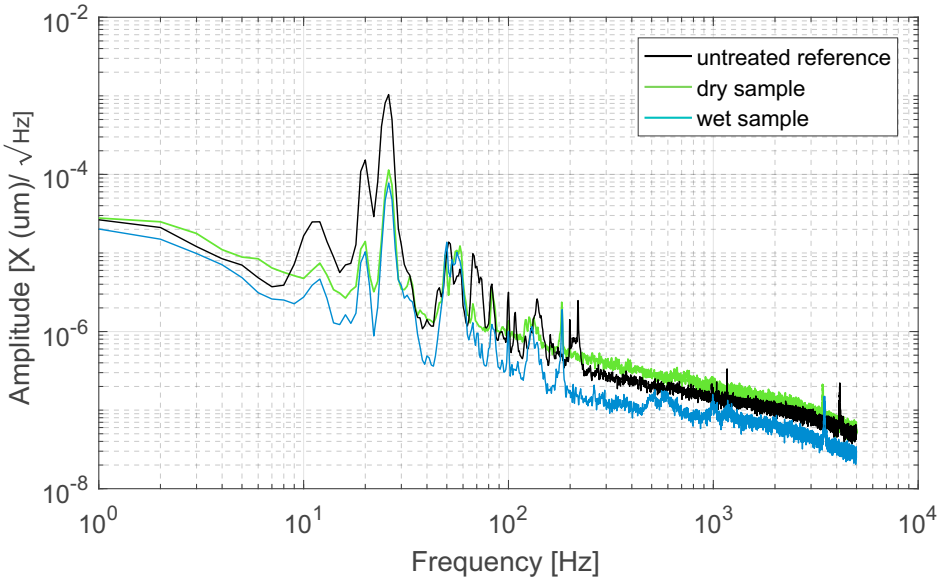

Figure 3.35: Comparison of several spectra over 15 seconds from a reference sample and the Stanton Moor sample after 2 minutes of water saturation previously treated with 14% Na_2SO_4-solution. In black is the spectrum of an untreated, dry Stanton Moor sample with similar dimensions. In green is the spectrum of the dry, salt treated sample and in blue the same salt treated sample but still wet taken over 15 s window.

gation itself as not smoothly with different periods of acceleration and deceleration.

Nishizawa & Nomo (1990) studied the statistical occurrence of AE events in granite under 200 MPA load for uniaxial creep in detail for several hours. They found a stationary Poisson background (repeated events in a certain time interval) for a smaller number of AE events (about 700 events in five hours). With an increase in AE events (600 per hour) a clustering of events occurred. For low AE rates they deduced a self-exciting interaction whereas for high AE rates their findings were inconclusive. The spatial distribution is of course strongly related to the identified temporal distribution as the material usually fails in a certain area. For this example assuming a constant occurrence of the Poisson distributed events, an events frequency of 0.04 Hz could be assigned. There is no information on how many clusters appear during the hour of high AE rates and no pattern could be observed for the events during high AE rates by Nishizawa & Nomo (1990).

Meng et al. (2018) measured the number of AE events for a load of up to 20 MPa on a sandstone sample. During an increased loading for about 10 s and followed by a decreased loading of 10 s the AE events reach a peak with smaller than 500 events at the maximum loading. The number of events falls constantly before and after constant loading/unloading. Such an event frequency for example should be able to be detected by the EUCLID. Xu et al. (2017), Fortin et al. (2009) tested sandstones under several loads with an increased load of 0.1 MPa/s and 1 MPa/s. They recorded rates of 10 - 60 events per second.

The events frequency is strongly dependent on the applied stress but also the set magnitude that defines an event of the author determines the number of events. The ranges of the fre-

quency of occurrence showed that it might be possible to investigate the events frequency for decay investigations.

When a porous stone with a salt solution dries, the salt ion in the solution can accumulate near the surface. Diffusion decreases the concentration gradient. Further drying will increase the gradient. When the evaporation rate is high, supersaturation near the surface leads to the crystallisation at the time. This would indicate a cluster of crystallisation (peak of crystallisation) events instead of a continuous crystallisation (Coussy 2006). As seen in Chapter 1 the crystallisation of salt in porous media is strongly dependent on the supersaturation, environmental conditions and the pore network properties. Even if nucleation of crystals could be precisely predicted, the time frame of pressure against the pore walls of individual crystals that will cause deformation is difficult to estimate. Other processes that cause volume changes such as swelling of clay minerals should be more like a continuous process. Therefore, such processes will not show up as excess events in any characteristic frequency range. The approach given in acoustic emission where the frequency of one event is considered instead of the approach where the occurrence of the events is considered has been shown to work well for several applications related to weathering. The frequency of the event itself is usually 10 times higher than the detection frequency of the EUCLID.

A fingerprint of the weathering process or water saturation of the sample was not identified with the describes methodology. The analysis of the spectra and spectograms was done visually to identify differences in the references and the weathered samples/wet samples. The differences could be less obvious and therefore a statistical analysis and comparison might be able to detect a fingerprint. In future work it might be possible, that a different time window, filtering or other data treatment will reveal a characteristic pattern to enable a deduction of the source and amount of decay. With the presented analysis a rough upper limit of maximum amplitude of decay effects can be set to about 1×10^{-12} m in the frequency range around 1 kHz.

3.6 Future Work

The future work should cover three main parts: possible changes in the approach of analysing the displacement data, further investigations with different building materials and the realisation of a portable tool for being used on site.

Analysis

- Slope of displacement analysis
  The frequency of rises and decreases in the displacement (the derivation of the displacement) might allow for a better deduction of the weathering processes. The best

time window needs to be determined for this approach. This time window might vary for the investigated process and stone type.

- Frequency range
  Filtering for the desired signal and letting search tools compare large data sets with different time windows might allow a link of the weathering process and the recorded signal of the EUCLID. This would require repeated tests of different building stones at different states of decay (different salt loads) to be used for this large data analysis. Statistical analysis of the data for certain events or events that appear at certain frequency clusters would be one goal for those tests.
  It needs to be investigated if certain amplitudes appear more often and if they appear with a certain frequency. This would also include checking if in a certain time window specific ranges of displacements appear with a repeated frequency (for example during a time window of 10 s 3 events with a 100 nm amplitude appear). This idea would be an in depth analysis of the spectrograms.

- New tool/setup
  Using a different device that measures displacement but with increased sampling rate could expand the investigated frequency range for lab based analysis.
  A change in the setup could enable a higher precision for the future analysis in two ways: A free hanging sample with two mirrors at the front and at the end allow to eliminate any influences of the setup itself. This would include a change of the the beam path and processing of the data.
  Alternatively two interferometers that measure the sample from both sides with two mirrors will also allow for a higher precision. This setup would also allow determination of drifts caused by the tool itself.

Building material investigations

- Extended sandstone tests
  Expanded tests with sandstone should reveal how well the stone's properties such as clay content and salt content can be linked to the displacement. This would allow the state of decay to be better understood and deduce the durability of the rocks. Samples with defined weathering states such as known salt content will enable a better prediction of the displacement. Weathered building stones from sites can then be measured and later compared to standards derived from the lab tests.
  The influence of the bedding on the different samples also needs to be investigated. Some sandstones in previous studies showed contraction when salt crystallises in the pores (Rüdrich et al. 2007). A detailed investigation of those samples would be interesting to identify causes of this behaviour. The sample size should be varied to

see which range is affecting the measured data. At the final stage this test would include a comparison of an unconstrained sample versus a sample in a wall.

- Other building materials
  Next to sandstone other building materials should be tested such as limestone or concrete. Different sample sizes should also be considered.

- Stone guide
  From the expanded building stone data it could be tested if stones can be grouped according to their properties and displacement behaviour. A catalog of typical displacement rates or another indicator could be used to analyse the stones properties or state of decay in field. These results could then be used as a guide for the behaviour of unknown samples.

Portable tool

- New assembly
  A tool holder that would ideally be attached to the investigated wall need to be designed. The used material need to be considered as well as the stability of the device.

- Noise investigations
  Measurements outside need to be undertaken to determine noise and other influences on the tool, such as changes in humidity. The tool holder needs to be adjusted accordingly.

- Different tool
  Long-gauge interferometric SOFO sensors have been used in the last decade at buildings and bridges for structural health monitoring (Inaudi 2004). The approach of analysing frequency occurrences of displacements could be used for the *SOFO* tool with the high precision and possible frequency range below 1 Hz.

3.7 Summary

This Chapter has shown that the EUCLID enables precise investigation of displacement changes of sandstones with a resolution of less than 1 nm under standard conditions. Several different setups were investigated for greatest noise reduction and sensitivity. The final setup in the lab includes a motion dampening granite table, with a low-expansion Invar optical breadboard and the interferometer and sample directly attached to the breadboard.

With the high resolution (subnanometre) of the laser interferometer, several error sources need to be considered when measuring under room conditions. One of the biggest temperature-related errors is the assumption of homogeneous temperature across the different parts of

the setup. The components have different thermal capacities and show hysteresis.
Over several hours or even days, the displacement can be corrected with the experimentally determined effective linear expansion coefficient of all components of the setup. The remaining drift is strongly depending on the temperature change and can be several nanometres to a few hundreds of nanometres over several days.

The length change of eight sandstone samples was investigated during repeated measurements. The samples were saturated with water and the drying behaviour was monitored. The set included unweathered and artificially weathered samples, and samples from two HES sites.
The time domain measurements of the drying tests showed that the displacement can be used to distinguish different sandstone types (Cullalo, Locharbriggs and Stanton Moor) as their drying behaviour varies. The measured displacement during drying differs for the same type of rock that has been treated with Na_2SO_4-solution. Again, all salt weathered rocks show a different drying behaviour, such that they can be distinguished. Especially prone to the salt contamination was the Stanton Moor sample, that expanded continuously for 90 hours after a short water bath. Two weathered samples from Dunkeld and Jedburgh showed also very different drying behaviour. The change in displacement after water immersion can therefore indicate the state of decay of the building stone. Further investigations are needed to estimate the exact increase or decrease in dilation to relate individual weathering processes.

A characteristic frequency range that could be used as a fingerprint for weathering processes was not identified under the given setup and with the EUCLID tool. It remains possible that weathering events leave a signature in the displacement with a certain amplitude and frequency at an unknown time window. These parameters are most likely varying for different rock types and weathering processes as well as the given environmental conditions. It is therefore difficult to track them.

The frequency domain analysis together with the displacement analysis would be a promising combination for determining a precise investigation of the state of decay. Further tests should be undertaken to implement the approach and develop a portable tool, that can be used on site.

Chapter 4

Ultrasonic drilling tool

This Chapter covers the development and use of an ultrasonic drilling tool. The focus is on the investigation of sandstones and the use of a feedback signal to characterise those building stones. The Chapter includes an overview of ultrasonic rock drilling and the design of the components such as the drill bit and the ultrasonic horn. Tested samples include building stones with different compressive strength together with artificially weathered samples. Results are compared to the performance of a conventional drilling tool.

4.1 Introduction to ultrasonic drilling

The aim of the development of the ultrasonic drilling tool is detection of structural changes caused by weathering. The minimally invasive tool drills a small hole (3 mm diameter) to a depth of up to 4 cm. A feedback signal allows to deduce changes during drilling. When penetrating the rock, rotation speed and cutting speed are kept constant and power consumption is monitored. The consumed power is used to deduce changes in the sample's properties such as its porosity or compressive strength. The tool needs to be able to penetrate hard building materials (compressive strength above 80 MPa) without inducing further damage to them. The wear of the tool tip should be low to avoid the need for frequent changes of expensive drill bits when penetrating hard material.

Ultrasound refers to all sound waves with frequency above 20 kHz. It is commonly used for non-destructive testing (see Chapter 1) and imaging using frequencies usually around several 100 kHz. Ultrasonic vibration that alters the physical, chemical or biological properties of a material is referred to as *power ultrasonics* (Gallego-Juarez & Graff 2015). Unlike non-destructive testing, such as with light, drilling with a frequency of 20 kHz of course introduces permanent changes in the drilled material.
Power ultrasonics for machining (such as cutting, grinding, drilling and welding) have been developed and used since the early 1950s all over the world (Neppiras 1964, Graff 1977).

Examples of an ultrasonic tool that combines drilling, thread cutting and milling, include works by Cohen in 1951, Zhustarec in the 1960, and are followed by drill tools for metal from Aeroprojects, Shoh and Grummann in the early 70s (Yang & Lin 2010, Gallego-Juarez & Graff 2015). Sonic drilling of rocks has been investigated since the late 1960s (Graff 1971). Ultrasonic drillers for machining can be purchased for example from the companies *Sauer Ultrasonics* or *DMG Mori* but, to the author's knowledge, no portable handheld tools yet exist.

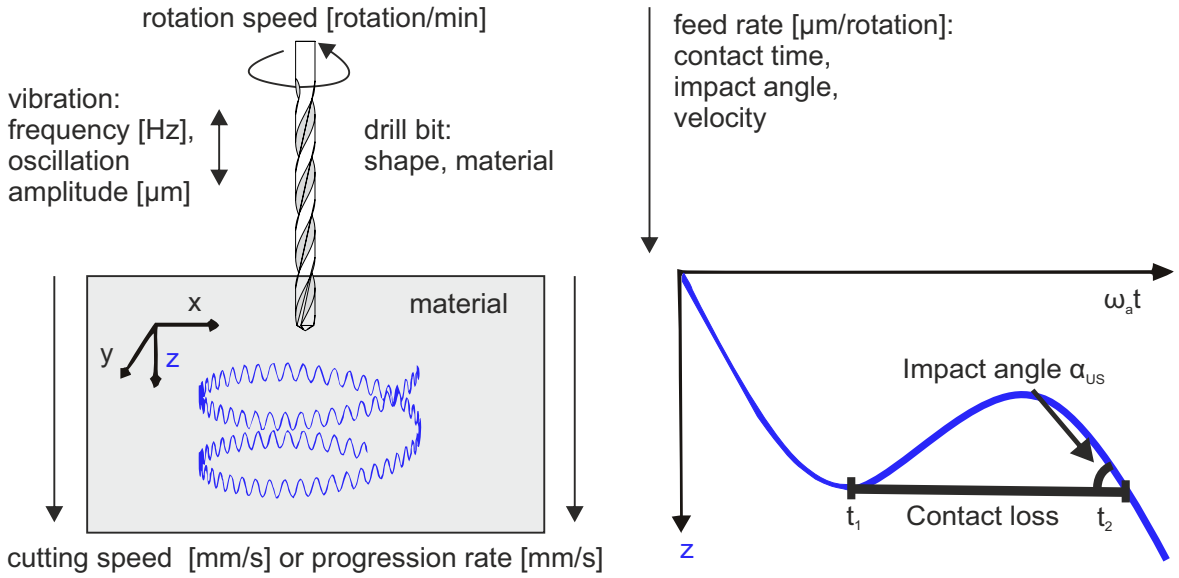

Figure 4.1: Main parameters for ultrasonic drilling with common units. In blue: vibration along the drilling direction creates a sinusoidal helix (from Heisel et al. 2011). On the right a short 2D section of the sinusoidal helix: the drill tip looses the contact to the drilled sample which enables advantages of the ultrasonic drilling.

Main advantages of the use of ultrasonics in comparison to conventional drilling (CD) include a force and torque reduction on the drilled sample (enabling penetration of hard materials), a longer lifespan of the drill tip and a cleaner cut (Maroju et al. 2014, Azarhoushang & Akban 2007). These improvements from the use of ultrasonics are strongly depended on operational settings (Figure 4.1). Such settings include the vibration frequency, the oscillation amplitude, the rotation speed and feed rate (how quickly the tool moves into the material) as well as the drilled material. Under certain settings, CD might for example show an improved tool life compared to ultrasonic assisted drilling (Chang & Bone 2009). It is therefore important when comparing CD and UAD (ultrasonic assisted drilling) to keep the parameters as similar as possible or consider which parameters are best for each technique and what are the limits or general benefits of the drilling technique.

When drilling brittle or vulnerable materials it is important to not expose the sample to a high force through the drill tool. UAD offers a reduction of the exerted force relative to CD. Heisel et al. (2011) lists three main reason for the reduction of force and torque for UAD relative to CD: a theoretical reduction in friction, a "micro-hammering effect" depending

on impact velocity and angle, and a reduction of "inner friction". With regards to the latter reason, Blaha & Langenecker (1959) have shown that metal crystals can be deformed more easily under the influence of an ultrasonic vibration or impacts.

Heisel et al. (2011) also showed a further reduction of torque with an increasing vibration amplitude. The ratio of the cutting velocity and the vibration amplitude is important to asses the force reduction (Brehl & Dow 2007) as well as the contact time of the drill tip and the sample. Impact angle, velocity and contact time are controlled by the set frequency, amplitude and rotation and cutting speed (Figure 4.1).

The following examples look at the exerted force due to vibrations along the drilling axis (ultrasonic cutting and/or drilling) for different materials with frequencies usually around 20 kHz. The axial force (thrust force) exerted on the drilled material is commonly measured with a dynamo meter/load cell. In comparison to CD, UAD has a shorter contact time to the drilled material (transient stress distribution) instead of a steady state stress distribution. This and the related reduction in friction as mentioned above should cause a lower thrust force (Paktinat & Amini 2017). Gallego-Juarez & Graff (2015) report a reduced thrust force and chip material (swarf) as well as an improved drilling rate in comparison to CD. Chang & Bone (2009) present a decreasing thrust force for aluminium for sonic drilling up to 10 kHz. A test at 12 kHz increases the thrust force, as shear strength (resistance against shear forces) becomes more important and the strain rate (deformation by shearing over time without changing volume) increases with higher frequencies. A decreasing thrust force for UAD can be caused by an increase in rotation speed and a decrease of the feed rate (Zhang & Babitsky 2011, Makhdum et al. 2012, Paktinat & Amini 2017).
Previous work (Vedvik 2015) has shown that the force reduction for sonic drilling at around 100 Hz and amplitudes of $20-30$ µm is 40-90% for Berea sandstone (46 MPa from Kim et al. 2016). For ceramics the decrease can be up to 50% for a 10 µm amplitude (Ishikawa et al. 1998). Ishikawa et al. (1998) also found that low-frequency vibrations (several micrometer movement of $5-50$ Hz) of the work piece combined with UAD ($0-10$ µm) decreases the drilling force by up to 70% compared to CD. Tests on stone showed that the force reduction is related to the hardness of the rock. For an example with an amplitude of 18 µm and a cutting speed of 3 mm/min the reduction in torque can be up to 80% for marble and 40% for granite (Heisel et al. 2011).
When discussing the force exerted on the sample, the sampling rates of the load cell or dynamo meter have to be considered. For most tests, these rates are unclear. The measured data are most likely an average over several cycles of small impacts. The previous studies usually do not discuss this or measure a force average. Wiercigroch et al. (2005) uses sampling rates (800 kHz) above the used percussive drilling tool (21 kHz), which enables monitoring of the oscillation in the measured force.

Although an increased rotation rate decreases the thrust force, it is important to be aware that for ultrasonic drilling this reduction has a limit. Increasing rotation speed and therefore material removal rate can result in increased thrust forces when debris accumulates in the drilled hole and can not be removed quickly enough (Baghlani et al. 2013). The same effect can be seen for too high weight on bits and soft materials (Zacny et al. 2008). When finding the best rotation speed for the removal of cuttings, the drill bit shape and diameter have to be considered next to the drilled material. The removal of material consumes power as well, and power consumption can therefore increase with the depth of drilling (Zacny et al. 2008).

Tool wear can be assessed indirectly by a lower average force on the tool, the tool life/ performance of the bits or by the loss of tip material. Tool wear for UAD decreases with lower loads on the small cross sectional tools (Adithan 1974), lower thrust force and slower cutting speeds (Dahnel et al. 2016, Geng et al. 2014, Feng et al. 2017). For tools with cross section above $10\,mm^2$ Adithan (1974) found that an optimum load exists to minimise tool wear.
A reduced wear on cutting tips (for varying materials including poly-crystalline diamond, PCD) compared to conventional cutting and a smoother surface was found by Koshimizu (2007), Nath et al. (2007), Zhou et al. (2003) and Dahnel et al. (2016). Less cratering on stones was observed for UAD but is again strongly material dependent (Heisel et al. 2011).
A lower tool wear (carbide drills and PCDs) or expanded life of the drill tips was also confirmed for ultrasonic assisted drilling by Azarhoushang & Akban (2007), Xu et al. (2009), Tsuboi et al. (2012) and Brehl & Dow (2007). Heisel et al. (2011) did not find a difference in tool wear when comparing UAD and CD when tested on marble and granite.

The developed ultrasonic drilling tool needs to enable a lower thrust force on the vulnerable sample, reduction of wear on the tip and the ability to penetrate hard rocks as well as soft rocks with the same settings to enable direct comparison of them. A feedback signal needs to enable deduction of the physical properties of the rock while drilling.

4.2 Methods

The methods section contains the general construction of an ultrasonic assisted drilling device and the design method including Finite Element Modeling (FEM) and Experimental Modal Analysis (EMA).

The tool was designed in SolidWorks and modeled with Abaqus. The data was collected with LABVIEW PicoScope and analysed with MATLAB and ME'scopeVES.

4.2.1 Assembly of the ultrasonic drilling device

The ultrasonic assisted drilling device (UAD) mainly consists of three parts: a transducer, usually an ultrasonic horn and the drill bit. The transducer couples a vibration that is amplified by an ultrasonic horn and transmitted to a drill bit.
Langevin transducers are energy converters that transform electrical energy into an oscillation. The transducer contains a piezoelectric material that when under a voltage changes its dimension (inverse piezo effect). An example of a piezocrystal can be a clean quartz crystal where its SiO_4 tetrahedra are oriented such that under compression/tension a polarisation develops. When an alternating current is applied, the quartz contracts and expands. This movement can be controlled to gain on oscillation at the desired frequency (here 20 kHz) but also for the desired mode of vibration. Three main modes of vibration can be distinguished: a longitudinal (forwards and backwards oscillation), a torsional (rotating) and a flexural (bending) mode. Depending on the application, the transducers are designed to maximise each mode or a combination of them. For drilling, the longitudinal mode is used to gain a nanometre scale hammering into the rock.

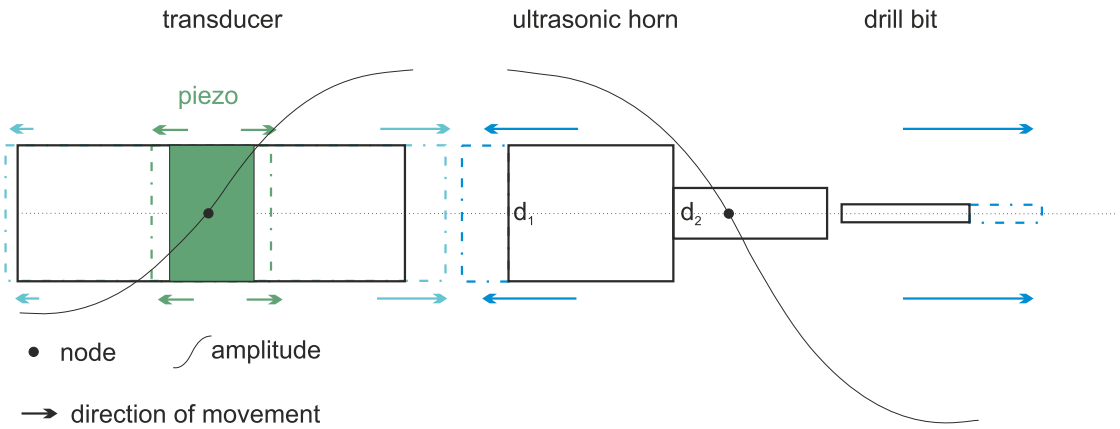

Figure 4.2: The vibration of the transducer is transferred to the ultrasonic horn and to the drill bit. The oscillation amplitude increases and is reaches its maximum at the tip of the drill bit. The minimum amplitude is shown with the node points.

When the driving frequency given by the piezoelectric crystal reaches the natural frequency of the transducer, the oscillation amplitude maximises; it reaches resonance. An example of resonance can be observed when looking at a person being pushed on a swing: an external force, here the pusher, will drive the swing in phase with the fall leading to the person on the swing achieving greater maximum height (amplitude).
In the transducer, a standing wave forms (a wave oscillating at the resonant frequency with constant phase) similar to a plucked guitar string. The standing wave is caused by the interference of the vibrations propagating in different directions within the transducer. The maximum amplitude (displacement of the piezoelectric crystal) is achieved by designing the parts of the transducer to resonate at $\frac{\lambda}{2}$ (Figure 4.2). This allows a minimum-amplitude

point (node) to be created half-way along the standing wave, in the middle of the transducer.
The transducer includes two masses that surround the piezoelectric crystal (a so-called *sandwich* transducer). The two masses can be made from different materials or have different weight or diameter in order to to produce a different acoustic impedance which changes the ability of sound to propagate in the material. By tuning these parameters, maximum energy can be transferred from the transducer in one direction (Figure 4.2).
The ultrasonic horn attached to the transducer amplifies the oscillation further while directing the oscillation over a smaller area. For a stepped horn (Figure 4.2) the increase in amplitude is given by the ratio of the two diameters $d1$ and $d2$ (Gallego-Juarez & Graff 2015). The increase of the amplitude or gain can be described as $(\frac{d1}{d2})^2$ for the step horn shown. The oscillation is then transferred to the drill bit that is connected to the horn. To remove the debris of the drilled material a rotation can be added to the whole assembly. A linear actuator moves the device constantly forward into the material.

Feedback signal for stone property characterisation
The idea behind the drilling tests is similar to cone penetration tests for soil, where a penetrometer with a cone shaped tip is forced into the soil at constant rates while the pressure is measured to deduce the properties of the soil. When drilling into the rock, the consumed power is monitored. The power consumption to maintain the oscillation while drilling varies depending on the physical properties of the drilled material. Next to the power consumption, the force experienced by the sample is measured. A reduced force indicates a material that is easier to penetrate and vice versa.

Components
The transducer used is a *L500 20 kHz half wavelength piezoelectric sandwich transducer* from *Sonic Systems*. A feedback control loop allows the frequency at resonance as well as the set oscillation amplitude to be maintained.
A Kistler force sensor (9321 B, shear and compression) and a position sensor (PS-C15M 200 PS-C15M Linear Potentiometer) are used. *PicoScope* records the data with a sampling rate of 5000 Hz. A linear actuator (Duff-Norton - LT225-1-300P) moves the device with a speed of 0.66 mm/s. A *Faulhaber DC motor* and later a *Maxon DC Geared Motor* (B72DB9E3BD8D) enable the rotation of the tool.

4.2.2 Data treatment

Power signal
A low pass filter (10 Hz cutoff frequency) is applied to the power signal (Figure 4.3). This enables a signal to be obtained without high frequency noise from other electronic parts.

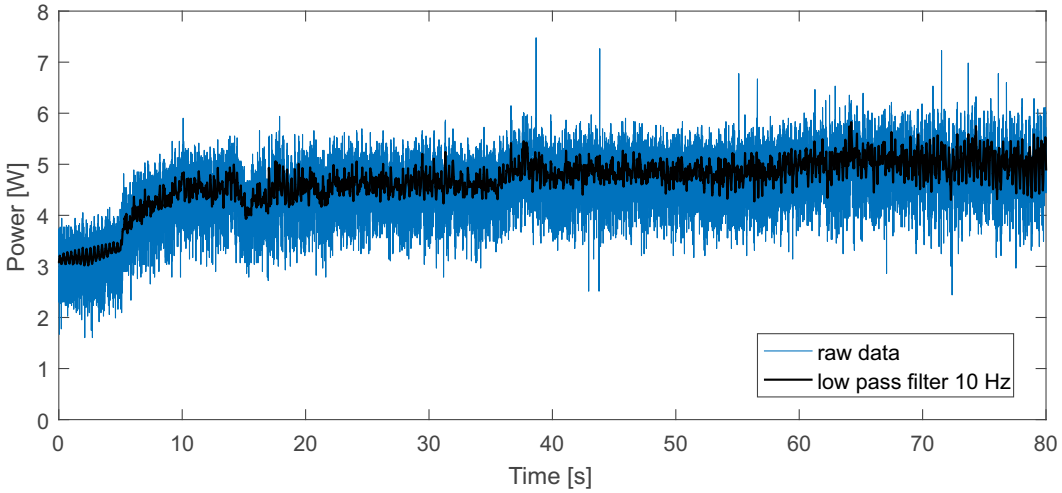

Figure 4.3: Low pass filter with cutoff frequency 10 Hz (black) applied on the recorded power consumption (blue).

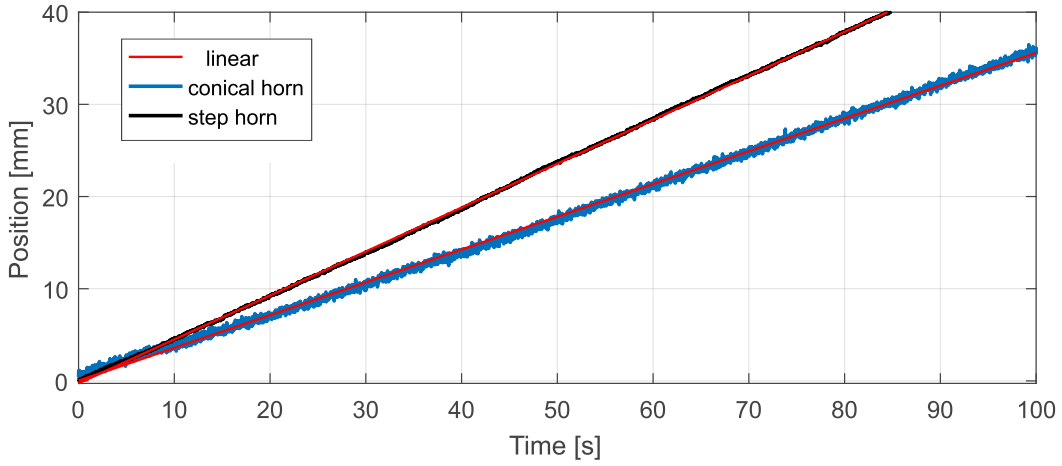

Figure 4.4: Position of the drill tool when penetrating a Cullalo sample with two different ultrasonic horns. In red is the linear regression of the measured position.

Furthermore a moving average of 40 for about 10000 data points is applied to the power signal for the figures that display five drilled holes to enable a better comparison.

Position of the drill tip

The position of the moving UAD of the tool is recorded while drilling. The position is then approximated with the linear regression to allow a less noisy plot of the position versus the power consumption (Figure 4.4). It can be seen that for two different horns the position variation is different. The step horn has a lower standard deviation of the linear regression with about 0.17 for the drilled Cullalo sample. The conical horn shows a standard deviation of 0.42. Also the rate of progress into the rock is different. For the Cullalo sample even though the same linear actuator settings were used, the progression rate for the step horn is 0.48 mm/s and for the conical horn 0.36 mm/s.

The recorded time, power and position are also down-sampled to 100 Hz from the previous sampling rate of 5 kHz. The recorded data were set to 0 when a force increase was measured. This should enable to set the most accurate start of the drilling.

4.2.3 Design method

The performance of the oscillating parts strongly depends on the geometry, material (mass and elasticity, shear and Poisson ratio) of the different parts; it is therefore necessary to model the designed horn and drill bit to check if they resonate at the intended transducer frequency with the desired mode of vibration.

Finite element modelling
Finite element modelling (FEM) can be used to predict and visualise the performance of the modelled parts before manufacturing. FEM creates a mesh of small elements approximating the structure of the parts, with which the corresponding vibrational modes of the parts can be estimated. The analysis was conducted with Abaqus which uses the 3D model of the parts designed in SolidWorks. Material properties such as density and elasticity are needed for the modelling of the vibration. The performance is analysed for linear perturbation and the analysed frequency window that contains the operating frequency of the transducer. A mesh of tetrahedras is created to simplify the shape of the components creating small *finite elements*. From the simplified shape, the deformation of the finite elements is approximated with the equation of motion in respect to the given constrains and interactions of the parts (Inman 2009). The results show the different modes of vibration for varying frequency and the location of the nodes. This is important to check if the desired mode of vibration matches the frequency of the transducer and any non desired modes overlap or are to close to the operating mode.

Impedance analysis
The electrical impedance of the device can be used to evaluate its performance. The impedance as a ratio of the excitation voltage (of the transducer/actuator) and the current drawn by the actuator will depend on its frequency. The resulting impedance spectrum shows at which frequencies peaks in the impedance appear, indicating resonance at those frequencies. For the designed longitudinal vibration the mechanical resonance is given by the electrical resonance. An *Agilent 4395A* is used for the impedance analysis.

Experimental Modal analysis
Experimental Modal analysis (EMA) investigates the movement of the manufactured tool to deduce the resonance frequency, mode shapes and the dynamic behaviour of the designed parts. It can be used to assess the accuracy of the analytical model of the FEM. EMA also enables testing the performance over time and dynamic environments. It can provide in-

formation about maintenance and is used in structural health monitoring (see Chapter 1). For more than one moving part (or degree of freedom) the mode shape describes the relative motion between the two parts. The resonance frequency of a two component system is never the same as one of its single components (Inman 2009). For the modal analysis the multiple degrees of freedom vibration is transformed into multiple single-degree of freedom vibrations.
An input excitation (such as a sine wave with constant amplitude swept across a frequency range) forces the investigated components to oscillate. The movement of the investigated tool or velocity is measured with a vibrometer. The vibrometer (CLV-3D Compact 3-D Laser vibrometer from Polytec) emits three converging beams that fall onto the surface of the investigated tool with a 12° angle to enable measuring three directions. The number of points measured by the vibrometer (marked with reflective tape) should be high enough to allow the identification of all mode shapes in the set frequency range. The grid of points was formed by four measurements for every 90° rotation of the tool and along 30 rows. The velocity of the designed parts to a single input is measured over a set frequency window. The frequency response function (FRF) describes the calculated response/magnitude to the set frequency window of each point. The magnitude of the FRF is gained from the power density functions (PSD) through the FFT of the measured velocity. The FRFs of all points for the resonance frequencies of the different mode shapes can be visualised spatially for the tool in ME'scopeVES (Mechanical Engineering Oscilloscope - Visual Engineering Series).

4.3 Development of the UAD tool

The section describes the development of the UAD tool including the design of the parts. The improvement of the assembly and a feedback signal to deduce the state of decay of rocks was one focus during the development. Special attention was given to the design and material of the drill bit that enables penetration into the abrasive sandstone with only little wear. FEM and EMA for the final parts are displayed. The design of a carving tip for the same device is briefly described. The section closes with the final prototype and its settings for best performance.

4.3.1 Ultrasonic percussive drilling

The project started with the use of an ultrasonic percussive drilling devices that was previously developed at the University of Glasgow (Li et al. 2017, Harkness et al. 2011). It was designed to penetrate and core rocks as part of a space exploration program. The Ultrasonic/Sonic Driller or Corer uses a free mass to oscillate chaotically between the horn and the drilling bit. The free mass intermittently gives this energy to the drill bit so that the rock is hit by strong impact events, drilling or hammering into the stone. Compared to

the constant hammering of the UAD at 20 kHz, the percussive drilling is characterised by high force impacts (Harkness et al. 2011). During the penetration, power is kept at a constant reference level (25 W) allowing a 10% variation through the integrated control system (Li 2015). The device is advancing through a linear actuator. The ultrasonic percussive drilling device showed a good performance for drilling sandstone including increased progression rates. A 3 mm diameter drill bit from *SINT* was used for drilling up to 3 cm into the rock. The device allows differentiation between sandstone types (Stanton Moor and Cullalo) when comparing the varying progression rate into the rock (Figure 4.5).

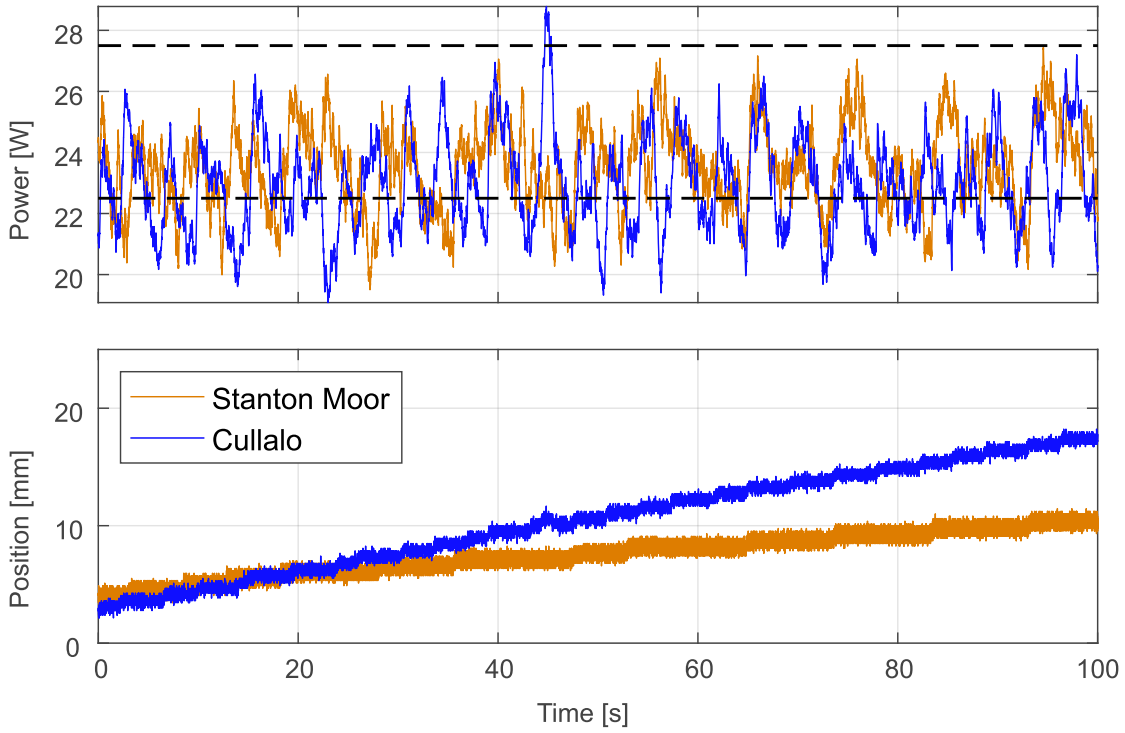

Figure 4.5: Ultrasonic percussive drilling: power consumption and drilling position of a Stanton Moor (orange) and Cullalo (blue) sample with a SINT 3 mm drill bit. The dashed line shows the allowed range of the consumed power (10%) around 25 W.

For the detection of small scale structural changes in the sandstones caused by weathering, the technique used shows several disadvantages. The impact force of the mass is non-linear (Wiercigroch et al. 2005). Thus using exerted force or power consumption during drilling as a feedback signal would make comparing between tests difficult. Small changes in the sample's physical properties might get lost by signals influenced by the movement of the free mass. The feedback control loop to keep the power at a certain range will not allow monitoring of differences in power consumption for changing rock properties and types. Using the progression rate as a feedback signal makes it hard to identify small scale structural changes in the rock.

Ultrasonic assisted drilling without percussion enables a 'cleaner' feedback signal. The next

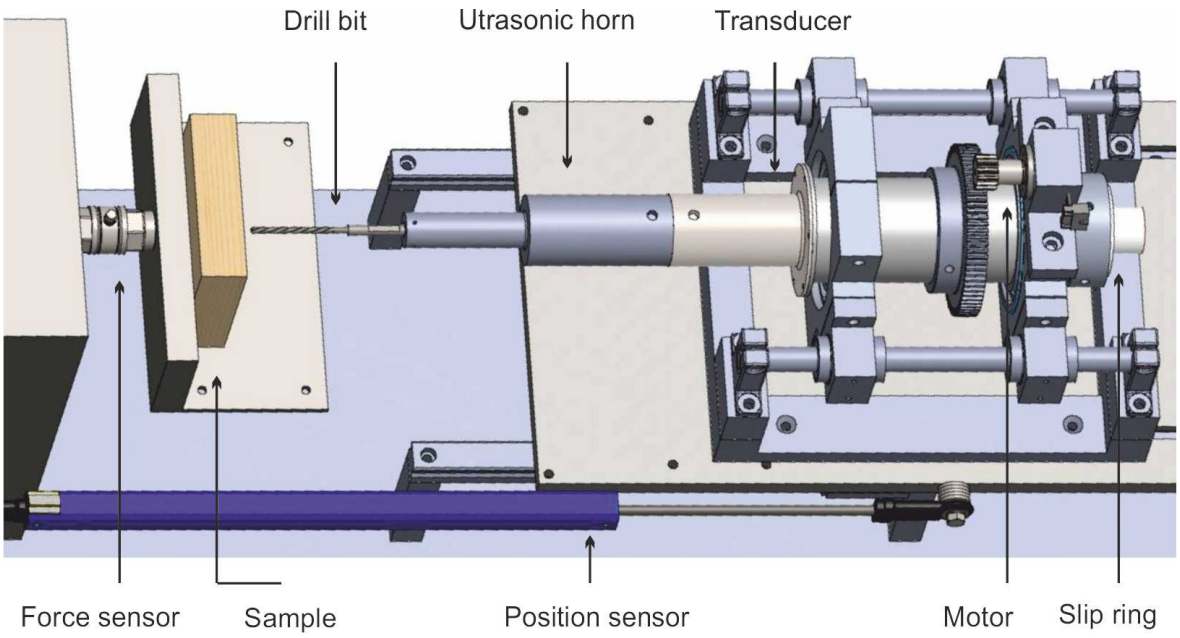

Figure 4.6: Assembly of the ultrasonic drilling tool (UAD) with the transducer, creating the oscillation, ultrasonic horn, amplifying the oscillation, and the drill bit at the tip of the horn (3 mm diameter). The tool is moved forward by a linear actuator to enable a constant penetration into the rock or by a constant weight on bit (not displayed). A position sensor detects the location of the drill bit.

steps focus on achieving a 'clean' signal for the power consumption to be used as a feedback signal that in turn can be used to assess the state of decay of the sandstone. In addition to the power consumption the impact force exerted on the sample is monitored.

4.3.2 Feedback signal

The setup of the ultrasonic drilling tool (UAD) was improved to gain an almost noise-free power consumption signal. Figure 4.6 shows the assembly, including the transducer, ultrasonic horn, drill bit, motor for rotation, a position sensor and a Kistler force sensor. The alignment of the tool and its drill bit can influence the power consumption. When a rotation is added to the design, a non-vertical penetration into the rock causes the power to oscillate at the given rotation speed. The alignment should be as straight as possible to allow the oscillating drill bit to penetrate the rock without any tilt.

Another key influence on the power consumption is the slip ring. A slip ring enables a signal transfer of rotating structures. Figure 4.7 a shows the power consumption during penetration of a Cullalo sample. In Figure 4.7 b the slip ring was replaced, a new motor was used that enabled a higher rotation speed, and the tool was aligned to enable a penetration of the rock without tilt or precession. These steps lead to an improvement compared to previous measurements with an oscillation in the power signal of up to 8 W with a low cost slip ring. A smaller oscillation in the power signal can still be seen and is correlated to the

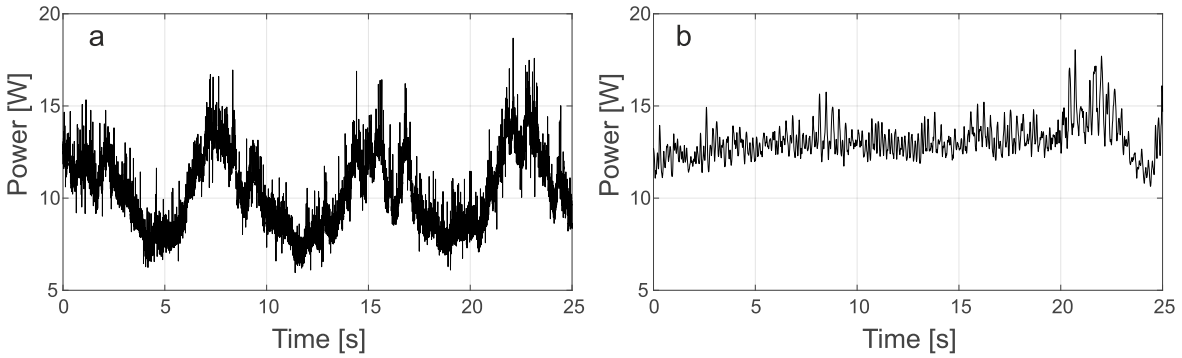

Figure 4.7: Power consumption for different setups when drilling a Cullalo sample. a: Previously used motor (14 rpm), slip ring and small tilt of the drill bit. b: improved setup with a new motor (200 rpm), new slip ring and aligned drill.

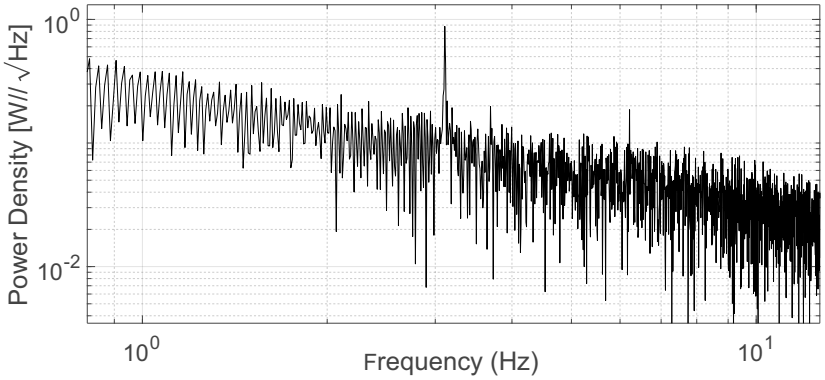

Figure 4.8: Spectrum of the oscillation in the power signal. The rotation speed from Figure 4.7 of the motor is 200 rpm. A peak can be identified around 3 Hz which is close to the rotation speed of 3.3 Hz.

rotation speed of 200 rpm around 3.3 Hz. When the FFT of the power signal is analysed a peak at about 3 Hz, close to the rotation speed, can be identified (Figure 4.8).
A pulley with an attached weight of around 20 N was used to move the drill forward. This has the advantage over a linear actuator in that when the sample is hard, progression into the rocks slows down or stops and the drill bit is less likely to break. On the other hand the progression rate into the rock changes and therefore the power consumption. If a harder layer in the rock is drilled, the progression rate into the rock might be slower but the power might not change enough to show a difference to enable a detection of that layer. The linear actuator was therefore chosen to overcome these problems and to enable practically constant speed of penetration into the rock for the slowest progression rate possible.

4.3.3 Drill bit

When penetrating abrasive stones such as quartz rich sandstone, the wear of the drill bits is a key factor for the development of a drilling tool; drill bits that are easy to exchange are crucial. Another challenge is the attachment of the tip to the horn: any gap caused by

Figure 4.9: Threaded shank cobalt drill bits with 3 mm diameter. a: new drill bit and used drill bit (b). The tip of the used drill bit wore down quickly.

a loose fit will influence the oscillation of the tool and will increase the build up of heat. The first approach for the drill bit of the UAD was using a PCD (poly crystalline diamond) tip with a HSS (high speed steel) drill bit from *SINT* that is provided when purchasing the DRMS (see Chapter 1). The drill bit was attached to the horn by press fit. The major disadvantage is that it can not be replaced easily. This was especially difficult after the bit overheated and then broke.

An aluminium collet holder was tried with the *SINT* drill bits. The teeth of the collet grip the drill bits and a matching ultrasonic horn, that allows the tool to resonate at 20000 Hz, was designed. The collet melted after the first application and could not be used again. The aluminium collet showed two main problems. Firstly, the aluminium might be too soft for ultrasonic applications; and secondly, when tightened, the jaws of the collet only grip the drill bit at three points. This leaves a small gap in between the jaws for a 3 mm diameter drill bit.

Bits with a threaded shank would allow a tight attachment and easy removal. Low-cost cobalt drill bits were purchased and a new horn was designed (Figure 4.9). After drilling 5 - 15 min, gaining a depth of max. 2 cm in softer rocks, the cobalt drill bits deteriorate quickly. The drill bits were dulled in less than a minute by sandstones like Stanton Moor (Figure 4.9 b).

The final drill bit was designed with a diameter of 3 mm and a PCD tip to decrease the wear effect of the abrasive sandstone. It was manufactured from *David Richards Engineering* and the PCD tip was supplied by *Element Six*. The properties of the PCD can influence the performance of the drill bit. The crystals have to be designed for the purpose of drilling to show the best performance (for example through grain size variation). The drill bit has a threaded shank (steel) and a body made of tungsten carbide (Figure 4.10). The PCD is

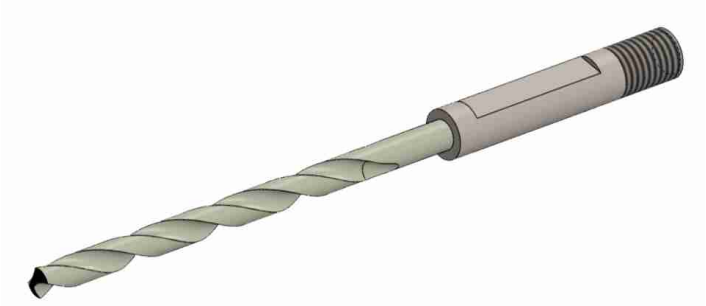

Figure 4.10: Drawing of the *David Richards Engineering* and *Element Six* drill bit made of tungsten carbide (SolidWorks). The threaded shank is made of steel and enables an easy grip to exchange the drill bit.

sintered (pressure and temperature deformation without melting) to the tip.
The specially designed drill bit is more expensive than the *SINT* bits but showed a better performance. A replacement of the tip was not necessary during the whole test series.

The performance of the *SINT* drill bit and the developed drill bit were evaluated. The exerted force on the sample was used to assess the wear of the bits. The drill bits were tested during conventional drilling with the DRMS for a Stanton Moor sample. The test settings were kept constant for both drill bits. The drill bits were clamped into the collet of the DRMS (see Chapter 1) and holes of 15 mm depth were drilled. The tool is moved forward with 10 mm/min and the rotation speed was set to 400 rpm.
With the given settings the *SINT* drill bit can be used to drill 26 holes with a total depth of 40 cm (Figure 4.11 a). The results highlights one of the main disadvantages of the *SINT* drill bit and CD. The drill bits have to be changed frequently when penetrating hard rocks. The wear does not allow a direct comparison of the exerted force for the different holes. Several laborious corrections with reference drilling during the tests or techniques such as the pilot hole technique can be applied to account for this effect (see Chapter1). Correcting the wear effect after the measurements of weathered material would be inaccurate as the wear depends on the material's state of decay. With increasing wear it gets harder to hold the handheld tool steady against a wall with leads to a variability in the force measurement. The same settings but the use of the developed drill bit enables drilling to a total depth of more than 75 cm (Figure 4.11 b). The test was stopped after 50 holes. The exerted force on the sample after 50 holes is still smaller than the exerted force of the *SINT* drill bit after 25 holes.
In Figure 4.11 c the average exerted force and the standard deviation for each hole are compared. With increasing depth drilled the standard deviation increases as well as the exerted force. The performance of the developed drill bit shows a reduction in exerted force by a factor of nearly 3.
When the shapes of the drill bits are compared before and after drilling (Figure 4.12), the

SINT bits look less worn than the developed drill bit, even though under the given setting the bit was not able to penetrate the rock anymore. The developed drill bit shows more abrasion, but nearly no loss in performance (Figure 4.12 d).
The test with the same settings was repeated with two more developed drill bits. These bits had been used previously for ultrasonic drilling to a depth of more than 50 cm for various rock types. When used in the DRMS, the performance of those drill bits was similar to the developed drill bit that had been used for the CD of only one hole. This result shows clearly that ultrasonic drilling has a lower wear effect on the drill bits when penetrating sandstones than CD. Although when comparing the surfaces of the drill bits (Figure 4.12 d+e), it can be seen that the PCD shows a bit more damage after ultrasonic drilling than after conventional drilling. The shape or material loss of the used drill bits can not be used to predict the performance of the drills. All developed drills performed well after several tests despite looking worn. In contrast the *SINT* drill bit stopped working with the 100 N limit of the DRMS (it also looked worn).

4.3.4 Ultrasonic horn

Every change in geometry of the oscillating parts will alter their resonance frequencies. In the process of finding the best drill bit, several horns were designed to match the resonance frequency of the transducer and the used drill bits. Variation of the length of the designed parts is the easiest way to influence the resonance frequency.
Described below is the FEM and EMA of the final two horns (both Titanium, Ti-6Al-4V). A step horn was used for its simple design and gain (see Section 4.1). A conical shaped horn was also tested to force the tip to have a smaller gain. This is beneficial when testing new drill bits to have a smaller tip movement and therefore reduce the risk of breaks when drilling hard rocks.
Figure 4.14 shows the resonance frequencies of different mode shapes at the tip of the tool. The FRF is produced for every measured point (see Section 4.2.3) and forms the input for a 3D model of the tool's movement. This allows one to deduce the proximity of mode shapes of the tool. At the transducer frequency at 20 kHz the second longitudinal mode (2nd L-mode) can be observed as intended. No overlapping of modes can be identified. The 3rd and 4th L-mode are also not overlapping.
The results of the EMA are compared to the model that was designed (Figure 4.15). The modeled resonance frequency for the second longitudinal mode of the step horn shows good correlation to the measurements. The 2nd L-Mode for the conical horn is a bit lower than modeled but still worked well for the designed drill bits.

The impedance analysis showed very similar results for the five developed drill bits (Figure 4.16). The small difference may be due to different tightening of the horn or drill bit.

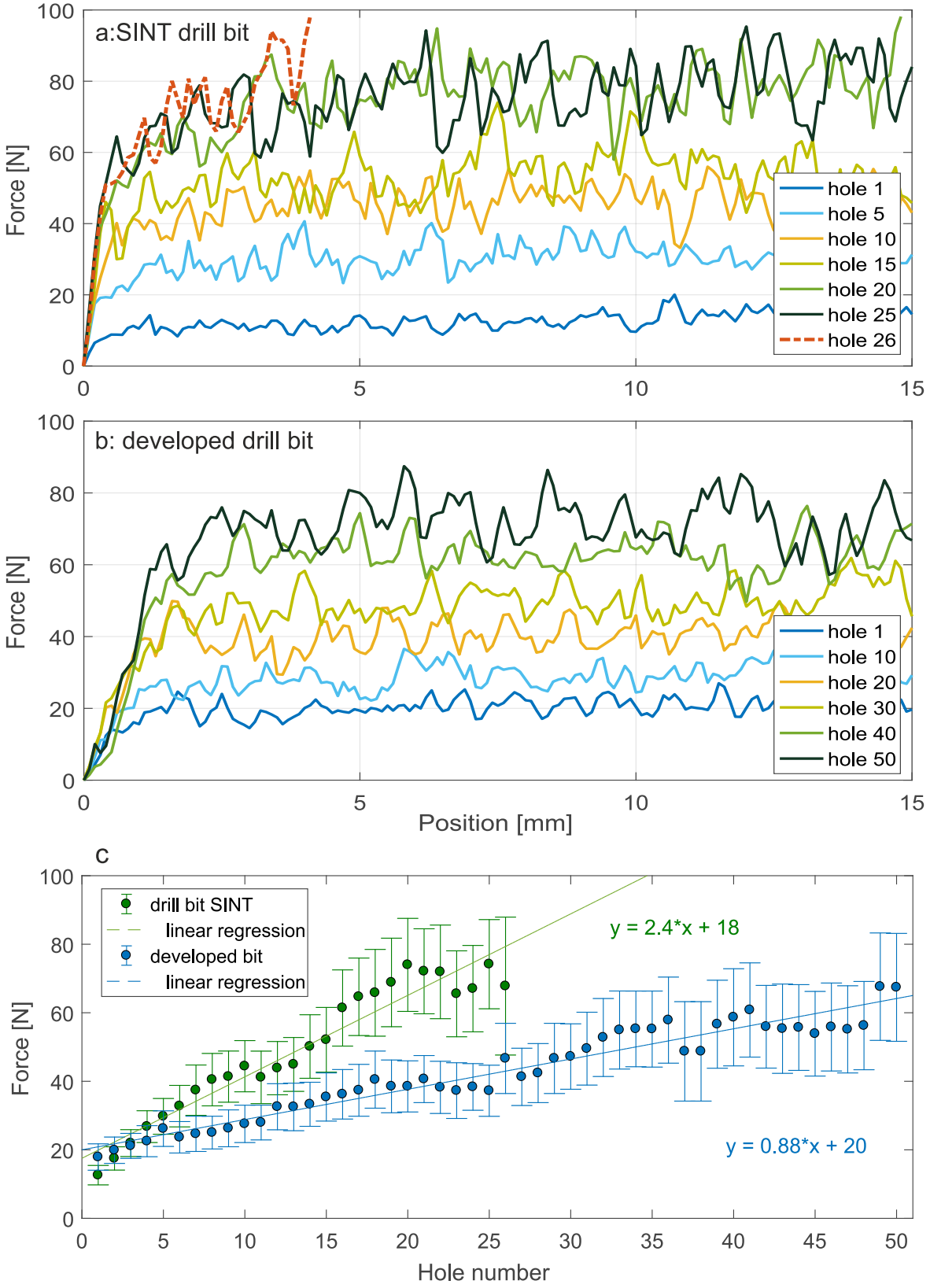

Figure 4.11: Wear of the *SINT* drill bit and developed drill bit for a Stanton Moor sample during conventional drilling. The wear is assessed through the exerted force on the sample. a: performance of the *SINT* drill bit. At hole 26 the DRMS force limit of 100 N was reached. b: performance of the developed drill bit. c: comparison of the two drill bits. The data points show the average force during drilling of one hole and the standard deviation.

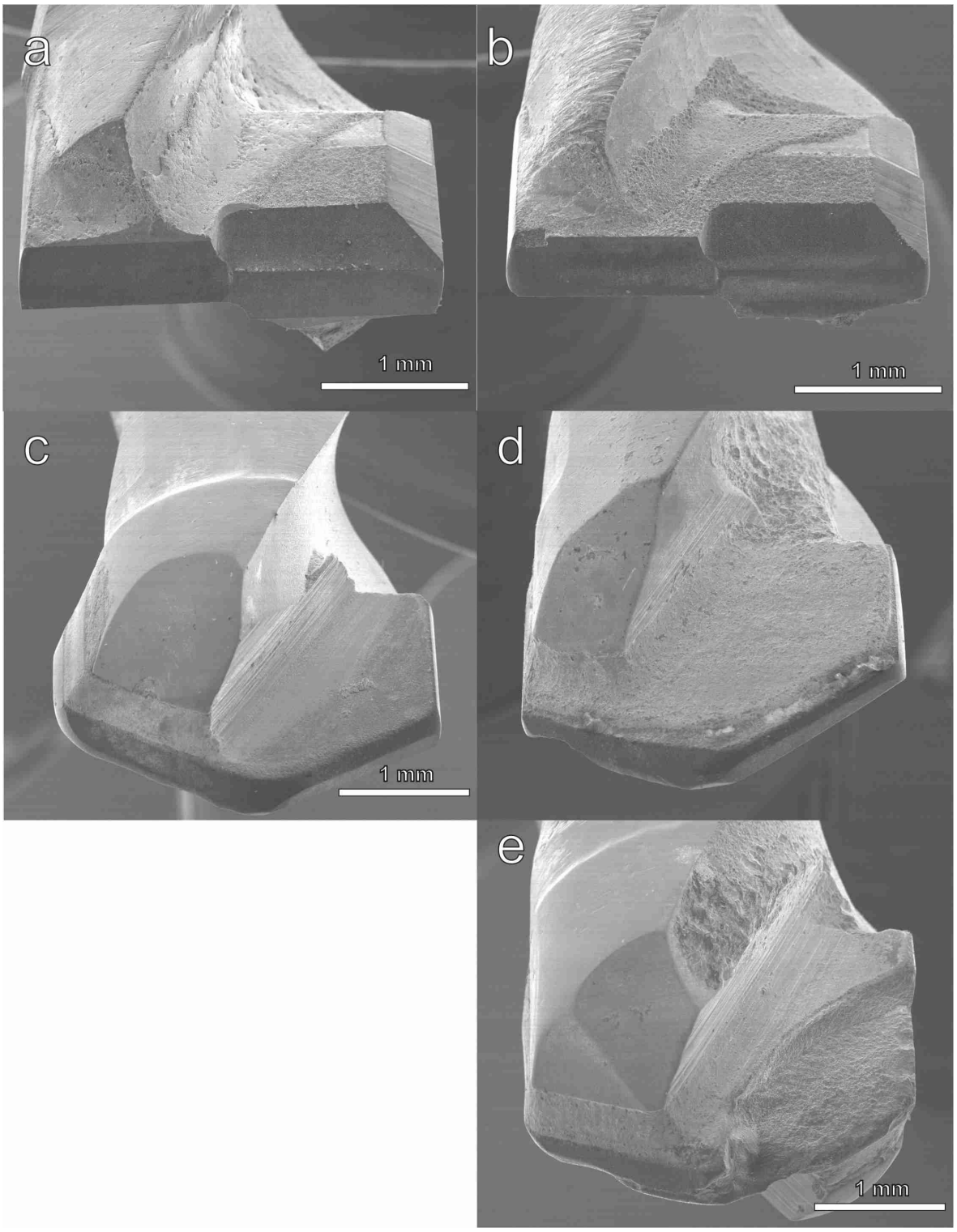

Figure 4.12: SE images of the *SINT* drill bit (a: new and b: after drilling 40 cm) and the developed drill bit (c: new, d: after drilling 75 cm and e: after ultrasonic drilling of >50 cm).

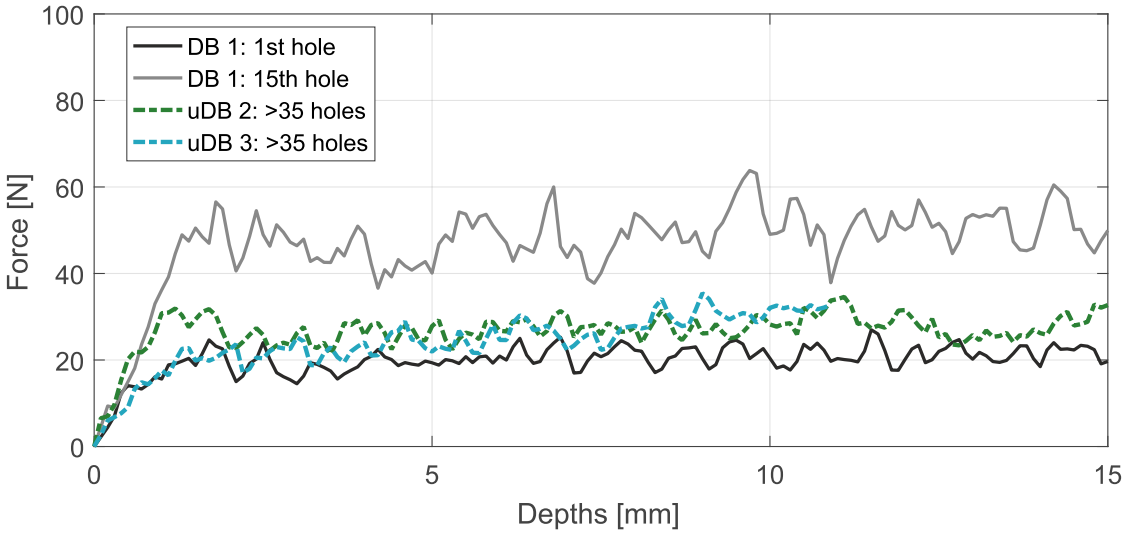

Figure 4.13: Exerted force on a Stanton Moor sample with different drill bits. The developed drill bit (DB 1) was used for conventional drilling of several holes with a depth of 1.5 cm. In black is the exerted force during drilling the first hole. The dashed lines show two of the same developed drill bits that had previously been used for ultrasonic drilling (uDB 2 + 3) of more than 50 cm in total. When used in the DRMS for conventional drilling, these used drill bits show a similar exerted force as the new drill bit (DB 1).

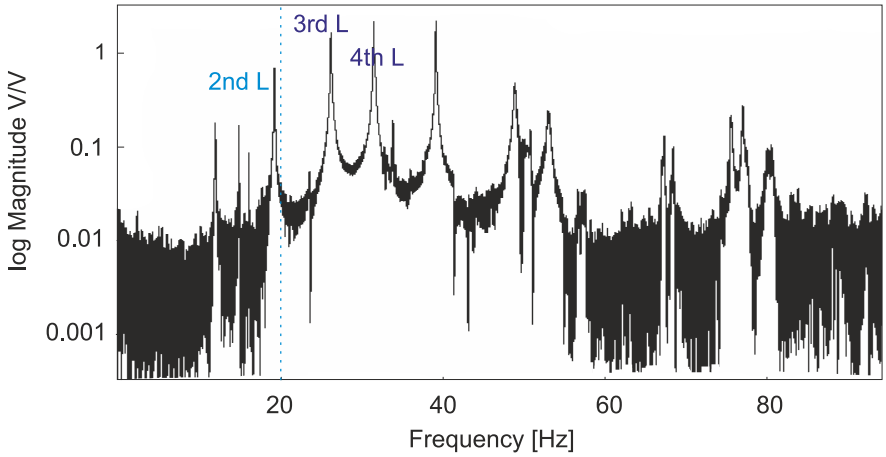

Figure 4.14: FRF of the tool tip showing the mode shapes at different frequencies. In blue the transducer frequency close to the second longitudinal mode (2nd L) followed with a large distance by the third and fourth longitudinal mode (3nd and 4th L).

Additionally, some drill bits showed a different flute orientation.

The final setup of the ultrasonic drilling device with the designed step horn and drill bit is displayed in Figure 4.17. The ultrasonic horn and drill bit can be changed easily.

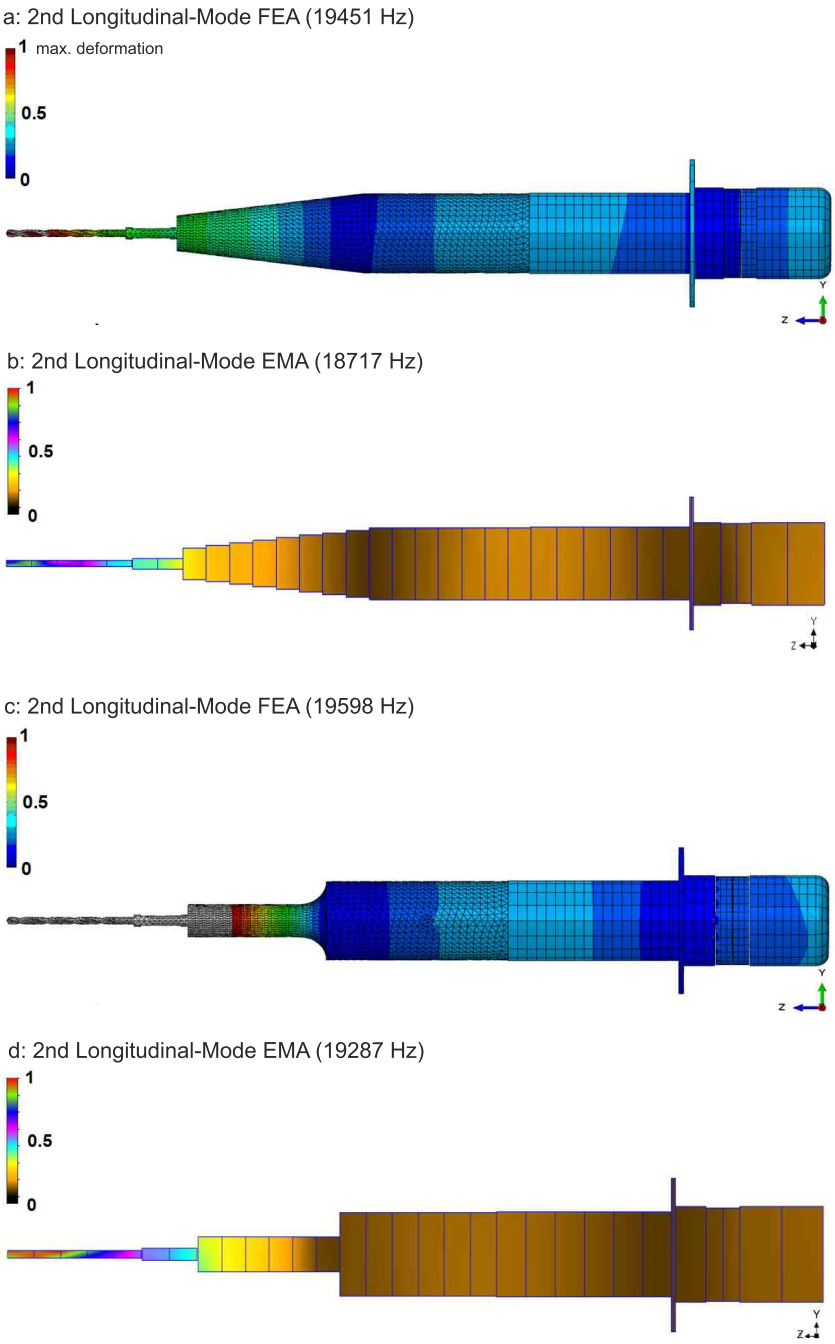

Figure 4.15: Comparison of the Finite Element Analysis and the Experimental Modal Analysis of the conical horn (a and b) and the step horn (c and d) in Abaqus and ME'scopeVES. The colour scale shows the deformation of the tool in three dimensions.

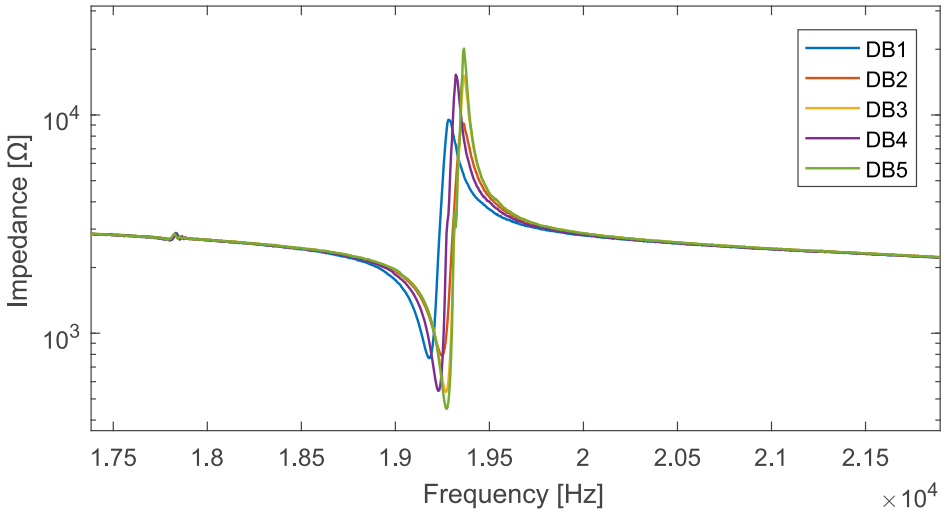

Figure 4.16: Impedance analysis of the different drill bits for the step horn.

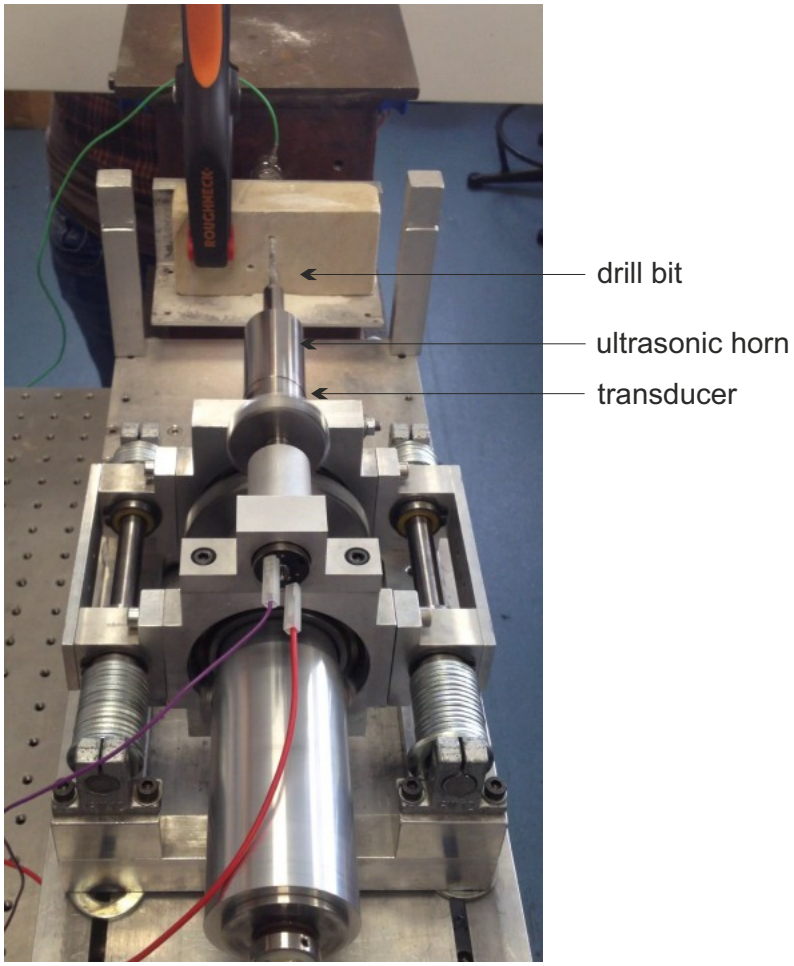

Figure 4.17: Final setup of the ultrasonic drilling tool. The tool is moved forward by a linear actuator to enable a constant penetration into the rock. A position sensor detects the exact location of the drill bit (both below the tool).

4.3.5 Carving

An exchangeable carving tip was designed for the developed horn and transducer (Figure 4.18). The carving tip would be beneficial in restoration works for example when removing mortars. The tool also enables small scale carving and was tested on a Locharbriggs sandstone. The prototype tip was made from titanium.

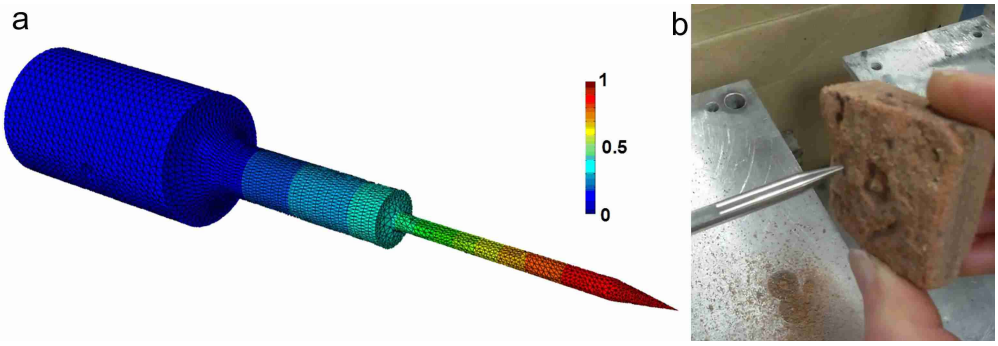

Figure 4.18: Exchangeable carving tip for the already designed step horn. a: Design in Abaqus showing longitudinal oscillation. b: The carving tip (titanium) was tested on a Locharbriggs sandstone.

4.4 Results and discussion of rock testing

The UAD was tested on different building materials (see sample description in Chapter 2). The findings can be summarised as follows:

1. Operational settings can be consistent for varying rock types (with different UCS)
2. UAD enables penetration and distinguishing of hard and soft/brittle rocks
3. Confirmed low average force exerted on the sample
4. Power consumption can be used for identification of sub-surface structural properties (such as porosity or depth of weathering)
5. There is an increase in power consumption as the hole deepens

4.4.1 Drilling settings

The rotation speed and oscillation amplitude was varied to identify the strongest response in power consumption to changes in the sample with two drilling tests. The settings should also be applicable to a variety of building stones. Materials of different compressive strength were considered to enable a comparison between the materials given the same operational conditions.

A Cullalo sample was drilled with varying oscillation amplitudes (2.1 µm, 2.5 µm and 5 µm) and a varying rotation speed of 100 rpm and 200 rpm. The used samples were drilled perpendicularly to bedding. The linear actuator moved the drill with the slowest speed possible (0.6 mm s^{-1}) into the rock. The Cullalo sample included a clearly visible clay layer of a few millimeters after 1 to 2 cm. This layer was used to induce a change in power consumption. Three trends can be identified while drilling the Cullalo sample (Figure 4.19): The power consumption is up to four times greater when maintaining an amplitude of 5 µm. For 2.1 µm, the smallest amplitude, the change in power consumption is the highest while drilling the clay layer (Figure 4.19 b). A decreasing motor rotation increases the power consumption by at least 10 %. Drilling without rotation is possible, but uses more power (up to three times) the further the drill penetrates into the rock and even stalls for a few seconds.
Although the clay layer is not homogeneous, one can deduce that for a Cullalo sample the smallest oscillation amplitude results in the best sensitivity to detect an inhomogeneity in the rock. The rise in power consumption is most likely caused by the porosity increase due to the increased amount of clay. The clay layer is drilled at different positions and the 5 µm run is repeated a third time to exclude any possible gaps within the clay layer. The 5 µm does not show any significant changes in power consumption while drilling. The change in rotation speed did not show important differences and was therefore kept at 200 rpm for the following tests to allow a better comparison to the conventional drilling tool.
The next experiment penetrates three sandstone types stacked behind each other. The samples include a Cullalo sample (18% porosity and an uniaxial compressive strength (UCS) of 49 MPa) and a Scotch Buff sample with similar physical properties (18% porosity and an UCS of 45 MPa). A St. Bees sample was used as a very hard sample (20% porosity and an UCS of 79 - 100 MPa). The rotation speed is kept constant at 200 rpm and the oscillation amplitude is varied. Three runs with 2.1 µm followed by the three runs with 2.5 µm and two runs with 5 µm were undertaken. The test run with 5 µm amplitude had to be interrupted when drilling St. Bees. After the second run with 5 µm amplitude the drill bit broke. A 5 µm oscillation amplitude is therefore not suitable under the given test settings to be used for hard rocks. As seen above it also consumes nearly five times more power.
Figure 4.20 shows that the linear actuator does not proceed as linear as expected for the three different sandstone types. A position sensor is therefore useful to provide the accurate positions instead of using the position calculated by the speed of the linear actuator.
Figure 4.21 shows the power consumption for an oscillation amplitude of 2.1 µm. The three sandstone samples can be distinguished. The power consumption is the highest for St. Bees, which has a high UCS. The power consumption is on average 2 W higher for Cullalo than Scotch Buff and shows more variation, which shows the greater inhomogeneity of the sample (Figure 4.21).

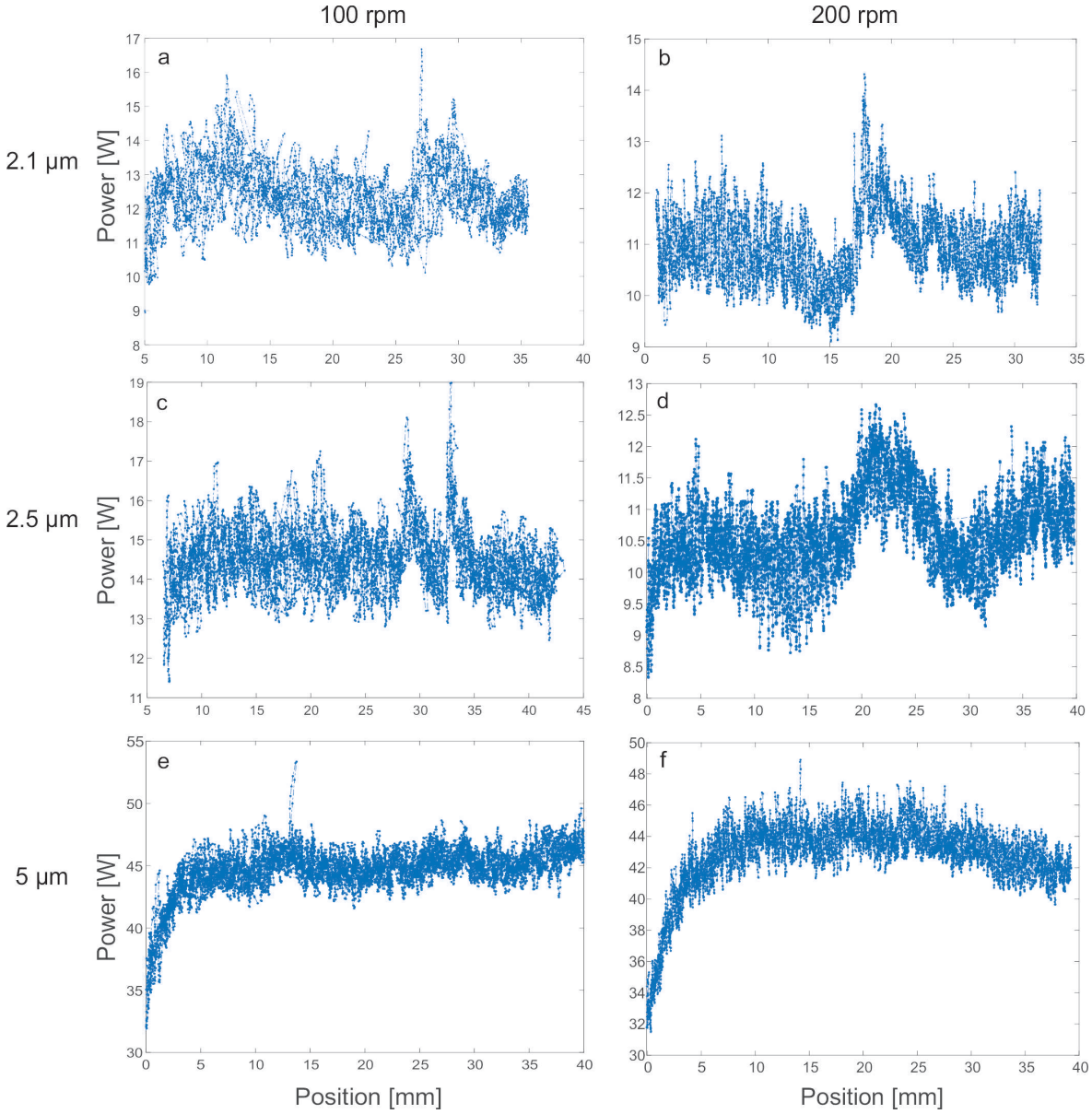

Figure 4.19: Power consumption of a Cullalo sample drilled perpendicular to the bedding with a clay layer of up to 10 mm. The oscillation amplitude is varied (2.1 µm, 2.5 µm and 5 µm) as well as the rotation speed (100 rpm and 200 rpm). The clearest peak during drilling can be seen in *b* for an amplitude of 2.1 µm and a rotation speed of 200 rpm. An amplitude of 5 µm does not show any changes in power consumption while drilling.

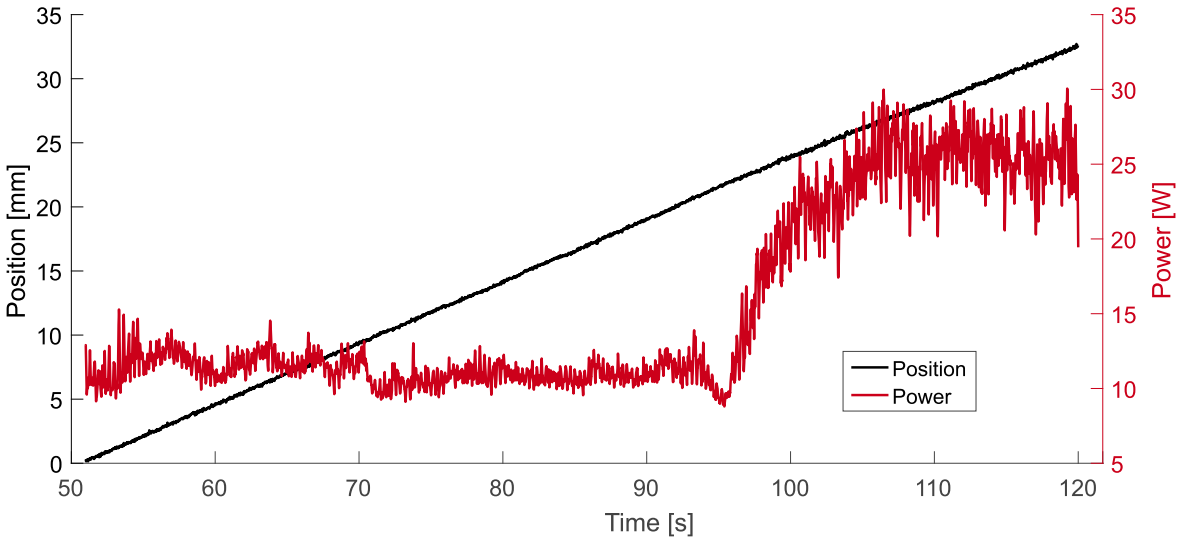

Figure 4.20: Three stacked sandstones drilled for 120 s. In red is the power consumption for an amplitude of 2.1 µm. In black is the position measured by the position sensor. For the last 25 s the linear actuator advance with a slower speed though it is set to a constant movement of 0.6 mm/s.

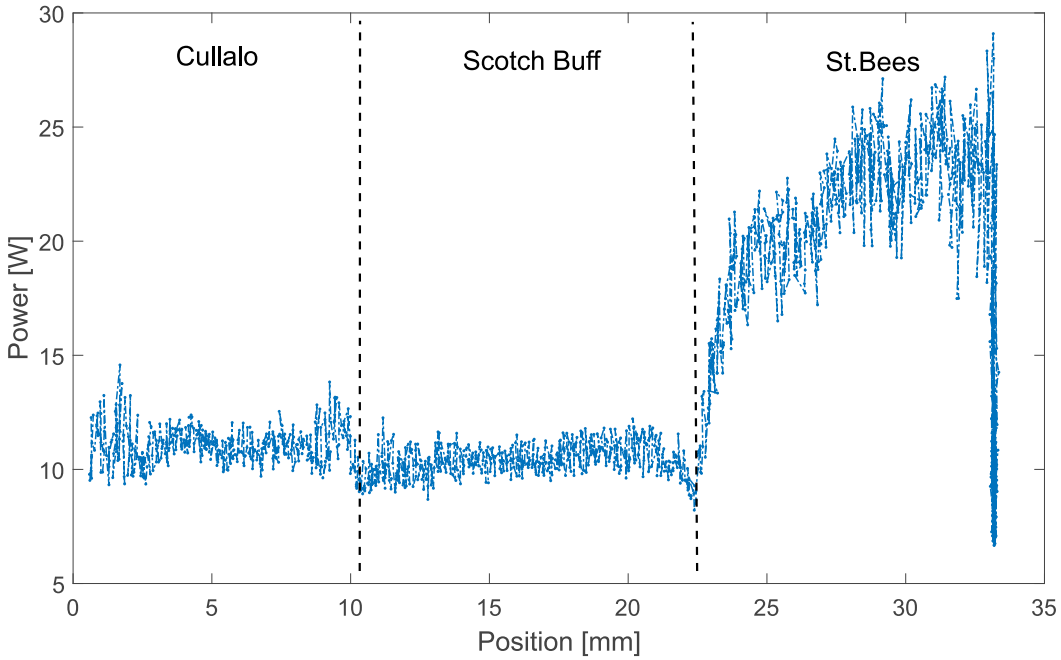

Figure 4.21: Three sandstones samples drilled stacked to each other. The graph shows the variation of power consumption for the different sandstone types during a test run with with 2.1 µm oscillation amplitude and a rotation speed of 200 rpm.

4.4.2 Weathered samples

Three sandstone samples and one carbonate rock were weathered artificially with NaCl or Na_2SO_4 to create a salt layer or damage below the surface of the sample (cryptoflorescence). The samples and the methodology are described in Chapter 2. Five holes were drilled into each sample including a reference sample of each stone type next to the two artificially weathered samples. The depth of weathering and the performance of the UAD (with two different ultrasonic horns) and CD with the DRMS (see Chapter 1 for DRMS) was investigated.

The samples where cut along the drilled holes and the depth of weathering, usually a clearly visible gap or bright accumulation of salt, was investigated by studying an image of the section (Figure 4.22). The measurement from the section is an estimation as the cut shows only the depth of weathering at the centre of the hole. The tools can therefore record a change before it is visible in the image. Salt accumulation can not always be identified well visually, but the visual identification provided a quick localisation of the weathering.

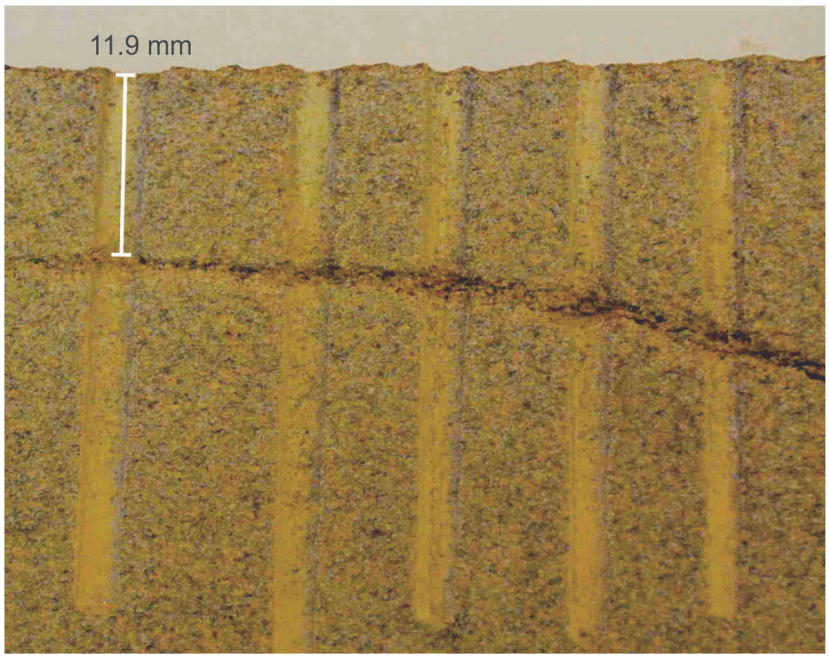

Figure 4.22: Stanton Moor sample treated with Na_2SO_4. The salt crystallisation forced a gap of a few millimetres into the sample. Five holes were drilled (see Figure 4.25) and the sample was cut along the axes of the holes.

Figure 4.23 shows an example of the drilled Stanton Moor sample seen in Figure 4.22. The power consumption drops when the gap caused by the salt expansion is reached and increases again after the gap when the stone is drilled. A very similar result can be obtained from the DRMS where the exerted force decreases when the gap is reached. The depth of weathering is not constant and varies for the individual hole as seen in Figure 4.22.

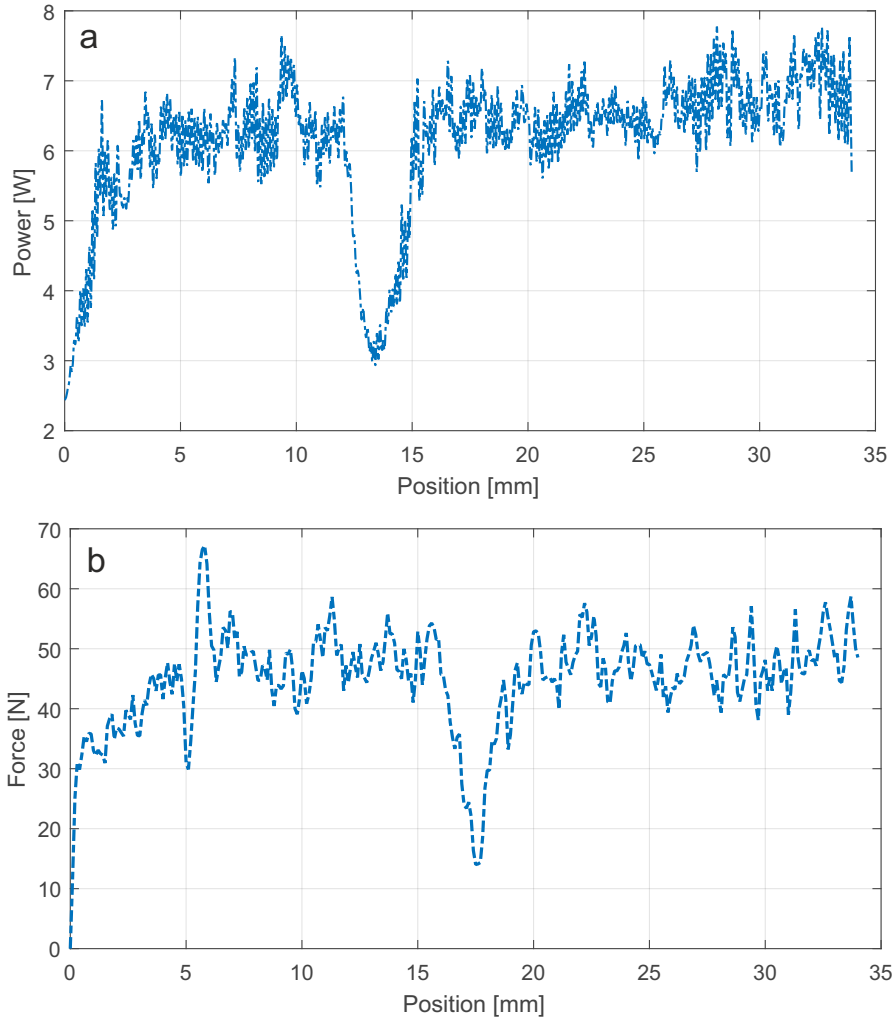

Figure 4.23: Measuring the depth of weathering from a Stanton Moor sample (Figure 4.22). a: UAD drilled with 200 rpm and a progression rate of 36 mm/min and b: DRMS drilled with 200 rpm and a progression rate of 10 mm/min.

The difference of the observed depth of weathering and the measured depth of weathering is compared for the UAD and the DRMS. The average difference of measurements for the different drilling techniques is summarised in Table 4.1. The mean difference for all investigations is below 1 mm which shows that the techniques can be used to compare the actual weathering depth with the tools under investigation. The high standard deviation and high mean values for the Na_2SO_4 treated samples are caused by the difficulties in observing the weathering in some samples. Figure 4.24 shows the differences of the measured depth by the tools and the observed depth for the individual holes. For the DRMS more negative differences appear. This shows that the DRMS detects the decay earlier than the deduced depth of weathering through the image analysis (Figure 4.24 b). It needs to be considered that the position of the tip or the depth of drilling in the DRMS is calculated from the drilling speed. The drilling speed is designed to be constant, but can show variation especially for hard materials.

Table 4.1: Average difference of weathering depth ($\mu(\Delta)$) measured with the UAD (conical horn or step horn) or DRMS to the observed depth of weathering.

Device	Treatment	$\mu(\Delta\ D)$	σ_x
UAD (conical)	NaCl	0.36	0.24
	Na_2SO_4	0.48	0.53
UAD (step)	NaCl	0.46	0.48
	Na_2SO_4	1.7	1.43
DRMS	NaCl	0.3	0.2
	Na_2SO_4	1.7	1.05

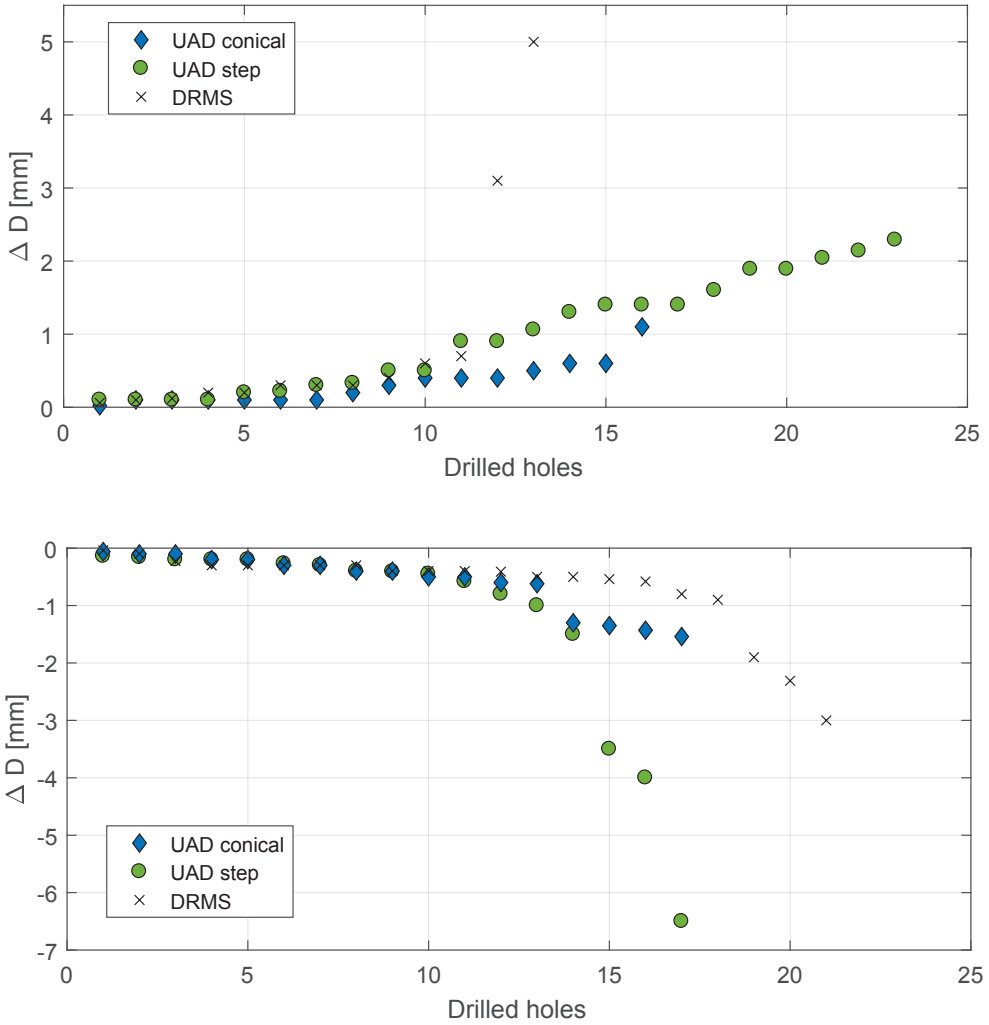

Figure 4.24: Comparison of the two techniques (DRMS in black and UAD in blue for the conical horn and in green for the step horn). Difference in depth of weathering ($\Delta D = D_{drilling} - D_{image}$) of the drilling technique ($D_{drilling}$) and the observed depth of weathering from the image analysis (D_{image}). Differences close to 0 show a good correlation of the drilling technique and the image analysis of the weathering depth. a: positive difference: The depth of weathering seen in the image could could be identified before the drilling technique measured any decay. b: negative difference: The drilling technique localised the damage before anything could be seen in the image analysis.

For the step horn, the weathering depth from the image analysis was mainly identified before the step horn measures damage (Figure 4.24 a). The conical horn shows a good correlation of the measured and observed depth of weathering. The step horn and DRMS show differences with outliers that can be quite high. This comparison shows that the depth of weathering can be measured quite well with an average overall difference of 1 mm for the DRMS and 0.75 mm for the UAD (from Table 4.1). The quality of the observed depth of weathering (image analysis) should be treated carefully as this was not a chemical or physical analysis. The outliers are very likely caused by hard to identify structural changes in the rock and not by the tool inaccuracy. The outliers also cause the high standard deviation. The tools furthermore identified areas of structural changes that could not be identified visually. Both tools allowed a good identification of the rock's damage, porosity or UCS in the three examples.

Figure 4.25 a shows the power consumption for the five holes drilled with the UAD into the weathered Stanton Moor sample. With this approach the damage seen in the section of the sample (Figure 4.22) can be located and the crack or gap in the sample can be mapped clearly. The average power consumption for each drilled hole stays constant around 6 W with a variation of ± 1 W (Figure 4.25 b).
The results of all drilled samples with the UAD and DRMS are displayed in the Appendix (B). The average power consumption for each sample, including the five holes, was calculated to compare the performance of the two ultrasonic horns. The conical horn has a lower power consumption than the step horn (Figure 4.26). The standard deviation of the power consumption for the drilled reference samples is 1.1 W for the step horn and a bit higher for the conical horn with 1.2 W. Three more references samples were investigated to add two more samples with high UCS (Clashach and St. Bees) and a soft halite sample.

The force exerted on the samples was analysed using the DRMS and the two ultrasonic horns. The step horn shows an increased variation of force on a halite and a Stanton Moor sample compared to the conical horn (Figure 4.27 and 4.28). The conical horn reaches partially higher values than the step horn. When analysing the exerted force of the ultrasonic drilling tool, it has to be considered that the force was recorded with a sampling rate of 5 kHz. That is only a quarter of the oscillation of the tool. It is therefore possible that some force values might be actually higher. The recorded force is an average at 5 kHz.
As mentioned in Section 4.2.2, the conical horn also showed a higher variation for the progression rate. The step horn would therefore be a better choice although the conical horn does not have significant disadvantages.

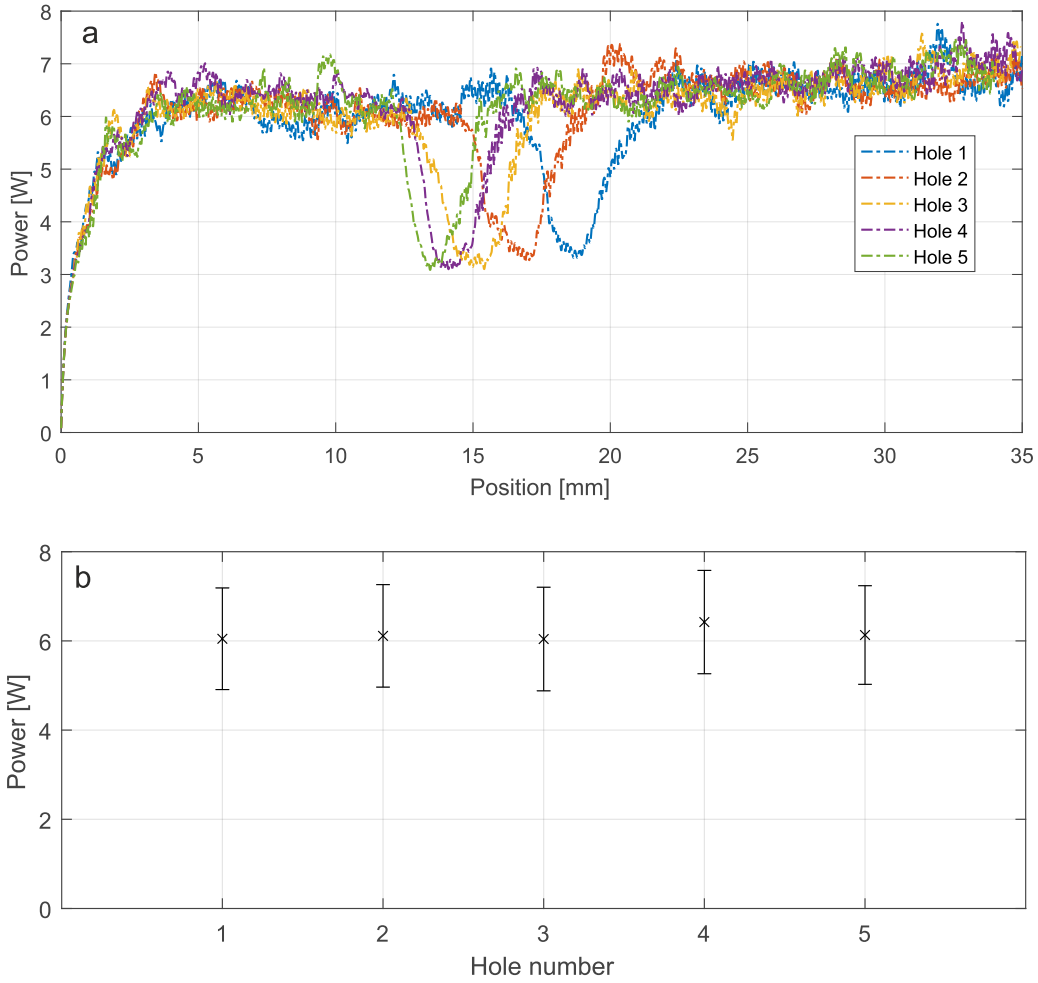

Figure 4.25: Five holes drilled with the UAD into the weathered Stanton Moor sample with a rotation speed of 200 rpm and a progression rate of 36 mm/min. a: for an easier comparison a moving average is applied to the power signal next to the 10 Hz filter (Section 4.2.2). b: the average power consumption for each hole is displayed with the standard deviation calculated from the 10 Hz filtered data.

The constant exerted force for conventional drilling is clearly higher for the halite sample (Figure 4.27 a). The operational settings were kept as similar as possible although the ultrasonic tool advanced even quicker into the rock. The DRMS uses a progression rate of 10 mm/min whereas the slowest progression rate of the UAD was set to 36 mm/min. The actual progression rate varies for the UAD depending on the rock type.

For the DRMS the position is calculated by the set progression rate and therefore might not actually be constant as well. The DRMS has a sample rate of 10 Hz and also uses a moving average.

For the Stanton Moor sample the rotation speed of the DRMS had to be increased to 400 rpm. Figure 4.28 shows the increase in force due to the tool wear when drilling only three holes. The average exerted force of the DRMS is still higher than the ultrasonic tool. It should be even higher when the drilling with 200 rpm would be possible. It can therefore be con-

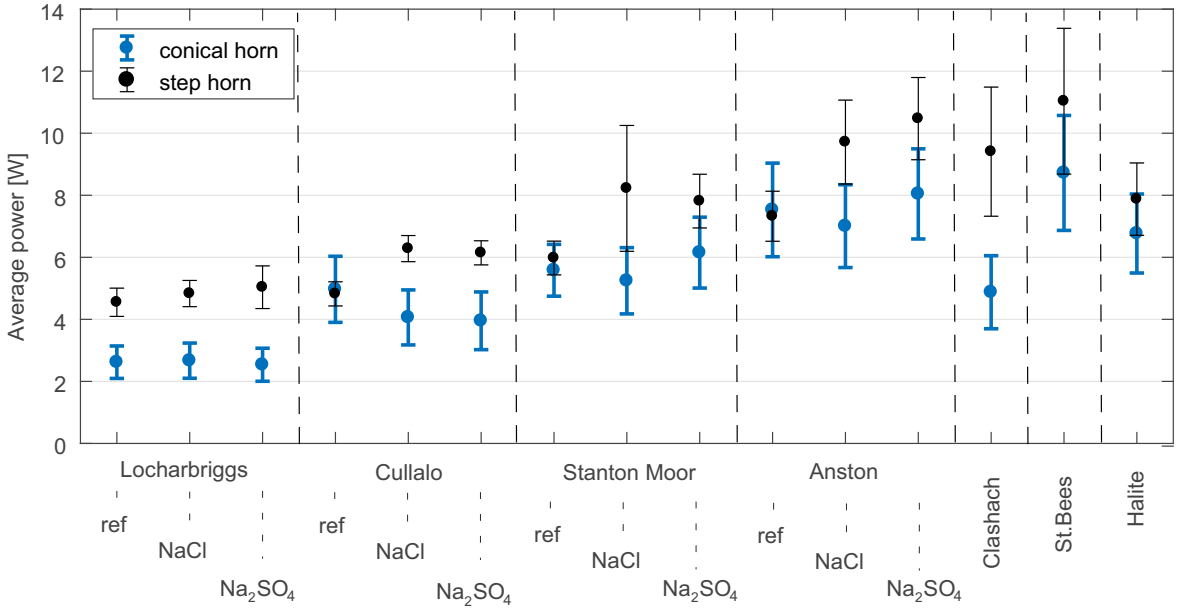

Figure 4.26: The average consumed power consumption for the two types of ultrasonic horns and the rock samples. In blue is the average power consumption and the standard deviation for the conical horn and in black, the step horn. In addition to the described artificially weathered samples a Clashach, St. Bees and halite sample were investigated.

cluded that the exerted force on the sample for ultrasonic drilling is lower than conventional drilling for all used samples. For the halite this could be even up to two times less force. Considering the oscillation of the tool, it is difficult to put actual values on the exerted force, but the slower progression rate of the DRMS decreases the difference of the exerted force of the two tools. Therefore the average force of the UAD is definitely significantly lower than the DRMS.

The UAD showed a good performance for the detection of structural properties of building stones. The exerted force on the sample is lower than the conventional drilling tool of the DRMS and the power consumption can be used as another feedback signal to map decay in rocks. The increased sampling rate and easy penetration of hard rocks as well as maintaining the same settings for different rock type are also advantages of the tool. Below some difficulties of the UAD are listed that showed up during the tests.

For one Na_2SO_4 treated Locharbriggs sample the gap caused by the salt expansion was not clearly detectable (Figure 4.29). The power did not decrease enough to reveal a definite identification. The exerted force on the sample had to be used to definitely locate the gap in the rock. This problem did not show up frequently in other samples and could be explained by a misalignment of the tool while drilling or blocked removed debris. The rock also split into two halves along the large gap, which could have loosened one of the pieces thus causing it to move when the tool tried to penetrate it.

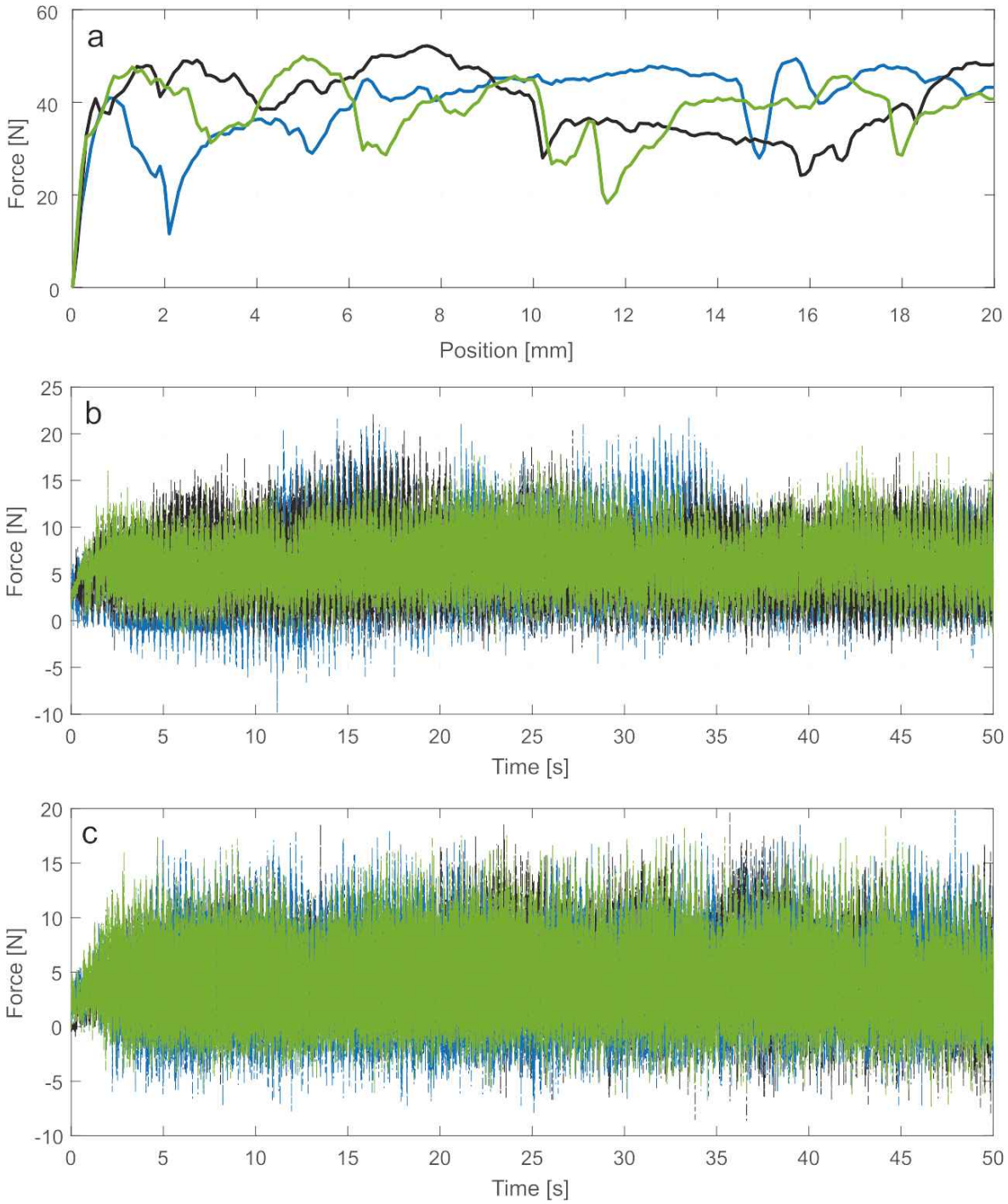

Figure 4.27: Force exerted on a halite sample when drilling. The rotation speed was set to 200 rpm for all tools. The progression rate of the DRMS was set 10 mm/min and for the UAD to 36mm/min. a: three holes drilled with the DRMS. b: three holes drilled with the conical horn of the UAD and c: three holes drilled with the step horn of t he UAD. The sampling rate of the force is 5 kHz for the UAD. Some information is therefore lost given the tool oscillates at 20 kHz. The DRMS sampling rate is 10 Hz.

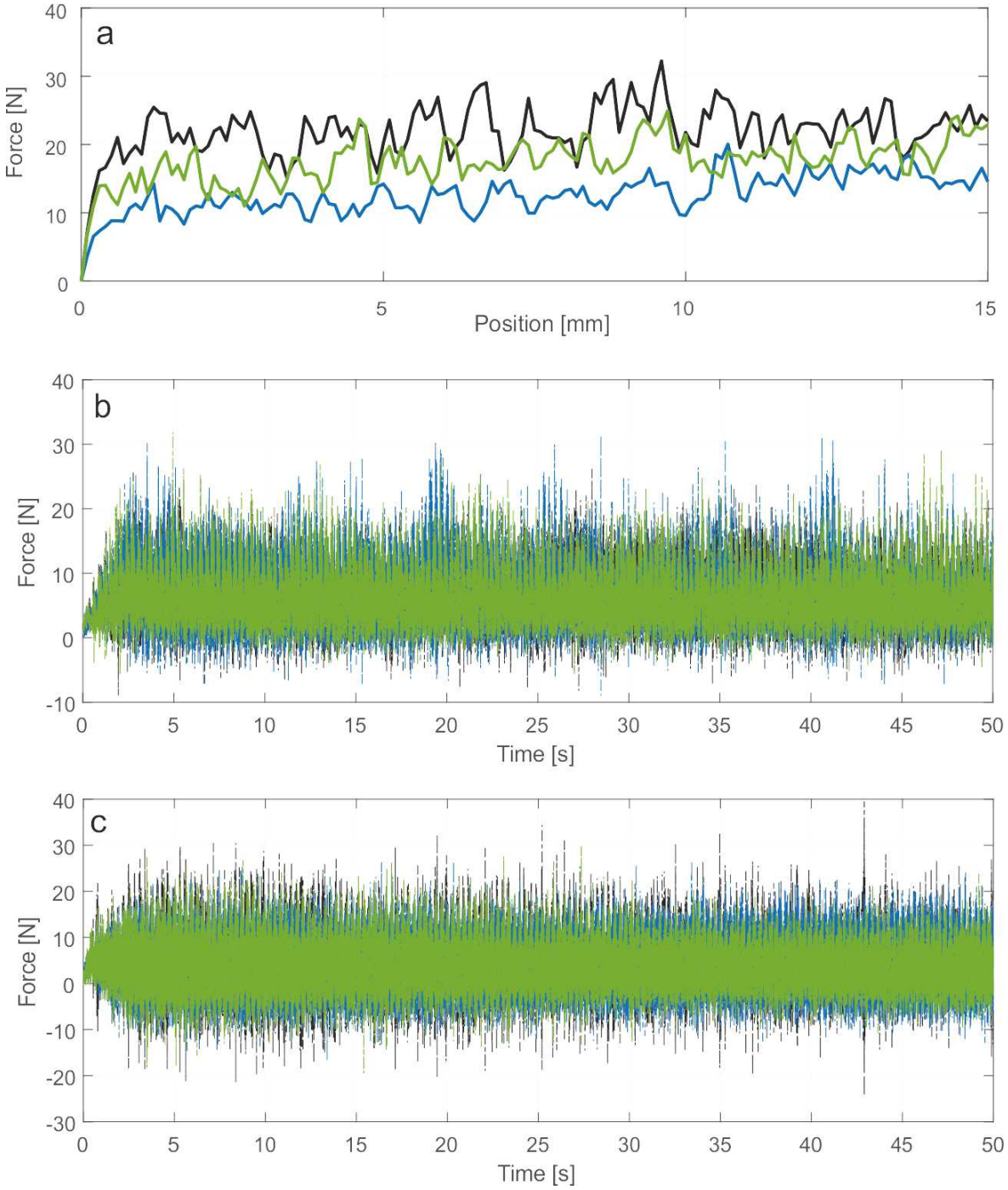

Figure 4.28: Force exerted on a Stanton Moor sample when drilling. The rotation speed was set to 200 rpm for the UAD and had to be increased to 400 rpm for the DRMS. The progression rate of the DRMS was set 10 mm/min and for the UAD to 36mm/min. a: three holes drilled with the DRMS. b: three holes drilled with the conical horn of the UAD and c: three holes drilled with the step horn of t he UAD. The sampling rate of the force is 5 kHz for the UAD. Some information is therefore lost given the tool oscillates at 20 kHz. The DRMS sampling rate is 10 Hz.

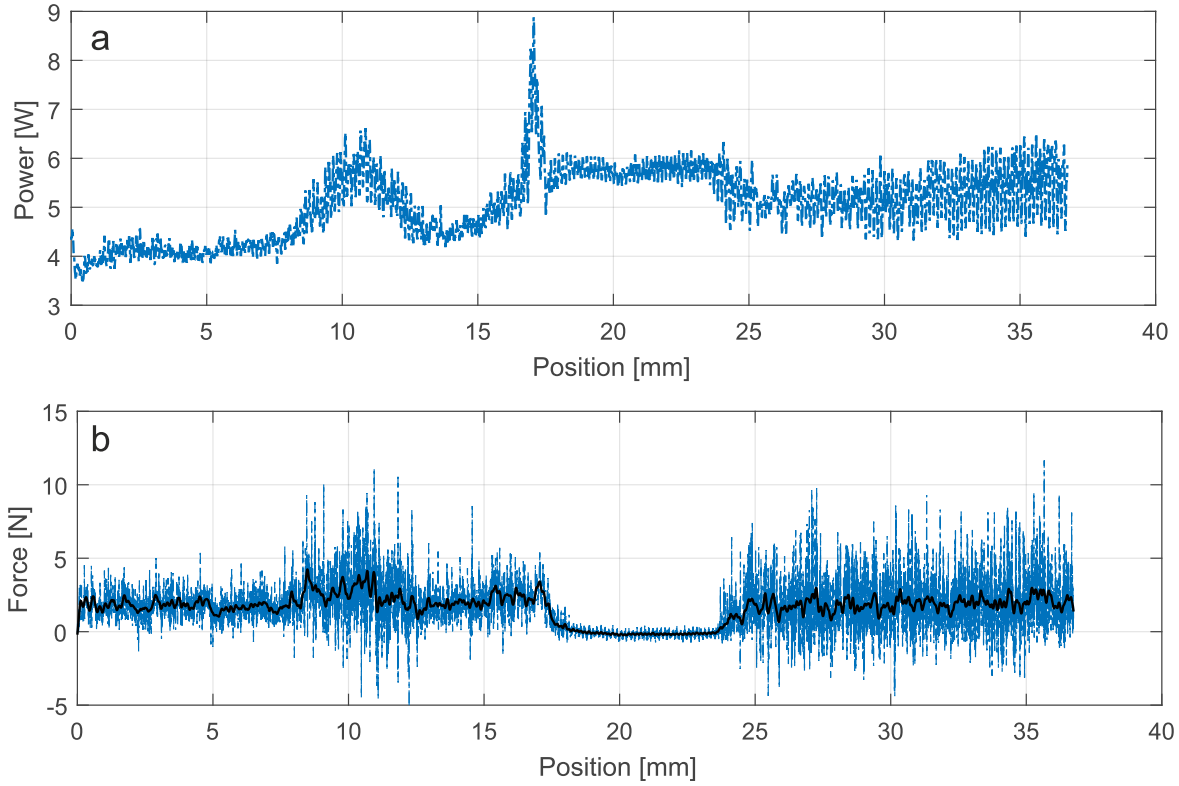

Figure 4.29: Na_2SO_4 treated Locharbriggs sample. a: power consumption does not decrease enough to identify a large gap between 17 -24 mm in the rock. b: the exerted force on the sample was recorded to better identify the gap. The force is here downsampled to 100 Hz which results in loosing some information. A moving average (40 for 10000 data points) is also applied (black) to visualise the gab better through the force variation.

Another problem that occurred for some rocks was a power increase with depth. Figure 4.30 shows a Na_2SO_4 treated Cullalo sample with a given progression rate of about 0.43 mm/s. The power increase after the first 10 mm depth is about 0.081 W/s or 0.035 W/mm. This was one of the highest increases seen in the data. Most samples show either no increase or a lower rate. The increase usually appears after 25 mm which is just after the flute ends. It is therefore likely that the power increase is caused by difficulty in removing debris out of the drilled hole and therefore to maintain the oscillation, the power is increased. Zacny et al. (2008) describe the increase of power consumption due to the material removal of up to 15 W/mm for an ultrasonically driven auger brill bit. Soft materials can easily exceed the capacity to remove the debris and can cause *auger choking*.

An overall power increase could be identified for the tool and can be seen in Figure 4.26. The reference samples were drilled first and later followed by the weathered samples. For the used horns it appears that the references show a lower power consumption than the weathered tools. This could be caused by tool wear. Although it has to be noted that the salt treated samples alter the physical properties and therefore cause a power increase through clogging of pores. Considering the slow wear of the tool (see Section 4.3.3) the

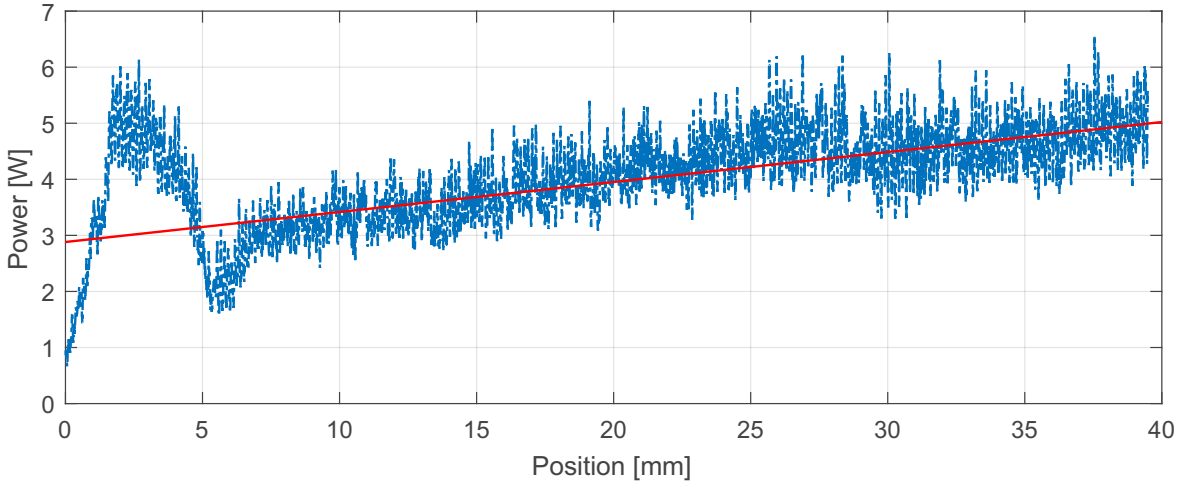

Figure 4.30: Power consumption increase when a Na_2SO_4 treated Cullalo sample was drilled. In red is the linear regression of the power after a depth of 10 mm depth was drilled. The increase in power consumption is about 0.035 W/mm.

power increase should not be too significant and is more likely caused by different structural properties of the rock or different material removing properties.

4.4.3 Pore space distribution after drilling

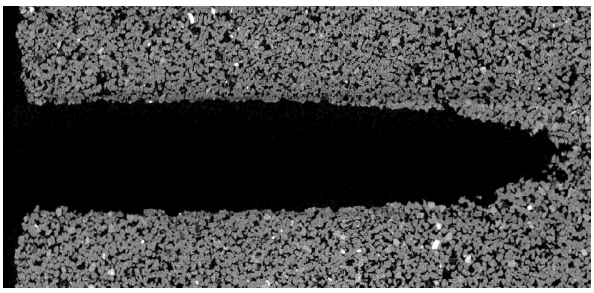

Figure 4.31: XCT image of a Locharbriggs sample drilled with the UAD. In black is the background or the pores of the sample. In grey are quartz and feldspar grains. White grains are mainly iron oxides. The hole diameter is 3 mm.

Damage of the rock caused by the drilling tools was investigated. Micro-computed tomography (XCT) analysis was used to assess the pore space distribution. The pore diameter was used to check if pore sizes increased or if pores combined into bigger pores. The *equi-diameter* is used (see Chapter 2) for the pore diameter. The length of the pores is used to indicate any cracks that appeared while drilling. Five holes were drilled into Stanton Moor with the UAD and the DRMS (Figure 4.31). A Locharbriggs sample was also investigated. The same volume of each sample with up to 200 mm^3 was analysed which accounts usually for 30,000 - 80,000 identified pores (Figure 4.32). The sample sizes determine the resolution, which is about 10 -20 µm. The results exclude therefore an important pore size.
Figure 4.33 shows the distribution of pore sizes separated into bins until 0.1 mm. When

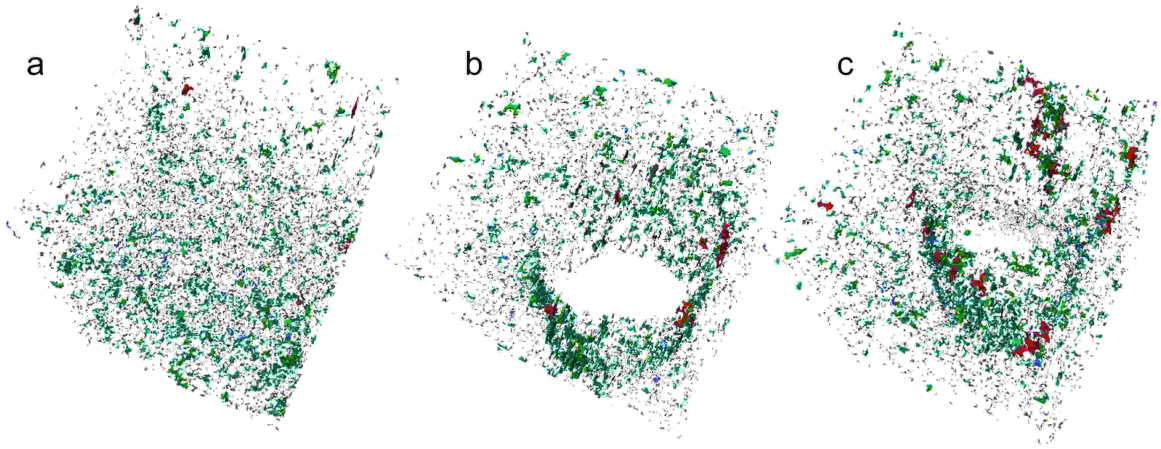

Figure 4.32: Pore space distribution of a 200 mm^3 Locharbriggs sample. a: reference, b: sample drilled with UAD and c: sample drilled with DRMS. Small pores (<0.025 mm) are displayed in blue. Pores bigger than 0.1 mm are displayed in red. The pores with sizes in between are green.

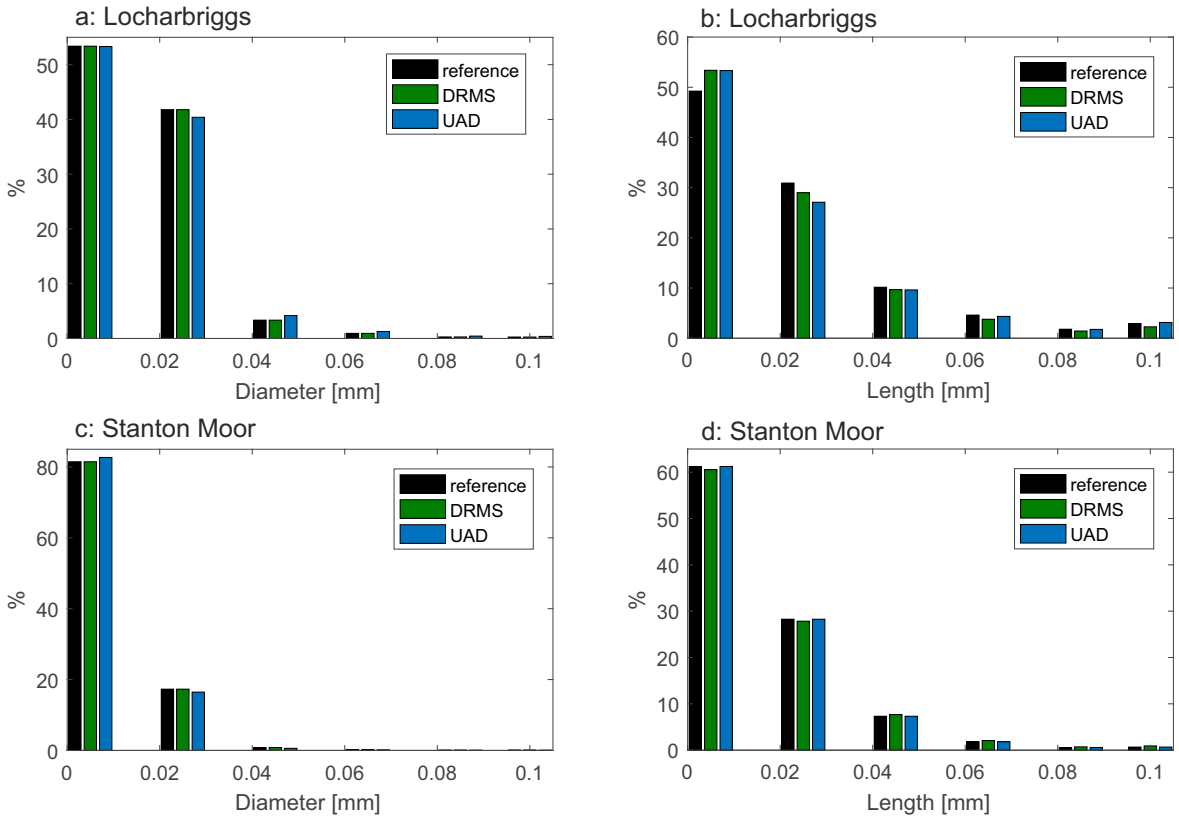

Figure 4.33: Pore diameter and pore length distribution for drilled samples with UAD and DRMS. Displayed pores for a volume of 200 mm^3 for Locharbriggs and Stanton Moor and their references. The pores are sorted into bins of the sizes: 0.005 - 0.025, 0.025 - 0.045, 0.045 - 0.065, 0.065 - 0.085, 0.085 - 0.1, 0.1 - 0.3, 0.3 - 0.5 and >0.5 mm. The bins bigger than 0.1 are listed in Table 4.2.

Table 4.2: Pore distribution for large bin sizes for Locharbriggs, Stanton Moor and their references. The bins are not displayed in Figure 4.33.

Bin	Pore	0.1-0.3 mm	0.3-0.5 mm	>0.5 mm
Locharbriggs reference	diameter	0.21	0.00	0.00
%	length	2.92	0.35	0.03
Locharbriggs UAD	diameter	0.38	0.00	0.00
%	length	3.14	0.62	0.08
Locharbriggs DRMS	diameter	0.26	0	0
%	length	2.28	0.40	0.07
Stanton Moor reference	diameter	0.08	0.004	0.0002
%	length	0.90	0.14	0.03
Stanton Moor UAD	diameter	0.056	0.05	0.003
%	length	0.67	0.11	0.02
Stanton Moor DRMS	diameter	0.10	0.006	0.0004
%	length	0.91	0.18	0.04

comparing the pore diameter and pore length for the Stanton Moor sample nearly no differences can be seen in between the drilled samples and the reference volume. Table 4.2 shows the fewer occurring, larger pore diameter and length. No significant difference can be observed for the analysed samples.

For the pore diameter of Locharbriggs a small change can be identified for the UAD sample (Figure 4.33 a). The pore sizes shift slightly (less than 3%) from the 0.025 - 0.045 mm bin into the next 0.045 - 0.065 mm bin and also a small increase can be seen in the following bins (less than 1%).

The number of shorter pores is increased by less than 5% for the UAD and DRMS in the Locharbriggs (Figure 4.33 b). This causes a decrease in the bin 0.025 - 0.045 bin especially for the UAD. A few longer pores, less than 1%, appear above 0.1 mm (Table 4.2).

With XCT no significant changes in the pore size distribution to the reference volume could be identified. Small scale changes (below 10 µm) cannot be excluded. The Locharbriggs sample showed very minor changes but both techniques seem to cause no significant harm to the rock. Both techniques do not show any outstanding differences on the pore size distribution. This needs to be investigated for other samples and pore sizes as well as different progression rates or rotation speeds of the tools.

4.5 Future work

Future work for the UAD should include two main aspects: tool development from the prototype and further building material investigations.

Tool development

- Portable tool
  The prototype needs to be converted into a cordless, handheld tool. A new cordless power supply with a matching transducer needs to be designed. Depending on the change of transducer a new horn needs to be designed for the PCD drill bit. A slip ring that fits the new design and does not cause any oscillation in the power signal needs to be selected as well as a new motor that allows the desired rotation speed. A linear actuator that pushes the tool at constant speed into the building material as well as a position sensor need to be developed. The tool could also include a stand/tripod. When used handheld, a plate with rubber feet (for rough surfaces) could be designed to push the tool against the wall to keep it at a fixed location. An ergonomic casing that holds the transducer should be added for the ready tool.

- Drill bit geometry
  Further investigation should be given to decide on the best shape of the drill bit. The flute/helix angle can be adjusted as well as the cutting edge to enable the best debris removal. This should allow a more stable drilling process meaning the power signal should be more constant. Better debris removal should also reduce the tool wear.
  A comparison of different PCD or another material like tungsten carbide might enable further improvement of the tool wear and debris removal.

- Carving tool
  An ultrasonic carving tool could be developed as a separate tool with exchangeable tips. On the other hand an exchangeable carving tip could be used on the ultrasonic drilling device, although the monitored power consumption while carving would not be of too much interest.
  The tips should include different diameters and shapes for variable carving methods. This should also account for different materials having different requirements on the carving tip.
  The amplitude of the oscillation could be varied to see which amplitude is the best for different materials and if the same amplitude can be used for a variety of materials.
  A longitudinal and torsional vibration could be better for carving to allow sideways carving. This would require a complete redesign of the tool with a different transducer.

- Rotation
  The quickest debris removal should be identified when varying the rotations per minute. An increasingly higher rotation does not guarantee a better removal. Allowing a comparison of the different materials, the rotation speed should be the same for every materials but might not be best for the individual rock/material. It is therefore

important to see at which rotation rate the different building materials show the best removal with ultrasonic drilling.

Building material investigation

- Reference catalogue
  A catalogue should be prepared that includes references of the power consumption for common building stones/materials. Next to the stones used in the thesis, further samples of sandstone, limestone, granite and other building materials like cement should be added. A detailed collection will also enable the power consumption to be related to the physical properties like UCS, porosity or cementation of the material to then predict average power consumption for unknown/uncharacterised materials. The model could also be used to predict the power consumption of the weathered rock. A detailed reference catalogue could also include typical values of weathered rocks.
  The reference should be at dry conditions, but could include trends for wet materials. The moisture of the rock will influence the removal rates and should be investigated depending on for different rock types/ properties like clay content.
  The reference catalogue of power consumption might be interesting for extraterrestrial in-situ characterisation of rocks. These would include tests at low gravity to adapt the catalogue to the different setting.

- Decay
  Another focus should be on how different weathering processes that change the rock influence the power consumption. This needs to be related to different rock types or rock properties as they could show contrasting results depending on the material. From several tests a prediction for the power change and therefore a characterisation of the state of decay should be possible.

- Consolidant
  Investigation on how sensitive the tool to rock consolidants is should be undertaken. This work will allow an on site evaluation of the penetration depth of the consolidant. Other treatments could also be investigated such as biomimetic apatite, clay swelling inhibitors, borax induced controlled crystallisation, or various kinds of desalination techniques (Karatasios et al. 2017, Granneman et al. 2017, Wangler 2017, Yang et al. 2012, Ruiz-Agudo & Rodriguez-Navarro 2010, Matyscaka et al. 2014).

- Humidity and moisture
  The influence of moisture in the rock on the changing power consumption needs to be evaluated. Especially when salts are involved in the analysed samples, the humidity or rock moisture needs to be considered. The salt could be in solution and therefore

show a different influence on the power consumption. Previously blocked pores and therefore decreased power consumption of the weathered rock could be measured.

- Stone damage
  The drilled samples could be tested for any damage caused by ultrasonic application. Porosimetry tests to cover a smaller pore fraction than the XCT measurements could be undertaken to exclude damage below 10 µm. The test could also show if the imaging technique of the XCT confirms the results from porosimetry. The operating setting should be varied to see any influence on the pore size distribution as well as the sample material.

- Temperatures
  As no coolant is used, the actual temperature of the drilled rock could be monitored, as usually coolants are needed for drilling.

- Stonemason disease
  Power tools that operate at lower frequencies (mainly sonic) usually are related to the increase of a *Hand-Arm Vibration syndrome* or *vibration white finger*, whereas higher frequencies are more locally exposing the fingers (Hua et al. 2017, Dong et al. 2004). It needs to be tested if handheld high frequency tools such as the drill and a carving tool can reduce the risks of these occupational illnesses.

4.6 Summary

During the project an ultrasonic drilling tool (20 kHz) was developed that allows identification of structural changes in building stones through a feedback power signal. An exchangeable carving tip was also developed. The increased sampling rate and easy penetration of hard rocks as well as maintaining the same settings for different rock type are the main advantages of the tool. Further results can be summarised as follows:

Operational settings of the tool can be kept constant for rocks with very different uniaxial compressive strengths. The best settings for the power consumption feedback signal were observed for an oscillation amplitude of 2.1 µm with a rotation speed of 200 rpm and a penetration rate of 0.6 mm/min. These settings allowed a penetration and differentiation of hard and soft/brittle rocks, the detection of for example clay layers or the investigation of the depth of weathering. No coolant is needed. The use of a conical horn or a step horn showed no significant difference for the purpose of identifying structural changes. The comparison of the FEM and EMA did not identify important differences.

When comparing conventional drilling (CD), the DRMS, and ultrasonic assisted drilling (UAD), the developed tool, a lower average force exerted on the sample was observed for ultrasonic drilling. The tool wear for the ultrasonic tool tips is also lower than for CD. This is especially critically when using CD in-situ. With increasing wear the tool cannot be held steady which leads to variations in the force feedback signal.
The developed drill bit showed less wear than commercially bought drill bits. When assessing the performance of the used drill bits, the material loss or shape of the tip is not the best approach to consider wear. Instead, the exerted force of the sample was used to determine wear or performance of the tool.
The analysis of the sample's pore space above 10 µm before and after drilling for the two techniques of UAD and CD showed no important differences. Both techniques do not exert significant damage on the tested samples.
The techniques allow for a good localisation of weathering depths for several tested building stones that were artificially weathered with NaCl and Na_2SO_4. A gap caused by the salts can be clearly mapped with both techniques. An increased power consumption of the ultrasonic drilling tool with depth could be observed for some samples and is most likely due to material removal rates.

Chapter 5

Micro-climate monitoring

This Chapter describes the monitoring of two of the most important drivers of building stone decay, namely temperature and humidity changes, at four Historic Environment Scotland sites using iButtons over the course of up to 22 months. The use of iButtons, tiny temperature and humidity data loggers, to measure micro-climates of sandstones is evaluated. Improvements to off-the-shelf iButtons to increase reliability and accuracy were tested. Specifically, aluminium and Tyvek covers were assessed to protect iButtons against solar irradiance and increase water-resistance, respectively.

5.1 Introduction

Environmental conditions and their influence on the local building stone at four Historic Environment Scotland sites are analysed. The sites where chosen due to the possibility to gain samples as it can be difficult to obtain material from protected sites. The HES sites also cover a diverse climate range of Scotland with the University of Glasgow in the central belt, Jedburgh in the borders, Dunkeld in the north and the Shetland Islands as a far north marine environment example (see Chapter 2).
Temperature and humidity data were collected to provide an assessment of the range of the micro-climate conditions that Scottish sandstones are subjected to. Temperature and humidity variation during an hour, a day or a year can give an overview of the environmental conditions the stone is exposed to and help to determine on the best conservation strategy. The identified temperature and humidity ranges also determine the environmental limits for the experiments with the drill tools and the laser interferometer to enable realistic conditions in the laboratory. Next to the monitoring of environmental conditions at the sites, the performance of the iButtons to monitor micro-climates are evaluated and improved. Two covers are applied and assessed on their influence on the measured data.

As described in Chapter 1, temperature and humidity changes cause weathering and con-

trol several other processes that influence weathering. An example is the evaporation rate of porous materials. A quick evaporation rate can lead to subflorescence. High temperatures and low humidity can enhance the evaporation rates (Gupta et al. 2014, Warke et al. 1996).
Temperature and humidity changes can directly cause stresses, for example between the surface and subsurface of the rock (Chapter 1). Monitoring environmental changes over years can help to predict material behaviour and therefore decay mechanisms (Warke & Smith 1998). Monitoring temperature close to surface of rocks is a quick way to deduce the influence of temperature on the whole rock as well as the moisture transport in deeper layers.
Relative humidity data from close to the rock surface can be used to identify which mineral phases are stable and influence the evaporation conditions of the rock, that in turn determine where florescence of salts occurs (Gupta et al. 2014).

Overview of the aims of the study

iButtons are proposed to be a cheap and easy tool for investigating micro-climates. The long-term monitoring at different sites at Scotland should therefore highlight conditions (such as season and aspect/orientation) of increased decay of the building materials.
Next to micro-climate monitoring, it is essential to know what influence covers have on the readings and whether, or how well, they improve the accuracy of an uncovered iButton. The aim of the cover investigation is to test two different covers of the iButtons compared to uncovered iButtons, investigating if the covers reduce solar radiance and ideally improve water resistance. The covers were tested outside a building for 6 weeks. To assess the temperatures most similar to that experienced by the building stones surfaces, no shields were used.

Overview of iButtons for environmental monitoring

This section focuses on the use of iButtons for environmental monitoring and the accuracy and error sources of the device. iButtons are small and comparably cheap temperature and humidity sensors (Figure 5.2 a). Two types of iButtons are available, temperature only sensors (thermochrons) and temperature and humidity sensors (hygrochrons).
iButtons are popular devices for monitoring temperature variations in a wide range of fields including atmospheric sciences, ecology, medicine, civil engineering and cultural heritage. Examples include temperature observations to study nests, traps or organisms (Crepeau et al. 2013, Lima et al. 2011), atmospheric temperatures and moisture contents near slopes, glaciers, as well as ground surface temperatures (Feld et al. 2012, Georges & Kaser 2002, Gubler et al. 2011) or the building environment such as cement curing or litter moisture monitoring (Choi & Won 2008, Wang et al. 2015). In cultural heritage they have been used to monitor micro-climates near the surfaces of building stones and/or to monitor temper-

atures at depth in the stone (Graham 2016, Diego et al. 2015, Beltran et al. 2013, Merello et al. 2012, Coombes 2011, Schnepfleitner et al. 2016). Studies on human skin temperatures include substantial considerations on the calibration or measurement errors (Hasselberg et al. 2013, Smith et al. 2010, van Marken Lichtenbelt et al. 2006).
The accuracy, reaction time and other influences that might alter the temperature and humidity readings need to be considered when using iButtons in the lab or in field. The supplier guarantees an accuracy of the iButtons of $\pm 0.5\,^{\circ}$C and $\pm 5\%$ RH (relative humidity). Individual iButtons should be calibrated to exclude any exception of this accuracy. iButtons are expected to be even more accurate varying with only up to 0.2° C (Smith et al. 2010, Hubbart et al. 2005). These tests were performed in a water bath although the iButtons are not waterproof (only water resistant) and should therefore be covered/coated when used in water (Maxxim 2015).
The mounting of the thermochrons has an effect on the temperature reading. The sensor is in the top part of the thermochrons and the battery in the lower part. Therefore changes can be seen quicker if the upper side of the thermochrons is in contact to the measured object (van Marken Lichtenbelt et al. 2006). This is also true for the humidity sensor.
The response time to temperature changes was measured to be 19 s by van Marken Lichtenbelt et al. (2006). This is the time required to change from the initial temperature to 63.2% of the new temperature value. Furthermore tests in water baths showed that the thermochrons need less than two minutes to measure a temperature change from 20° C to 40° C. The manufacture states the response time of the iButtons to 130 s (Maxxim 2015). For shorter response times the sensor can be removed from its casing.

Shin et al. (2017) investigated the performance of hygrochrons. The measured mean humidity difference to a humidity calibration chamber was -1.08%. The hygrochrons overestimated %RH at the lower range (40-60%) and underestimated RH at the higher range (80-90%) during tests of less than three hours. A strong influence on the humidity reading is the long-term exposure to high humidity values (>70%). For capactive sensors such as the hygrochrons this exposure leads to an increasing error in the measurements (see Section 5.2.2).
In addition to device errors, environmental conditions can alter the data recorded in the field. Main influences for monitoring temperature and humidity include sensor heating, wind speed and reflected solar radiation (Huwald et al. 2008). Solar radiance causes sensor heating, especially for the metallic cover of the iButtons. Hubbart et al. (2005) tested shielded and un-shielded iButtons in a closed greenhouse over a day without ventilation. The iButtons showed a maximal differences of 16.5° C during 24 hours. The initial temperature was 7° C. The maximum average temperature difference of a shielded and un-shielded iButton was about 5° C during the whole day. Although the shields prevented sensor heat-

ing, they can also trap heat. When used to determine human skin temperature, the ambient temperature influences the readings by errors from nearly 0.3 - 1° C for ambient temperatures at 30° C or 10° C (Smith et al. 2010).
Covers of the iButtons are added to improve the reduction of the strong influence of solar radiance and/or add waterproofing to the thermochrons. Covers depend on the application and iButtons type as, for example, the hygrochron needs a small opening to let in the humid air. To date, there have been various tests to try to increase the resilience of iButtons for environmental monitoring, using a variety of techniques. Gubler et al. (2011) used pouches of polyamide to protect thermochrons against water and solar radiation for near-ground surface measurements. Tyvek (a semi permeable layer, see Section 5.2) was used to cover the iButtons' exposed circuit boards which was attached to a shell to monitor mussel temperatures during tides (Lima et al. 2011).
For air temperature measurements usually radiation shields or funnels with varying shapes and materials such as aluminium are used (Holdena et al. 2013). Aluminium covers were also used in lab-based experiments with thermochrons to reduce direct heating from an infrared lamp (Coombes 2011). Roznik & Alford (2012) and Coombes et al. (2013) used plastic coatings or covers of thermochrons to increase water resistance and therefore instrument life. Tests showed only small difference in accuracy after plastic coating, i.e. smaller than 1.3° C (Roznik & Alford (2012)). A small effect on the rates of warming and cooling are observed for plastic wrapped sensors (Willis et al. 2009).

5.2 Methodology

Temperature and humidity data were collected with iButtons. The comparably cheap and small data loggers with a good reliability allow close to the surface measurements of temperature and humidity. The iButtons were used to monitor the micro-climate of sandstone at historic buildings over up to 22 months. Temperature measurements and humidity measurements reflect the local environmental conditions of the building stone. The main influences on the recorded a data are displayed in Figure 5.1.

Main components of iButtons
iButtons (thermochrons and hygrochrons) are coin sized data loggers that can store up to 8192 8-bit readings or 4096 16-bit temperature and humidity readings (Figure 5.2 a). The temperature sensor has an accuracy of better than $\pm$0.5° C at a range of -10° C to +65° C. The resolution of the readings can be set to 0.5° C or for 16 bit to 0.0625° C. The operating range is stated to range from -20° C to +85° C, and from 0 to 100% RH for the DS1923 (Maxxim 2015). hygrochrons have a 1.27 mm diameter hole at the top to allow humidity to reach the sensor. Moisture reaches the hygroscopic, dielectric layer, which attracts and holds water molecules

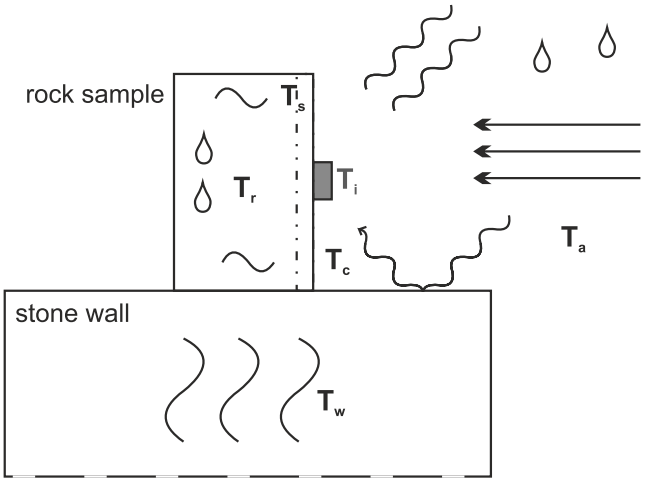

Figure 5.1: Main influence on the temperature recorded by the iButton (T_i). Surface temperature (T_s), rock temperature (T_r), wall temperature (T_w), ambient temperature (T_a) and close by ambient temperature (T_c) will determine the temperature reading of the iButton. The temperatures are mostly influenced by the solar irradiance, the reflected, radiated and conducted solar energy as well as the wind speed and direction. Sensor heating is another big influence on the recorded data. The local humidity of the rock is mainly determined by the ambient relative humidity, the moisture of the rock and temperatures dictating evaporation rates.

in an electrical isolator material, which can be polarised. This causes a change in the electric field and therefore the electrical capacitance of the sensor. With a long exposure of the sensor to high humidities (>70%), the hysteresis of the sensor increases. The manufacture provides a saturation drift compensation for this effect, which is described in Section 5.2.2. The resolution of the capacitive humidity sensor is 0.6%RH or for 12 bit readings 0.04%RH with an accuracy of 5%RH. The sampling rate can be set from 1 second to 273 hours. The lifetime at constant operation varies from less than one year up to 10 years depending on the sampling rate and exposed temperature.

Covers

As described in Section 5.1 iButtons are not waterproof and are strongly influenced by solar radiation. Therefore two covers were tested: aluminium tape and Tyvek. Aluminium tape was stuck to the thermochrons to increase reflectance and so reduce sensor heating. Tyvek is a water vapour permeable sheet made of polyethylene fibers commonly used in roof construction (DuPont 2004). Superglue was used to attach the Tyvek sheet to the iButton (Figure 5.2 b).

Rock samples

The iButtons were placed on Locharbriggs and Cullalo samples of 15 cm edge length with a width of 8 cm. *Thermal Conductive Adhesive* (from *R+S*) was used to attach the iButtons. Although the sensor is located in the top of the iButton which should therefore be in contact with the rock, the iButtons were glued face up to the rock as the hygrochrons would

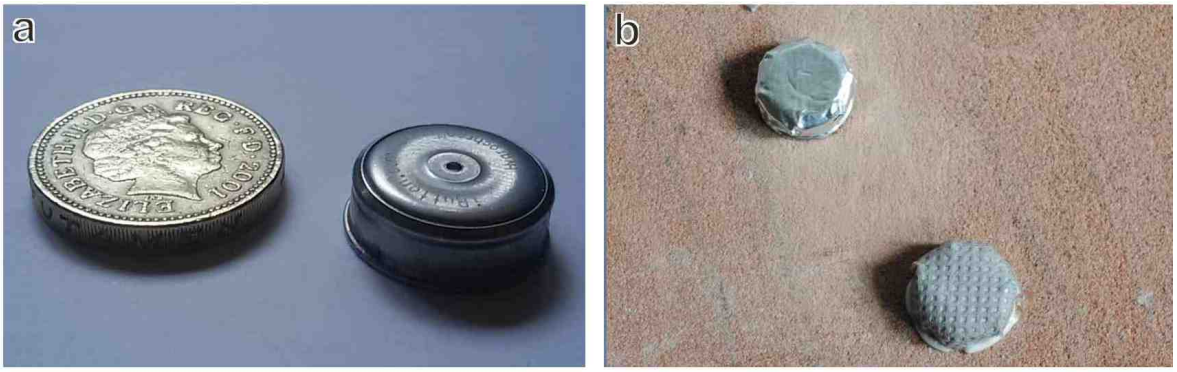

Figure 5.2: a: hygrochron, the temperature and humidity sensor used. b: thermochron with an aluminium cover (top) and a hygrochron with a Tyvek cover on a Locharbriggs sample.

otherwise not be able to monitor the humidity near the surface. This attachment also allows data to be retrieved without detachment of the sensor.

Thermal camera

An Infrared camera (*FLIR E50bx*) was used to monitor rock surface temperatures (Young 2015). The measurements require further apparent settings that are briefly described below such as the emissivity. Emissivity gives a value for the emission of thermal radiation of a surface in comparison to an ideal black body. The ideal black body absorbs every type of electromagnetic radiation, so that an emissivity of 1 is assigned. The emissivity of a Cullalo and Locharbriggs sample was determined with Scotch tape (Super 33+ 3M). The rock was covered half in tape and placed in oven at 60° C for 6 hours. The temperature of the rock half with tape was measured and the emissivity then adjusted to match the temperature reading at the bare rock surface (Young 2015). The test was repeated five times to confirm repeatability and showed an emissivity for Locharbriggs of 0.89 and 0.93 for Cullalo.
Atmospheric temperature and humidity were determined with an iButton or gained from the weather station close to one of the trials. Reflected apparent temperature was measured with aluminum foil on a carton board.

Pyranometer

The solar irradiance (electromagnetic radiance per area) was measured with a Pyranometer from Campbell Scientific (CMP3 Pyranometer 071096). The solar irradiance per day for example in the midlands of the UK in winter is on average around 40 W/m^2, in summer the average is around 170 W/m^2 and on a sunny day in winter measurements can be as high as 500 W/m^2 (Burnett et al. 2014).

Weather station

The trial was performed at Garscube Estate Observatory where the samples were placed next to a weather station which allowed to retrieve atmospheric temperature, humidity and wind data during the measurements.

5.2.1 Test series

Two main sets of measurements were undertaken. The first test series (experiment I) includes the investigations of the covers and the influence of solar radiation on the covers and uncovered iButtons (Table 5.1). The test was conducted over six weeks and includes intermittent recordings of solar irradiance and surface temperatures. The next test series (experiment II) contains long term monitoring of temperature and humidity of four Historic Scotland sites of nearly 2 years.

Table 5.1: Overview of the two, short-term (I) and long-term (II), iButtons investigation.

	Experiment I	**Experiment II**
aim	investigation of aluminium and Tyvek covers	micro-climate monitoring of HES sites
setup	air suspended (I a), glued to stone (I b)	glued to Locharbriggs and Cullalo
duration	20/02/18 - 04/04/18	∼Oct 2015 - ∼Oct 2017 (depending on site)
number of iButtons	3 (I a) and 5 (I b) for each cover type	9 for each site
sampling time	every 15 min	every 40 min (20 min during the first months)
location	Garscube Observatory	1. Dunkeld Cathedral, 2. Fort Charlotte (Shetlands), 3. Jedburgh Abbey, 4. Garscube Observatory
position	ground	1. cathedral spire, 2. roof, 3. stone wall (north facing with roof), 4. ground (north facing with roof)

Experiment I: Cover experiment

The performance of two covers is evaluated: aluminium for thermochrons and Tyvek for hygrochrons. The trial is performed at Garscube Estate Observatory consisting of two test series: iButtons suspended in air (I a) and iButtons glued to Locharbriggs samples (I b). The first batch consists of 9 iButtons (I a) and the second batch consists of 15 iButtons (I b) with the same amount of uncovered iButtons (UI), aluminium covered iButtons (ACI) and Tyvek covered iButtons (TCI) for each batch.

The aim is to minimise sensor heating and additionally add an increased water-resistance to the iButtons. The tests provide a detailed example on how the temperature and humidity readings from covered (Tyvek and aluminium tape) iButtons differ from readings of uncovered iButtons (UI) for the purpose of micro-climate monitoring of building stones.

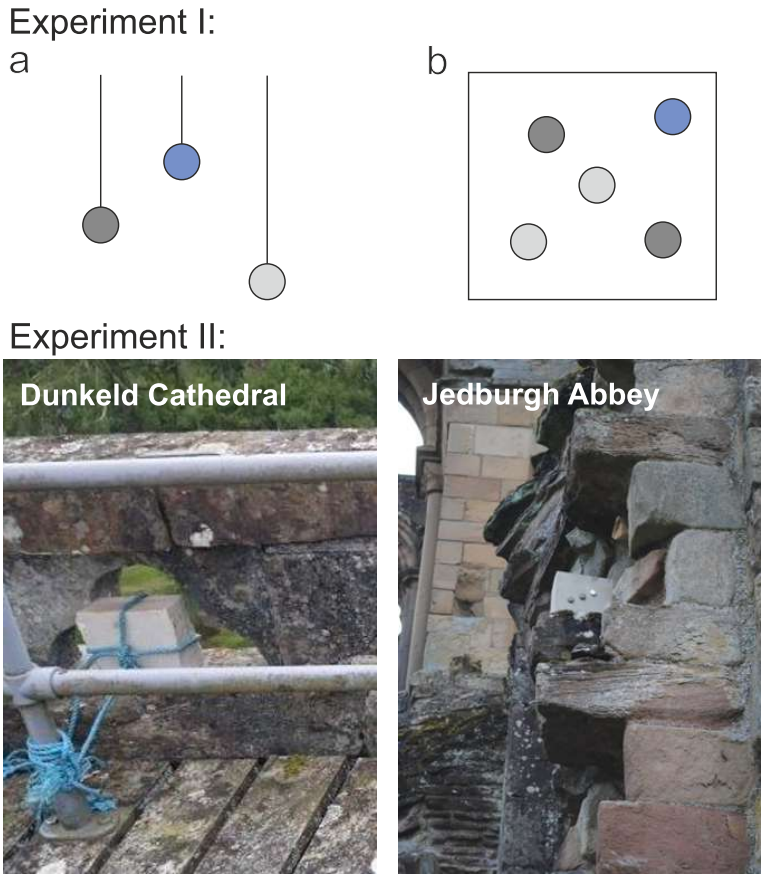

Figure 5.3: Setup of the experiments. I a: iButtons suspended in air with different covers (blue: Tyvek, dark grey: aluminium and light grey: uncovered iButtons). I b: Locharbriggs samples with iButtons glued to the surface, both at Garscube Observatory. II : South facing Cullalo sample at the spire of Dunkeld cathedral secured with a rope. North facing Cullalo sample at Jedburgh Abbey.

The iButtons suspended in air with a plastic string provide a measurement independent of the close-by material. The sampling rate for the freely hanging iButtons was set to 15 min. 9 iButtons suspended in air with different covers (3 each) of ACI, TCI and UI were compared.

The iButtons glued to the stone (I b) yield data specific to the example of a 15 x 15 x 8 cm sandstone samples, the glue, the given air temperature, humidity, wind and solar radiation, as well as the ground temperature during the day of investigation. The solar irradiance, surface temperature and wind speed was therefore also recorded for 15 min at several days during the test at Garscube. The iButtons were placed on Locharbriggs samples (Figure 5.3 b), a common red building stone in Scotland. Four Locharbriggs samples were placed on the ground at Garscube Estate Observatory holding 15 iButtons with ACI, TCI and UI (5 each). The sampling rate was 15 min for over 6 weeks.

Experiment II: Micro-climate monitoring

Micro-climate monitoring at four Historic Environment Scotland sites were undertaken over 22 months. The sites include the observatory at Garscube (University of Glasgow),

Dunkeld Cathedral, Jedburgh Abbey and Fort Charlotte (Shetland Islands). Humidity and temperature measurements were undertaken every 20 min in the first 4 months and then every 40 min for the last 1.5 years at the different HES sites to reduce data collection intervals. iButtons data were collected every three to four month. During the monitoring, the iButtons were attached to two samples of white Cullalo sandstone and one sample of red Locharbriggs sandstone. The samples were placed close to the building walls at the sites with two of them facing south (Locharbriggs and Cullalo) and one facing north (Cullalo). Each sandstone sample carried three iButtons with one ACI and two TCI. The samples were placed at a safe spot at the sites to allow visitor safety (Figure 5.3 II). At Dunkeld the samples were placed at the old spire, sitting in small stone windows of original rock (see Figure 5.3 II). At the Shetlands the rocks were at the roof of Fort Charlotte. At Jedburgh Abbey the rocks were placed on a south facing wall and a slightly sheltered north facing wall (Figure 5.3 II). At Garscube the rocks were placed in front of a south facing wall and sheltered north facing wall both at the ground.

5.2.2 Data treatment

All data analysis was done in MATLAB. For accurate humidity readings the collected data need to be corrected to compensate for temperature characteristics of the humidity sensor and a saturation drift. This drift increases when humidity is high (>70 %) in capacitive humidity sensors, such as those in iButtons. The temperature compensation of the sensors is corrected with equation 5.1 (Maxxim 2015). The compensation constants, K, α, β, γ and δ are given by the supplier. The humidity (H) and temperature (T) for the humidity conversion are measured by the hygrochron.
The saturation drift is corrected with equation 5.2 (Maxxim 2015). This includes the humidity reading at the end of the Nth hour with the temperature compensation already applied ($HTcorr$) with N, the number of hours that the device is continuously exposed to >70%RH. T_k is the average temperature reading of the kth hour that the device is continuously exposed to >70%RH and ARH_k, the average temperature-compensated humidity reading of the kth hour.

$$HTcorr = \frac{H \times K + \alpha \times (T - 25^\circ C) - \beta \times (T - 25^\circ C)^2}{K + \gamma \times (T - 25^\circ C) - \delta \times (T - {}^\circ C)^2} \tag{5.1}$$

$$HScorr = HTcorr - \sum_{N}^{k=1} \frac{0.0156 \times ARH_k \times 2.54^{-0.3502 \times k}}{1 + \frac{T_k - 25}{100}} \tag{5.2}$$

The correction largely removes humidity values above 100%RH although some remain after

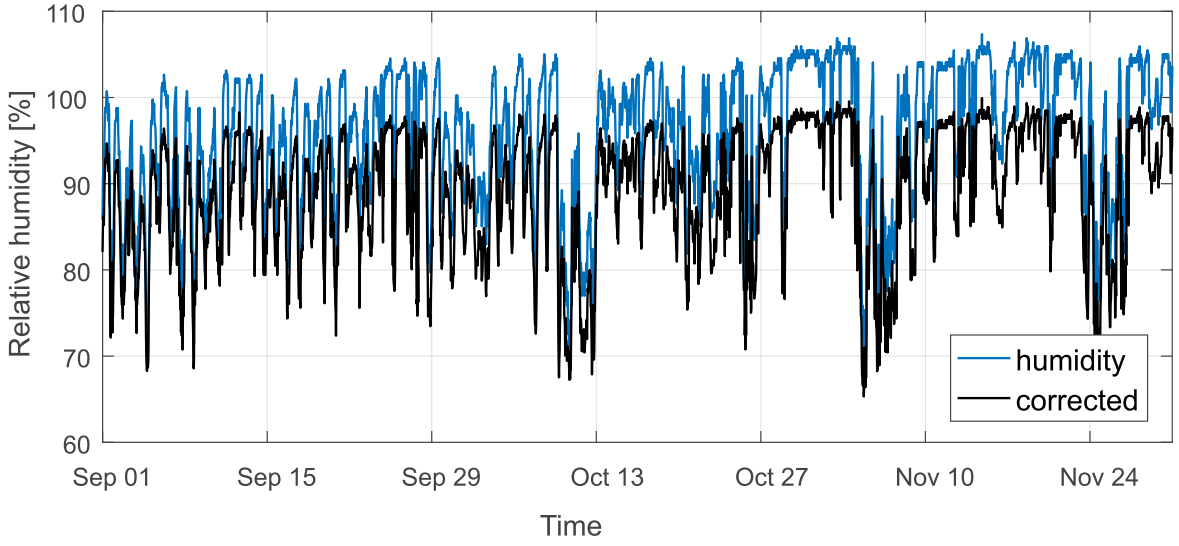

Figure 5.4: Example of a humidity measurement obtained at Garscube over three months on the surface of a Cullalo sample facing south. The saturation drift of the humidity (blue) is corrected (black).

correction (Figure 5.4).

Sensor heating is therefore also influencing the correction of the measured humidity. Increased temperature measurements will lead to a smaller correction of the humidity value. Although the introduced error will be small. For a high humidity lasting for example about 5 hours and a temperature difference of 5° C, this will introduce an error that will be below 0.5 %RH.

Uncertainty of the calculated mean

The cover experiment (I) uses the mean of either three or five measurements from different iButtons for the same time window. The uncertainty (u_x) of the average ($\bar{v}_x$) can be calculated with Equation 5.3 to gain a better value for the measured value (v). With the given accuracy of ±0.5° C which is here used as the standard deviation (s), Equation 5.3 can be summarised to Equation 5.4. For the measurement with three iButtons the uncertainty will be 0.29° C and for five iButtons 0.22° C.

$$u_x = \sqrt{\frac{1}{N(N-1)} \sum_{j=1}^{N} (v_j - \bar{v}_x)^2} \tag{5.3}$$

$$u_x = \frac{1}{\sqrt{N}} s \tag{5.4}$$

Rate of temperature and humidity change

Instead of comparing absolute temperature and humidity values, the rate of change was calculated over 60 min for experiment I (sliding time window for the 15 min sampling rate)

and 40 min at the sites (experiment II). The sampling rate of 40 min allowed for data collection every 4 months and enabled monitoring of rapid temperature and humidity changes. The main advantage of analysing changes in temperature and humidity is that they are one of the main drivers of decay (Benavente et al. 2008). Short term temperature changes (minutes to hours) show the highest amplitudes of change during a day (Coombes & Naylor 2012). Rapid changes can cause high thermal stresses but also influence other factors such as evaporation rates. Absolute temperature values are interesting for nucleation and crystal growth of salts as well as phase changes. Changes in humidity can indicate stress on the porous building materials through hygric and hydric dilation. Humidity changes also influence the drying rate of stones.

Statistical analysis

The frequency of the calculated changes in temperature and humidity was calculated over the whole experiment duration. An example is given at the beginning of Section 5.3. The resulting histogram has a bin size of 1° C which allows the previously calculated uncertainty to fall into the set bin size. Histograms of temperature and humidity change over 40 or 60 min do not show a normal distribution nor log-normal distribution. Most changes appear in the range of -2 to 2° C/h. For more than 3000 (experiment I) and around 20000 (experiment II) data points per iButton, these large data sets show a pointy tip in the distribution of frequencies (Figure 5.7 b). For the analysis, the less common (<5%) but larger or *rapid* temperature and humidity changes (>4° C/h and >15%RH/h) are analysed. A Kruskal-Wallis test was used to statistically analyse the difference in these less frequent, high rates of change for two or more different groups (Bewick et al. 2004, Coombes et al. 2017).
The test assumes a H_0-hypothesis that the medians of the given populations of two or more groups are equal, meaning there are no differences in the investigated groups. An H value is calculated from Equation 5.5 and compared to the critical χ^2 value with $c-1$ degrees of freedom and p, the 1 or 5% significance level.

$$H = (N-1)\frac{\sum_{i=1}^{c} n_i(\bar{r}_i - \bar{r})^2}{\sum_{i=1}^{c}\sum_{j=1}^{n_i}(r_{ij} - \bar{r})^2} \tag{5.5}$$

Here c is the number of investigated groups and i the number of the group. N is the number of observations across all groups and n_i the number of observations in group i. $\bar{r}_i$ is the average rank of all ordered observations in group i and r_{ij} is the rank (in-between all observations) of observation j from group i. $\bar{r}$ is the average of all r_{ij}.
For H larger than the χ^2 value, the H_0 hypothesis is rejected, i.e. the groups can be assumed to be different (p<0.05). The test assigns a rank to each measurement. The median of the ranked observations for different groups can then be compared. An example is shown in Figure 5.5. An assumption of the test includes the same shape of distribution of the ob-

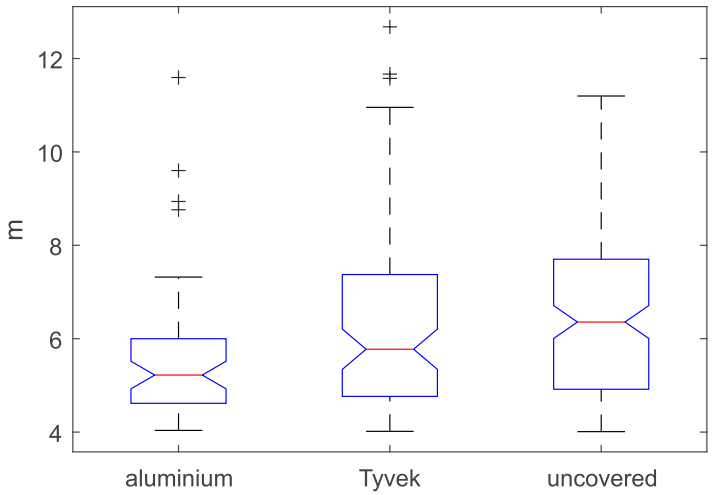

Figure 5.5: Kruskal-Wallis test comparing the median of ranked observations (red), their spread (25th and 75th percentiles in blue) to the extreme data points not considering outliers. The outliers are plotted individually (+).

servations in the groups. In this context, the exclusion of slower temperature and humidity changes can lead to only a few samples (<2000) present in the rapid change analysis and therefore influence the shape of the distribution of those observations.

5.3 Cover experiment (I)

iButtons suspended in air (I a)

iButtons suspended in air with different covers (3 each) of ACI, TCI and UI were compared over a month (Figure 5.6) with a sampling rate of 15 min. During cloudy days there was no difference in the temperature recording of the different iButtons (variation below the $\pm 0.44^{\circ}$ C). On sunny days, the ACI gave the lowest temperature readings, of up to 5° C lower than the UI. An example of the absolute temperature measurements on a sunny day is displayed in Figure 5.6 a (03/03/17).

Instead of looking at the absolute temperature values, the rate of temperature change over one hour was calculated and analysed in the next steps (Figure 5.6 c). An overlapping sliding window was used to infer the changing temperature over one hour for each data point. The frequency of those temperature changes for the whole recorded 6 weeks is compared for the three different treatment types in Figure 5.7. For a better overview, the temperature changes per hour were divided into bins of 1° C with temperature changes of up to $\pm 10^{\circ}$ C/h.

The histogram in Figure 5.7 shows an example of the frequency of temperature change per hour for the ACI during the 6 weeks of measurement. Most temperature changes (usually more than 30%) appear between -2 to 2° C/h. Rapid temperature changes are observed less often. The frequency is therefore displayed for those less frequent events in a range from

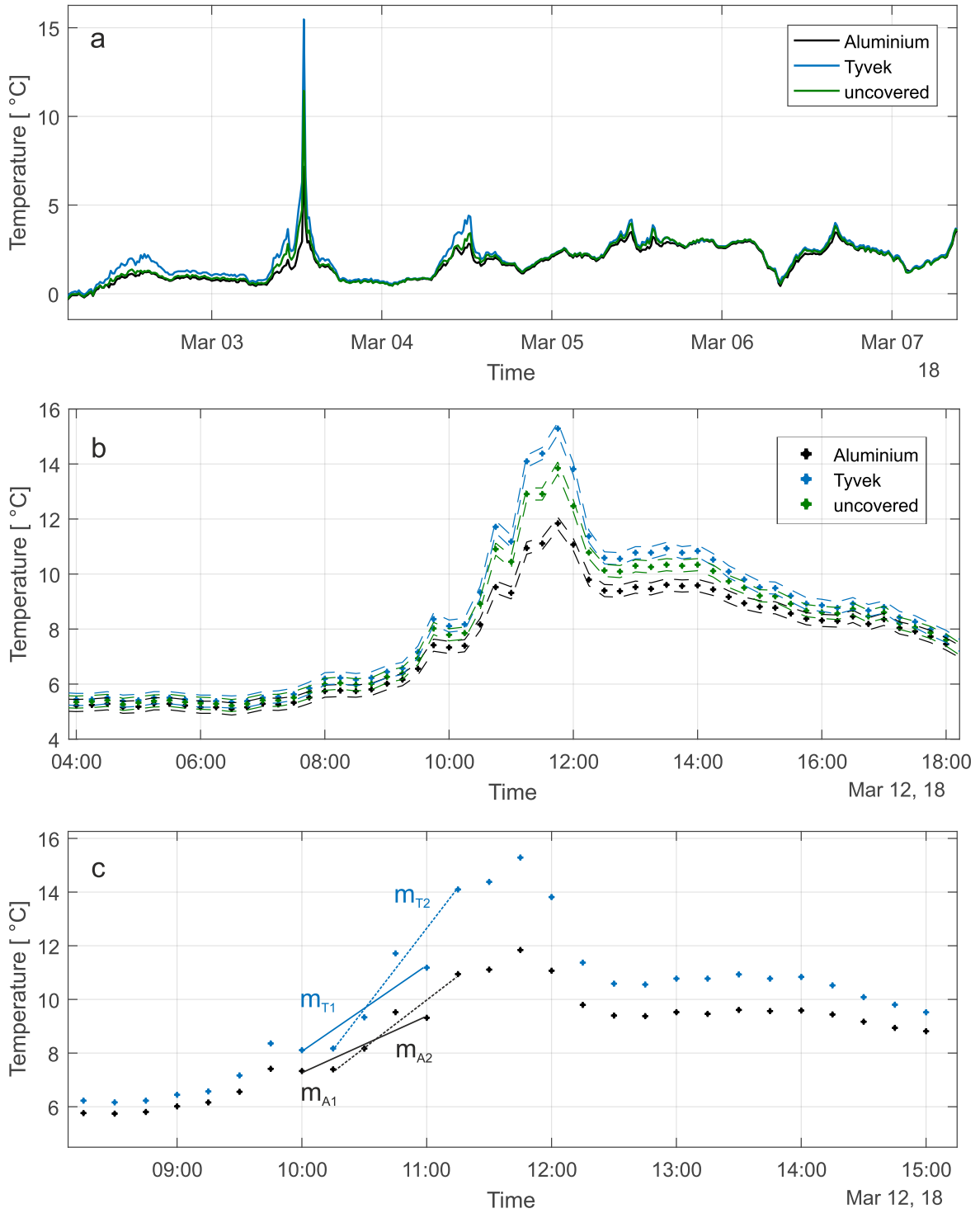

Figure 5.6: Trial data of iButtons (experiment I a) suspended in air with different covers (aluminium in black, Tyvek in blue and uncovered in green. a: Average of the recorded temperature data for an example of a five day measurement during the 6 weeks trial period. b: Example of a 12 hours measurement of the recorded data with the uncertainty of $\pm 0.44^{\circ}$ C (dashed lines). c: Temperature change over one hour (m) for two examples of the Tyvek (m_T) and aluminium covers (m_A). The deviation (m) of the temperature per hour is calculated for all data with an overlapping sliding window of 1 hour.

0 to 5%.

Figure 5.7 c shows a comparison of the frequency of temperature changes per hour for the three different covers in experiment I. The Kruskal-Wallis test revealed, there is a significant influence of the ACI compared to the UI ($H(2) = 4.5$, $p < 0.05$). Analysis of the group medians suggests that compared to the UI, rapid rates of heating were significantly reduced. The histogram shows that the ACI had slower heating rates than the UI (Figure 5.7 c). Rapid heating rates (above 6° C/h) of UI are more than two times more frequent than the ACI. The ACI on the other hand show slightly slower cooling rates than the UI (Figure 5.7 c). Although this decrease in cooling rates is not statistically significant ($H(2) = 0.7$, $p > 0.05$). TCI behave very similarly to the UI, but show slightly increased numbers of rapid heating and cooling rates (Figure 5.7 c). Again these small differences are not significant ($H(2) = 0.3$, $p > 0.05$).

iButtons on Locharbriggs sample (I b)

Four Locharbriggs samples holding 15 iButtons with covers of Tyvek, aluminium and no cover (5 each) were analysed. The sampling rate was 15 min over 6 weeks. Figure 5.8 a shows the average absolute temperature of the different covers for an example of 4 days. The ambient temperatures recorded by the weather station are also displayed. Similar to the iButtons in experiment I a, no difference can be seen on cloudy days (variation below the ± 0.22° C). When comparing the absolute temperature difference between the UI and ACI over 4 weeks of measurements, it can be seen that on sunny days, the ACI show the lowest values. The temperature was up to 3° C lower than the UI during sunshine (Figure 5.8 b). For the absolute temperature differences of UI and TCI, it can be seen that both show very similar values although during sunshine TCI can heat up up to 2.5° C more than the UI (Figure 5.8 b).

When looking at the change in temperature per hour (Figure 5.8 c), TCI performed in a very similar manner to UI and show only a few more frequent heating rates compared to the UI. The difference of the two covers for high rates of heating or cooling is not significant ($H(2) = 0.7$ and 0.04, $p > 0.05$). The ACI measured less frequent rapid temperature changes than the UI and TCI especially for rates above 8° C/h ($H(2) = 5$, $p < 0.05$). A difference in the cooling rate of the ACI and UI is not statistically significant ($H(2) = 1.7$, $p > 0.05$). Compared to the results of experiment I a, the difference between UI and ACI is not as high. This could be caused by the influence of the Locharbriggs sample 'dampening' the temperature response. Additionally for all iButtons tested on the stone's surface (experiment I b), it can be observed that the histograms are not as symmetrical as for experiment I a. Rapid heating rates are more common on the Locharbriggs sample than rapid cooling rates. This could be mainly due to the Locharbriggs sample slowly cooling down after insolation, preventing to give away thermal energy quickly compared to the whole system with the iButton heating up during insolation. It also has to be considered that the ambient temperature shows more

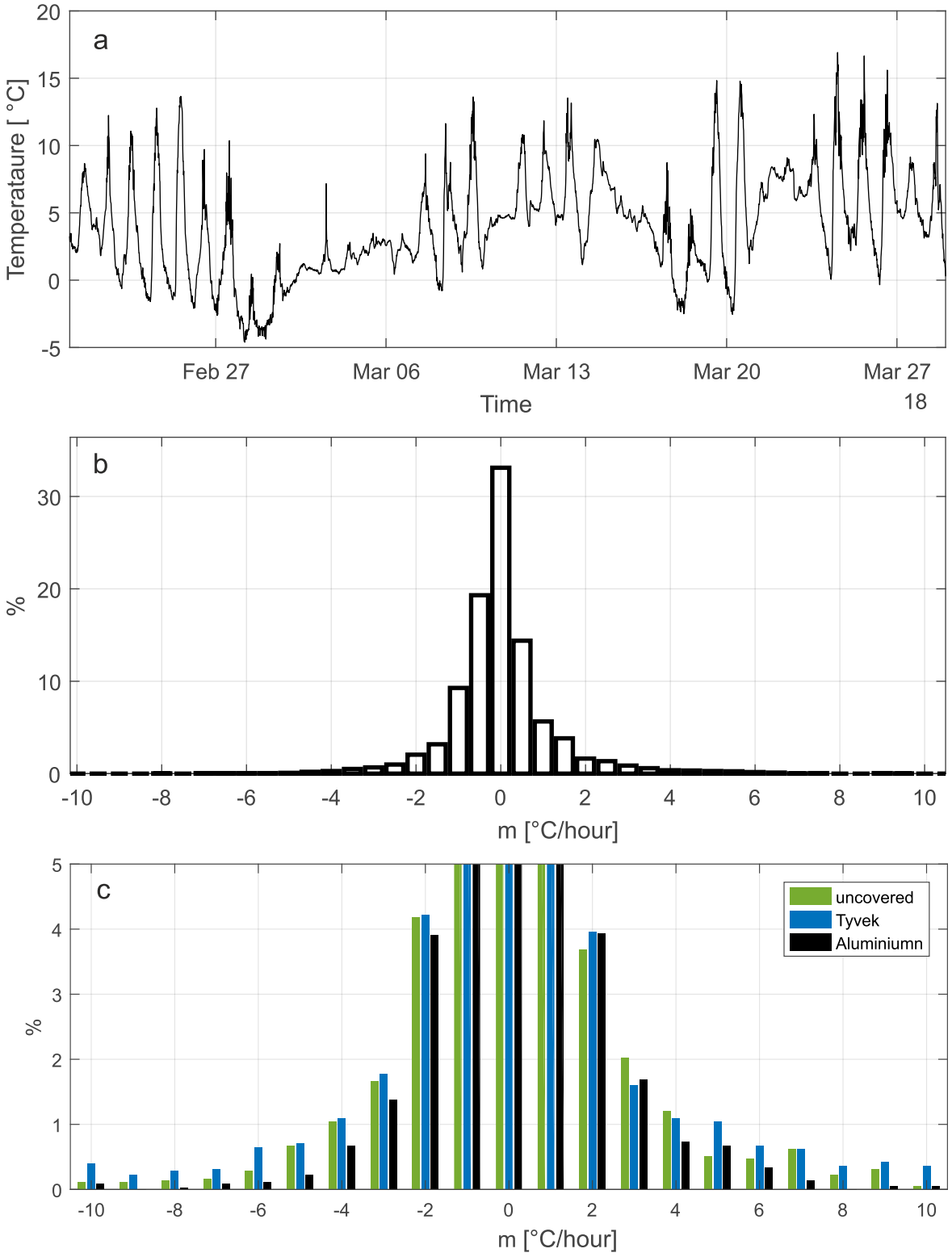

Figure 5.7: Experiment I comparison. a: Example of temperature measurements of iButtons suspended in air with aluminium cover over 6 weeks. The derivation (m in °C/h) of the data is used to analyse the temperature changes of the covers. b: Histogram of the derivation. Example for the temperature change slopes (m) of the aluminium cover. Large positive slopes indicate a rapid heating and large negative slopes indicate a rapid cooling rate. c: Frequency of temperature changes per hour for the aluminium cover (black), Tyvek cover (blue) and uncovered iButtons (green).

frequent heating rates than cooling rates (Figure 5.8 c).

To assess the performance of the iButtons to monitor near surface temperatures, solar irradiance and stone surface temperature measurements were recorded on six days (Table 5.2). These dates were picked to cover a variety of temperature, wind speed and cloud cover.
When comparing the micro-climate data of the ACI with the surface temperatures, higher absolute values were recorded for the ACI (Table 5.2). This difference could be caused by several factors: sensor heating, surrounding air heating quicker than the surface and/or variability in the settings of the thermal camera. Compared to the ambient temperature, the ACI and surface temperature showed higher temperatures. For the very little number of examples the ACI gives a good approximation of the close-by temperatures. On a cloudy day (15/02/2018) with only little solar irradiance, the three temperature measurements showed as expected only little variation. The wind speed was low on all recorded days.
Unfortunately during the 6 week trail, 1 week of heavy snowfall and mainly no change in cloud cover and wind speed took place. Furthermore the weather station stopped recording after the summer time change at the 25/03/18 and was not restored until April. Another problem was the measurement of the surface temperature on sunny days. On a cold and sunny day the reflected temperature was determined with tin film on a paper card (Young 2015). The technique introduces a high variation which can result in an error for the surface temperature of $\pm 2^{\circ}$ C. The reflected temperature measurements need to be improved to gain more reliable surface temperature measurements.
To evaluate the iButtons for monitoring micro-climates with several influences such as ambient temperature, surface temperature, wind speed, wind direction, solar irradiance and humidity more samples need to be taken. So far the iButtons can be used to monitor close to the rock conditions with a small influence of sensor heating as seen in the small comparison to the surface temperature. To calculate the exact influence of the sensor heating more data must be collected (see Section 5.5).

In summary, the ACI reduced the rate of rapid temperature changes and therefore provided an increased protection for sensor heating compared to no cover or Tyvek cover. The Tyvek cover showed a slight increase in the number of rapid temperature changes but not a significant differences of Tyvek cover and uncoverd iButtons could be observed in experiment I. If hygrochrons are used both for temperature and humidity investigations, hygrochron should be covered with aluminium tape with a small hole for the humidity sensor. This hole could be covered with a piece of Tyvek, with as small as possible dimension. It needs to be tested if the Tyvek cover is benefical for the lifespan of the hygrochron.
None of the thermochrons and hygrochrons failed during experiment I. During the micro-climate monitoring described in experiment II (Section 5.4) with ACI and TCI, 5 thermochrons failed and 3 were lost of initially 12 thermochrons. Out of the 24 hygrochrons at

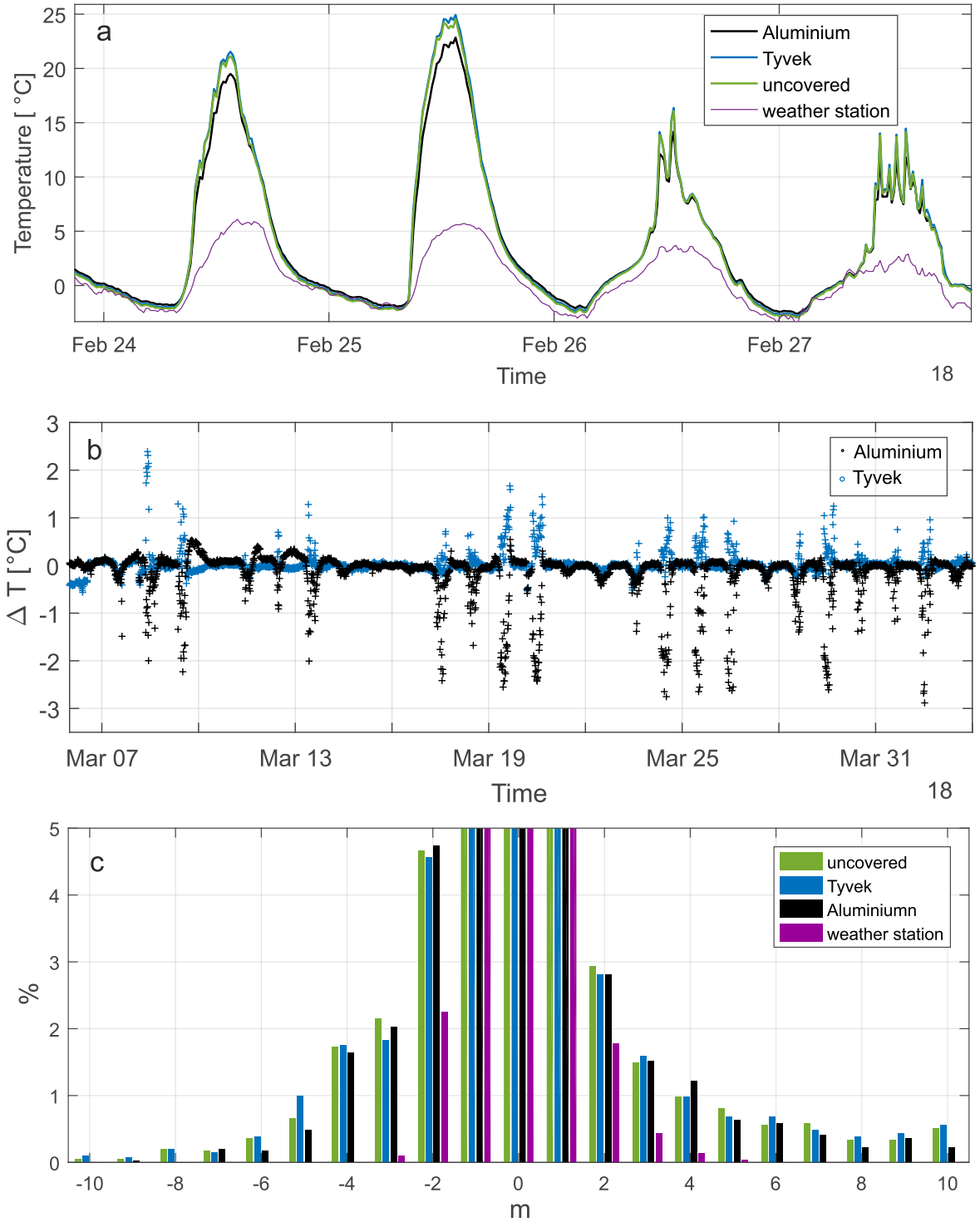

Figure 5.8: Experiment I b with different covers on a Locharbriggs sample. a: Average temperature of five iButtons with aluminium covers (black), Tyvek covers (blue) and uncovered iButtons (green) for an example measurement over 4 days. The ambient temperature was recorded by the local weather station (purple). b: Temperature difference of the measurements of the UI and the ACI iButtons (black). The ACI recorded up to 3° C less. The temperature difference of TCI and UI (blue) shows partially up to 3° C. c: Histogram of the temperature changes per hour of the different covers and ambient temperature (purple).

Table 5.2: Additional environmental measurements during micro-climate monitoring for 6 dates during the trial of 6 weeks. T_A is the temperature measurement from the aluminium cover, T_s is the surface temperature of the rock, T_a is the ambient temperature given by the weather station. The wind speed and direction as well as humidity is also provided by the weather station.

Date	T_A [°C]	T_s [°C]	T_a [°C]	Solar irradiance $[W/m^2]$	Humidity [%RH]	Wind speed [mph]	Wind direction
13/03/2018 10:15	15.5	13.7	6.7	500	89	0	-
13/03/2018 10:30	8.9	10	7.2	160	86	1	W
15/03/2018 09:30	6.8	5.3	5.8	60	81	3	NE
26/03/2018 09:30	15.9	13.1	-	500	-	-	-
26/03/2018 09:45	17.2	15.5	-	530	-	-	-
29/03/2018 09:00	9.5	6	-	450	-	-	-

the start of the trial, 4 were lost and 11 failed. At the Shetland Islands only new hygrochrons were used and one failed after the first year. The iButtons at the other sites had all been used previously in other experiments including submersion into water. It is therefore difficult to evaluate the protective performance of the Tyvek. The good lifespan of the iButtons (more than 1.5 years) covered with aluminium and Tyvek demonstrated on the Shetland Islands suggests a positive effect, but this needs to be further investigated (see Section 5.5).
The long-term investigation of experiment II have been started with both aluminium and Tyvek covers in 2015 before experiment I. For the analysis of the recorded temperature data, ACI are used in respect to the result of experiment I to reduce sensor heating.

5.4 Micro-climate monitoring of HES sites (II)

5.4.1 Overview

To monitor environmental conditions that sandstones in Scotland are exposed to, micro-climate measurements at Historic Environment Scotland sites Jedburgh Abbey, Dunkeld Cathedral and Fort Charlotte (Lerwick, Shetland Islands), as well at the University of Glasgow (Garscube Observatory), have been undertaken. The situated sample position varied from site to site due to safety reasons either endangering visitors or protecting the stone from visitors (see Section 5.1).
Humidity and temperature measurements (every 20 min in the first 4 month and then every 40 min for the last 1.5 years) with thermochrons and hygrochrons have been performed over nearly up to two years. This section starts with an overview of the absolute temperature and humidity readings at the different sites. The rate of temperature and humidity

change is then investigated. Changes in temperature are referred to as heating and cooling rates (see Section 5.3). Humidity changes are called wetting and drying rates although the close-by humidity does not actually measure moisture/saturation of a rock and is therefore only an approximation of wetness of the rock. The focus is set on the analysis of the observed environmental changes with respect to the two used stone types (Cullalo and Locharbriggs), aspect (north and south), season (summer and winter) and the different sites.

An overview of the collected absolute temperature measurements of the sites is displayed in Figure 5.9 and Figure 5.10. The displayed temperature data were recorded by iButtons placed on a south facing Cullalo. These recordings enable a nearly continuous temperature and humidity display for the sites. Missing data were caused by iButton failure or where data collection had to be postponed. ACI were used for temperature analysis of all samples and TCI for the humidity analysis.
Humidity readings can be as low as 20%RH in summer, but are frequently high for all four sites (Figure 5.9 and Figure 5.10). The recorded temperatures can go up to 42° C in summer at Jedburgh and Garscube (Figure 5.10). The samples at Dunkeld and the Shetland Islands had to be placed high up at the historic buildings and were therefore more exposed to wind, which could explain why they instead reach up to 33 and 39° C. For the Shetlands of course the ambient temperature is lower which will also influence the micro-climate temperatures (9.6° C average annual high temperature). For Dunkeld the ambient average high temperature is similar to Garscube and Jedburgh with 12.7° C (both averages from Met Office accessed 2017).

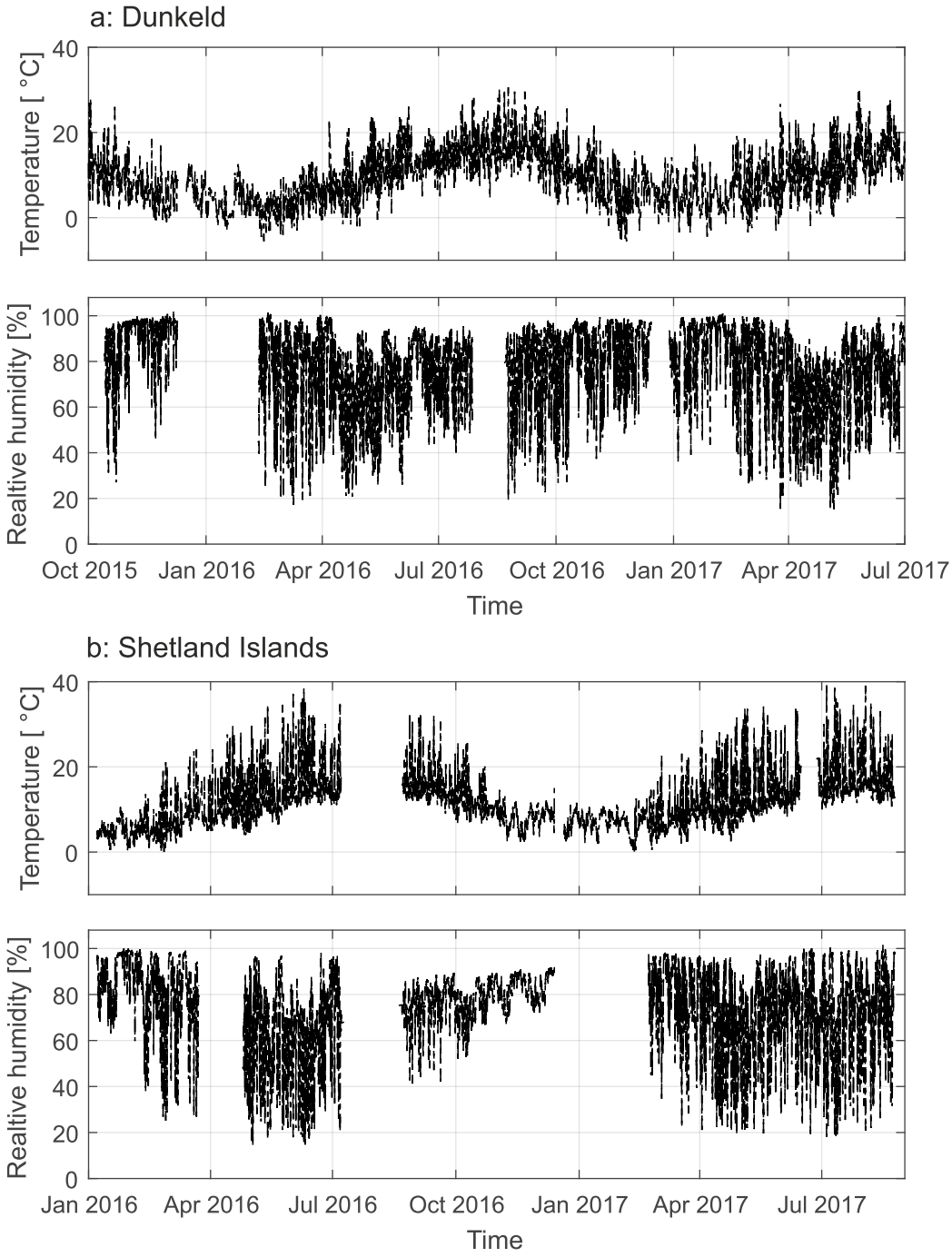

Figure 5.9: Temperature and humidity measurements of ACI and TCI from south facing Cullalo sample (experiment II). The data are recorded every 20 min in the first 4 months and afterwards every 40 min for nearly two years. a: Example measurement at Dunkeld. b: Example measurement at Lerwick (Shetland Islands).

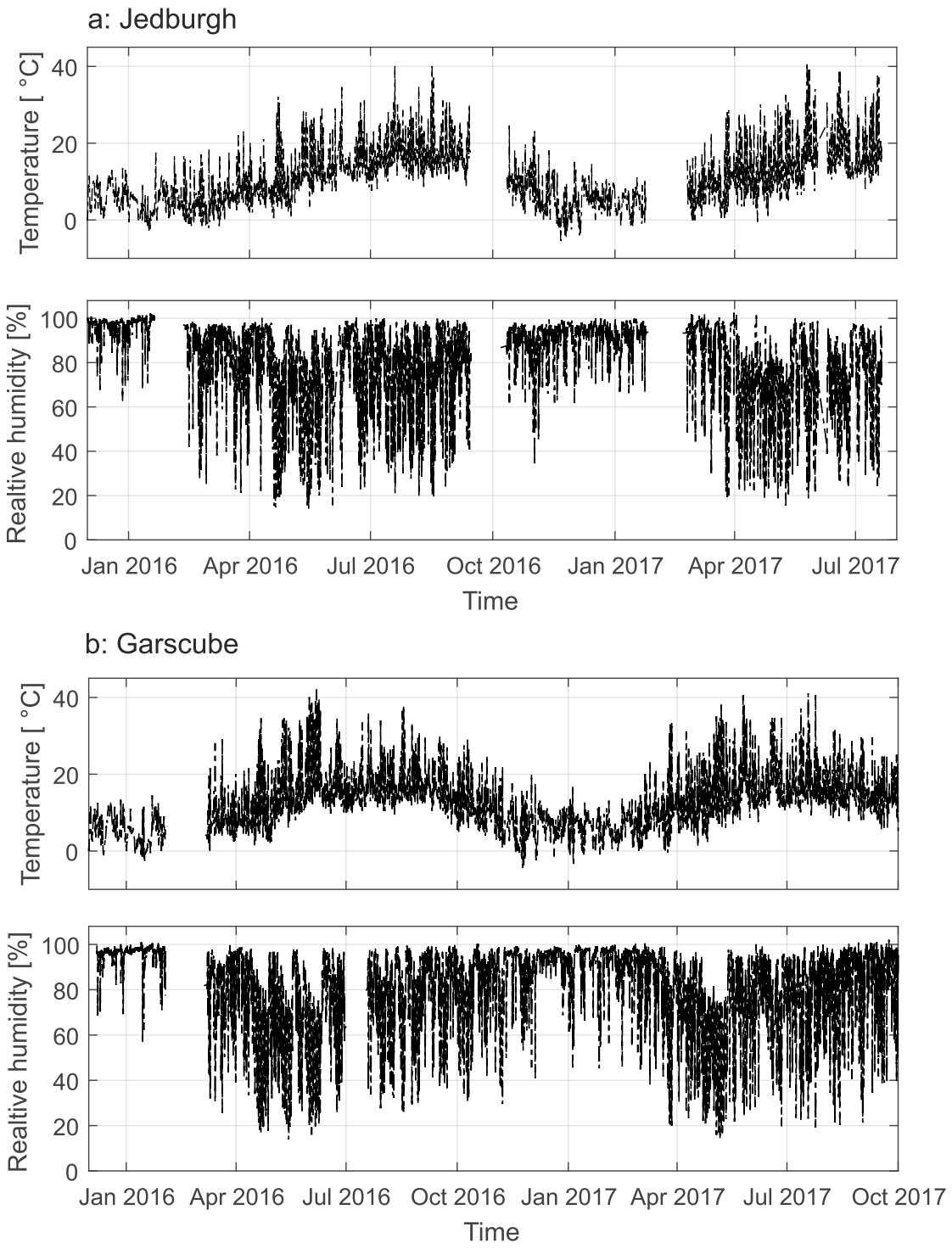

Figure 5.10: Temperature and humidity measurements of ACI and TCI from south facing Cullalo sample (experiment II). The data are recorded every 20 min in the first 4 months and afterwards every 40 min for nearly two years. a: Example measurement at Jedburgh. b: Example measurement at Garscube (University of Glasgow).

5.4.2 Stone type and rate of temperature and humidity changes

For the comparison of the two stone types, Culllalo and Locharbriggs, the rates of temperature and humidity changes were analysed. For a better overview the following analysis combines the results of south facing samples of the four sites into one figure for temperature and humidity measurements respectively. The change is calculated with a sliding time window of 40 min and number of changes summarised in bins of 1° C/40 min (see Section 5.2.2). In the Appendix C, Figure C.1 the temperature changes for the different rock types are displayed for the individual sites.

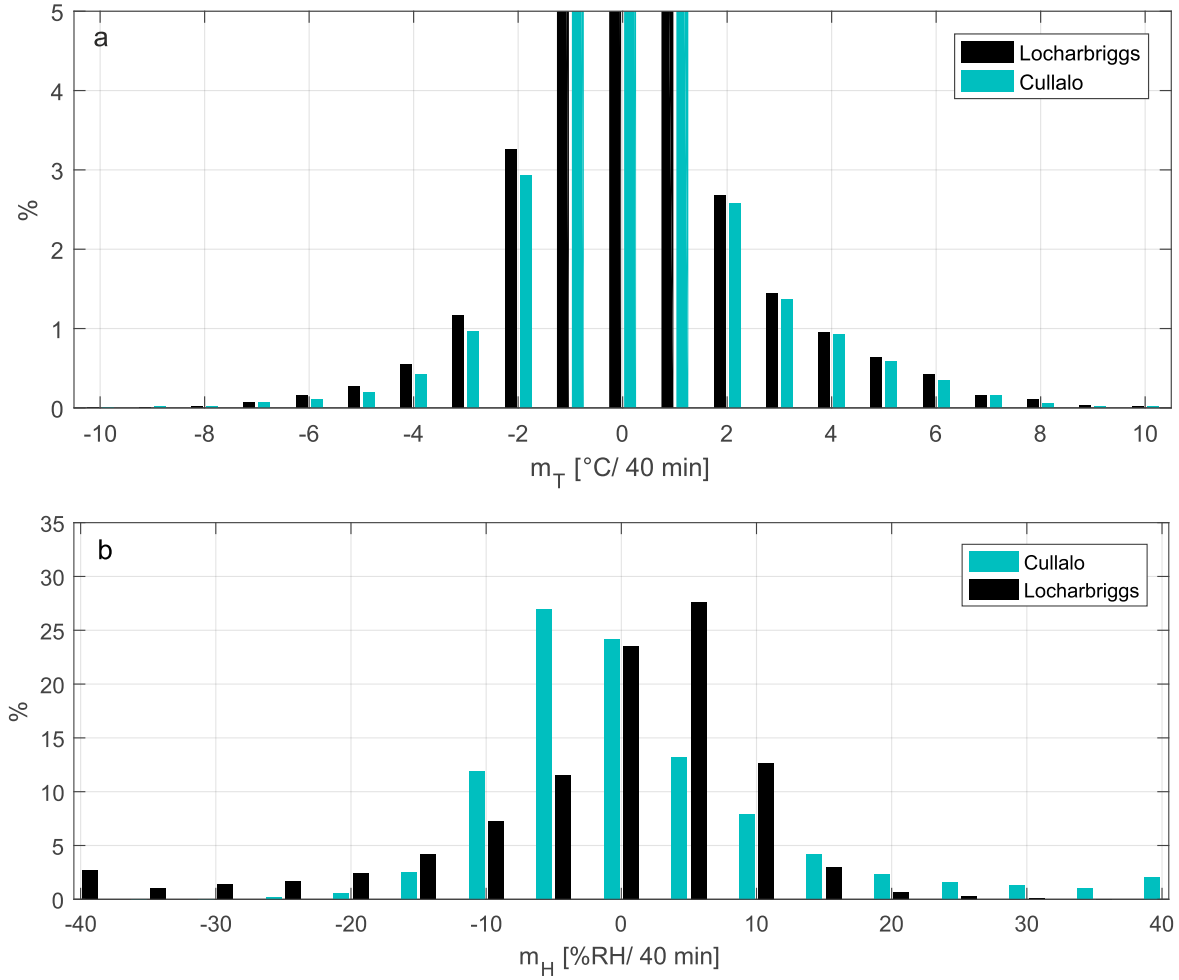

Figure 5.11: Frequency of environmental changes for the two stone types Locharbriggs and Cullalo both facing south at the four sites. a: 5% cut of the less frequent rapid temperature changes. The bin size is 1° C/ 40 min. b: histogram of the humidity changes. The bin size is 5 %RH/ 40 min.

Figure 5.11 shows the frequencies of temperature changes that are less common (<5%). Most temperature changes happen in a range of -2 to 2° C/ 40 min. Rapid temperature changes of up to 10° C/ 40 min are less common. The south facing Cullalo and the south facing Locharbriggs show very similar rates of change (Figure 5.11 a). Despite the different colour and different petrological properties of the rocks, they behave similarly when con-

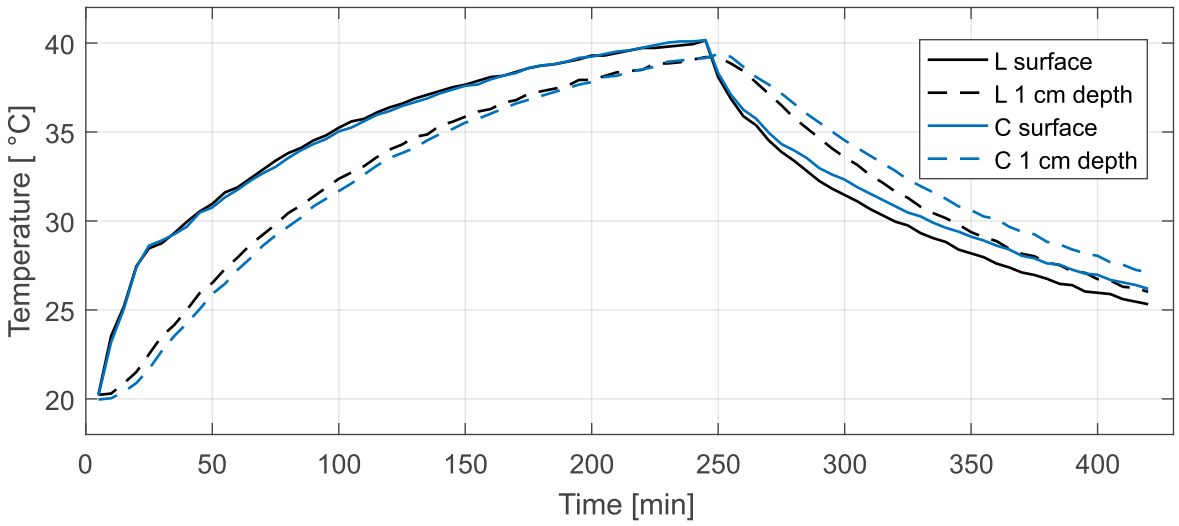

Figure 5.12: Heating and cooling of a Locharbriggs sample (black) and a Cullalo sample (blue) during a small lab trial. The temperature near the surface and the temperature at a depth of 1 cm (dashed line) is measured.

sidering the close to surface temperature variation (heating and cooling, H(2) = 0.08 and 2.77, p> 0.05).

As described in Section 5.2 the emissivity of the two sandstone types is very similar. The similar behaviour was also seen in a small lab investigation, where heating and cooling temperatures of Cullalo and Locharbriggs samples were compared (Turlewicz 2016). Here the samples were heated in an oven to 40° C and then cooled to room temperature (Figure 5.12). The dimension of the test samples was similar (165 x 135 x 90 mm) to the used samples at the sites. One iButton was placed from the back of the test sample inside the sample, so that the depth of the iButton from the surface is 1 cm. Another iButton was placed at the surface of the sample. Furthermore the samples were insulated with Styrofoam leaving one surface open. The iButtons of the different stones recorded very similar temperature data for the heat conducted to the iButton inside the sample as well as for the different surfaces (Figure 5.12).
It can not be excluded that for these sample dimensions and radiative heat transfer, the similar size of the different rock types is the cause of the same behaviour of the stones. At larger scales, for example a whole building wall, other influences such as reflection, adsorption and/or conductive heat transfer might cause different behaviour for the two rock types (see Chapter 1). Other important influences on the close to surface temperature is the moisture of the rock (influenced by its pore properties) and the proximity to the historic building site/wall.

Looking at the humidity for the different rock types, common drying and wetting rates are in between -5 to 5 %RH/ 40 min (Figure 5.11 b). The set range of humidity from 0 to 100%RH

and their changes over 40 min allows the investigation of the whole frequency range rather than a small band (such as the previously studied 5% for the temperature changes). The different rock types show very different changes in humidity. In general Locharbriggs shows more frequent wetting rates around 5 %RH/ 40 min. After 15 %RH/ 40 min rapid wetting rates are less common for the Locharbriggs in comparison to the Cullalo ($H(2) = 5.62$, $p < 0.05$). On the other side, a larger amount of rapid drying rates can be observed ($H(2) = 402.13$, $p < 0.01$). Cullalo shows the opposite behaviour with less frequent rapid drying rates and more frequent wetting rates (Figure 5.11 b). These differences seem surprising at first sight as similar wetting rates would be expected for rain events which should influence the two rocks to same amounts and the two south facing samples were placed next to each other at the different sites. Comparing the results to the small scale measurements with the EUCLID, the displacement changes of a drying Locharbriggs sample reached constant length quicker than the Cullalo (Chapter 3, Figure 3.27). As seen earlier that the difference in temperature changes between the rock type is very small, the difference in drying and wetting must therefore result from the pore properties of the rocks. In Chapter 2 we could see that Locharbriggs has a higher water saturation than Cullalo and a high constant drying rate, which would explain the shape of the two histograms.
The humidity is especially critical as quick drying rates can enhance subflorescence, because the drying front is moved inside the rock. The investigations showed that Locharbriggs samples seems to be more frequently influenced by rapid drying rates. It could be therefore concluded that Locharbriggs samples experience more frequent damage through weathering related to moisture changes than the Cullalo sample. This conclusion was confirmed by Graham (2016).

5.4.3 Aspect and rate of temperature and humidity changes

For the analysis of the influence of the aspect (north and south) of the samples, the south and north facing Cullalo samples of Jedburgh Abbey, Garscube and Shetlands were compared (Figure 5.13). In Dunkeld the position of the north and south facing samples, both at the top of the spire, did not allow to separate the influence of the aspect well. The back of the north facing sample at Dunkeld was reached by sunlight, which will reduce the difference of the north and south facing measurements.

The north facing Cullalo shows in general slower heating and cooling rates than the south facing Cullalo and Locharbriggs samples, of course because of the lack of insolation (Figure 5.13 a). In the south the samples experience more frequent rapid temperature changes ($H(2)= 4.83$ and 3.87, $p < 0.05$).
Looking at the differences in the humidity changes, the north facing Cullalo and south facing Cullalo show very different trends (Figure 5.13 b). It is important here to consider that

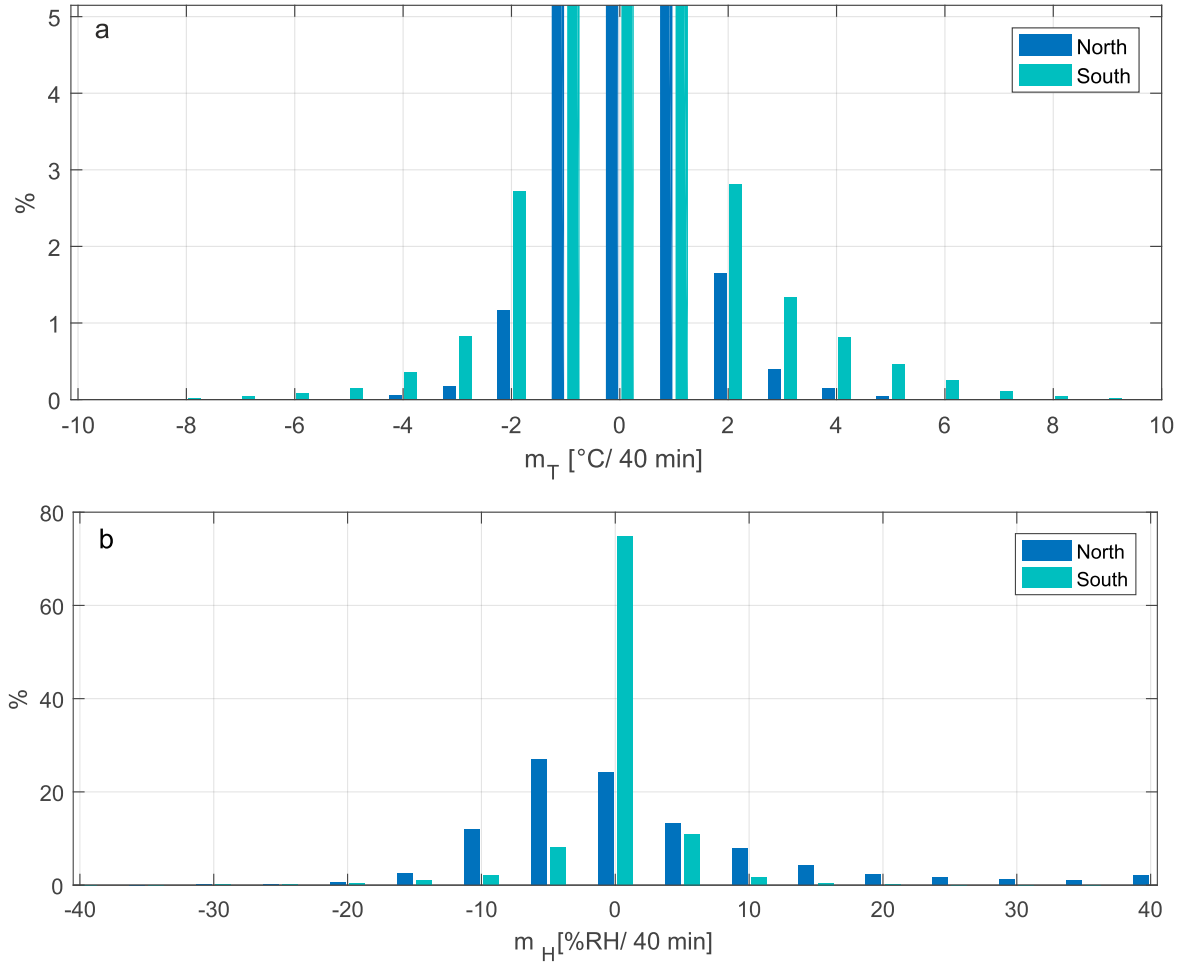

Figure 5.13: Frequency of environmental changes for the north and south facing Cullalo samples at three sites (Jedburgh, Dunkeld, Shetlands). a: 5% cut of the less frequent rapid temperature changes. The bin size is 1° C/ 40 min. b: histogram of the humidity changes. The bin size is 5 %RH/ 40 min.

the north facing samples at Jedburgh and Garscube were sheltered from rain and partially sheltered at the Shetlands. The measurements in Dunkeld can also not be considered because of the position of the two samples at the tower. It is therefore difficult to evaluate the influence of the different aspects on the humidity changes. The south facing Cullalo sample although shows in general very frequent slow temperature changes. This needs further investigation as well as the overall influence of the aspect on humidity changes.

5.4.4 Season and rate of temperature and humidity changes

In the next step the temperature and humidity changes of the south facing Locharbriggs and Cullalo samples of all sites were analysed with respect to the season (Figure 5.14). The data were separated into winter (October to March) and summer (April to September). In summer more frequent rapid temperature changes occur for heating and cooling ($H(2)=5.97$ and 8.02, $p< 0.05$). These rates are more than two times more frequent for the individual steps of temperature change in summer (Figure 5.13 a). For the lower ambient tempera-

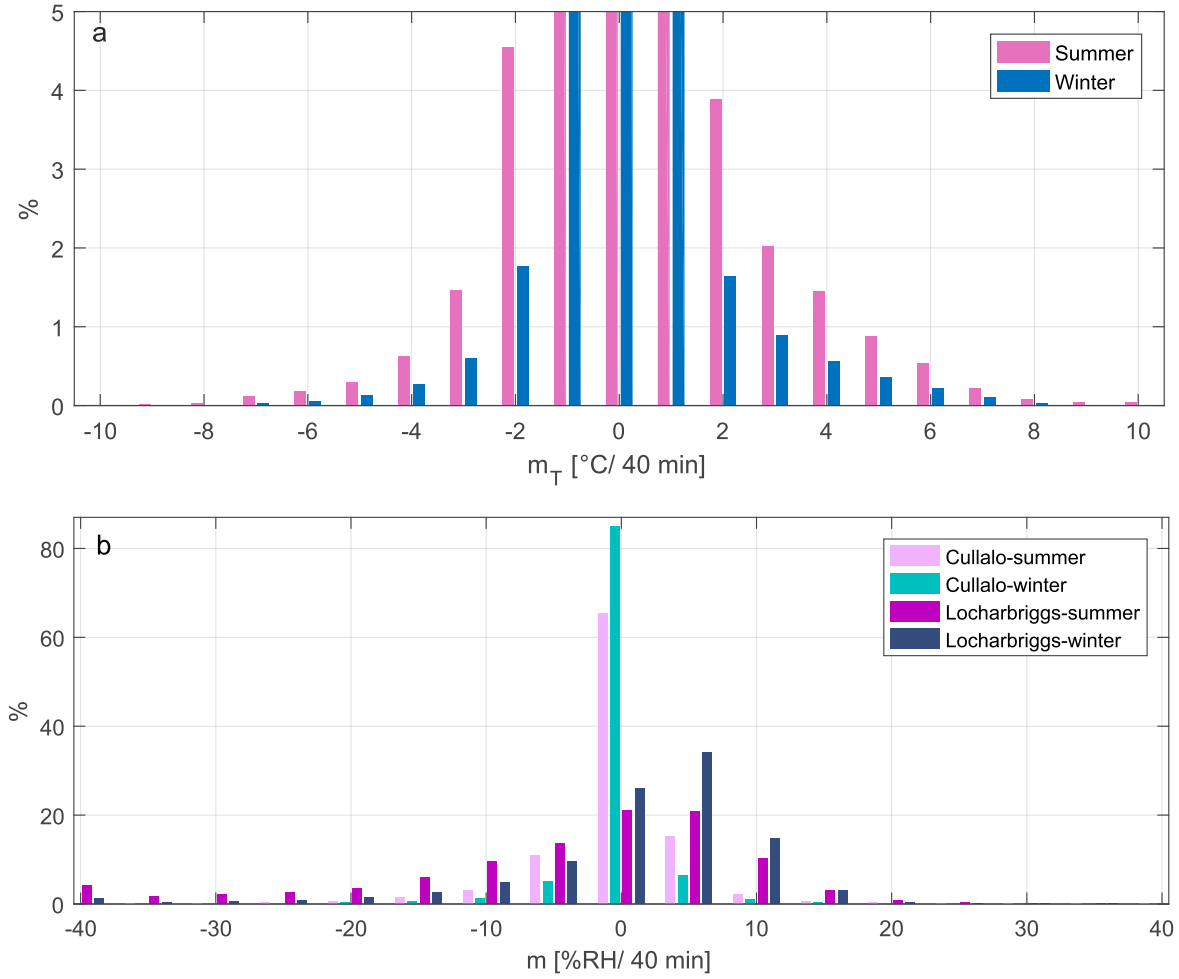

Figure 5.14: Frequency of environmental changes for summer and winter for the south facing samples at four sites. a: 5% cut of the less frequent rapid temperature changes. The bin size is 1° C/ 40 min. b: histogram of the humidity changes. The bin size is 5 %RH/ 40 min.

tures in winter it could have been expected that the insolation has a stronger effect and causes rapid heating of the surface of the sample and rapid cooling as soon as the sun is covered by clouds. It can be therefore concluded that summer month cause more frequent thermal stress events on the samples than winter months. When assessing the influence of the season on weathering in general, the magnitude of damage from for example freezing and thawing events needs to be considered as well as humidity, moisture and other environmental influences.

For the seasonal influence on the changes in humidity, the south facing Cullalo and Locharbriggs samples were analysed separately as they showed different behaviour (Section 5.4.2). In general the Lochabriggs sample shows again more frequent rates of rapid drying than the Cullalo sample (Figure 5.14 b). In summer months more frequent rates of rapid drying are observed for the Lochabriggs samples than in winter months ($H(2)=109.26$, $p< 0.01$). The Kruskal-Wallis test furthermore showed that in summer the Lochabriggs sample experiences significantly more frequent rapid wetting rates than in winter ($H(2)=36.53$, $p< 0.01$).

Rates of rapid wetting are also significant higher for Cullalo samples in summer than in winter (H(2)=7.78 and, $p < 0.01$). For rapid drying rates no statistical differences were found between summer and winter for Cullalo samples (H(2)=0.2, $p > 0.05$).

5.4.5 Site and temperature and humidity changes

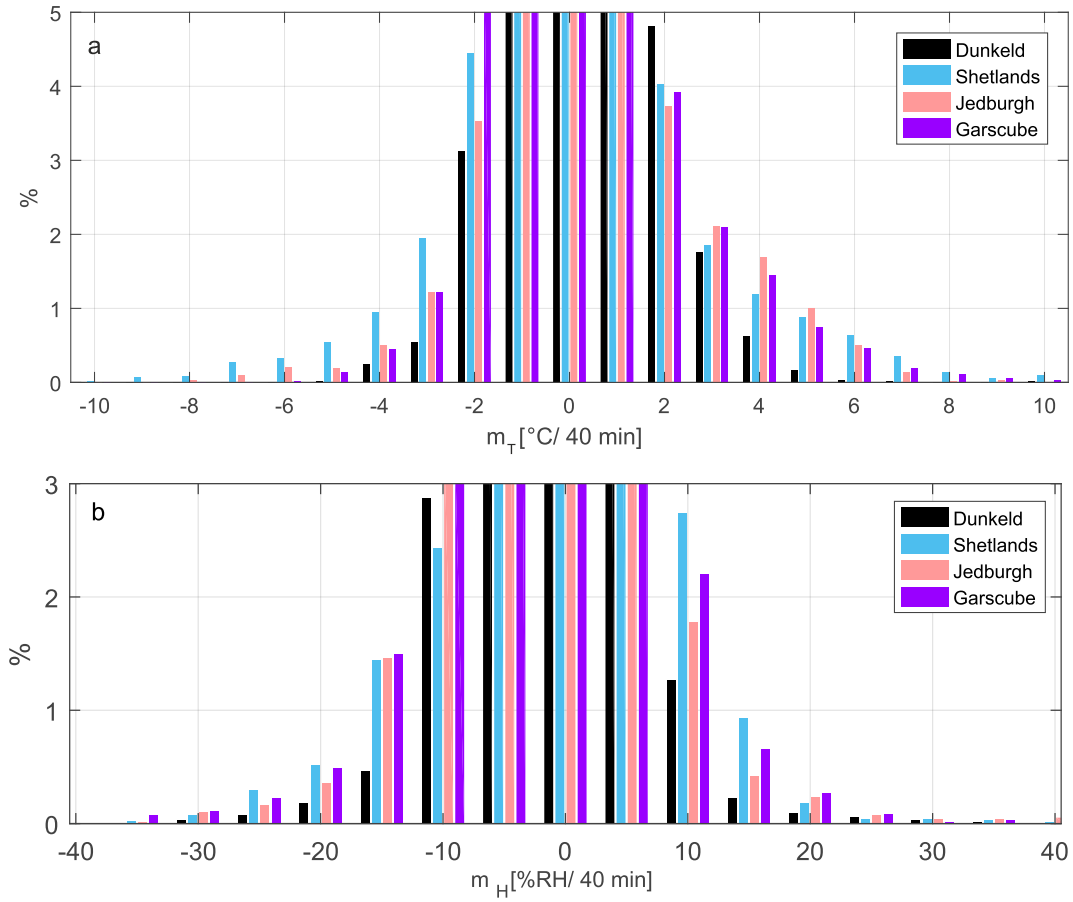

Figure 5.15: Frequency of environmental changes for the different sites of south facing Cullalo samples. a: 5% cut of the less frequent rapid temperature changes. The bin size is 1° C/ 40 min. b: histogram of the humidity changes. The bin size is 5 %RH/ 40 min.

When comparing the temperature and humidity data of the sites, a special focus needs to be on the sample position. The measurements of a south facing Cullalo are compared for the different sites (Figure 5.15). The frequency of rapid heating rates is increased at the Shetlands (H(4)=59.39, $p < 0.01$) and the lowest for Dunkeld (H(3)=9.93, $p < 0.01$). More frequent rapid cooling rates are given for Shetlands and Jedburgh (H(4)=10.89, $p < 0.05$). The samples at Dunkeld are placed at the top of the spire inside small stone windows. It is therefore likely that they have the lowest changing rates as they are most embedded in the historic building/connected to the wall but also exposed to strong winds. The samples on the Shetlands are standing freely on the roof and can therefore lose and gain heat quickly. With the different positions of the samples it is difficult to make a direct comparison of the

conditions at the sites. On the other hands this shows how strongly the position of a sample can influence the rates of temperature changes.
The frequency of rapid wetting rates for the different sites reveals no significant differences ($H(4)= 3.79$, $p> 0.05$). For the rapid drying rates, Jedburgh shows significantly increased numbers ($H(4)=10.89$, $p< 0.05$). The other three sites show no significant differences in rates of rapid drying ($H(3)=0.72$, $p> 0.05$).

Table 5.3: Summary of the findings in the long-term (II) iButtons investigation.

	frequency of rapid ΔT	**frequency of rapid ΔH**
stone type	similar	Locharbriggs: rapid rates of drying more frequent, Cullalo: rapid rates of wetting more frequent
aspect	south: more frequent changes (heating and cooling)	–
season	summer: more frequent rates of rapid changes (heating and cooling)	summer: frequent rates of rapid changes for Locharbriggs and Cullalo (no difference for the seasons in rapid drying rates on Cullalo)
site	rapid heating rates most frequent for Shetlands and rarest for Dunkeld, rapid cooling most frequent at Jedburgh and Shetlands	increased rates of rapid drying in Jedburgh (no other significant differences of the sites)

Table 5.3 summarises the results of experiment II with the influence on the rates of temperature and humidity changes by the stone type, aspect, season and site. Figure 5.16 combines the influences of stone type, aspect and season into one figure. It can be seen that the most frequent rapid temperature changes occur for the south facing Locharbriggs in summer month followed by the south facing Cullalo in summer. Interestingly they are followed by the south Cullalo and Locharbriggs in winter months before the north facing Cullalo. This suggests that the aspect of the building stone influences the rates of rapid temperature changes more than the seasonal influences. For the changes in humidity the stone type influences the frequency of rapid humidity changes more than seasonal influences. Lochabriggs has the most frequent rapid drying rates and Cullalo shows the most frequent wetting rates. (Again for the aspect further investigations are needed.)
The investigations with the iButtons can therefore be used to identify times and areas of high environmental stresses for building stones and therefore allow predictions of the damage in those areas. To evaluate these results further a closer visual investigation of the historic building sites was undertaken.

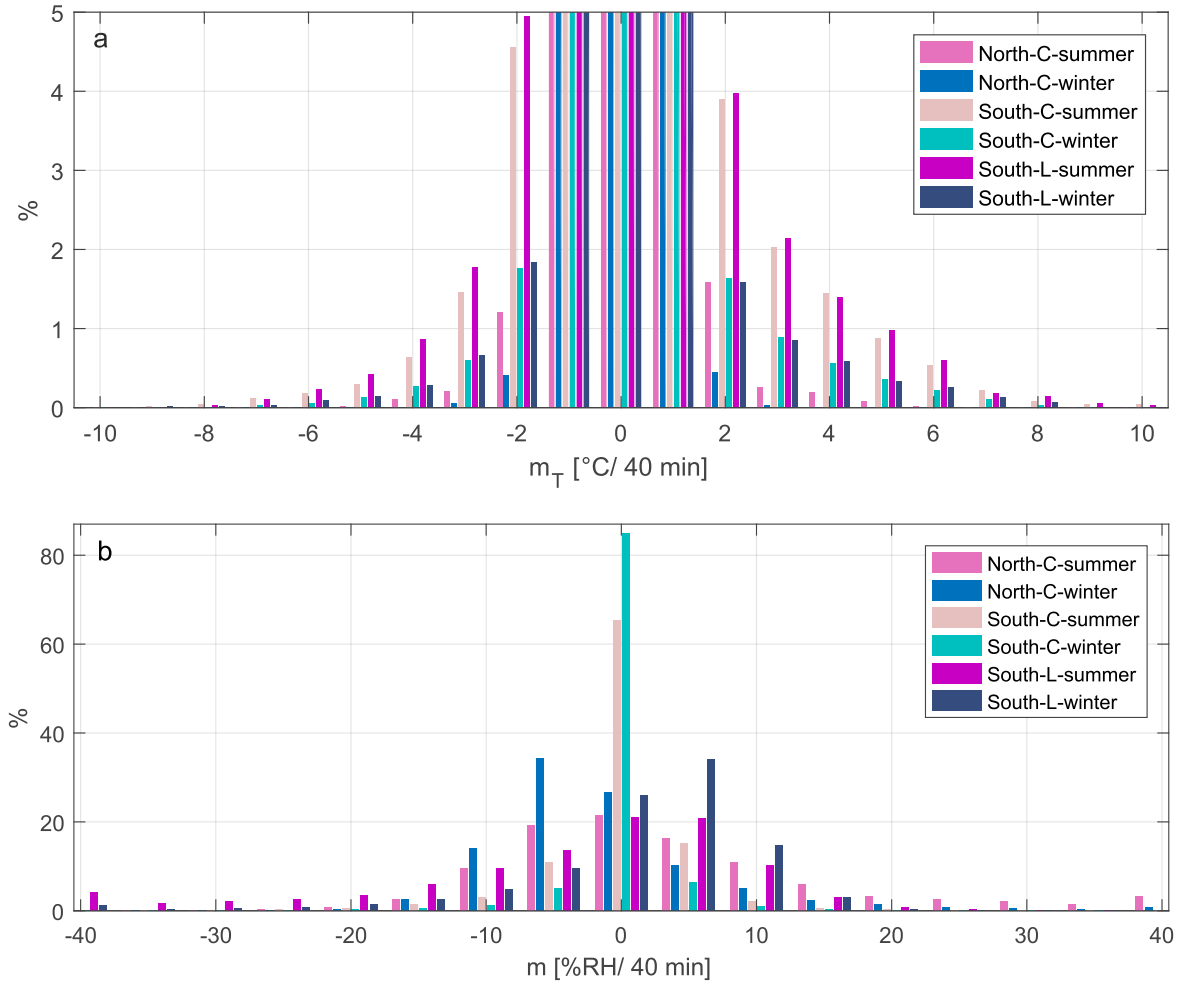

Figure 5.16: Frequency of environmental changes for the different samples, aspect and season. a: 5% cut of the less frequent rapid temperature changes. The bin size is 1° C/ 40 min. b: histogram of the humidity changes. The bin size is 5 %RH/ 40 min.

Stability of Na_2SO_4 at the sites

To evaluate which influence the temperature and humidity changes have on the building stone, an example calculation was made for the phase stability of one of the most damaging building stone salts, Na_2SO_4 (see Chapter 1), although the salts occurring at the different sites have not been analysed. When thenardite (Na_2SO_4) changes to mirabilite ($Na_2SO_4 \cdot 10\,H_2O$) a volume increase three times larger than before the hydration can be observed (Laue 2002). This change from thenardite to mirabilite is described as phase change 3∗ in the phase diagram of sodium sulphate (Figure 5.17 a). The number of phase changes is calculated for the different sites for the recorded temperature and humidity of a south facing Cullalo sample over one year. Several influences on this calculation have to be considered. First the sampling frequency of the iButtons was 40 min. Some phase changes might not be covered by this time window in the calculation as they could appear within

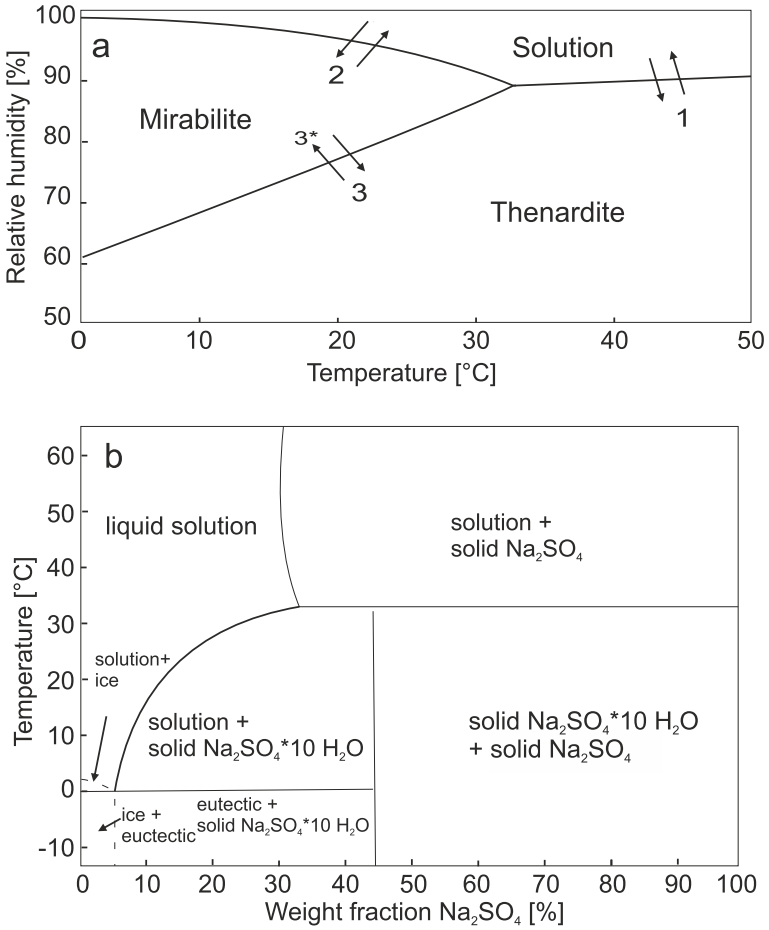

Figure 5.17: Stability of sodium sulphate. a: Phase diagram of sodium sulphate with the phase change of thenardite (Na_2SO_4) to mirabilite ($Na_2SO_4 \cdot 10\,H_2O$) marked as 3*. b: Partial phase diagram of the sodium sulfate water system after Biswas (1977).

the 40 min sampling rate. As mentioned earlier the close-by humidity is used to approximate moisture contents of the stones and might not reflect internal moisture and therefore exactly when phase changes occur inside the stone. Phase change 2 is approximated with a linear transition. Aside from this, the actual water content inside the rock is unknown. In Figure 5.17 b the influence of Na_2SO_4 with its fraction in water is displayed depending on the temperature. Considering that the salts will be in solution when the stone is actually wet the calculated frequencies for phase changes should be lower. With an increasing temperature the solubility of Na_2SO_4 also increases which further lowers the amount of actual phase changes.

Table 5.4 shows the phase changes with the assumption of Na_2SO_4 not in solution. Phase change 1 (solution-thenardite) is the less common change as it involves high humidities at high temperatures. Phase change 2 (mirabilite-solution) is frequent at Garscube and Jedburgh involving high humidities. This could be due to the ground/wall position of the sample. For all sites phase change (3) is common. Giving this calculation, highly damaging

Table 5.4: Number of approximated phase changes of sodium sulfate for the different sites analysed for a south facing Cullalo sample over one year.

Phase change	1	2	3	3*
Dunkeld	92	450	620	296
Shetlands	69	329	577	305
Jedburgh	100	740	415	224
Garscube	103	751	428	237

phase changes of thenardite to mirabilite occur most frequently at the Shetland Islands and Dunkeld.

Building stones at the sites

Similar building stones and time frames of exposure need to be assessed to compare the weathering potential of the environmental conditions at the monitored sites. This can be very challenging as most sites are characterised by the proximity of the quarry for the building stones used. A chance to observe the behaviour of the same stone at different sites is sometimes given through the replacement stones. An example can be seen on the Shetland Islands and at the University of Glasgow. A popular replacement stone, Stanton Moor, was used 25 years ago at Lerwick town hall (Shetlands) and over the last few decades (including as recently as 2017) at the University of Glasgow main building.
The Stanton Moor samples at Lerwick already show signs of decay (Figure 5.18 a+b), which include scaling and sanding especially at the south-west facing corner of the building (see ICOMOS 2008 for types of weathering). The closeness to the sea and strong winds at the site likely cause a quick deterioration of the replacement stone, which is vulnerable to subflorescence (Graham 2016). At the main building of the University of Glasgow, Stanton Moor has not shown any severe signs of deterioration (Figure 5.18 b).

As described in Chapter 2 the mineralogical properties of the building stones at the sites differ and strongly determine the durability of the rock. Differences in aspect can also be compared for the individual buildings to evaluate this effect on rock durability. Considering the strong influence of the different aspects on temperature changes, the weathering at the north and south facing walls at the sites were evaluated. Parts of the sites are ruins, which will not allow a clear separation of the influence of the different aspects.
To compare observations of stone decay at the historic building sites to the monitored data, visual examinations of weathering were made. The building stones at Dunkeld Cathedral are strongly decayed. Replacement works are undertaken at the whole site. In Dunkeld the south facing and north facing walls show severe signs of damage. Sanding up to the complete detachment of the rocks is common along all building sides. Especially the tracery of

Figure 5.18: Stanton Moor used as a replacement stone at Lerwick town hall, Shetland islands and the University of Glasgow. a: Delamination (D) around the tracery at Lerwick town hall. Sanding (S) can be observed at the quatrefoil (around the window glass) and b: at the frame of a south facing window. c: Stanton Moor replacing the original stone at the bottom of a column at the cloisters at the University of Glasgow.

the south facing side is highly deteriorating (Figure 5.19 a). When comparing the south and north facing walls it has to be considered that the north wing of the cathedral suffered from a fire and shows a darker black crust than the black crust that can be seen on the south side (Figure 5.19 c+d).

At Fort William on the Shetland Islands, the comparably young site (see Chapter 2) shows mainly a dark crust and sanding. Severe damage can be found at the south facing windows (Figure 5.20 a+b) whereas the north facing window frames are only showing sanding. At the south and south-west entrance lamination and scaling are common (Figure 5.20 c+d). The whole fort shows black crust and efflorescence of other salts.

In Jedburgh several local different building stones were used and show different stages of weathering. The original, layered, clay rich sandstone, that was especially used for the cellars in the south, is strongly decaying (Figure 5.21). In the centre of the Abbey some stones are completely intact (Figure 5.21 a). Replacement works were done in the last century at the Abbey itself mainly at the south side. The walls that are still standing in the south show

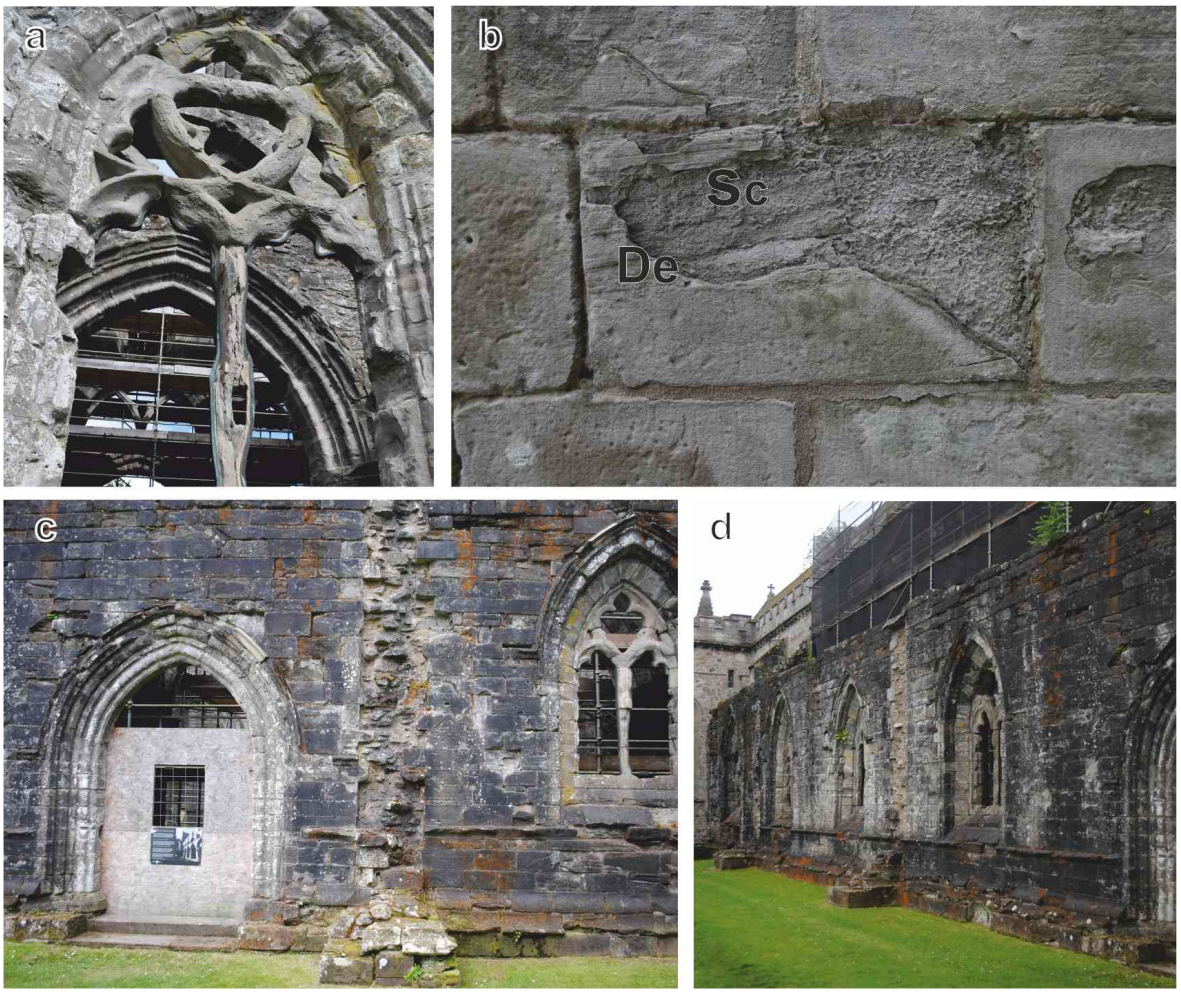

Figure 5.19: Dunkeld Cathedral. a: Badly decaying tracery at the south side of the cathedral. b: Close up of the original (locally quarried) sandstone showing advanced scaling (Sc) and detachment (De) of the stone. c: Dark crust on the south facing facade and d: black crust at the north facing facade.

sanding, scaling and alveolisation (Figure 5.21 b+c). At the north facing side of the abbey scaling and flaking are most common (Figure 5.21 d).
At the University of Glasgow weathering also occurs at varying stages because of the different building stones. Efflorescence appears even on recent buildings (Figure 5.22 a) due to wrong placement of a water impermeable layer. Older parts of the building near Pearce lodge at the east face show severe decay including subflorescence that cause complete detachment (Figure 5.22 b). The south side mainly suffers from black crust and the poor durability of one of the building stones that is being replaced (Figure 5.22 c+d).

All sites indicate an increased progress of weathering at the south facing facades. The progress of weathering is mainly dependent on rock type. The same results were shown for the long term monitoring (experiment II) of temperature and humidity. Both environmental conditions can be used to deduce areas of increased damage at the building sites.

Figure 5.20: Fort Charlotte (Shetland Islands). a: Sanding (S) and flaking (F) on a south-west facing window frame. b: Alveolisation (Av) and peeling (P) on a south-west facing window frame. c: Efflorescence (Eff), exfoliation (Ex) and delamination (De) on at the south-west entrance. d: Efflorescence (black crust), blistering (B), scaling (Sc)and abrasion (Ab) at the south entrance.

Figure 5.21: Jedburgh Abbey. a: Centre of the Abbey with different local building stones showing very different states of decay. b: South facing wall showing scaling (Sc), sanding(S) and rounding (R). c: Alveolisation (Av) at the south side columns. d: Sanding (S), flaking (F) and delamination (De) of the different building stones at the north facing facade.

Figure 5.22: Glasgow University main building. a: Efflorescence (Eff) at the James Watt building (south-east). b: Subflorescence (Sf) nears Pear's lodging (south-east). c: Black crust, delamination (De) and scaling (Sc) of the Gilmorehill building stones (see Chapter 2). d: Replacement of the Gilmorehill building stone at the south face of the tower.

5.5 Future work

This Sections covers the identified limitations of the investigations and the resulting future work for the different experiments as well as further applications and experiments related to micro-climate monitoring.

Cover experiments (experiment I)

- Combination of Tyvek and aluminium foil
  The performance of hygrochrons with a combined cover of aluminium and a smaller piece of Tyvek should be evaluated with respect to sensor heating/trapped heat.

- Investigation on the lifespan
  New iButtons with covers worked very well for nearly 2 years in comparison to used iButtons with covers. This needs to be confirmed in further long term studies of uncovered and covered, but importantly, unused iButtons. The good performance of the unused/new Buttons might have only been due to the fact that these iButtons had not been used previously and not due the covers. In addition a test with different covers and new iButtons under extreme conditions (for example cyclic freezing and/or wetting) could gain quicker results to evaluate lifespan, but will be expensive and needs to be assessed for its applicability from lab to field conditions.

Evaluating micro-climate monitoring (experiment II)

- Evaluation of iButtons for micro-climate monitoring
  Next steps improving the evaluation of the potential of iButtons for micro-climate monitoring should include extended data collection from a weather station (ambient temperature, humidity, wind speed and wind direction), accompanied by the surface temperature and solar irradiance measurements in comparison to iButton surface measurements. The extended data can be used to determine the influence of solar irradiance with regard to other determining factors such as wind speed and ambient temperature. This will allow to make exact predictions of the conditions stones are exposed to at the sites. The tests could expand to different sample sizes up to a whole stone wall for varying season and different aspects (north, east, south and west).
  Another focus should be set on the moisture content of the rock and how the content can be approximated by the close-by humidity measurements. Again the influence of wind, solar irradiance etc. needs to be determined.

- Site comparison
  To evaluate micro-climate conditions of different sites, the positioning of the samples should be comparable. This could include sheltered iButtons next to iButtons at the top of the sites and/or close to the ground to cover a variety of locations at the

building. When the ambient temperature and the micro-climate of an unweathered reference stone is known, the comparison of those to the local micro-climate could indicate the state of decay of the building stone. Further investigation to confirm this approach should be undertaken.

- Statistical analysis
  The relation or dependence of the analysed influences could be tested such as humidity influence on temperature readings of different stone types. Carter & Viles (2003) showed that the thermal gradients of surfaces decrease when the samples are moist. In this case this would mean that the wetter stone has less frequent high thermal gradients and therefore eventually less frequent rapid drying rates.
  Further data needs to be gained to investigate the influence of the different aspects on the humidity changes of rocks.

Further application

- Building investigations
  The micro-climate data could help to develop a model of high stress/high weathering areas on buildings to identify areas that need special attention for the preservation of the building stone. The model would pay special attention to the building material, aspect, building shape, wind direction, moisture movement to determine with small scale investigations the micro-environment of the whole building.

- Reburial
  Another possible application for the use of the iButtons would be to test micro-climates for reburied building material. Reburial or *backfilling* is a common practise for stones that highly decay to preserve them better underground (Demas 2013). In Jedburgh parts of the original south facing cellars are already reburied to stop the extensive decay of one of the clay rich building stones. The iButtons with the Tyvek cover could be buried at different depths attached to a plastic string that can be easily retrieved when collecting data. The performance of the Tyvek covers under these condition could also be evaluated.

- Salt damage
  Long term monitoring of temperature and humidity can approximate possible phase changes of building stone salts. An investigation with local sample material and the content of salt minerals could test how well the prediction from the calculated phase changes matches the actual salt damage/content of the local building stone.

- Assessing conservation methods
  Conservation methods that influence temperature and wetting profiles or moisture contents of building stones could be monitored. Such treatments include, for example,

Phase Change Material or silicon based consolidants (Kyriakou et al. 2017, Karatasios et al. 2017) as well as coverage of monuments in winter, roofing for rain protection or other large scale reparation works (Rüdrich, Rieffel, Pirskawetz, Alpermann, Joksch, Gengnagel, Weise, Plagge, Zhao & Siegesmund 2011, Demas 2002).

- Used stone samples
  The state of decay of the used Locharbriggs and Cullalo samples that were placed at the sites could be checked in depth as no visual deterioration could be observed. This could for example include tests with the newly developed ultrasonic drilling tool, laser interferometer, SEM, XRD and/or porosimetry.

5.6 Summary

Two experiments were conducted with small and cheap temperature and humidity sensors (iButtons). Experiment I focussed on the evaluation of the performance of two covers for iButtons. The aim of the covers was to minimise sensor heating and additionally to increase lifespan. An aluminium cover for thermochrons and a Tyvek cover for hygrochrons were compared over a 6 week trial in winter/spring to uncovered iButtons. The focus is set on the analysis of the frequency of rapid temperature changes, thus rapid heating and cooling rates over one hour. During the trial iButtons with different covers were suspended in air or glued to a Locharbriggs sample with the size of (15 x 8 x 8 cm). The aluminium covers reduced sensor heating compared to uncovered iButtons. High heating rates of 6° C/hour are more than two times more frequent for the uncovered iButtons than the aluminium covered iButtons. This effect was stronger for freely hanging iButtons than for the iButtons placed on a Locharbriggs sample due to the interaction of the close to surface iButton temperature with the sample temperature. The aluminium cover did not influence rapid cooling rates of the iButtons in comparison to uncovered iButtons. Tyvek covered and uncovered iButtons did not show a significant difference in the rate of heating although the Tyvek covers slighlty increased the frequency of high heating rates most likely caused by trapped heat.

Long term monitoring over nearly two years at four different HES sites was undertaken in experiment II. There it was assessed how rates of temperature and humidity changes are influenced by stone type (Locharbriggs and Cullalo), aspect (south and north) and season (winter and summer). The frequency of rapid temperature (>4° C/40 min) and humidity changes (>15%RH/40 min) can identify areas and times of high stress for the building stone. The used stone types did not influence temperature changes significantly. As shown in Hall et al. (2005) albedo-controlled thermal differences can not just be assumed for varying rock types. Frequent rates of rapid heating were more common for south facing samples and during summer. This was expected due to the difference in insolation and was, for exam-

ple, shown in McIlroy de la Rosa et al. (2013). In general the highest changing rates can be observed for the different aspects in summer. When comparing the seasonal data with aspects, aspect influenced temperature data more than the season. More frequent rates of changes are observed for winter months of south facing samples than for summer months of north facing samples.
Changes in humidity are strongly influenced by the stone type and also by seasonal changes. Locharbriggs shows more common rapid 'drying' rates whereas for Cullalo rapid 'wetting' rates were more common. In summer both samples experience more frequent rapid changes in humidity. For rapid drying rates no seasonal difference could be observed for Cullalo samples. In general rapid 'drying' rates are most common for south facing Locharbriggs samples in summer and winter, where its winter drying rates still exceed the drying rates of the summer measurements of Cullalo. Measurements during the different seasons show clear differences but again stone type is the main influence on the humidity changes. Previous studies underline the importance of all environmental conditions, such as wind direction and speed, for the evaluation of seasonal influences on the rock weathering (Basheer et al. 2008, Carter & Viles 2003). Trends observed here are as discussed specific for the rock type, size and site location.
Monitoring the micro-climate with just temperature and humidity data nevertheless allows the identification of areas with increased risk of weathering and can help to decide on the best pinpointed conservation strategy/investigations for those areas.

Observations at the sites confirmed the strong influence of the aspect and the type of building stones. An increased progress of weathering at the south side was especially observed at Jedburgh Abbey and Fort Charlotte on the Shetland Islands. The oldest parts of Dunkeld Cathedral show severe damage at the whole site. The University of Glasgow is a comparably young site and shows subflorescence at some south-east facing facades of the main building. The used building stone of the sites strongly determines the rate of decay. A good example is Jedburgh Abbey as the very different local building stones show weathering at variable states of decay.

Chapter 6

Summarised implications and conclusion for decay investigation

This thesis has presented a multidisciplinary approach to assess the state of decay of building stones. Three different lab or field techniques were developed and applied. The main results of these techniques are described below.

In Chapter 3 the application of a non-destructive tool was investigated to monitor length changes of building stones that indicate subsurface decay. A laser interferometer (EUCLID) was used to measure the expansion and contraction of sandstones at a subnanometre scale. Its high resolution enables dilation experiments where little sample material is available. Drying tests with water saturated sandstone samples showed that their behavior can be used to distinguish between different properties of sandstones such as porosity and permeability. The same differentiation was made for both weathered samples from two historic buildings (Dunkeld and Jedburgh) and artificially weathered sandstones (Cullalo, Locharbriggs and Stanton Moor). The sandstone's state of decay was inferred from the interferometric measurement of the displacement. This method was especially useful to analyse the Stanton Moor samples which are prone to subflorescence. The contraction coefficient after water saturation of an artificially weathered Stanton Moor sample was higher than 3 mm/m during drying over 90 hours. In comparison the drying of an unweathered Stanton Moor sample indicated a contraction coefficient of around 0.3 mm/m. Analysis of the frequency of displacement events did not indicate any characteristic signal that would enable deduction of the type or amount of weathering. This approach needs further investigation as the joint measurement of total displacement and frequency of displacement events shows promise as a quick and comprehensive analysis of building stone decay.

In Chapter 4, a minimally invasive tool was developed to identify stone decay below the surface. The ultrasonic drilling tool (UAD) was used to drill holes with a diameter of 3 mm in samples while the tool's power consumption during drilling is monitored. In comparison to other commercially available drilling tools for material investigations, the UAD has several

advantages: the use of ultrasonics enables easy penetration of different types of building stones; the change in power consumption during drilling can be used as a feedback signal to distinguish stone types; the average force exerted on the sample is low, which is beneficial for penetration of brittle building materials; and hard building stones (UCS above 90 MPa) can be drilled easily without change of operational setting. The drill allowed better comparisons to be made between different types of stones: structural and mineralogical changes in the rock below the surface could be located; and the depth of weathering was mapped for artificially weathered rocks with NaCl and Na_2SO_4. It was shown, furthermore, that the use of ultrasonics has a lower wear effect on drill bits. The increased lifespan of the drill bit over commercially bought PCD bits reduces maintenance costs of the tool. Although the performance of the technique was only demonstrated in the lab, ultrasonic drilling shows great potential to be used in field; future work should therefore investigate the design of a portable tool.

In Chapter 5, micro-climate monitoring was conducted at four historic buildings in Scotland: the University of Glasgow, Dunkeld Cathedral in Perthsire, Jedburgh Abbey in the Scottish Borders and Fort Charlotte in the Shetland Islands. Rapid temperature and humidity changes promote decay as they are the main drivers of weathering. So-called *iButtons* were employed to monitor humidity and temperature changes at the four sites to identify areas that are endangered by frequent and rapid rates of environmental change. The compact data loggers were glued to the surface of sandstone samples to measure the conditions that the stones are exposed to over approximately two years. The collected data was examined with respect to each samples' aspect (including south and north), seasonal changes (summer and winter) in each location, and the stone types used (Cullalo and Locharbriggs). The two investigated sandstone types did not have a significant influence on measured temperature changes over 40 min. For the measured changes in humidity, however, the stone types showed very different behaviour. Locharbriggs for example experienced more frequent rates of rapid 'drying'. Seasonal changes caused different rates of temperature and humidity changes. Samples facing south and samples during summer months experienced more frequent and rapid rates of temperature and humidity change in comparison to the winter months. South facing stones in winter showed more frequent temperature changes than north facing stones in summer.

A second experiment investigated the performance of two protective covers of iButtons in comparison to uncovered iButtons. An aluminium cover reduced the number of rapid temperature changes, whereas a Tyvek cover did not show significant differences to uncovered iButtons.

Combined approach of the techniques

The three techniques presented in this thesis enable a precise characterisation of stones in historic buildings. At the start of a combined investigation with the tools, micro-climate

monitoring should be conducted over at least several weeks in the summer months with a focus on the south facing areas of sites. The environmental monitoring can identify areas of the building that need special attention or an increased survey with other NDT tools. In the areas experiencing high rates of temperature and humidity changes, the laser interferometer could be installed to monitor displacement changes after a wetting and drying event. Different temperature and humidity regimes, that would be beneficial during the monitoring with the interferometer or drilling tool, can be deduced from the long term micro-climate monitoring to decide on the best time scale for the analysis. For the investigations with the EUCLID, high rates of changing temperature and humidity would be of most interest. The tool should be placed on a south facing wall to investigate strong temperature differences and in the north and south of a building to monitor high rates of changes in humidity. The laser interferometer can be installed for short term measurements over night to see how much the stone is expanding and shrinking. Long term measurements can be used to survey the movement of the rocks over years.
Depending on the environmental conditions, different salts are crystallised or in solution. For example, May showed the driest conditions during this investigation and could be used for drilling tests. The ultrasonic drilling tool can be used to give a quick characterisation of the subsurface decay in identified areas. This could be conducted during and after water saturation of the rock to estimate the amount of salt crystallisation under changing environmental conditions. This test could be performed under varying moisture conditions of the rock to gain further insight of the structure of the building material and its salt phases. These results can then be directly linked to the observations from the interferometric measurements during drying and wetting to warn of imminent failure.

Further combined applications of the techniques

Further applications of these three techniques combined could include on-site evaluation of conservation methods. Conservation methods that induce structural and/or mineralogical changes and therefore alter the properties of the stone can be studied in detail. Such methods include, for example, the use of consolidants, biomimetic apatite, clay swelling inhibitors, borax induced controlled crystallisation, or various kinds of desalination techniques. Combining these approaches can deliver quantitative results and directly compare the impact of the treatment. The drill tool can be used to identify structural changes caused by a treatment. The use as a portable tool can enable conservators to obtain a quick on-site evaluation of subsurface damage, for example from beneath black crusts. The laser interferometer would monitor the increase or decrease in dilation behaviour after salt removal or other treatment. The iButtons can also identify changes in wetting profiles or moisture contents caused by treatment with borax, or similar conservation strategies. The treatment of porous building stones with *Phase Change Material* or silicon based consolidants is espe-

cially applicable for monitoring with iButtons as they induce changes in temperature and humidity profiles. The quality of other interventions at the building sites can, furthermore, be studied, such as coverage of monuments in winter, roofing for rain protection or other large-scale reparation works.

Using these three minimally invasive techniques can locate areas of increased decay, which can help tailor the best conservation strategies for individual rocks and walls of historic buildings.

Appendix A

Sample methods

A.1 EDX map

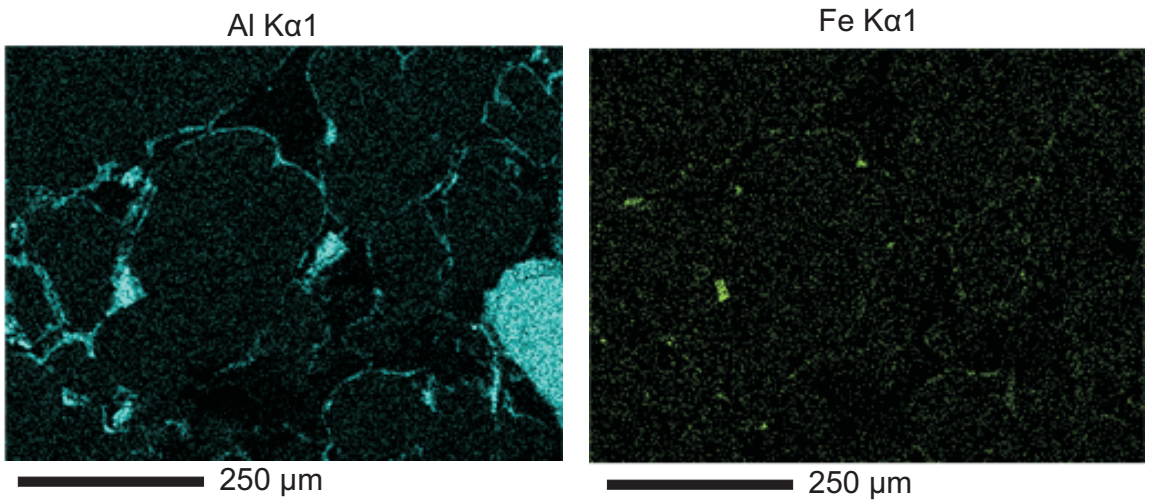

Figure A.1: EDX map of a Locharbriggs sample. In blue are the counts for aluminium (accumulating around the grain boundaries) and in yellow the counts for iron.

A.2 XRD results

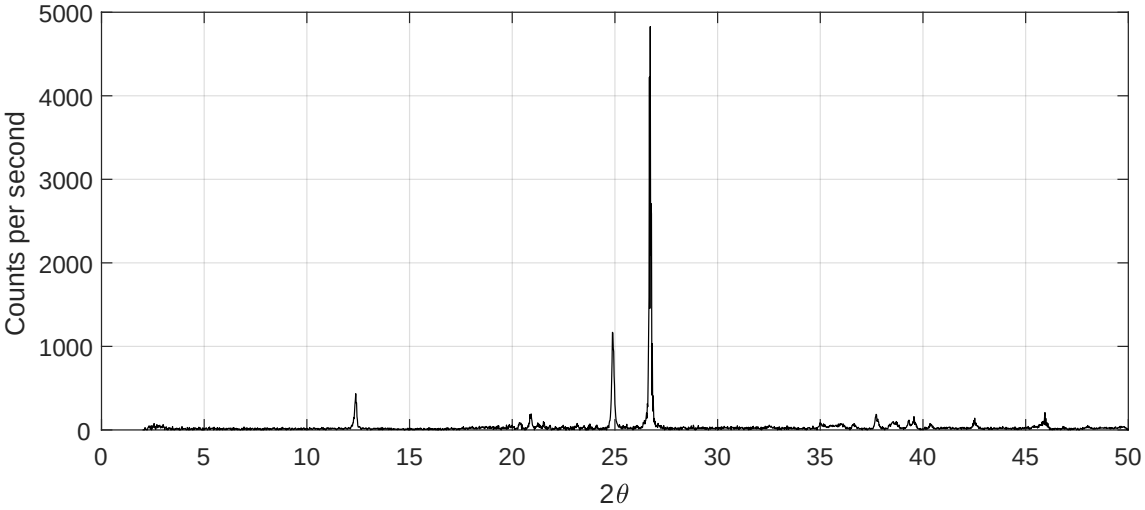

Figure A.2: XRD of the clay Cullalo sandstone: Counts per second for 2θ scan with 0.02°steps.

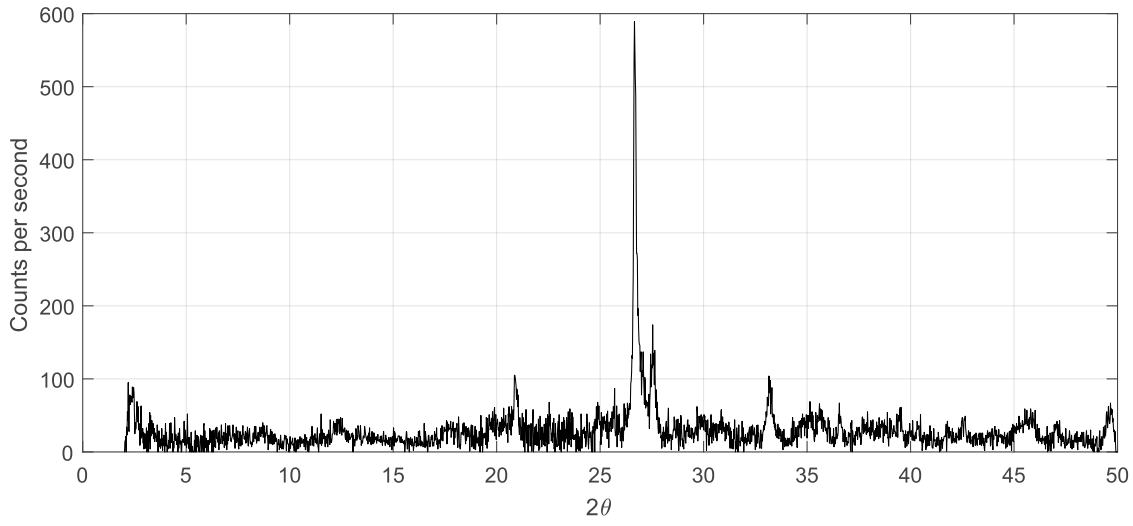

Figure A.3: XRD of the clay Locharbriggs sandstone: Counts per second for 2θ scan with 0.02°steps.

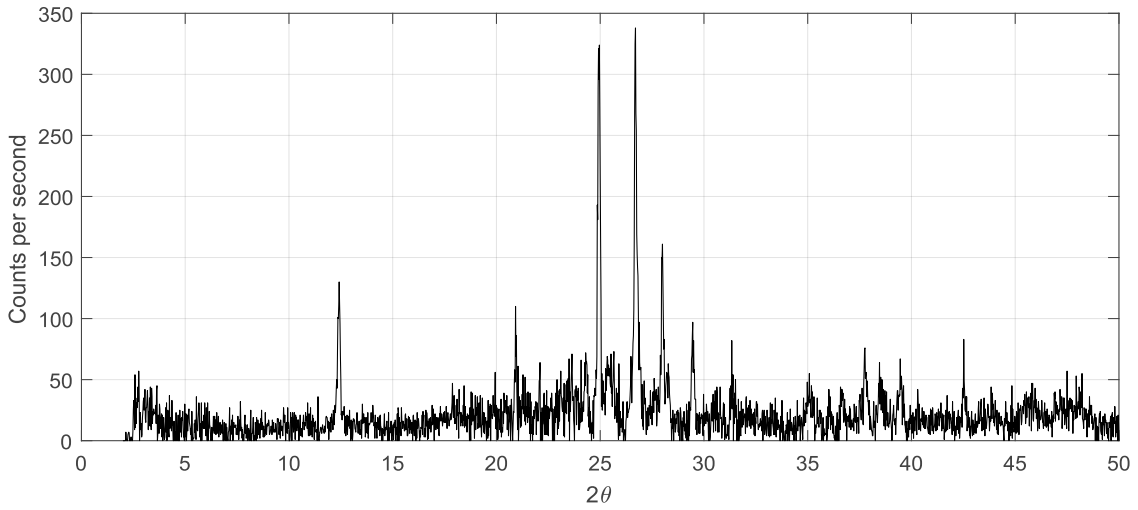

Figure A.4: XRD of the clay Stanton Moor sandstone: Counts per second for 2θ scan with 0.02°steps.

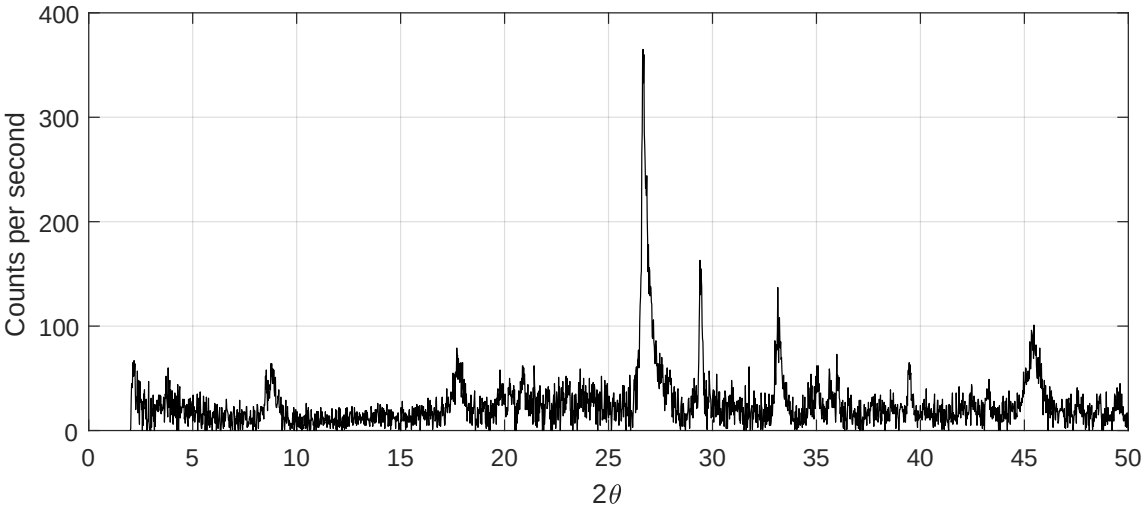

Figure A.5: XRD of the clay St. Bees sandstone: Counts per second for 2θ scan with 0.02°steps.

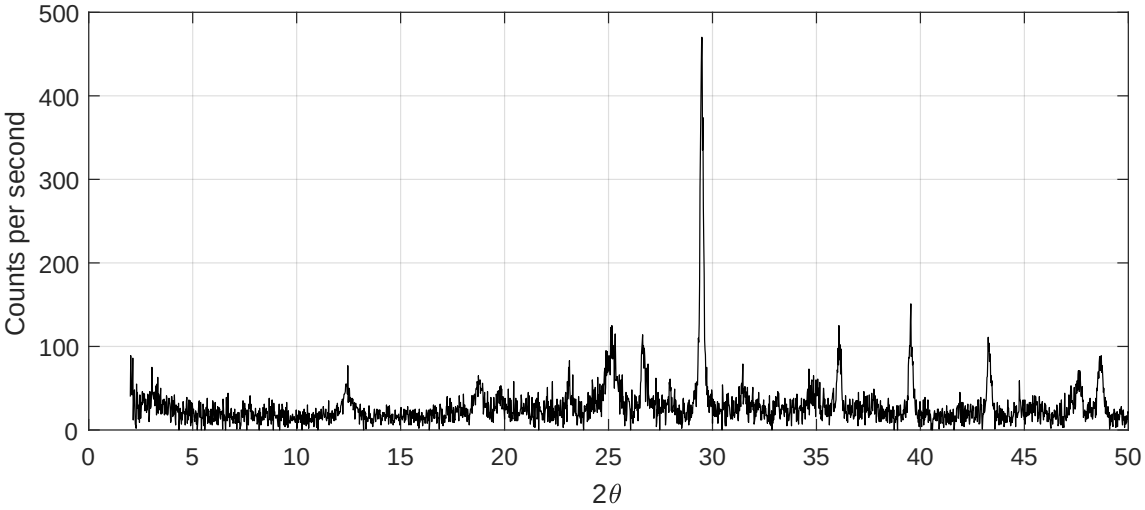

Figure A.6: XRD of the clay Dunkeld sandstone: Counts per second for 2θ scan with 0.02°steps.

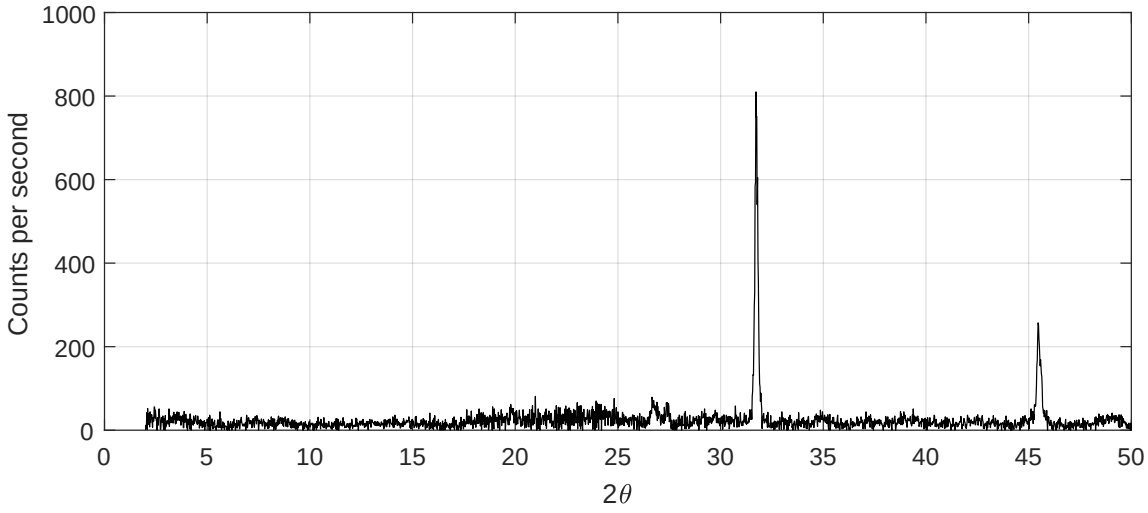

Figure A.7: XRD of the clay Shetlands sandstone: Counts per second for 2θ scan with 0.02°steps.

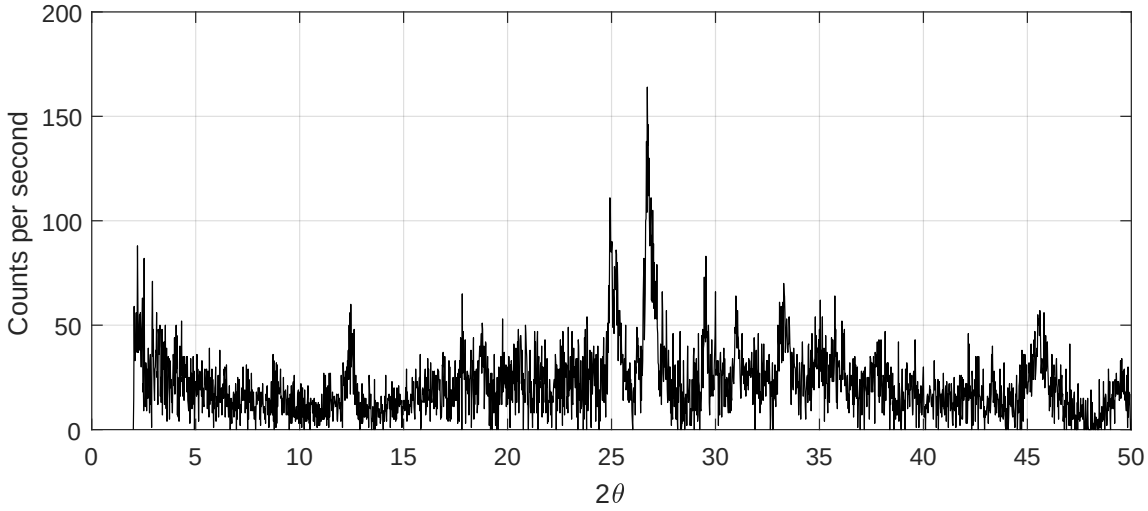

Figure A.8: XRD of the clay Jedburgh sandstone: Counts per second for 2θ scan with 0.02°steps.

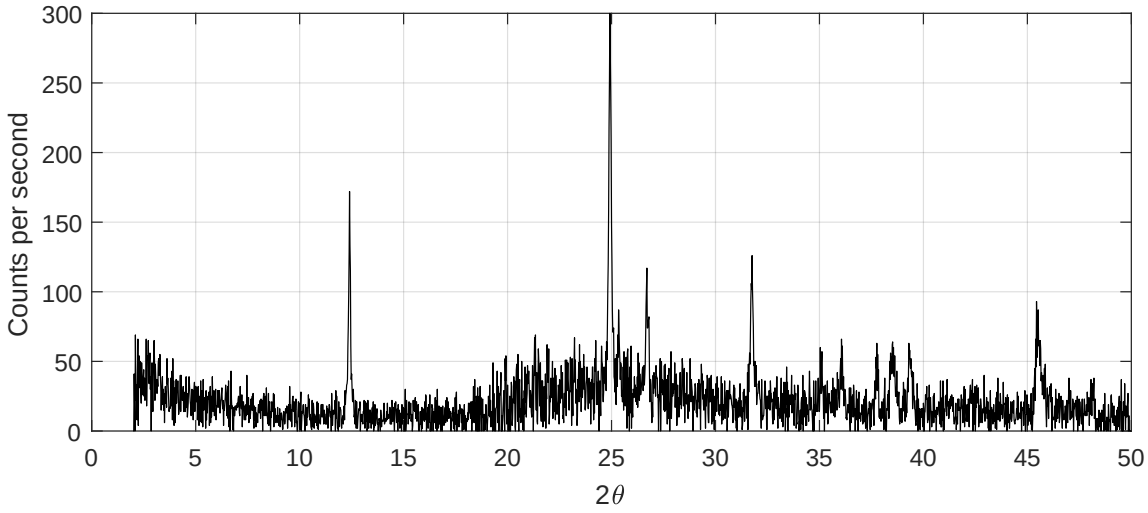

Figure A.9: XRD of the clay Gilmorehill sandstone: Counts per second for 2θ scan with 0.02°steps.

Appendix B

Drilling results

B.1 UAD - Step horn

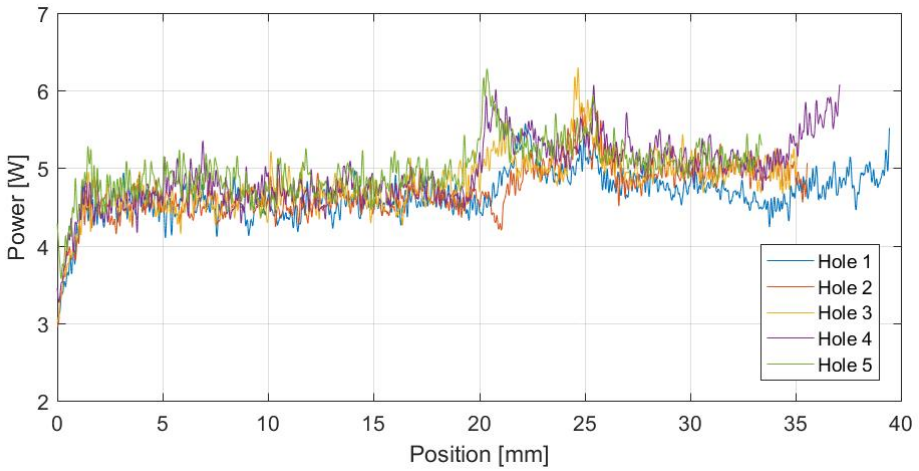

Figure B.1: UAD step horn: Power consumption during drilling of a Cullalo sandstone.

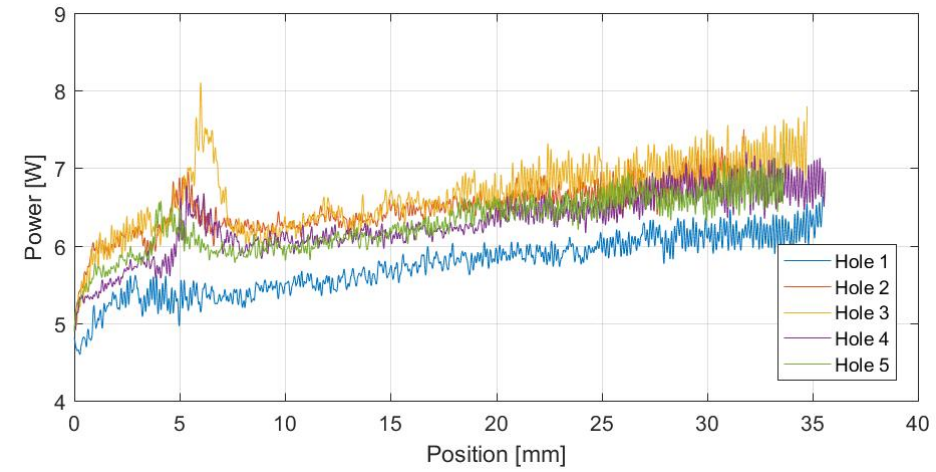

Figure B.2: UAD step horn: Power consumption during drilling of a Cullalo sandstone. The sample was treated with NaCl and a water repellent to induce subflorescence.

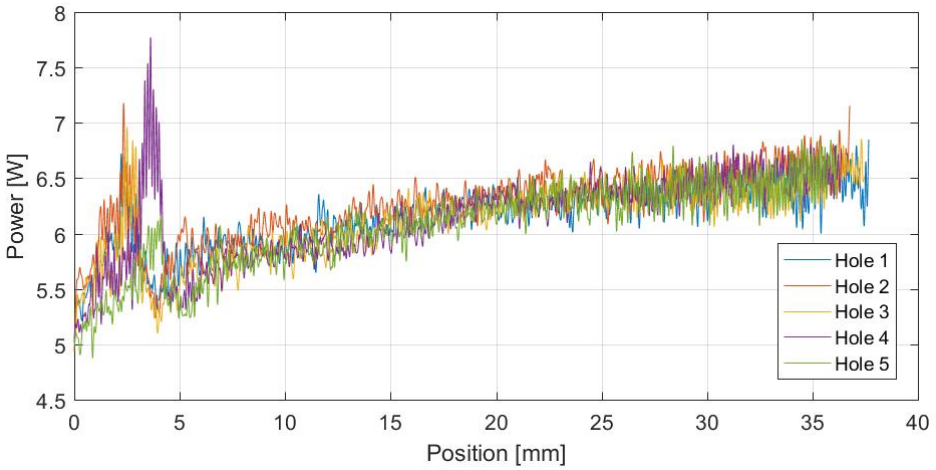

Figure B.3: UAD step horn: Power consumption during drilling of a Cullalo sandstone. The sample was treated with Na_2SO_4 and a water repellent to induce subflorescence.

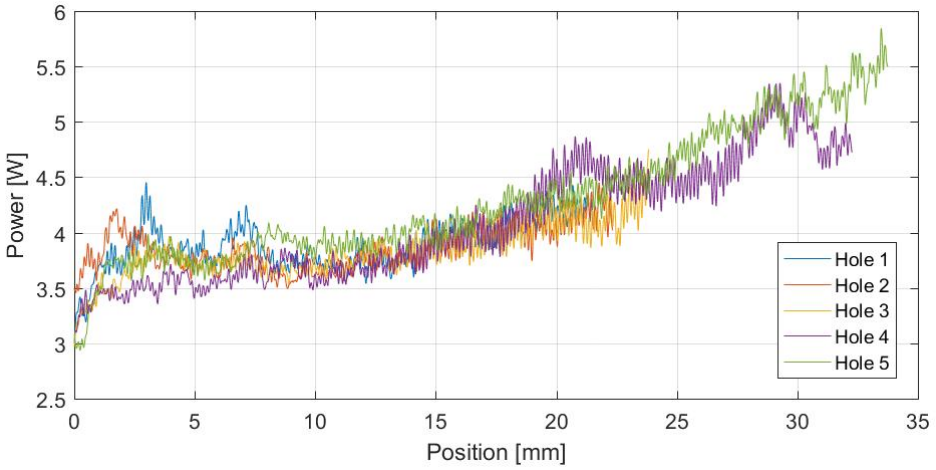

Figure B.4: UAD step horn: Power consumption during drilling of a Locharbriggs sandstone.

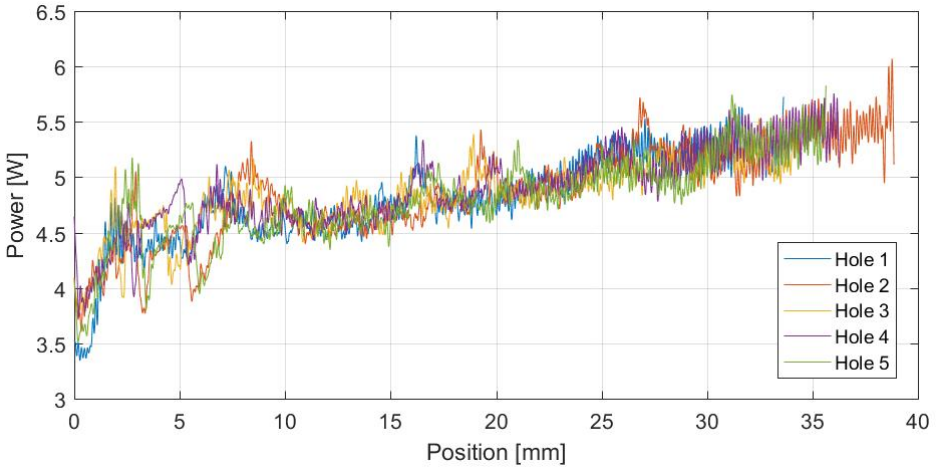

Figure B.5: UAD step horn: Power consumption during drilling of a Locharbriggs sandstone. The sample was treated with NaCl and a water repellent to induce subflorescence.

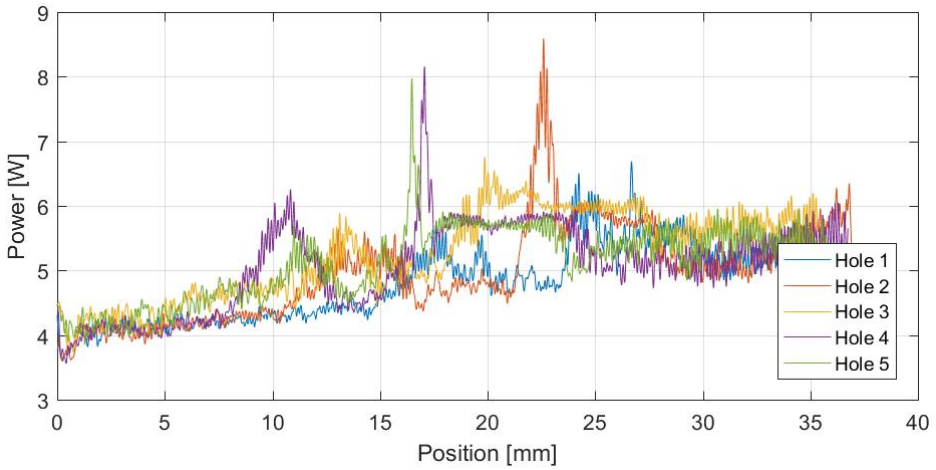

Figure B.6: UAD step horn: Power consumption during drilling of a Locharbriggs sandstone. The sample was treated with Na_2SO_4 and a water repellent to induce subflorescence.

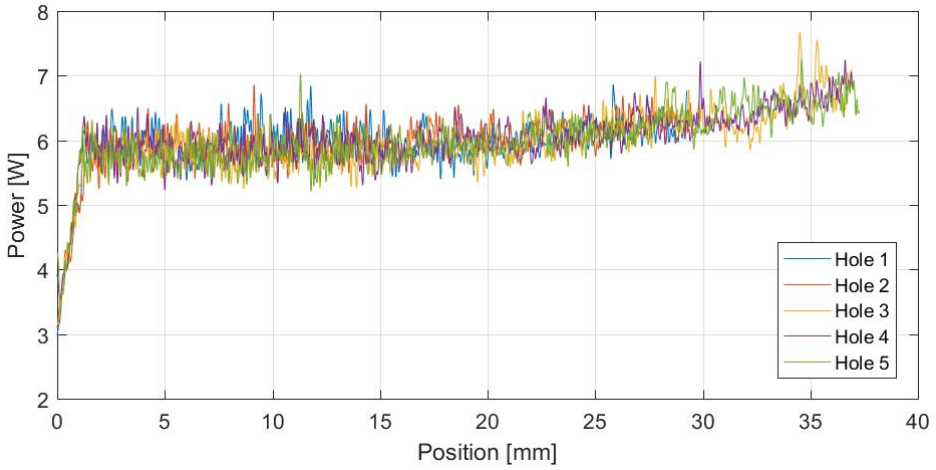

Figure B.7: UAD step horn: Power consumption during drilling of a Stanton Moor sandstone.

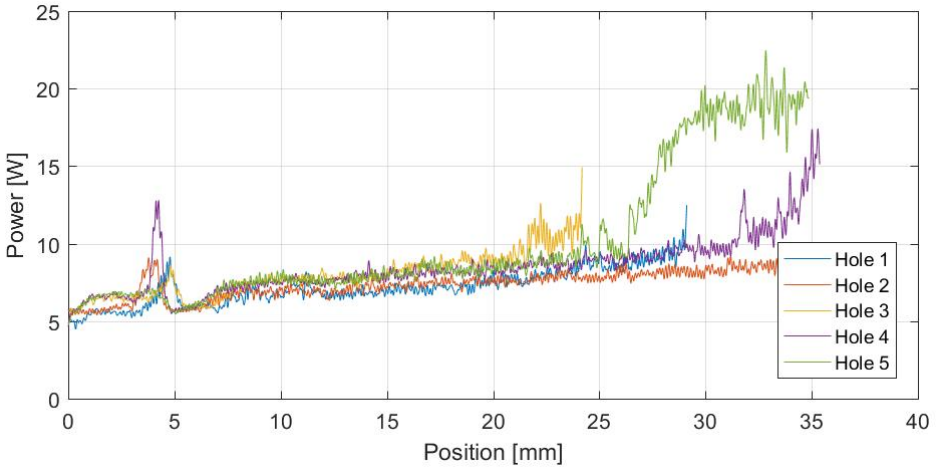

Figure B.8: UAD step horn: Power consumption during drilling of a Stanton Moor sandstone. The sample was treated with NaCl and a water repellent to induce subflorescence.

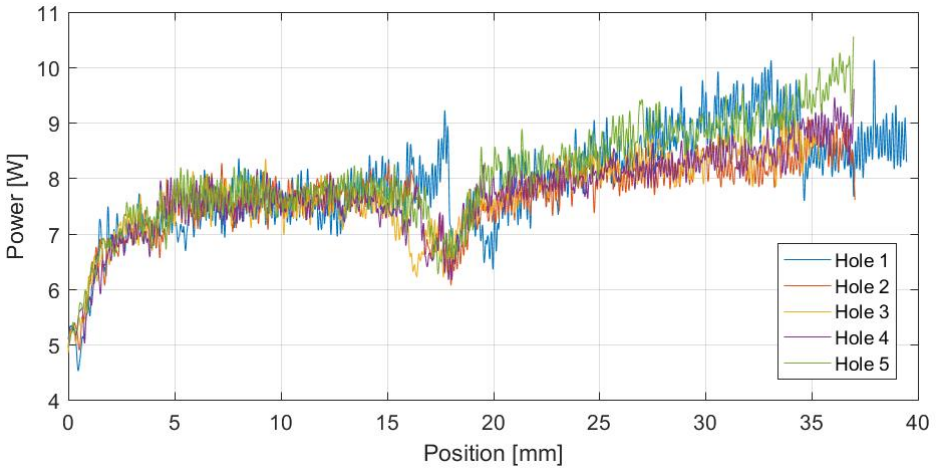

Figure B.9: UAD step horn: Power consumption during drilling of a Stanton Moor sandstone. The sample was treated with Na_2SO_4 and a water repellent to induce subflorescence.

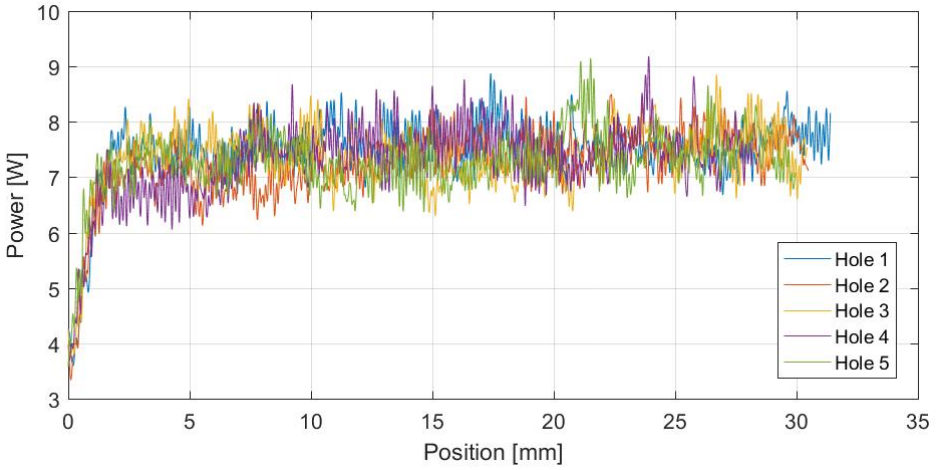

Figure B.10: UAD step horn: Power consumption during drilling of an Anston carbonate rock.

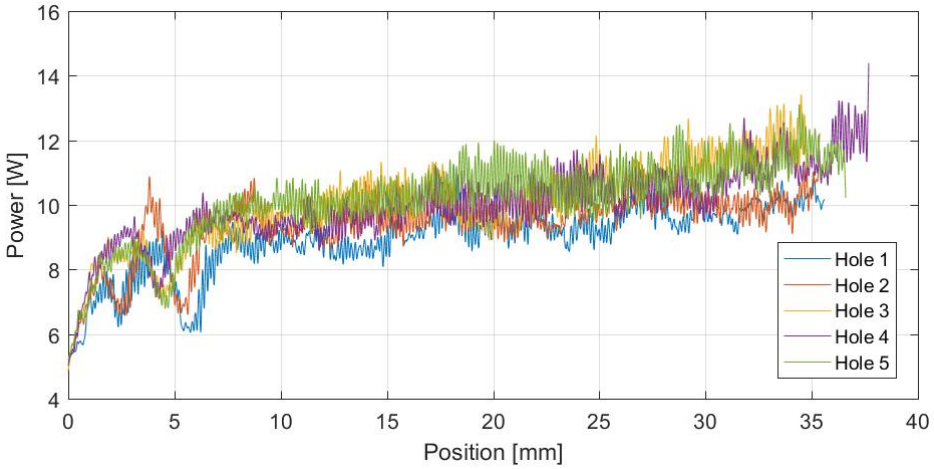

Figure B.11: UAD step horn: Power consumption during drilling of an Anston carbonate rock. The sample was treated with NaCl and a water repellent to induce subflorescence.

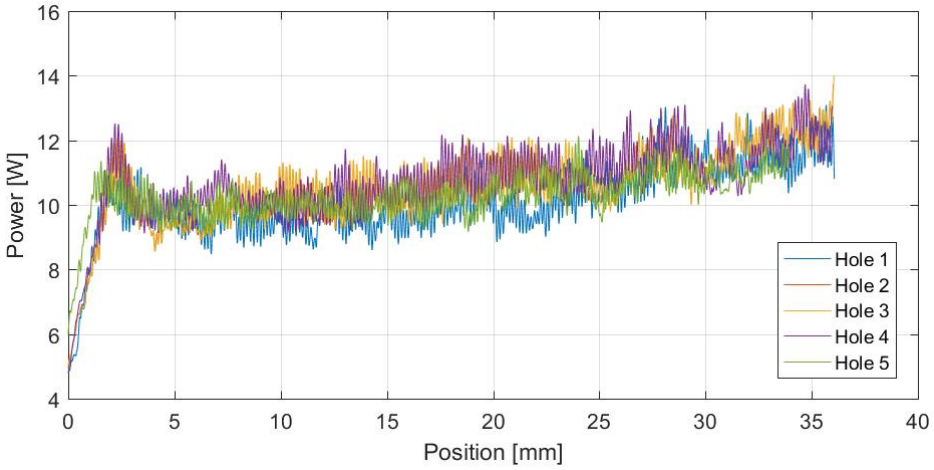

Figure B.12: UAD step horn: Power consumption during drilling of an Anston carbonate rock. The sample was treated with Na_2SO_4 and a water repellent to induce subflorescence.

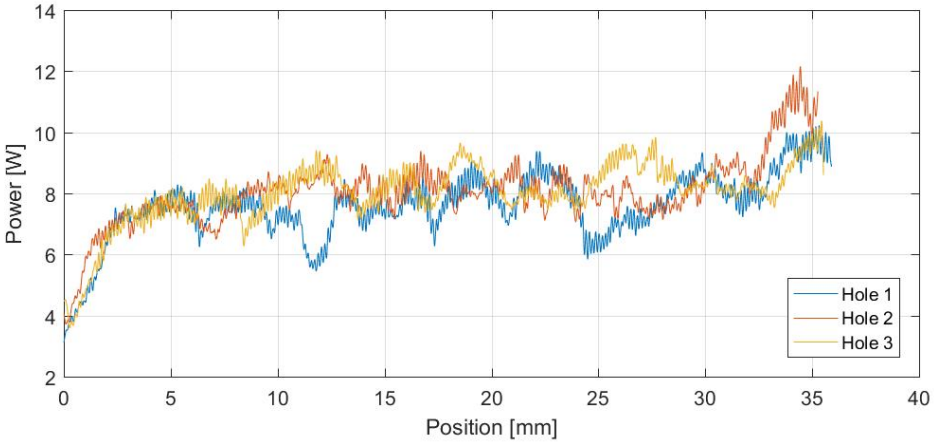

Figure B.13: UAD step horn: Power consumption during drilling of a Halite sample.

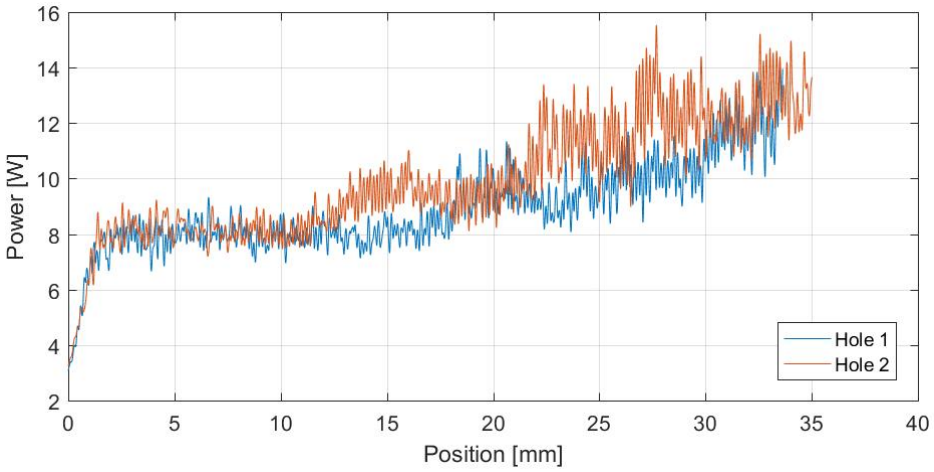

Figure B.14: UAD step horn: Power consumption during drilling of a Clashach sandstone.

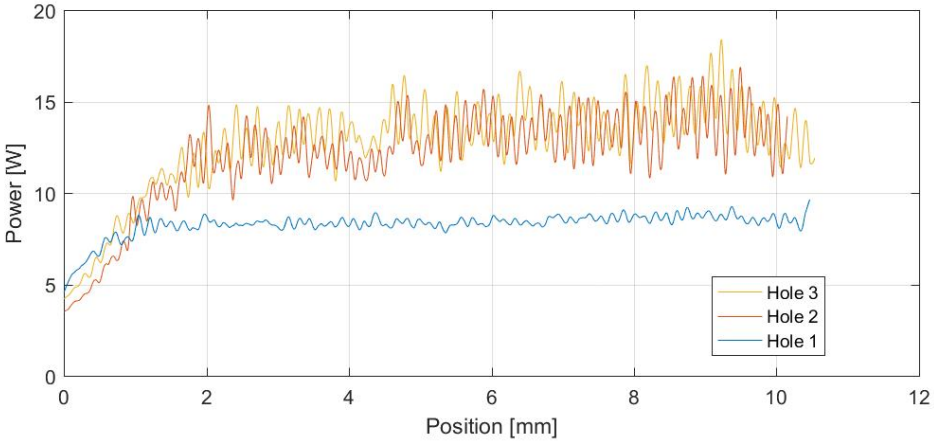

Figure B.15: UAD step horn: Power consumption during drilling of a St. Bees sandstone.

B.2 UAD - Conical horn

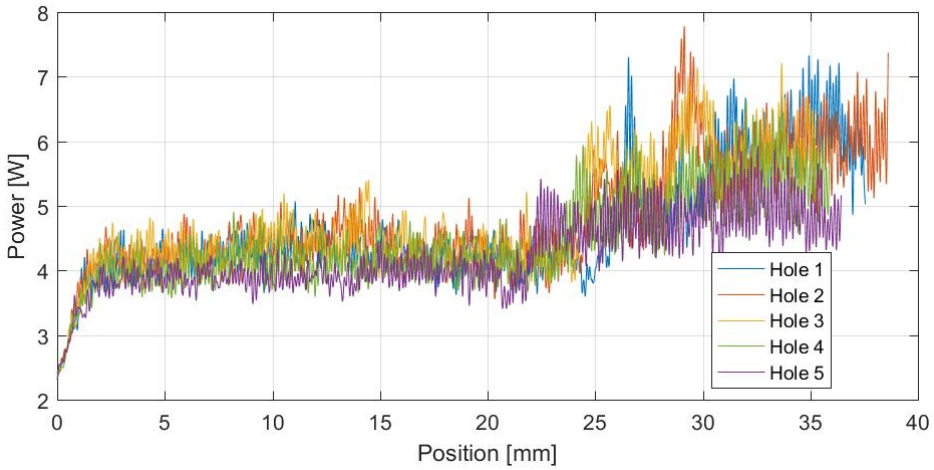

Figure B.16: UAD conical horn: Power consumption during drilling of a Cullalo sandstone.

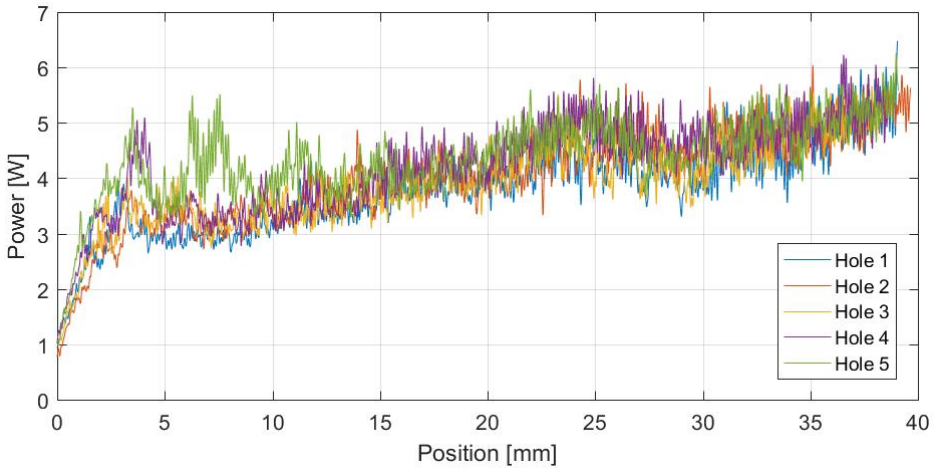

Figure B.17: UAD conical horn: Power consumption during drilling of a Cullalo sandstone. The sample was treated with NaCl and a water repellent to induce subflorescence.

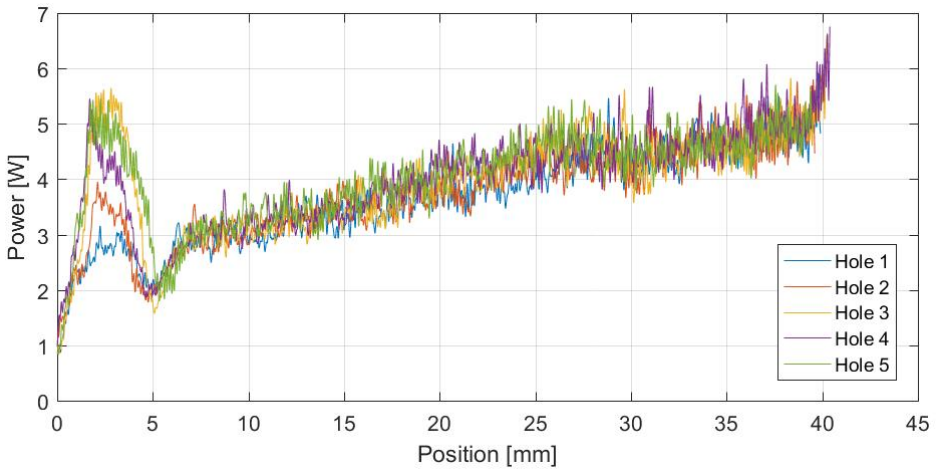

Figure B.18: UAD step horn: Power consumption during drilling of a Cullalo sandstone. The sample was treated with Na_2SO_4 and a water repellent to induce subflorescence.

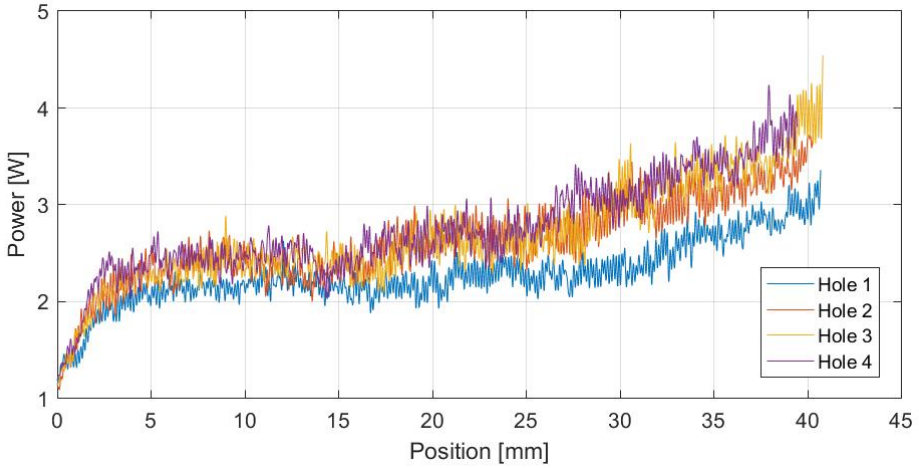

Figure B.19: UAD conical horn: Power consumption during drilling of a Locharbriggs sandstone.

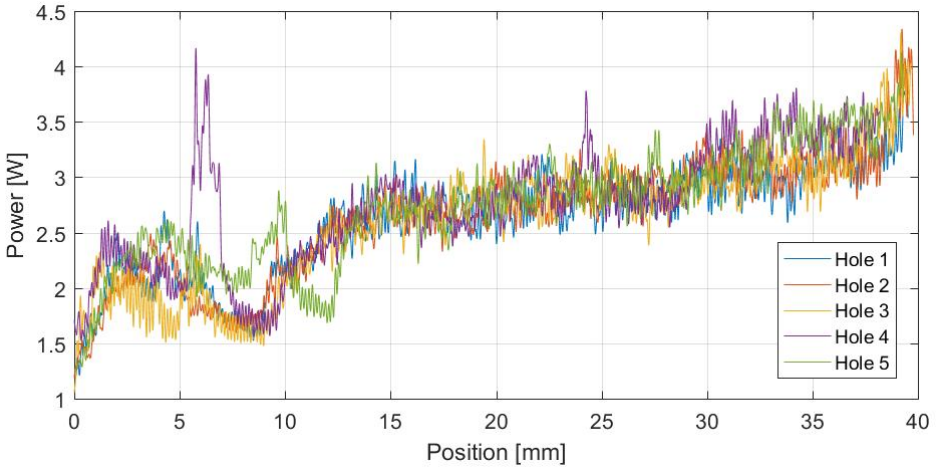

Figure B.20: UAD conical horn: Power consumption during drilling of a Locharbriggs sandstone. The sample was treated with NaCl and a water repellent to induce subflorescence.

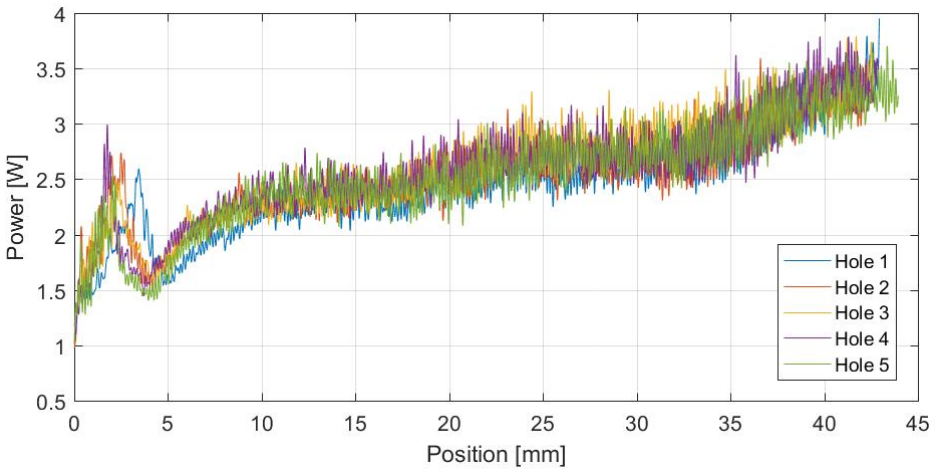

Figure B.21: UAD conical horn: Power consumption during drilling of a Locharbriggs sandstone. The sample was treated with Na_2SO_4 and a water repellent to induce subflorescence.

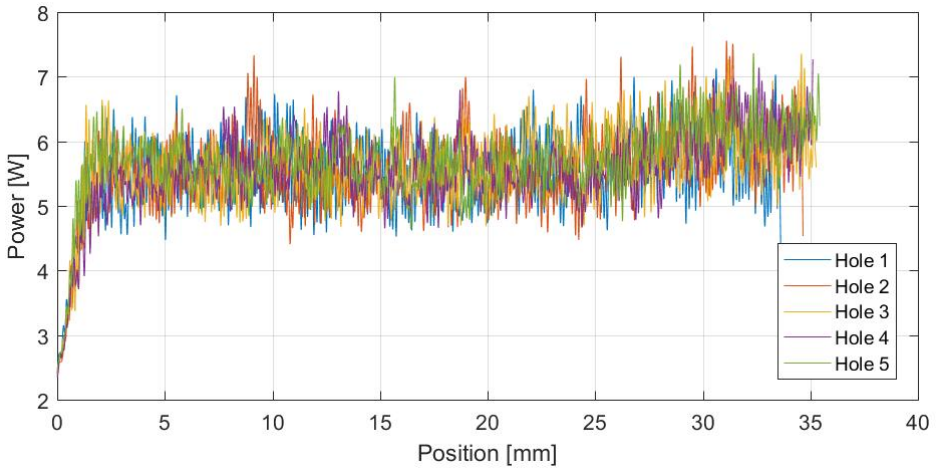

Figure B.22: UAD conical horn: Power consumption during drilling of a Stanton Moor sandstone.

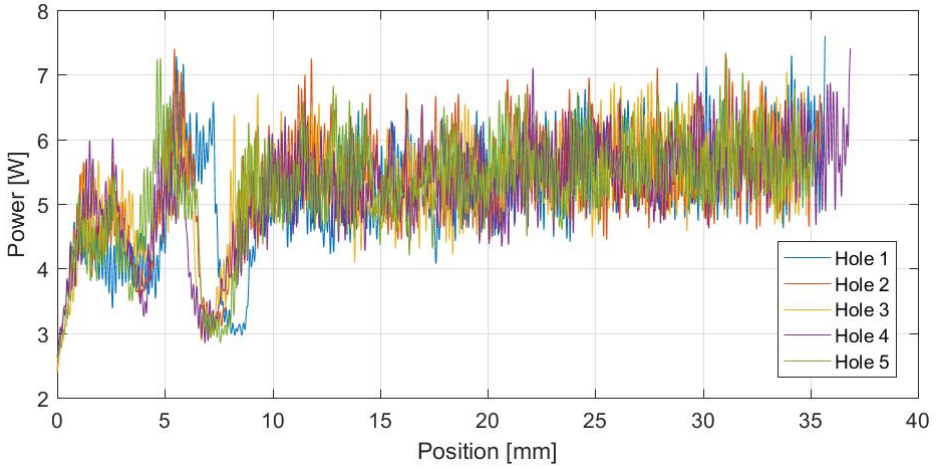

Figure B.23: UAD conical horn: Power consumption during drilling of a Stanton Moor sandstone. The sample was treated with NaCl and a water repellent to induce subflorescence.

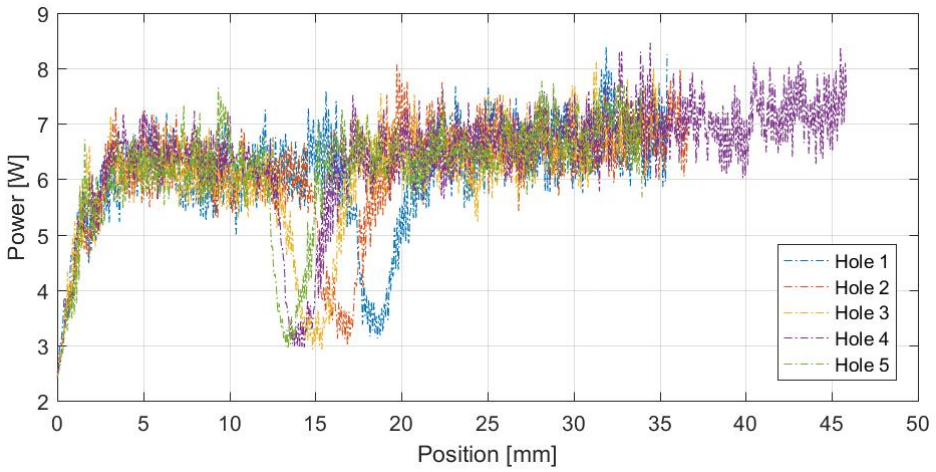

Figure B.24: UAD conical horn: Power consumption during drilling of a Stanton Moor sandstone. The sample was treated with Na_2SO_4 and a water repellent to induce subflorescence.

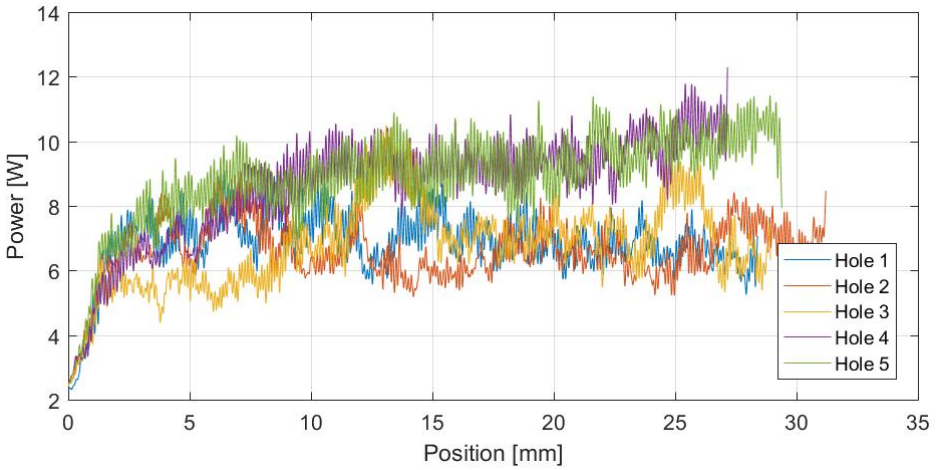

Figure B.25: UAD conical horn: Power consumption during drilling of an Anston carbonate rock.

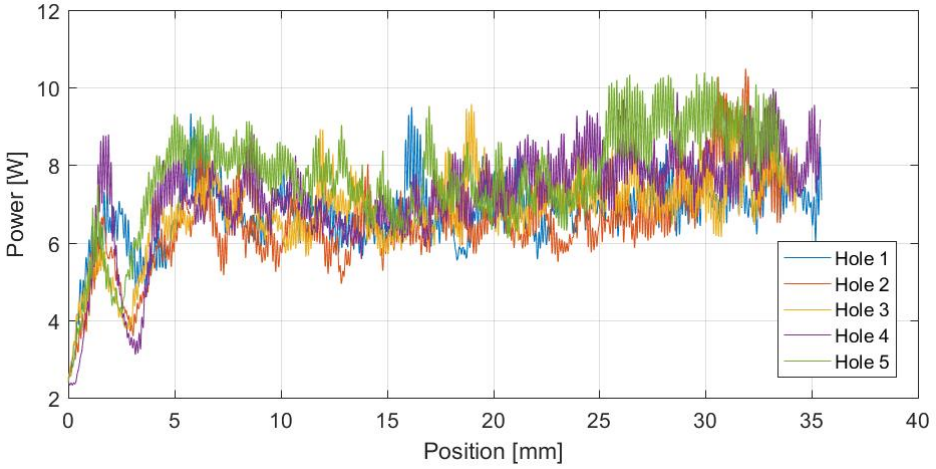

Figure B.26: UAD conical horn: Power consumption during drilling of an Anston carbonate rock. The sample was treated with NaCl and a water repellent to induce subflorescence.

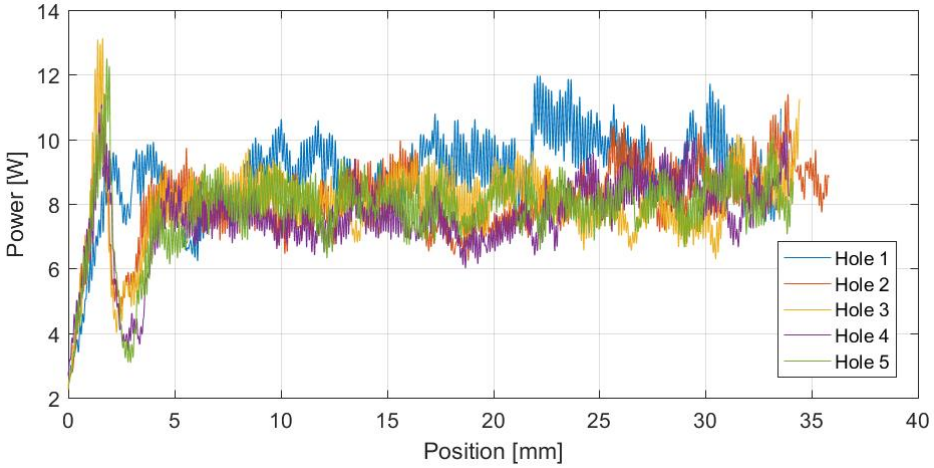

Figure B.27: UAD conical horn: Power consumption during drilling of an Anston carbonate rock. The sample was treated with Na_2SO_4 and a water repellent to induce subflorescence.

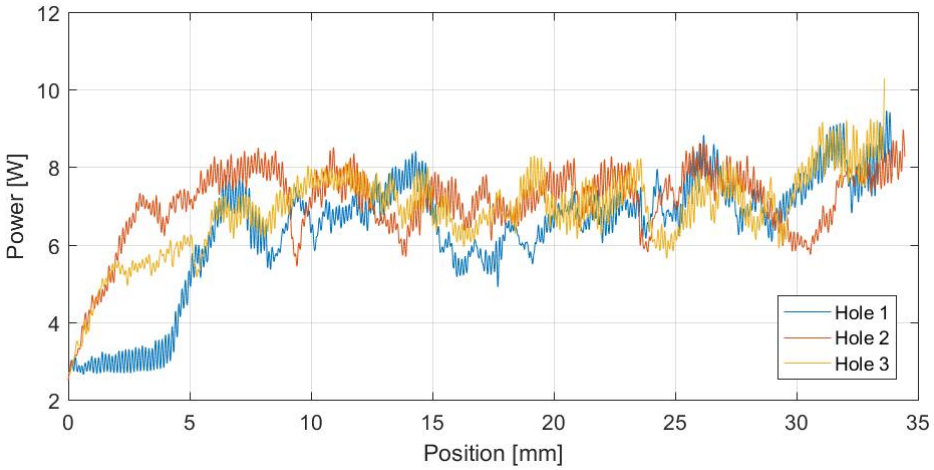

Figure B.28: UAD conical horn: Power consumption during drilling of a Halite sample.

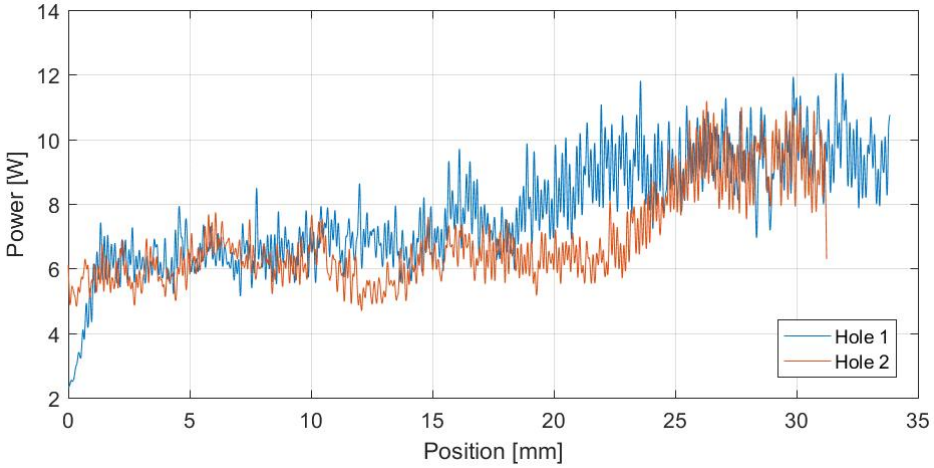

Figure B.29: UAD conical horn: Power consumption during drilling of a Clashach sandstone.

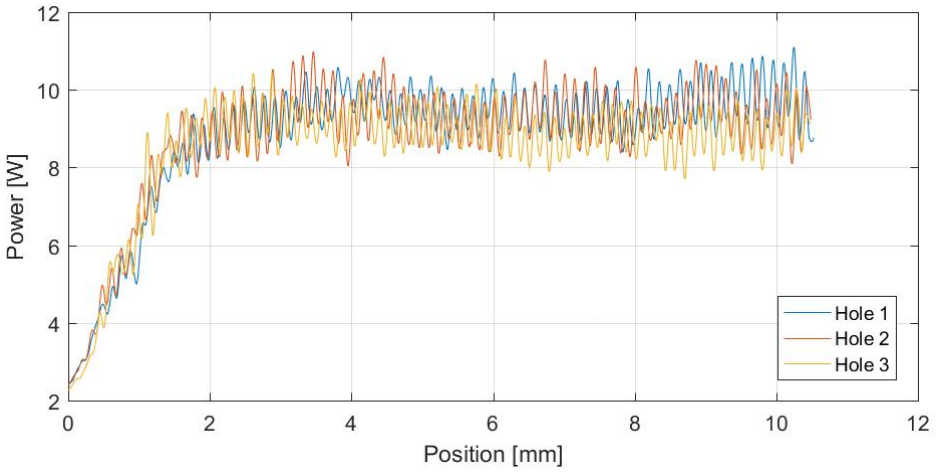

Figure B.30: UAD conical horn: Power consumption during drilling of a St. Bees sandstone.

B.3 DRMS

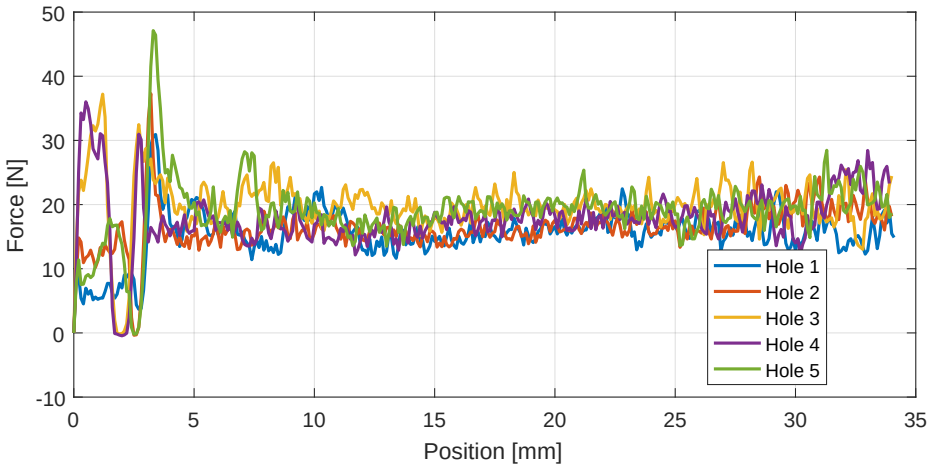

Figure B.31: DRMS: Exerted force on Cullalo sandstone while drilling. The sample was treated with NaCl and a water repellent to induce subflorescence.

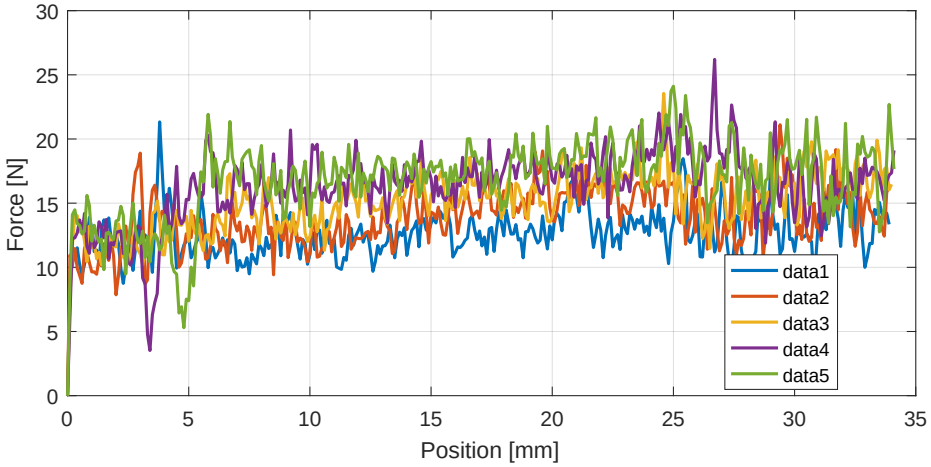

Figure B.32: DRMS: Exerted force on Cullalo sandstone while drilling. The sample was treated with Na_2SO_4 and a water repellent to induce subflorescence.

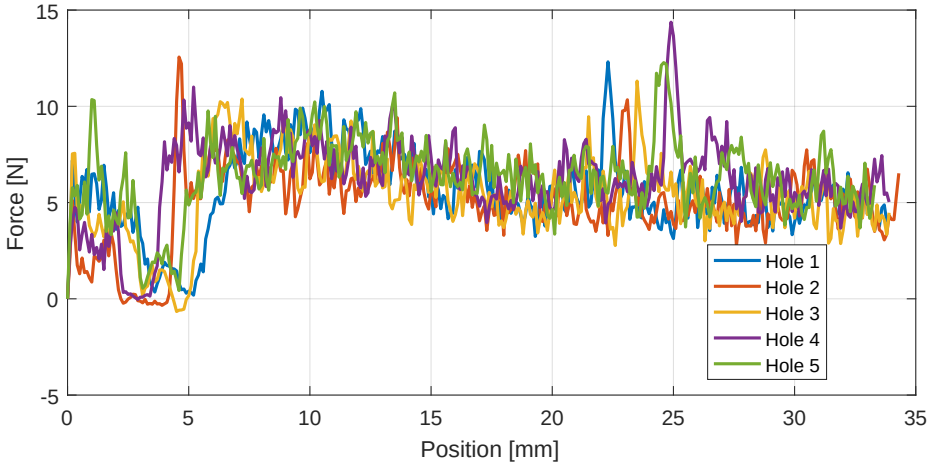

Figure B.33: DRMS: Exerted force on Locharbriggs sandstone while drilling. The sample was treated with NaCl and a water repellent to induce subflorescence.

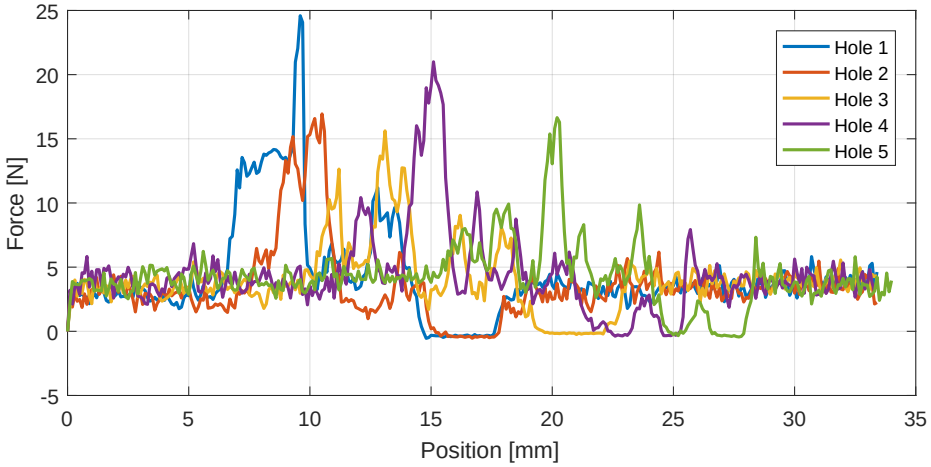

Figure B.34: DRMS: Exerted force on Locharbriggs sandstone while drilling. The sample was treated with Na_2SO_4 and a water repellent to induce subflorescence.

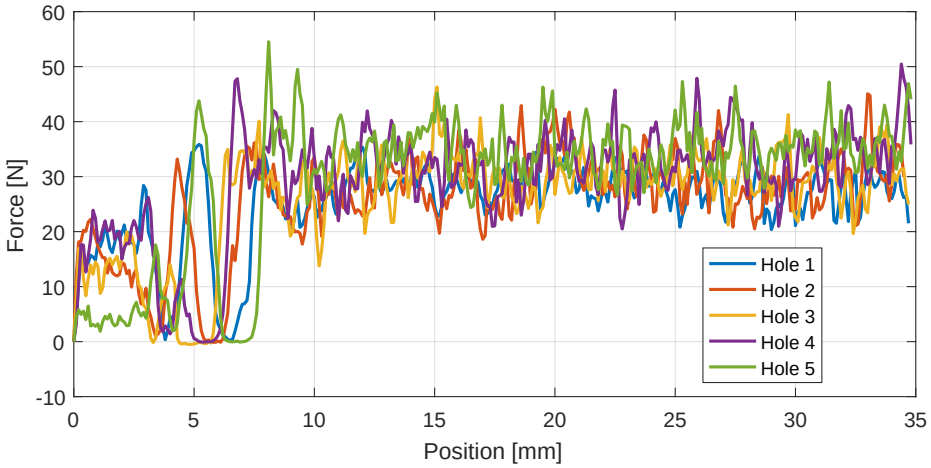

Figure B.35: DRMS: Exerted force on Stanton Moor sandstone while drilling. The sample was treated with NaCl and a water repellent to induce subflorescence.

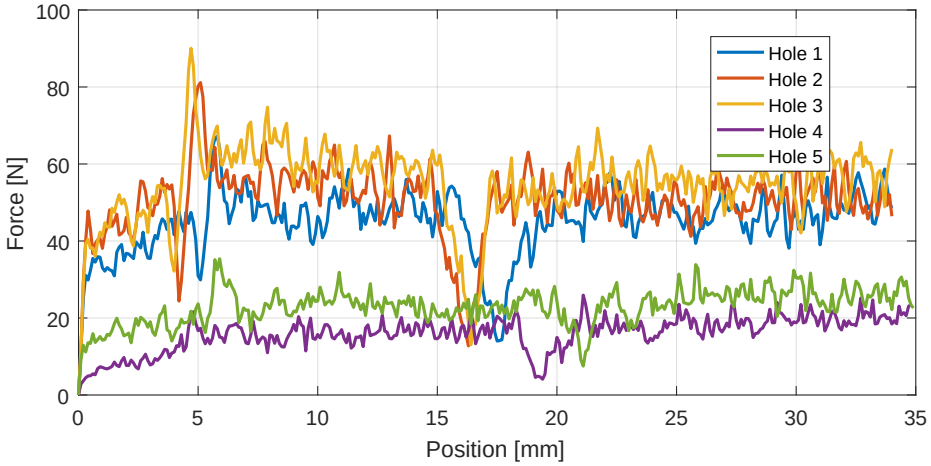

Figure B.36: DRMS: Exerted force on Stanton Moor sandstone while drilling. The sample was treated with Na_2SO_4 and a water repellent to induce subflorescence.

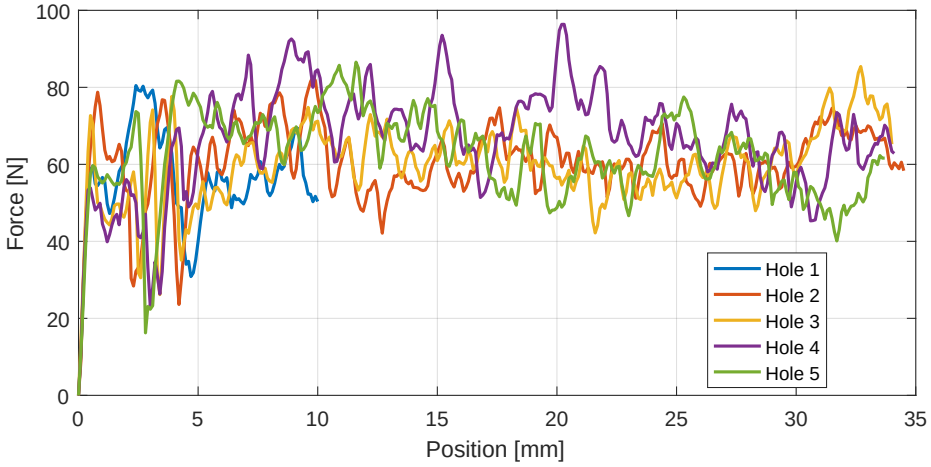

Figure B.37: DRMS: Exerted force on Anston carbonate rock while drilling. The sample was treated with Na_2SO_4 and a water repellent to induce subflorescence. (When the appendix was created the results of the Anston NaCl sample were accidentally overwritten with the Anston Na_2SO_4 sample.)

Appendix C

Micro-climate monitoring results

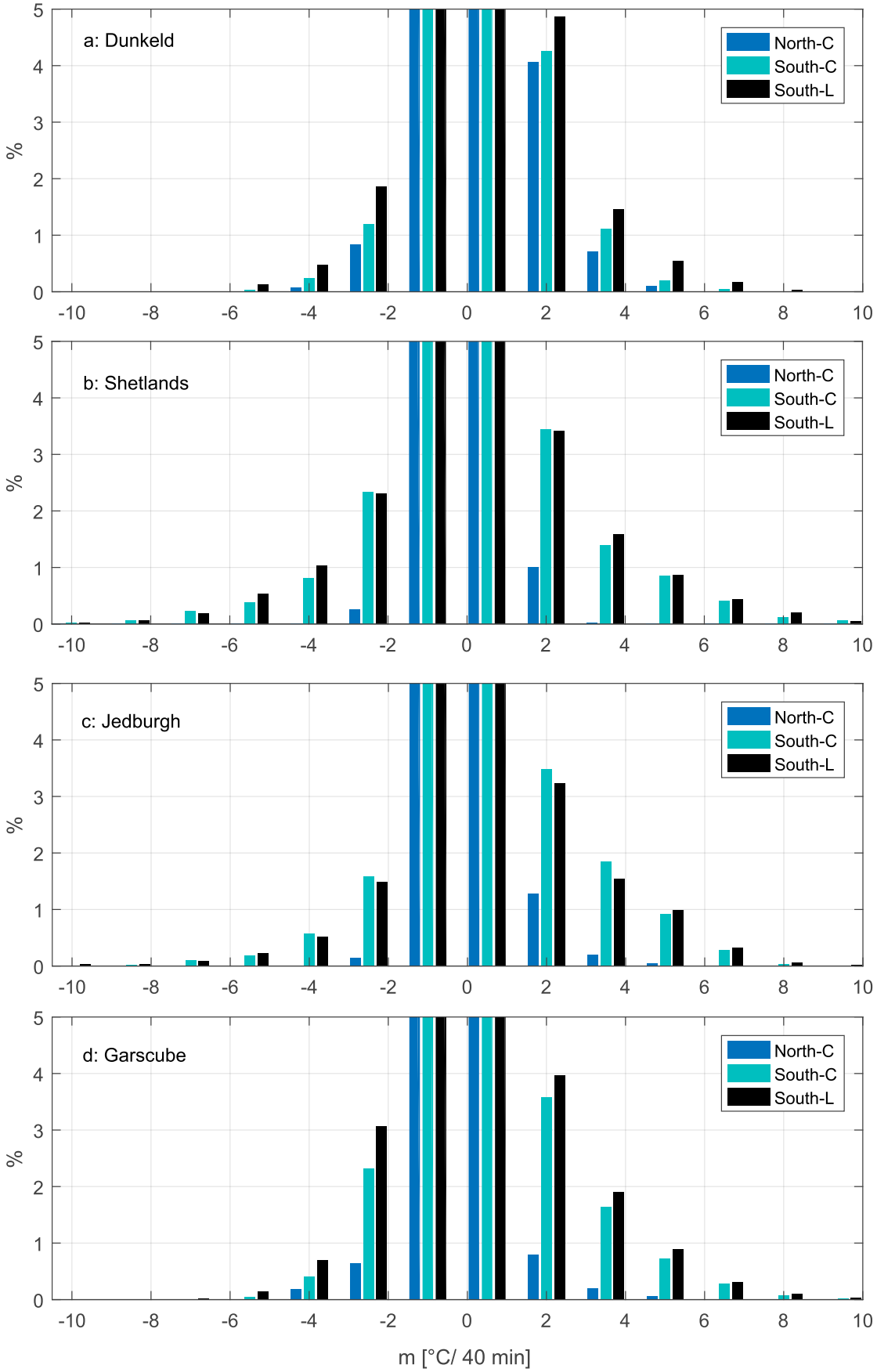

Figure C.1: Detail (5%) of the frequencies of temperature changes in 40 min. Comparison of the iButtons attached to a north (blue) and south facing Cullalo (light blue), and a south facing Locharbriggs sample (black). The histograms are displayed for the sites Dunkeld (a), Shetland Islands (b), Jedburgh (c) and Garscube (d). The size of the used bins is 1.5 °C/ 40 min.

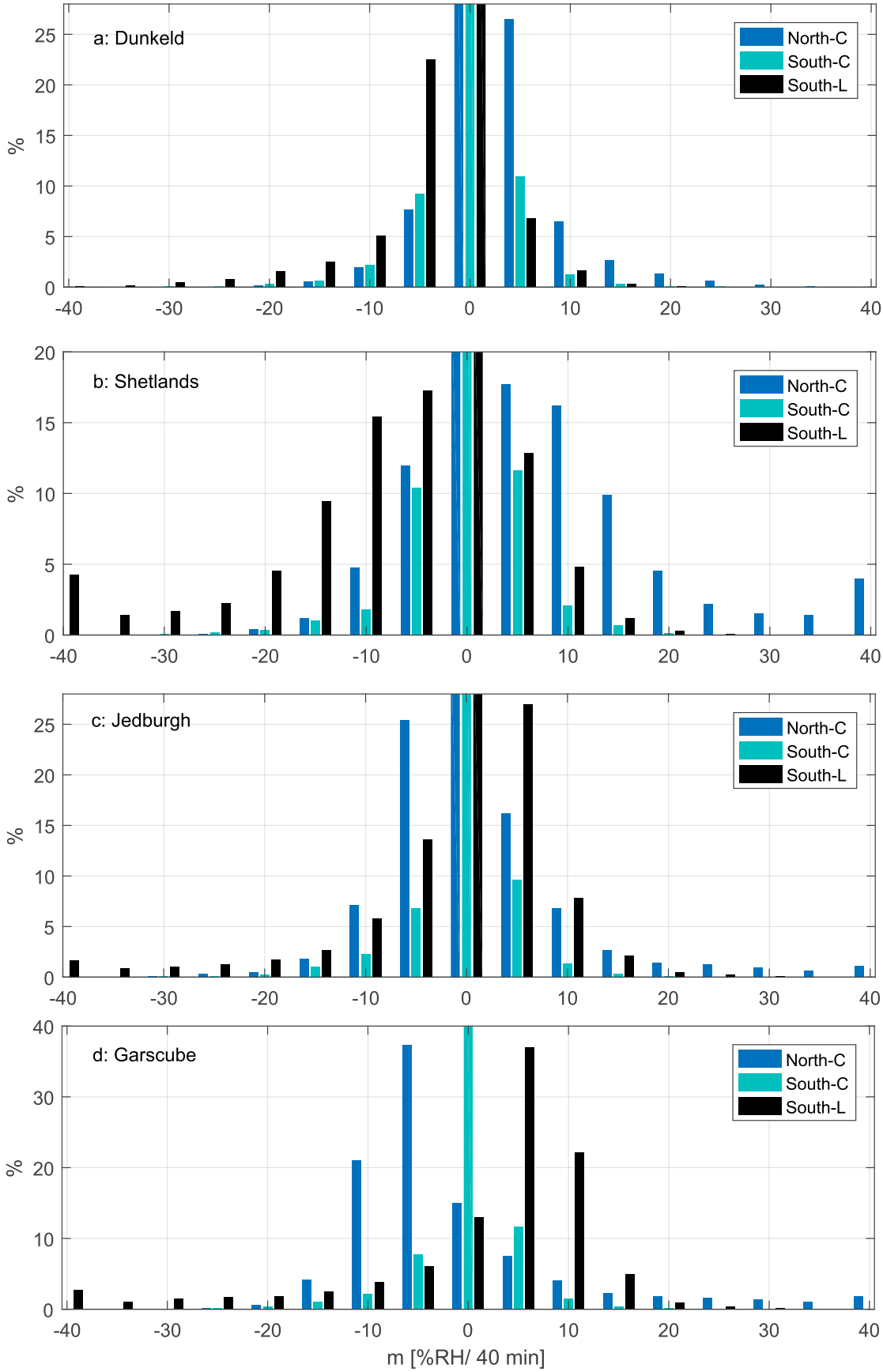

Figure C.2: Detail of the frequencies of humidity changes in 40 min. Comparison of the iButtons attached to a north (blue) and south facing Cullalo (light blue), and a south facing Locharbriggs sample (black). The histograms are displayed for the sites Dunkeld (a), Shetland Islands (b), Jedburgh (c) and Garscube (d). The size of the used bins is 5 %RH/ 40 min.

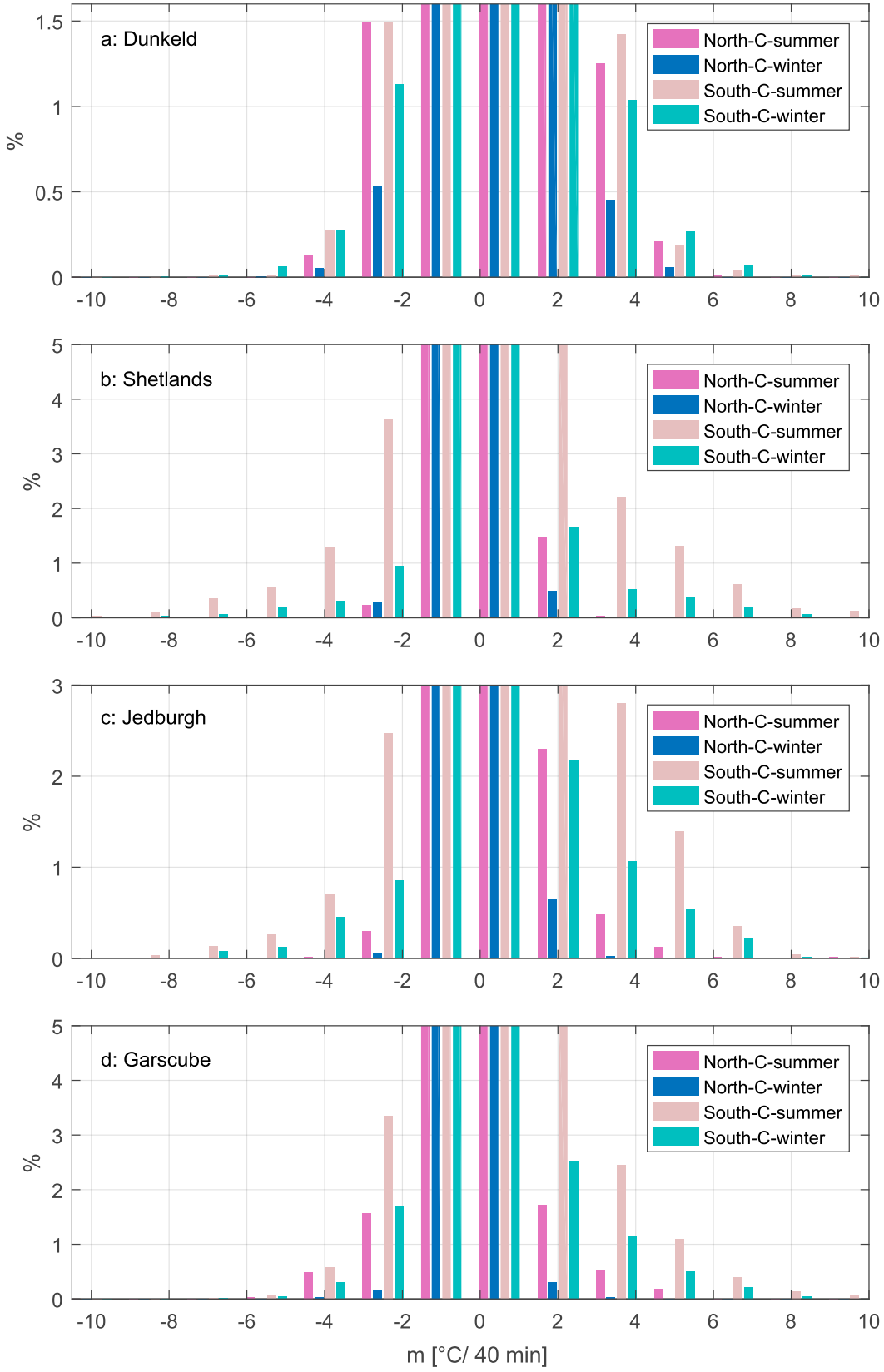

Figure C.3: Detail of the frequencies of temperature changes in 40 min. Comparison of the iButtons during summer (pink for the north facing Cullalo and lighter pink for the south facing Cullalo) and winter (blue for the north facing Cullalo and lighter blue for the south facing Cullalo). The histograms are displayed for the sites Dunkeld (a), Shetland Islands (b), Jedburgh (c) and Garscube (d). The size of the used bins is 1.5 ° C/ 40 min.

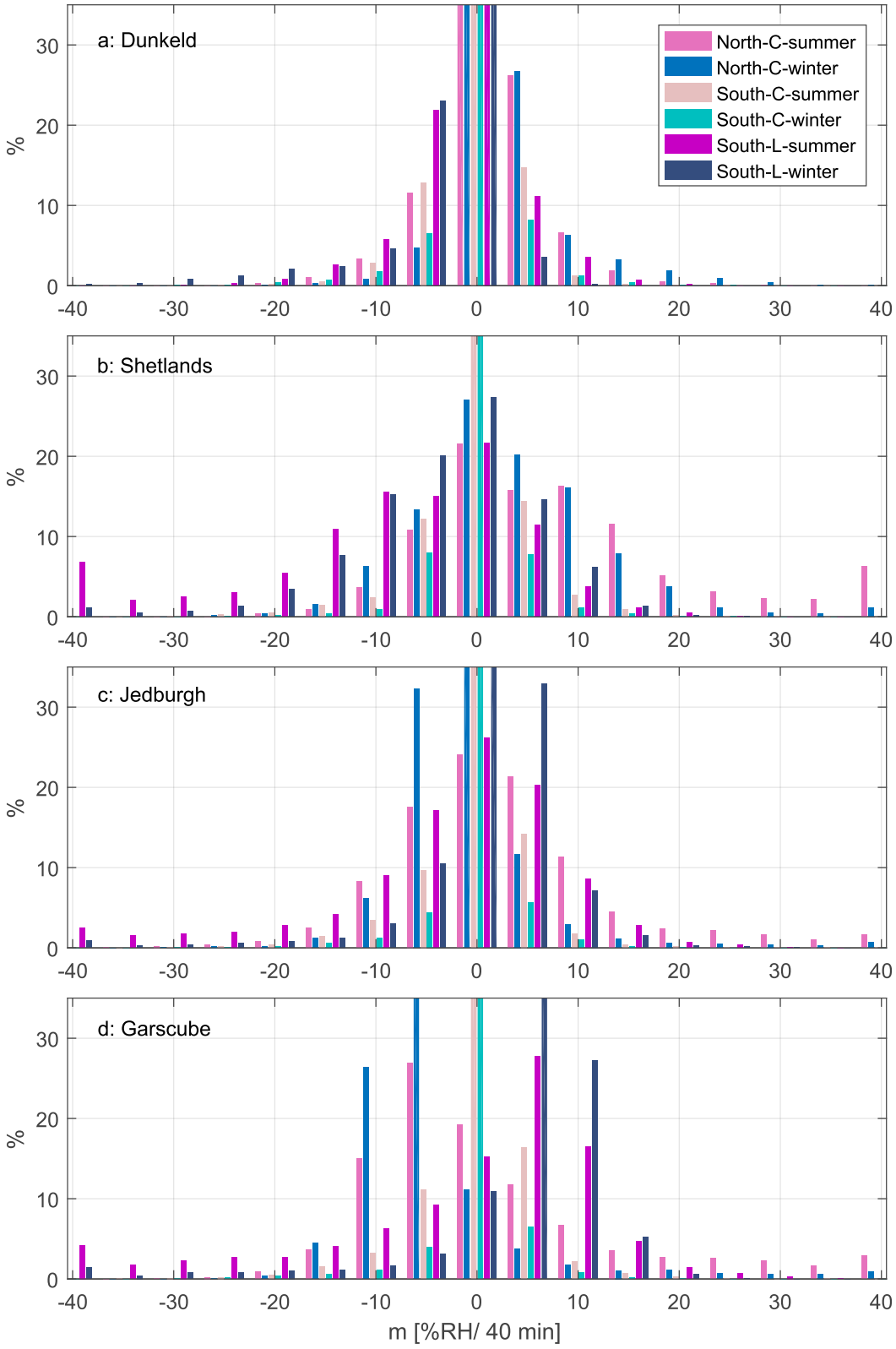

Figure C.4: Detail (35%) of the frequencies of humidity changes in 40 min. Comparison of summer and winter measurements of a north facing Cullalo (summer data in pink and winter data in blue), a south facing Cullalo (summer data in light pink and winter data in light blue), and a south facing Locharbriggs sample (summer data in violet and winter data in dark blue). The histograms are displayed for the different sites (a-d). The size of the used bins is 5 %RH/ 40 min.

Acronyms

AE Acoustic emission. 31–34, 67, 99

BSE Back scatter electrons. 43, 49, 52, 55, 57, 62, 63

CD Conventional drilling. 110–112, 123, 132, 153

DFT Discrete Fourier transform. 74

DRMS Drilling Resistance Measurement System. 35, 36, 121, 123, 124, 126, 132–136, 145, 146, 153

EDX Energy-dispersive X-ray spectroscopy. 44, 51

EMA Experimental Modal analysis. 112, 117, 118, 126, 153

EUCLID Easy to Use Compact Laser Interferometric Device. 65, 71, 72, 75, 76, 78, 79, 105

FEM Finite element analysis. 118, 126

FEM Finite element modelling. 112, 116, 117, 153

FFT Fast Fourier transform. 74, 117, 120

FRF Fourier response function. 117, 126, 127

HES Historic Environment Scotland. 2, 58, 156, 170

ICOMOS Illustrated glossary on stone deterioration patterns. 28

LVDT Linear variable differential transformers. 66

NDT Non-destructive Testing. 28, 31, 38, 65

O Octahedra. 12, 13

PCD Poly crystalline diamond. 112, 121–123, 150

QFL Quartz, feldspar and lithic fragments. 5, 44

SE Secondary electrons. 43, 49, 51, 53, 57, 59, 61, 63, 125

SEM Scanning electron microscope. 43, 44, 51

T Tetrahedra. 12, 13

UAD Ultrasonic assisted drilling. 110–113, 115, 118–121, 131–137, 141–143, 145, 146, 148–150, 153

UCS Uniaxial Compressive Strength. 5, 16, 35, 36, 131, 132, 134, 151

XCT Micro-computed X-ray tomography. 45, 136, 137, 148, 152

XRD X-ray diffraction. 44, 51, 54, 56, 58

Bibliography

Abbott, B., Abbott, R., Abbott, T., Abernathy, M., Acernese, F., Ackley, K., Adams, C., Adams, T., Addesso, P. & Adhikari, R. (2016), 'Observation of gravitational waves from a binary black hole merger', *Physical Review Letters* . (LIGO Scientific Collaboration and Virgo Collaboration).

Adamovic, J., Mikulas, R. & Bohmova, J. S. V. (2011), 'Porosity changes induced by salt weathering of sandstones, Bohemian Cretaceous Basin, Czech Republic', *Acta Geodynamica et Geomaterialia* .

Adithan, M. (1974), 'Tool wear studies in ultrasonic drilling', *Wear* **29**, 81–93.

Ainsworth, S. & Pearson, T. (2002), Stanton Moor, Derbyshire, Archaeological Investigation AI/6/2002, English Heritage.

Aksu, I., Bazilevskaya, E. & Karpyn, Z. (2014), 'Swelling of clay minerals in unconsolidated porous media and its impact on permeability', *GeoResJ* .

Al-Naddaf, M., Wakid, F. & Alhassan, A. Y. (2013), 'Micro-drilling resistance measurement: A new technique to estimate porosity of a building stone', *Mediterranean Archaeology and Archaeometry* **13**, 225–233.

Ambrose, K., Hough, E., Smith, N. J. P. & Warrington, G. (2014), 'Lithostratigraphy of the Sherwood Sandstone Group of England, Wales and south-west Scotland', *British Geological Survey Geology and Regional Geophysics Directorate* (RR/14/01).

Anjos, S. M. C., de Ros, L. F. & Silva, C. M. A. (2003), Chlorite authigenesis and porosity preservation in the Upper Cretaceous marine sandstones of the Santos Basin, offshore eastern Brazil, *in* S. M. Richard H. Worden, ed., 'Clay Mineral Cements in Sandstones', number 34 *in* 'International Association of sedimentologists Special Publications', Blackwell Publishing.

Anzalone, A., Boles, J., Greene, G., Young, K., Israelachvili, J. & Alcantar, N. (2006), 'Confined fluids and their role in pressure solution', *Chemical Geology* **230**, 220–231.

Armstrong, M., Paterson, I. B. & Browne, M. A. E. (1985), *Geology of the Perth and Dundee district*, Memoir fo 1: 50000 geolocial sheets 48W, 48 E, 49, British Geological Survey.

Arnold, A. & Zehnder, K. (1989), Salt weathering on monuments, *in* 'La conservazione dei monumenti nel bacino del Mediterraneo Atti del I' Simposio internazionale'.

Asmussen, S. (2007), Experimente zur Salzverwitterung von Naturwerkgesteinen mittels Dehnungsmessungen, PhD thesis, Universität Hamburg.

Aston, S. M. (2011), Optical Read-out Techniques for the Control of Test-masses in Gravitational Wave Observatories, PhD thesis, The University of Birmingham.

Aston, S. M., Hoyland, D. & Speake, C. (2013), *EUCLID User Guide*, University of Birmingham.

Azarhoushang, B. & Akban, J. (2007), 'Ultrasonically-assisted drilling of Inconel 738-LC', *International Journal of Machine Tools and Manufacture* **47**, 1027–1033.

Badami, V. & de Groot, P. (2013), *Handbook of Optical Dimensional Metrology*, Taylor and Francis, chapter Displacement Measuring Interferometry, pp. 157–238.

Baghlani, V., Mehbudia, P., Akbarib, J. & Sohrabi, M. (2013), Ultrasonic assisted deep drilling of Inconel 738LC superalloy, *in* 'The Seventeenth CIRP Conference on Electro Physical and Chemical Machining'.

Balboni, E., Espinosa-Marzal, R. M., Doehne, E. & Scherer, G. W. (2011), 'Can drying and re-wetting of magnesium sulfate salts lead to damage of stone?', *Environmental Earth Sciences* **63**.

Baraka-Lokmane, S., Main, I., Ngwenya, B. & Elphick, S. (2007), 'Application of complementary methods for more robust characterization of sandstone cores', *Marine and Petroleum Geology, Elsevier* **26**.

Barnes, R. P., Ambrose, K., Holliday, D. W. & Jones, N. S. (1994), 'Lithostratigraphical subdivision of the Triassic Sherwood Sandstone Group in west Cumbria', *Proceedings of the Yorkshire Geological Society* **50**(1), 51– 60.

Basheer, M., Srinivasan, S., Smith, B. & Gomez-Heras, M. (2008), Micro-environmental monitoring of temperature and moisture changes in building stone, *in* 'Structural Faults and repair 2008 - Edinburgh'.

BBC (2016), 'news'.
URL: *https://www.bbc.co.uk/news/uk-38025513*

Beltran, P., Garcia-Diego, F.-J., Fernandez-Navajas, A. & Merello, P. (2013), 'Multivariate thermo-hygrometric characterisation of the archaeological site of Plaza de l'Almoina (Valencia, Spain) for preventive conservation', *Sensors* .

Benavente, D. (2011), 'Why pore size is important in the deterioration of porous stones used in the built heritage', *Macla : revista de la Sociedad Espanola de Mineralogia* **15**.

Benavente, D., Brimblecombe, P. & Grossi, C. M. (2014), 'Thermodynamic calculations for the salt crystallisation damage in porous built heritage using PHREEQC', *Environmental Earth Sciences* .

Benavente, D., Cultrone, G. & Gomez-Heras, M. (2008), 'The combined influence of mineralogical, hygric and thermal properties on the durability of porous building stones', *European Journal of Mineralogy* **20**.

Benedetti, D., Alessandri, I., Bergese, P., Bontempi, E., Colombi, P., Garipoli, D., Pedrazzani, R., Zanola, P. & Depero, L. E. (2006), 'Laboratory microbeam analysis applied to cultural heritage studies', *Microchimica Acta* **155**, 101–104.

Bewick, V., Cheek, L. & Ball, J. (2004), 'Review statistics review 10: Further nonparametric methods', *Critical Care* **8**(3).

BGS (2007), 'Building and roofing stone mineral planning factsheet'. British Geological Survey Communities and Local Government.

Biswas, D. R. (1977), 'Thermal energy storage using sodium sulfate decahydrate and water', *Solar Energy* .

Bjorlykke, K. & Aagaard, P. (1992), Clay minerals in north sea sandstones, in *Origin, Diagenesis, and Petrophysics of Clay Minerals in Sandstones* Houseknecht & Pittmann (1992), pp. 65–80.

Blaha, F. & Langenecker, B. (1959), 'Plastizitätsuntersuchungen von Metallkristallen im Ultraschallfeld', *Acta Metallurgica* **7**.

Bluck, B. J., ed. (1973), *Excursion Guide to the Geology of the Glasgow district*, Geological Society of Glasgow.

Boggs-Junior, S. (2014), *Principles of Sedimentology and Stratigraphy*, Pearson New International edn, Pearson Education Limited.

Bourges, A. (2006), Holistic Correlation of Physical and Mechanical Properties of Selected Natural Stones for Assessing Durability and Weathering in the Natural Environment, PhD thesis, Ludwigs-Maximilians-Universität München.

Bradshaw, M. J. (2015), nEUCLID: A new homodyne interferometer with space applications, PhD thesis, University of Birmingham.

BRE (1997 and 2000), 'Stonelist'.
URL: *http://projects.bre.co.uk/ConDiv/stonelist/stonelist.html*

Brehl, D. & Dow, T. (2007), 'Review of vibration-assisted machining', *Pre* **32**, 153–172.

Bunyan, I. T., Fairhurst, J. A., Mackie, A. & McMillan, A. A. (1987), *Building Stones of Edinburgh*, Edinburgh Geological Society.

Burnett, D., Barbour, E. & Harrison, G. P. (2014), 'The UK solar energy resource and the impact of climate change', *Renewable Energy* **71**.

Burton, C. (2013), 'Building stone of the University of Glasgow a geological trail round the campus', reconfigured by Strathclyde Geoconservation Group (The Geological Society of Glasgow).

Butt, H., Graf, K. & Kappl, M. (2003), *Physics and Chemistry of Interfaces*, WILEY-VCH GmbH & Co. KGaA, chapter Surface forces, pp. 80–116.

Cameron, D. G., Bide, T. B., Parry, S. F., Parker, A. S. & Mankelow, J. M. (2014), Directory of mines and quarries, Technical Report 10, Britigh Geological Survey.

Carlisle, N. (1813), *A Topographical Dictionary of Scotland and of the islands in the british seas*, Vol. 2.

Carpinteri, A. & Lacidogna, G. (2006), 'Damage monitoring of an historical masonry building by the acoustic emission technique', *Materials and Structures* **39**.

Carter, N. E. A. & Viles, H. A. (2003), 'Experimental investigations into the interactions between moisture, rock surface temperatures and an epilithic lichen cover in the bioprotection of limestone', *Building and Environment* **38**, 1225–1234.

Chang, S. S. F. & Bone, G. M. (2009), 'Thrust force model for vibration-assisted drilling of aluminum 6061-T6', *International Journal of Machine Tools and Manufacture* **49**, 1070–1076.

Cherblanc, F., Berthonneau, J., Bromblet, P., & Huon, V. (2016), 'Influence of water content on the mechanical behaviour of limestone: Role of the clay minerals content', *Rock Mechanics and Rock Engineering* **49**.

Choi, S. & Won, M. (2008), Identification of compliance testing method for curing effectiveness, Technical Report FHWA/TX-09/0-5106-2, Center for Transportation Research The University of Texas at Austin.

Colas, E., Mertz, J. D., Thomachot-Schneider, C. & Barbin, V. (2011), Salt crystallization effect on the swelling behavior of clayey sandstones, *in* 'Salt Weathering on Buildings and Stone Sculptures'.

Coombes, M. A. (2011), 'Rock warming and drying under simulated intertidal conditions, part I: experimental procedures and comparisons with field data', *Earth Surface Processes and Landforms* **36**.

Coombes, M. A. & Naylor, L. (2012), 'Rock warming and drying under simulated intertidal conditions, part II: weathering and biological influences on evaporative cooling and near-surface micro-climatic conditions as an example of biogeomorphic ecosystem engineering', *Earth Surface Processes and Landforms* **37**.

Coombes, M. A., Naylor, L. A., Viles, H. A. & Thompson, R. C. (2013), 'Bioprotection and disturbance: Seaweed, microclimatic stability and conditions for mechanical weathering in the intertidal zone', *Geomorphology* **202**.

Coombes, M. A., Viles, H. A., Naylor, L. A. & La Marca, E. C. (2017), 'Cool barnacles: Do common biogenic structures enhance or retard rates of deterioration of intertidal rocks and concrete?', *Science of the Total Environment* **580**.

Correns, C. W. & Steinborn, W. (1939), 'Experimente zur Messung und Erklärung der sogenannten Kristallisationskraft', *Zeitschrift für Kristallographie - Crystalline Materials* **101**, 117–133.

Coussy, O. (2006), 'Deformation and stress from in-pore drying-induced crystallization of salt', *Journal of the Mechanics and Physics of Solids* **54**, 1517–1547.

Crepeau, T. N., Healy, S. P., Bartlett-Healy, K., Unlu, I., Farajollahi, A. & Fonseca, D. M. (2013), 'Effects of biogents sentinel trap field placement on capture rates of adult asian tiger mosquitoes, aedes albopictus', *Plos one* .

Cruden, S. (1960), *Scottish abbeys: an introduction to the medieval abbeys and priories of Scotland*, her Majesty's stationery office.

Cunha, A., Caetano, E., Magalhaes, F. & Moutinho, C. (2013), 'Recent perspectives in dynamic testing and monitoring of bridges', *Structural Control and Health Monitoring* .

Dahnel, A. N., Ascroft, H. & Barnes, S. (2016), 'The effect of varying cutting speeds on tool wear during conventional and Ultrasonic Assisted Drilling (UAD) of Carbon Fibre Composite (CFC) and titanium alloy stacks', *Procedia CIRP* (46), 420–423.

Demarco, M. M., Jahns, E., Rüdrich, J., Oyhantcabal, P. & Siegesmund, S. (2007), 'The impact of partial water saturation on rock strength: an experimental study on sandstone', *Zeitschrift der Deutschen Gesellschaft für Geowissenschaften* .

Demas, M. (2002), 'Annotated bibliography on protective shelters for archaeological sites', *Conservation and Management of Archaeological Sites* .

Demas, M. (2013), 'Site unseen: the case for reburial of archaeological sites', *Conservation and Management of Archaeological Sites,* **6**.

Derjaguin, B. V. & Churaev, N. V. (1974), 'Structural component of disjoining pressure', *Journal of Colloid and Interface Science* **49**.

Derluyn, H. (2006), Salt transport and crystallization in porous limestones: neutron-X-ray imaging and poromechanical modeling, PhD thesis, ETH Zurich.

Derluyn, H., Poupeleer, A., Gemert, D. V. & Carmeliet, J. (2008), Poromechanical modelling of hygric shrinkage and crystallization swelling in layered porous materials, *in* 'Proceedings of the 3rd International Symposium GeoProc'.

Desarnaud, J., Derluyn, H., Molari, L., de Miranda, S., Cnudde, V. & Shahidzadeh, N. (2015), 'Drying of salt contaminated porous media: Effect of primary and secondary nucleation', *Journal of Applied Physics* **118**.

Dickinson, W. R. (1970), 'Interpreting detrital modes of graywacke and arkose', *Journal of Sedimentary Petrology* **40**, 695–707.

Diego, F.-J. G., Esteban, B. & Merello, P. (2015), 'Design of a hybrid (wired/wireless) acquisition data system for monitoring of cultural heritage physical parameters in smart cities', *Sensors* **15**.

Dong, R., Schopper, A., McDowell, T., Welcome, D., Wu, J., Smutz, W., Warren, C. & Rakheja, S. (2004), 'Vibration energy absorption (VEA) in human fingers-hand-arm system', *Medical Engineering & Physics* .

Dong, Y. & Song, R. (2010), Bridges structural health monitoring and deterioration detection - synthesis of knowledge and technology, Technical report, Alaska University Transportation Center.

DuPont (2004), Dupont tyvek users manual, Technical report, DuPont Nonwovens-Tyvek.

Eloukabi, H., Sghaier, N., Nasrallah, S. B. & Prat, M. (2013), 'Experimental study of the effect of sodium chloride on drying of porous media: The crusty-patchy efflorescence transition', *International Journal of Heat and Mass Transfer* **56**.

Eppelbaum, L. (2014), *Applied Geothermics*, Springer Berlin Heidelberg, chapter Thermal Properties of Rocks and Density of Fluids, pp. 99 – 142.

Espinosa-Marzal, R. M. & Scherer, G. W. (2008), 'Crystallization of sodium sulfate salts in limestone', *Environmental Earth Sciences* **56**, 605–621.

Espinosa-Marzal, R. M. & Scherer, G. W. (2013), 'Impact of in-pore salt crystallization on transport properties', *Environmental Earth Sciences* **69**.

Everett, D. H. (1961), 'The thermodynamics of frost damage to porous solids', *Transactions of the Faraday Society* **57**.

Feld, S. I., Cristea, N. C. & Lundquist, J. D. (2012), 'Representing atmospheric moisture content along mountain slopes: Examination using distributed sensors in the Sierra Nevada, California', *Water Resources Research* **49**.

Feng, P., Wang, J., Zhang, J. & Zheng, J. (2017), 'Drilling induced tearing defects in rotary ultrasonic machining of C/SiC composites', *Ceramics International* **43**, 791–799.

Flatt, R. J. (2002), 'Salt damage in porous materials: how high supersaturations are generated', *Journal of Crystal Growth* **242**, 435–454.

Flügel, E. (2004), *Microfacies of Carbonate Rocks Analysis, Interpretation and Application*, Springer Berlin Heidelberg New York.

Fortin, J., Stanchitis, S., Dresen, G. & Gueguen, Y. (2009), 'Acoustic emissions monitoring during inelastic deformation of porous sandstone: Comparison of three modes of deformation', *Pure applied Geophysics* .

Franzen, C. & Mirwald, P. W. (2004), 'Moisture content of natural stone: Static and dynamic equilibrium with atmospheric humidity', *Environmental Geology* **46**, 391–401.

Fratini, F., Rescic, S. & Tiano, P. (2006), 'A new portable system for determining the state of conservation of monumental stones', *Materials and Structures* **39**, 139–147.

Gallego-Juarez, J. A. & Graff, K. F., eds (2015), *Power Ultrasonics*, Woodhead Publishing.

Ge, X., Mao, Y., Liu, X., Cheng, Y., Yuan, B., Chao, M. & Liang, E. (2016), 'Negative thermal expansion and broad band photoluminescence in a novel material of $ZrScMo_2VO_{12}$', *Nature Scientific Reports* .

Geikie, S. A. (1900), *The Geology of Central and Western Fife and Kinross*, Memoirs of the geological survey Scotland, Order of the Lords Commissioners of her Majesty's Treasury.

Geng, D., Zhang, D., Xu, Y., He, F. & Liu, F. (2014), 'Comparison of drill wear mechanism between rotary ultrasonic elliptical machining and conventional drilling of CFRP', *Journal of Reinforced Plastics and Composites* **33**(9), 797–809.

Georges, C. & Kaser, G. (2002), 'Ventilated and unventilated air temperature measurements for glacier-climate studies on a tropical high mountain site', *Geophysical Research* **107**.

Gillespie, M. R. & Tracey, E. A. (2016), Scotland's building stone industry: a review, Commissioned Report CR/16/026N, British Geological Survey Minerals & Waste Programme.

Gomez-Heras, M. & Fort, R. (2007), 'Patterns of halite (NaCl) crystallisation in building stone conditioned by laboratory heating regimes', *Environmental Geology* **52**.

Gomez-Heras, M., Smith, B., Viles, H., Meneely, J. & McCabe, S. (2008), HD laser scanning for the evaluation of salt decay laboratory simulations of building limestone, *in* 'Salt Weathering on Buildings and Stone Sculptures'.

Graff, K. F. (1971), Fundamental studies in the use of sonic power for rock cutting, Technical report, Ohio State University Research Foundation.

Graff, K. F. (1977), *Ultrasonics: Historical Aspects*.

Graham, C. J. (2016), A petrographic investigation into the durability of common replacement sandstones to the crystallisation of de-icing salts, PhD thesis, University of Glasgow.

Granneman, S. J. C., Shahidzadeh, N., Lubelliac, B. & van Heesac, R. P. J. (2017), 'Effect of borax on the wetting properties and crystallization behavior of sodium sulfate', *Crystal Engineering Communication* .

Grapsas, N. & Shokri, N. (2014), 'Acoustic characteristics of fluid interface displacement in drying porous media', *Multiphase Flow* .

Greig, D. (1971), *British Regional Geology the South of Scotland*, 3 edn, Edinburgh: Her Majesty's Stationary Office. Institute of Geological Sciences Natural Environment Research Council.

Grossi, C. M. & Murray, M. (1999), 'Characteristics of carbonate building stones that influence the dry deposition of acidic gases', *Construction and Building Materials* **13**.

Gubler, S., Fiddes, J., Keller, M. & Gruber, S. (2011), 'Scale-dependent measurement and analysis of ground surface temperature variability in alpine terrain', *The Cryosphere* **5**.

Gülker, G., El Jarad, A., D. Hinsch, K., Juling, H., Linnow, K., Steiger, M., Brüggerhoff, S. & Kirchner, D. (2007), Monitoring of deformations induced by crystal growth of salts in porous systems using microscopic speckle pattern interferometry, *in* 'Lasers in the Conservation of Artworks', pp. 553–560.

Gupta, S., Huinink, H. P., Prat, M., Pel, L. & Kopinga, K. (2014), 'Paradoxical drying of a fired-clay brick due to salt crystallization', *Chemical Engineering Science* **109**.

Hall, I. H. S., Browne, M. A. E. & Forsyth, I. H. (1997), *Geology of Glasgow district*, Memoir for 1:50 000 Geological Sheet 30E (Scotland), The Stationery Office. British Geological Survey Natural Environment Research Council.

Hall, K., Lindgren, B. S. & Jackson, P. (2005), 'Rock albedo and monitoring of thermal conditions in respect of weathering: some expected and some unexpected results', *Earth Surface Processes and Landforms* **30**.

Harkness, P., Lucas, M. & Cardoni, A. (2011), 'Maximization of the effective impulse delivered by a high-frequency/low-frequency planetary drill tool', *IEE* .

Harwood, G. M. (1986), The diagenetic history of Cadeby Formation carbonate (EZ1 Ca), Upper Permian, eastern England, *in* 'The English Zechstein and Related topics'.

Harwood, G. M. & Smith, F. (1986), Mineralization in Upper Permian carbonates at outcrop in eastern England, *in* 'The English Zechstein and Related topics'.

Hasselberg, M. J., McMahon, J. & Parker, K. (2013), 'The validity, reliability, and utility of the iButton for measurement of body temperature circadian rhythms in sleep/wake research', *Sleep Medicine* **14**.

Heddle, J. M. & Mainland, T. (1920), *Cambridge County Geographies Orkney and Shetland*, Cambridge University Press.

Heisel, U., Eisseler, R., Eber, R., Wallaschek, J., Twiefel, J. & Huang, M. (2011), 'Ultrasonic-assisted machining of stone', *Production Engineering Research and Development* **5**, 587–594.

Heubeck, C. (2007), *Der belebte Planet II*, Fachbereich Geowissenschaften der Freien Universität Berlin, chapter Porosität und Permeabilität in natürlichen Gesteinen, pp. 36–44.

Historic Environment Scotland (2015).
URL: *https://www.historicenvironment.scot/about-us/who-we-are/why-is-the-historic-environment-important/*

Historic Environment Scotland (2017), Annual Report, Technical report, HES.

Holdena, Z. A., Klene, A. E., Keefe, R. F. & Moisen, G. G. (2013), 'Design and evaluation of an inexpensive radiation shield for monitoring surface air temperatures', *Agricultural ad Forest Metrology* **180**.

Holliday, D. W., Jones, N. S. & A (2005), Lithostratigraphical subdivision of the Sherwood Sandstone Group (Triassic) of the north-eastern part of the Carlisle Basin, Cumbria, and adjacent parts of Dumfries and Galloway, UK, Technical Report IR/05/148.

Hourihane, C. (2012), *The Grove Encyclopedia of Medieval Art and Architecture*, Vol. 1, Oxford University Press.

Houseknecht, D. W. & Pittmann, E. D. (1992), *Origin, Diagenesis, and Petrophysics of Clay Minerals in Sandstones*, number 47 *in* 'Special Publications', SEPM (Society for Sedimentary Geology).

Howard, J. J. (1992), Influence of authigenic clay minerals on permeability, *in* 'Origin, Diagenesis, and Petrophysics of Clay Minerals in Sandstones', SEPM (Society for Sedimentary Geology), pp. 257– 264.

Hua, Y., Lemerle, P. & Ganghoffer, J.-F. (2017), 'A two scale modeling and computational framework for vibration-induced Raynaud syndrome', *Biomedical Materials* .

Huang, Y.-H., Yang, S.-Q., Hall, M. R. & Zhang, Y.-C. (2018), 'The effects of NaCl concentration and confining pressure on mechanical and acoustic behaviors of brine-saturated sandstone', *Energies* .

Hubbart, J., Link, T., Campbell, C. & Cobos, D. (2005), 'Evaluation of a low-cost temperature measurement system for environmental applications', *Hydrological Processes* **19**.

Huwald, H., Higgins, C. W., Boldi, M.-O., Bou-Zeid, E., Lehning, M. & Parlange, M. B. (2008), 'Albedo effect on radiative errors in air temperature measurements', *Water Resources Research* **45**.

Hyslop, E. K. & Albornoz-Parra, L. (2008), 'Developing a future repairs strategy for a sandstone city: A petrographic investigation of building stone in Glasgow, Scotland', *Material Characterisation* (60).

Hyslop, E. K., Albornoz-Parra, L. J., Fisher, L. C., & Hamilton, S. L. (2006), Safeguarding Glasgow's stone built heritage skills and materials requirements: facade surveys and building stone analysis, Technical report, British Geological Survey.

Hyslop, E. K., Albornoz-Parra, L. J. & Tracey, E. A. (2009), Assessing the potential for reopening a building stone quarry: Newbigging sandstone quarry, Fife, Technical report, British Geological Survey.

ICOMOS (2008), 'Illustrated glossary on stone deterioration patterns of the International Scientific Committee for Stone, International Council on Monuments and Stones'.

Inaudi, D. (2004), Sofo sensors for static and dynamic measurements, *in* 'International Symposium on Engineering Surveys for Construction Works and Structural Engineering'.

Inaudi, D., Elamarib, A., Pflug, L., Gisinb, N., Breguetb, J. & Vurpillot, S. (1994), 'Low-coherence deformation sensors for the monitoring of civil-engineering structures', *Sensors and Actuators* **44**, 125–130.

Inman, D. J. (2009), *Engineering Vibrations*, Pearson Prentice Hall.

Ishikawa, K., Suwabe, H., Nishide, T. & Uneda, M. (1998), 'A study on combined vibration drilling by ultrasonic and low-frequency vibrations for hard and brittle materials', *Precision Engineering* **22**, 196–205.

Jamtveit, B. & Hammer, O. (2012), *Geochemical Perspectives*, European Association of Geochemistry.

Jarad, A. E., Gülker, G. & Hinsch, K. D. (2005), A combination of ESPI, microscopic ESPI and digital speckle-correlation to study salt-induced deterioration in porous materials, *in* 'Deutsche Gesellschaft für angewandte Optik Jahrestagung'.

Jimenez-Gonzalez, I., Rodriguez-Navarro, C. & Scherer, G. W. (2007), 'Role of clay minerals in the physicomechanical deterioration of sandstone', *Journal of Geophysical Research* **113**.

Juling, H., Kirchner, D., Brüggerhoff, S., Linnow, K., Steiger, M., Jarad, A. E., Gülker, G. & Ossietzky, C. V. (2004), Salt damage of porous materials: a combined theoretical and experimental approach, *in* '10th International Congress on Deterioration and Conservation of Stone'.

Kaldi, J. (1986), Diagenesis of nearshore carbonate rocks in the Sprotbrough member of the Cadeby (Magnesian Limestone) Formation (Upper Permian) of eastern England, *in* 'The English Zechstein and Related topics'.

Kamh, G. (2004), 'Weathering at high latitudes on the Carboniferous Old Red sandstone, petrographic and geotechnical investigations, Jedburgh Abbey Church, Scotland, a case study', *Environmental Geology* .

Karatasios, I., Michalopoulou, A., Amenta, M. & Kilikoglou, V. (2017), 'Modification of water transport properties of porous building stones caused by polymerization of silicon-based consolidation products', *Pure and Applied Chemistry* **89**.

Kerr, J. G., ed. (1928), *Glasgow Sketches by various Authors*, Handbook, British association for the advancement of science.

Kim, K. Y., Zhuang, L., Yang, H., Kim, H. & Min, K.-B. (2016), 'Strength anisotropy of Berea sandstone: Results of X-ray computed tomography, compression tests, and discrete modeling', *Rock Mechanics and Rock Engineering* **49**, 1201–1210.

Kirk, S. & Williamson, D. (2012), 'Structure and thermal properties of porous geological materials', *American Institute of Physics (AIP) Conference Proceedings* **1426**, 867–870.

Kocher, M. (2005), Quelldruckmessungen und thermische Druckmessungen an ausgewählten Sandsteinen, PhD thesis, Ludwig-Maximilians-Universität München.

Kong, B., Wang, E., Li, Z., Wang, X., Liu, J. & Li, N. (2016), 'Fracture mechanical behavior of sandstone subjected to high-temperature treatment and its acoustic emission characteristics under uniaxial compression conditions', *Rock Mechanics and Rock Engineering* **49**.

Koshimizu, S. (2007), 'Ultrasonic vibration-assisted cutting of titanium alloy', *American Society for Precision Engineering conference proceedings* .

Kottke, J. (2009), An investigation of quantifying and monitoring stone surface deterioration using three dimensional laser scanning, Master's thesis, University of Pennsylvania.

Kreitlow, H., Miesner, J. & Stockmann, J. (1994), Measurement of absolute object deformations by means of two wavelength ESPI, *in* 'Proceedings Interferometry 94: New Techniques and Analysis in Optical Measurements', Vol. 2340.

Krzemien, L. & Lukomski, M. (2014), 'Combining digital speckle pattern interferometry with shearography in a new instrument to characterize surface delamination in museum artefacts', *Journal of Cultural Heritage* .

Kyriakou, L., Theodoridou, M. & Ioannou, I. (2017), Assessment of the durability of lime renders with Phase Change Material (PCM) additives against salt crystallization, *in* '4th International Conference on Salt Weathering of Buildings and Stone Sculptures'.

Laue, S. (2002), Verwitterung von Naturstein durch lösliche Salze an wechselfeuchter Luft, Technical report, Institut für Steinkonservierung.

Lawson, J. A. (1981), *Building Stones in Glasgow*, Geological Society of Glasgow.

Lecampion, B. (2010), 'Stress-induced crystal preferred orientation in the poromechanics of in-pore crystallization', *Journal of the Mechanics and Physics of Solids* **58**, 1701–1715.

Lewis, J. H. & Ewart, G. J. (1995), *Jedburgh Abbey The Archaeology and Architecture of a Border Abbey*, Society of Antiquaries of Scotland.

Li, X. (2015), A motion control system design for an ultrasonic planetary core drill (UPCD) unit, *in* 'AIAA Space 2015 Conference'.

Li, X., Harkness, P., Worrall, K., Timoney, R. & Lucas, M. (2017), 'A parametric study for the design of an optimized ultrasonic percussive planetary drill tool', *IEEE Transactions on Ultrasonics, Ferroelectrics and Frequency Control* .

Li, Y. H., Liu, J. P., Zhao, X. D. & Yang, Y. J. (2010), 'Experimentalstudies of the change of spatial correlation length of acoustic emission events during rock fracture process', *Journal of Rock Mechanics and Mining Sciences* **47**.

Lima, F. P., Burnett, N. P., Helmuth, B., Kish, N., Aveni-Deforge, K. & Wethey, D. S. (2011), *Biomimetic Based Applications*, IntechOpen, chapter Monitoring the Intertidal Environment with Biomimetic Devices.

Lindström, N., Talreja, T., Linnow, K. & Steiger, M. (2014), Crystallization behavior of a Na_2SO4-$MgSO_4$ salt mix-ture and comparison to single salt behavior, *in* '3rd International Conference on Salt Weathering of Buildings and Stone Sculptures'.

Linnow, K. & Steiger, M. (2005), Thermodynamische Modellierung und experimentelle Untersuchung von Phasenumwandlungen, Technical report, Institut für Anorganische und Angewandte Chemie, Universität Hamburg.

Linseis (2018).
URL: *https://www.linseis.com/en/our-products/dilatometer/*

Lockner, D. (1993), 'The role of acoustic emission in the study of rock fracture', *International Journal of Rock Mechanics & Mining Sciences* **30**(7), 883–899.

Lorenzoni, F. (2013), Integrated Methodologies Based on Structural Health Monitoring for the Protection of Cutural Heritage Buildings, PhD thesis, University of Trento.

Lorenzoni, F., Casarin, F., Caldon, M., Islami, K. & Modena, C. (2016), 'Uncertainty quantification in structural health monitoring: Applications on cultural heritage buildings', *Mechanical Systems and Signal Processing* **66**, 268–281.

Lott, G. & Cooper, A. (2005), The building limestones of the Upper Permian, Cadeby Formation (Magnesian Limestone) of Yorkshire, Technical report, British Geological Survey.

Lott, G. K. & Richardson, C., eds (1997), *Yorkshire stone for building the Houses of of Parliament (1839-c.1852)*, Vol. 51, Proceedings of the Yorkshire Geological Society.

Lubelli, B., van Hees, R. P. J. & Huinink, H. P. (2006), 'Effect of NaCl on the hydric and hygric dilation behaviour of lime-cement mortar', *HERON* .

Luzi, G., Montuori, A., Bignami, C., Crosetto, M. & Stramondo, S. (2014), Radar interferometry for cultural heritage monitoring, *in* 'art14 11th International Conference'.

MacGregor, A. G. & Eckford, R. J. A. (1952), 'The Upper Old Red and lower Carboniferous sediments of Teviotdale and Tweed side, and the stones of the Abbeys of the Scottish Borderland', *Trans Edinburgh Geological Society* **14**.

MacGregor, A. R. (1968), *Fife and Angus An Excursion Guide*, William Blackwood & Sons Ltd for the University of St. Andrews.

Madsen, F. T. & Müller-Vonmoos, M. (1989), 'The swelling behaviour of clays', *Applied Clay Science* **4**, 143–156.

Makhdum, F., Jennings, L. T., Roy, A. & Silberschmidt, V. V. (2012), Cutting forces in ultrasonically assisted drilling of carbon fibre-reinforced plastics, *in* 'Modern Practice in Stress and Vibration Analysis 2012'.

Manthei, G. (2018), 'Application of the cluster analysis and time statistic of acoustic emission events from tensile test of a cylindrical rock salt specimen', *Engineering Fracture Mechanics* .

Manthei, G. & Eisenblätter, J. (2008), *Acoustic emission testing Basics for Research Applications in Civil Engineering*, Springer Berlin Heidelberg, chapter Acoustic Emission in Study of Rock Stability, pp. 239–310.

Maroju, N. K., Subbu, S., Krishna, V., Vamsi, A. & Venugopal, A. (2014), 'Vibration assisted conventional and advanced machining: A review', *Procedia Engineering* **97**, 1577 – 1586.

Masuda, K., Erskine, D. & Anderson, O. (2000), 'Differential laser-interferometer for thermal expansion measurements', *American Mineralogist* **85**, 279–282.

Matiasovsky, P. & Mihalka, P. (2014), *Drying and Wetting of Building Material and Components*, Vol. 4, Springer Berlin Heidelberg, chapter Pore Structure Parameters and Drying Rates of Building Materials, pp. 71–90.

Matyscaka, O., OttosenbInge, L. M. & Rörig-Dalgaard (2014), 'Desalination of salt damaged Obernkirchen sandstone by an applied DC field', *Construction and Building Materials* **71**.

Maxxim (2015), Temperature/Humidity Logger with 8 KB Datalog Memory DS1923, Technical report.

McCabe, S., McKinley, J., Gomez-Heras, M. & Smith, B. (2011), 'Dynamical instability in surface permeability characteristics of building sandstones in response to salt accumulation over time', *Geomorphology* **130**, 65–75.

McCabe, S., Smith, B. J., McAlister, J. J., Gomez-Heras, M., McAllister, D., Warke, P. A., Curran, J. M. & Basheer, P. A. M. (2013), 'Changing climate, changing process: Implications for salt transportation and weathering within building sandstones in the UK', *Environmental Earth Sciences* **69**, 1225–1235.

McCallien, W. J. (1938), *Geology of Glasgow and District*, Blackie and son limited.

McGreevy, J. P., Warke, P. A. & Smith, B. J. (2000), 'Controls on stone temperatures and the benefits of interdisciplinary exchange', *Journal of the American Institute for Conservation,* **39**.

McIlroy de la Rosa, J. P., Porcel, M. C. & Warke, P. A. (2013), 'Mapping stone surface temperature fluctuations: Implications for lichen distribution and biomodification on historic stone surfaces', *Journal of Cultural Heritage* **14**.

McKinley, J. M. & Warke, P. A. (2007), Controls on permeability: implications for stone weathering, *in* 'Building Stone Decay: From Diagnosis to Conservation', Vol. 271, Geological Society, London, Special Publications, pp. 225–236.

McKinley, J. M., Worden, R. H. & Ruffell, A. H. (2003), Smectite in sandstones: A review of the controls on occurrence and behaviour during diagenesis, *in* 'Clay Mineral Cements in Sandstones', Blackwell Publishing, chapter Smectite in Sandstones: A Review of the Controls on Occurrence and Behaviour During Diagenesis.

McMillan, A. A. (2002), *Geology of the New Galloway and Thornhill district*, Memoir for 1:50000 Geological Sheets 9W and 9E (Scotland), The Stationery Office, Bristish Geolocial Survery.

McMillan, A. & Hyslop, E. (2005), *Building with Scottish Stone*, Natural Stone Institute and Arcamedia.

Menendez, B. (2016), *Non-Destructive Testing*, IntechOpen, chapter Non-Destructive Techniques Applied to Monumental Stone Conservation, pp. 173–214.

Meng, Q., Zhang, M., Han, L., Pu, H. & Chen, Y. (2018), 'Acoustic emission characteristics of red sandstone specimens under uniaxial cyclic loading and unloading compression', *Rock Mechanics and Rock Engineering* .

Merello, P., Garcaa-Diego, F., Perez-Miralles, J., Fernandez-Navajas, A. & Garcia, M. D. C. P. (2012), Basic descriptive statistical methods for monitoring and evaluation of microclimates in cultural heritage, *in* 'Science and Technology for the Conservation of Cultural Heritage'.

Met Office (accessed 2017).
URL: *https://www.metoffice.gov.uk/*

Mimoso, J. M. & Costa, D. (2006), 'The DRMS drilling technique with pilot holes', *Heritage, Weathering and Conservation* .

Modestou, S., Ioannou, I. & Theodoridou, M. (2011), Salt distribution mapping in natural building and decorative stones, *in* 'Advances in Construction Materials through Science and Engineering Conference (RILEM)'.

Mogi, K. (1969), 'Laboratory study of elastic shocks prior to rock failure', *Transactions American Geophysical Union* .

Mykura, W. (1976), *British Regional Geology Orkney and Shetland*, her Majesty's stationery office. Natural Environment Research Council Institue of Geological Sciences.

Nath, C., Rahman, M. & Andrew, S. S. K. (2007), 'A study on ultrasonic vibration cutting of low alloy steel', *Journal of Materials Processing Technology* .

Neppiras, E. A. (1964), *Ultrasonics*, Vol. 2, chapter Ultrasonic machining and forming, pp. 167–173.

Nishizawa, O. & Nomo, H. (1990), 'A self-exciting process of acoustic emission occurrence in steady creep of granite under uniaxial stress', *Geophysical Research Letters* .

Okrusch, M. & Matthes, S. (2005), *Mineralogie: Eine Einführung in die spezielle Mineralogie, Petrologie und Lagerstättenkunde*, 7th edn, Springer Berlin Heidelberg.

Ordonez, S., Fort, R. & del Cura, M. A. G. (1997), 'Pore size distribution and the durability of porous limestone', *Quarterly Journal of Engineering Geology* .

Orr, S., Viles, H., Leslie, A. & Stelfox, D. (2016), Comparability of non-destructive moisture measurement techniques on masonry during simulated wetting, *in* 'Conference: 13th International Congress on the Deterioration and Conservation of Stone'.

Paktinat, H. & Amini, S. (2017), 'Ultrasonic assistance in drilling: FEM analysis and experimental approaches', *International Journal of Advanced Manufacturing Technology* .

Pamplona, M., Kocher, M. & Snethlage, R. (2010), 'Halite - a new calibration material for microdrilling resistance measurements', *Journal of cultural heritage* **11**(2), 180–184.

Pamplona, M., Kocher, M., Snethlage, R. & Barros, L. A. (2007), 'Drilling resistance: overview and outlook', *Zeitschrift der Deutschen Gesellschaft für Geowissenschaften* **158**, 665–676.

Papida, S., Murphy, W. & May, E. (2000), 'Enhancement of physical weathering of building stones by microbial populations', *Biodegradation* **46**.

Peeters, B., Maeck, J. & Roeck, G. (2001), 'Vibration-based damage detection in civil engineering: excitation sources and temperature effects', *Smart Materials and Structures* .

Penn, R. L., Zhu, C., Xu, H. & Veblen, D. R. (2001), 'Iron oxide coatings on sand grains from the Atlantic coastal plain: High-resolution transmission electron microscopy characterization', *Geology* **29**(9), 843–846.

Pettijohn, F. J. (1975), *Sedimentary Rocks*, third edn, Harper & Row.

Pettijohn, F., Potter, P. E. & Siever, R. (1987), *Sand and Sandstone*, 2nd edn, Springer-Verlag.

Phillips, E. (2007), Petrology and provenance of the Siluro-Devonian (Old Red Sandstone facies) sedimentary rocks of the Midland Valley, Scotland, Geology and Landscape Northern Britain Programme Internal Report IR/07/040, British Geological Survey.

Ping, X. & Beaudoin, J. J. (1992), 'Mechanism of sulphate expansion i. thermodynamic principle of crystallization pressure', *Cement and Concrete Research* .

Potvin, Y. & Hudyma, M. R. (2001), Seismic monitoring in highly mechanised hardmine mines in Canada and Australia, *in* 'The Fifth International Symposium on Rockburst and Seismicity in Mines'.

Press, F., Siever, R., Jordan, T. H. & Grotzinger, J. (2008), *Allgemeine Geologie*, 5th edn, Springer Verlag.

Pringle, J. (1948), *British Regional Geology The South of Scotland*, 2 edn, Edinburgh: Her Majesty's Stationary Office.

Putnis, A. & Mauthe, G. (2001), 'The effect of pore size on cementation in porous rocks', *Geofluids* **1**, 37–41.

Quantum Alloys Ltd (2005).
URL: *http://www.quantumalloys.com/data/nickel/aln36.html*

Rad, M. N. (2014), Pore-Scale Investigation of Salt Precipitation during Evaporation from Porous Media, PhD thesis, University of Manchester.

Rad, M. N., Shokri, N., Keshmiri, A. & Withers, P. J. (2015), 'Effects of grain and pore size on salt precipitation during evaporation from porous media', *Transport Porous Media* **110**, 281–294.

Radley, J. (1965), Anston Stone: The stone for the rebuilding of the Houses of Parliament, 1834-1852, Technical report, Royal Commision on Historical Monuments, The White House, Clifton.

Riminesi, C. & Olmi, R. (2017), Diagnostics and monitoring of moisture and salt in porous materials by evanescent field dielectrometry, *in* '4th International Conference on Salt Weathering of Buildings and Stone Sculptures'.

Rodrigues, J. D. & Costa, D. (2004), 'A new method for data correction in drill resistance tests for the effect of drill bit wear', *International Journal for Restoration* **10**(3), 1–18.

Rodriguez-Navarro, C., Doehne, E. & Sebastian, E. (2000), 'How does sodium sulfate crystallize? Implications for the decay and testing of building materials', *Cement and Concrete Research* **30**.

Rossi-Manaresi, R. & Tucci, A. (1991), 'Pore structure and the disruptive or cementing effect of salt crystallization in various types of stone', *Studies in Conservation* **36**.

Rotherford, T. R. (1903), *The British Journal of Photography*, Vol. 50 of *2251*, Apptitude Media Ltd.

Royal Commision (1956), *An Inventory of the Ancient and Historical Monuments of Roxburgh*, Vol. 1 of *Royal Commission on the Ancient Monuments of Scotland*, Her Majesty's Stationery Office.

Royne, A. & Jamtveit, B. (2015), 'Pore-scale controls on reaction-driven fracturing', *Reviews in Mineralogy and Geochemistry* **80**, 25–44.

Roznik, E. A. & Alford, R. A. (2012), 'Does waterproofing thermochron iButton dataloggers influence temperature readings?', *Thermal Biology* .

Rüderich, J. (2003), Gefügekontrollierte Verwitterung natürlicher und konservierter Marmore, PhD thesis, Georg-August-Universität Göttingen.

Rüdrich, J., Bartelsen, T., Dohrmann, R. & Siegesmund, S. (2011), 'Moisture expansion as a deterioration factor for sandstone used in buildings', *Environmental Earth Sciences* .

Rüdrich, J., Rieffel, Y., Pirskawetz, S., Alpermann, H., Joksch, U., Gengnagel, C., Weise, F., Plagge, R., Zhao, J. & Siegesmund, S. (2011), 'Development and assessment of protective winter covers for marble statuaries of the Schlossbrücke, Berlin (Germany)', *Environmental Earth Sciences* **63**.

Rüdrich, J., Seidel, M., Kirchner, D. & Siegesmund, S. (2005), 'Beanspruchungen von Naturwerksteinen durch Salz- und Eiskristallisation im Porenraum sowie hygrische Dehnungsvorgänge', *Zeitschrift der Deutschen Geologischen Gesellschaft* **156**.

Rüdrich, J., Seidel, M., Rothert, E. & Siegesmund, S. (2007), Length changes of sandstones caused by salt crystallization, *in* R. Prikryl & B. J. Smith, eds, 'Building Stone Decay: From Diagnosis to Conservation', Vol. 271, Geological Society, London, Special Publications, chapter Length changes of sandstones caused by salt crystallization, pp. 199–209.

Rüdrich, J. & Siegesmund, S. (2007), 'Salt and ice crystallisation in porous sandstones', *Environmental Geology* **52**, 225–249.

Ruiz-Agudo, E., Martin-Ramos, J. D. & Rodriguez-Navarro, C. (2007), 'Mechanism and kinetics of dehydration of epsomite crystals formed in the presence of organic additives', *Journal of Physical Chemistry* **111**.

Ruiz-Agudo, E. & Rodriguez-Navarro, C. (2010), *Limestone in the Built Environment: Present-Day Challenges for the Preservation of the Past*, Geological Society, London, Special Publications, chapter Suppression of salt weathering of porous limestone by borax-induced promotion of sodium and magnesium sulphate crystallization.

Scherer, G. W. (1990), 'Theory of drying', *Journal of the American Ceramics Society* **73**, 3–14.

Scherer, G. W. (1999), 'Crystallization in pores', *Cement and Concrete Research* **29**, 1347–1358.

Scherer, G. W. (2004), 'Stress from crystallization of salt', *Cement and Concrete Research* **34**, 1613–1624.

Schnepfleitner, H., Sass, O., Fruhmann, S., Viles, H. & Goudie, A. (2016), 'A multi-method investigation of temperature, moisture and salt dynamics in tafoni (Tafraoute, Morocco)', *Earth Surface Processes and Landforms* **41**.

Scholz, C. H. (1968), 'The frequency-magnitude relation of microfracturing in rock and its relation to earthquakes', *Bulletin of the Seismological Society of America* **58**(1), 399–415.

Scottish Government (2014), Our place in time, The Historic Environment Strategy for Scotland, Technical Report DPPAS22629, Scottish Government.

Scottish Government (2017).
URL: *http://www.gov.scot/Topics/Statistics/Browse/Tourism*

Serafeimidis, K. & Anagnostou, G. (2014), 'On the crystallisation pressure of gypsum', *Environmental Earth Sciences* **72**.

Shin, M., Patton, R., Mahar, T., Ireland, A., Swan, P. & Chow, C. M. (2017), 'Calibration and validation processes for relative humidity measurement by a Hygrochron iButton', *Physiology and Behavior* **179**.

Siegesmund, S. & Dürrast, H. (2011), *Stone in Architecture*, Springer Berlin Heidelberg, chapter Physical and Mechanical Properties of Rocks, pp. 97–225.

Siegesmund, S. & Snethlage, R. (2011), *Stone in Architecture*, 4th edn, Springer Berlin Heidelberg, chapter Characterisation of Stone Deterioration on Buildings, pp. 347–411.

Sirdesai, N., Gupta, T., Singh, T. & Ranjith, P. (2018), 'Studying the acoustic emission response of an Indian monumental sandstone under varying temperatures and strains', *Construction and Building Materials* .

Smith, D. H., Crabtree, D. R., Bilzon, J. L. & Walsh, N. P. (2010), 'The validity of wireless iButtons and thermistors for human skin temperature measurement', *Physiological Measurement* **31**.

Sohn, H. (2007), 'Effects of environmental and operational variability on structural health monitoring', *Philosophical Transactions of the Royal Society A* **365**, 539–560.

Sorace, S. (1996), 'Long-term tensile and bending strength of natural building stones', *Materials and Structures* **29**.

Stahlbuhk, A., Nissen, J., Linnow, K. & Steiger, M. (2014), Influence of the salt concentration on the damage potential of mirabilite and thenardite, *in* '3rd International Conference on Salt Weathering of Buildings and Stone Sculptures'.

Stancliffstones (2012).
URL: *http://www.stancliffe.com/UK-Stone-Types-And-Colours/*

Stavropoulou, M. (2006), 'Modeling of small-diameter rotary drilling tests on marbles', *International Journal of Rock Mechanics & Mining Sciences* .

Stefano, A. D. & Ceravolo, R. (2007), 'Assessing the health state of ancient structures: The role of vibrational tests', *Journal of Intelligent Material Systems and Structures* **18**.

Steiger, M. (2005*a*), 'Crystal growth in porous materials-II: Influence of crystal size on the crystallization pressure', *Journal of Crystal Growth* **282**, 470–481.

Steiger, M. (2005*b*), 'Crystal growth in porous materials: The crystallization pressure of large crystals', *Journal of Crystal Growth* **282**, 455–469.

Steiger, M., Linnow, K., Juling, H., Gülker, G., Jarad, A. E., Brüggerhoff, S. & Kirchner, D. (2008), 'Hydration of $MgSO_4$ H_2O and generation of stress in porous materials', *Crystal Growth & Design* **8**(1).

Stone, P., McAdam, A. D. & Chrisholm, J. I. (1996), *Geology in south-west Scotland: An excursion guide*, Bristish Geological Survey. supported by Edinburgh Geological Society, NERC.

Strojecki, M., Lukomski, M., Colla, C. & Gabrielli, E. (2011), *Non-destructive Testing of Materials and Structures*, Springer, Dordrecht, chapter Acoustic emission as a non-destructive method for tracing damage: from laboratory testing to monitoring historic structures, pp. 1131–1136.

Strojecki, M., Lukomski, M., Krzemien, L., Sobczyk, J. & Bratasz, L. (2014), 'Acoustic emission monitoring of an eighteenth century wardrobe to support a strategy for indoor climate management', *Studies in Conservation* .

Suarez del Rio, L. M., Ruiz de Argandona, V. G., Calleja, L., Rey, A. R., Grossi-Sampedro, C. M. & Montoto, M. (2010), *Materials, Technologies and Practice in Historic Heritage Structures*, Springer Dordrecht Heidelberg London New York, chapter Acoustic Emission Monitoring of the Cathedral of Palma de Mallorca (Spain), pp. 351–370.

Sun, X., Xu, H., Zhend, L., He, M. & Gong, W. (2016), 'An experimental investigation on acoustic emission characteristics of sandstone rockburst with different moisture contents', *Science China Technological Scienes* .

Svahn, H. (2006), Non-destructive field tests in stone conservation, Technical Report 2006:3, Riksantikvarieämbetet.

Tao, K. & Zheng, W. (2018), 'Automatic selection of low-permeability sandstone acoustic emission feature parameters and its application in moisture identification', *Applied Sciences* .

Theodoridou, M., Dagrain, F. & Ioannou, I. (2012), Correlation of stone properties using standardized methodologies and non-standardized micro-destructive techniques, *in* 'Proceedings of the 12th International Conference on the Deterioration and Conservation of Stone'.

Thomson, B. J., Bridges, N. T., Cohen, J., Hurowitz, J. A., Lennon, A., Paulsen, G. & Zacny, K. (2013), 'Estimating rock compressive strength from rock abrasion tool (RAT) grinds', *Journal of Geophysical Research: Planets* .

Tiano, P., Rodrigues, J. D., Witte, E. D., Verges-Belmin, V., Massey, S., Snethlage, R., Costa, D., Cadot-Leroux, L., Garrod, E. & Singer, B. (2000), 'The conservation of monuments: A new method to evalute consolidating treatments', *Internationale Zeitschrift fuer Bauinstandsetzen und Baudenkmalpflege* **6**(2), 133–150.

Török, A. (2010), *Materials, Technologies and Practice in Historic Heritage Structures*, Springer Dordrecht Heidelberg London New York, chapter In Situ Methods of Testing Stone Monuments and the Application of Nondestructive Physical Properties Testing in Masonry Diagnosis, pp. 177–193.

Tsuboi, R., Kakinuma, Y., Aoyama, T., Ogawa, H. & Hamada, S. (2012), 'Ultrasonic vibration and cavitation-aided micromachining of hard and brittle materials', *Procedia CIRP 1* pp. 342–346.

Tucker, M. (1988), *Techniques in Sedimentology*, Blackwell Scientific Publications.

Turlewicz, A. (2016), 'Improving environmental monitoring of building stones', Thesis University of Glasgow.

Ubertini, F., Comanducci, G. & Cavalagli, N. (2016), 'Vibration-based structural health monitoring of a historic bell-tower using output-only measurements and multivariate statistical analysis', *Structural Health Monitoring* .

Valentini, E., Benincasa, A., Tiano, P., Fratini, F. & Rescic, S. (2008), 'On site drilling resistance profiles of natural stones', *ICVBC: Istituto per la Conservazione e la Valorizzazione dei Beni Culturali, Florance* .

van Marken Lichtenbelt, W. D., Daanen, H. A. M., Wouters, L., Fronczek, R., Raymann, R. J., Severens, N. M. W. & Someren, E. V. (2006), 'Evaluation of wireless determination of skin temperature using iButtons', *Physiology and B* **88**.

Vandevoorde, D., Cnudde, V., Dewanckele, J., Brabant, L., de Bouw, M., Meynen, V. & Verhaeven, E. (2013), 'Validation of in situ applicable measuring techniques for analysis of the water adsorption by stone', *Procedia Chemistry* **8**, 317–327.

Vazquez, P., Thomachot-Schneider, C., Mouhoubi, K., Fronteau, G., Gommeaux, M., Benavente, D., Barbin, V. & Bodnar, J.-L. (2015), 'Infrared thermography monitoring of the NaCl crystallisation process', *Infrared Physics & Technology* **71**.

Vedvik, N. (2015), Assessment of ultrasonic assisted drilling, Master's thesis, Norwegian University of Science and Technology.

Velde, B. (1992), *Introduction to clay Minerals chemistry, origin, uses and environmental significance*, Chapman & Hall.

Vivi, T., Bernikola, E., Hatzigiannakis, K., Melessanaki, K. & Pouli, P. (2013), 'Synchronized deformation monitoring in laser cleaning: an application for cultural heritage conservation', *Universal Journal of Physics and Application* .

Vivi, T., Bernikola, E., Leissner, J., Bertolini, C. & Camuffo, D. (2013), Experimental methods on monitoring of materials surfaces in climate change conditions, *in* '3rd European Workshop on Cultral Heritage Preservation'.

Vivi, T., Tsiranidou, E. & Bernikola, E. (2012), 'Interference fringe-patterns association to defect-types in artwork conservation: An experiment and research validation review', *Applied Physics A* **106**, 397–410.

Wang, L., Throop, H. L. & Gill, T. (2015), 'A novel method to continuously monitor litter moisture - a microcosm-based experiment', *Arid Environments* **115**.

Wangler, T. (2017), Swelling clay and its inhibition in the Villarlod Molasse, *in* '13th International Congress on the Deterioration and Conservation of Stone'.

Warke, P. A. & Smith, B. J. (1998), 'Effects of direct and indirect heating on the validity of rock weathering simulation studies and durability tests', *Geomorphology* **22**, 347–357.

Warke, P., Smith, B. J. & Magee, R. W. (1996), 'Thermal response characteristics of stone: Implications for weathering of soiled surfaces in urban environments', *Earth Surface Processes and Landforms* **21**.

Waters, C. N. (2009), 'Carboniferous geology of Northern England', *Open University Geological Society* **30**(1), 5–16.

Waters, C. N., Browne, M. A. E., Jones, N. S. & Somerville, I. (2011), *A Revised Correlation of Carboniferous Rocks in the British Isles*, number 26 *in* 'Special Report', The Geological Society, chapter Midland Valley of Scotland, pp. 1–3.

Webb, M. B., Garofalini, S. H. & Scherer, G. W. (2011), 'Molecular dynamics investigation of solution structure between NaCl and quartz crystals', *Journal of Physical Chemistry* .

Wedekind, W., Lopez-Doncel, R., Dohrmann, R. & Siegesmund, S. (2012), Hygric and hydric expansion of tuffs exclusively caused by clay minerals?, *in* '12th International Congress on the Deterioration and Conservation of Stone'.

Weiss, T., Siegesmund, S., Kirchner, D. & Sippel, J. (2004), 'Insolation weathering and hygric dilatation: two competitive factors in stone degradation', *Environmental Geology* **46**, 402–413.

Wentworth, C. K. (1922), 'A scale of grade and class terms for clastic sediments', *The Journal of Geology* **30**(5), 377 – 392.

Wiercigroch, M., Wojewoda, J. & Krivtsov, A. M. (2005), 'Dynamics of ultrasonic percussive drilling of hard rocks', *Journal of Sound and Vibration* .

Willis, C. K. R., Jameson, J. W., Faure, P. A., Boyles, J. G., Jr, V. B. & Cervone, T. H. (2009), 'Thermocron iButton and iBBat temperature dataloggers emit ultrasound', *Comparative Physiology B* **179**.

Wilson, M., ed. (1994), *Clay mineralogy: spectroscopic and chemical determinative methods*, Chapman & Hall.

Won, M. S. & Dharan, C. K. H. (2002), 'Chisel edge and pilot hole effects in drilling composite laminates', *Journal of Manufacturing Science and Engineering* **124**.

Worden, R. H. & Morad, S. (2003), Clay minerals in sandstones: control on formation, distribution and evolution, *in* S. M. Richard H. Worden, ed., 'Clay Mineral Cements in Sandstones', number 34 *in* 'International Association of sedimentologists Special Publications', Blackwell Publishing.

Worthington, P. F. (2003), Effect of clay content upon some physical properties of sandstone reservoirs, *in* 'Clay Mineral Cements in Sandstones', number 34, Blackwell Publishing.

Xu, J., Jiang, J., Zuo, L. & Gao, Y. (2017), 'Acoustic emission monitoring and failure precursors of sandstone samples under various loading and unloading paths', *Shock and Vibration* .

Xu, X., Mo, Y. L., Liu, C. S. & Zhao, B. (2009), 'Drilling force of SiC particle reinforced aluminum-matrix composites with ultrasonic vibration', *Key Engineering Materials* **416**, 243–247.

Yang, F. W., Liu, Y. & Zhu, Y. C. (2012), 'Conservation of weathered historic sandstone with biomimetic apatite', *Chinese Science Bulletin* .

Yang, Y. & Lin, B. (2010), 'Situations and development trends of ultrasonic machining tool and ultrasonic machining technology', *Applied Mechanics and Materials* **37-38**.

Young, M. (2011), Jedburgh Abbey: lower south range X-ray diffraction report on mineralogy of decayed sandstone, Technical Report XRD016/MEY/1111, Historic Environment Scotland.

Young, M. (2015), Short guide: Thermal imaging in the historic environment, Technical report, Historic Enviroment Scotland.

Zacny, K., Bar-Cohen, Y., Brennan, M., Briggs, G., Cooper, G., Davis, K., Dolgin, B., Glaser, D., Glass, B., Gorevan, S., Guerrero, J., McKay, C., Paulsen, G., Stanley, S. & Stoker, C. (2008), 'Drilling systems for extraterrestrial subsurface exploration', *Astrobiology* **8**(3), 665–706.

Zhang, Y., Huang, X. H. & Tian, B. Z. (2014), 'Spectrum characteristics of acoustic emission signals for sandstone instability', *Engineering Science and Technology Review* .

Zhang, Z. & Babitsky, V. I. (2011), 'Finite element modeling of a micro-drill and experiments on high speed ultrasonically assisted micro-drilling', *Journal of Sound and Vibration* .

Zhao, Z., Yang, J., Zhang, D. & Peng, H. (2017), 'Effects of wetting and cyclic wetting-drying on tensile strength of sandstone with a low clay mineral content', *Rock Mechanics and Rock Engineering* .

Zhou, M., Eow, Y., K. A. Ngoi, B. & Lim, N. (2003), 'Vibration-assisted precision machining of steel with PCD tools', *Materials and Manufacturing Processes* **18**(5), 825–834.